Universidade de Aveiro
Departamento de
Electrónica, Telecomunicações e Informática
2019

Ricardo João Luis Marques Correia

Sensores Passivos alimentados por transmissão de energia sem fios para aplicações de Internet das coisas

Passive Backscatter Wireless Sensor with Wireless Power Transmission for IoT applications

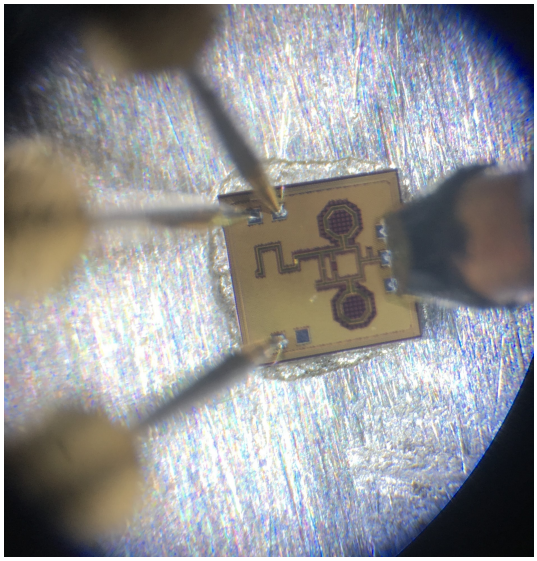

Universidade de Aveiro Departamento de Electrónica, Telecomunicações e Informática
2019

Ricardo João Luis Marques Correia

Sensores Passivos alimentados por transmissão de energia sem fios para aplicações de Internet das coisas

Passive Backscatter Wireless Sensor with Wireless Power Transmission for IoT applications

Tese apresentada à Universidade de Aveiro para cumprimento dos requisitos necessários à obtenção do grau de Doutor em Engenharia Eletrotécnica, realizada sob a orientação científica do Prof. Doutor Nuno Miguel Gonçalves Borges de Carvalho, Professor Catedrático do Departamento de Electrónica, Telecomunicações e Informática da Universidade de Aveiro.

o júri / the jury

Presidente / president

Professora Doutora Ana Isabel Couto Neto da Silva Miranda
Professora Catedrática, Universidade de Aveiro

vogais / examiners committee

Professor Doutor Rui Manuel Escadas Ramos Martins
Professor Auxiliar, Universidade de Aveiro

Professor Doutor Jorge Manuel dos Santos Ribeiro Fernandes
Professor Associado, Instituto Superior Técnico da Universidade Técnica de Lisboa

Professor Doutor Jorge Manuel Lopes Leal Rodrigues da Costa
Professor Associado Com Agregação, Instituto Universitário de Lisboa

Professor Doutor George Goussetis
Professor, Heriot-Watt University

Professor Doutor Nuno Miguel Gonçalves Borges de Carvalho
Professor Catedrático, Universidade de Aveiro (orientador)

agradecimentos / acknowledgments

O presente documento termina o fim de uma etapa muito importante sobre a qual tive o privilégio de viver. Esta missão tornou-se possível através do apoio, amizade, colaboração de muitas pessoas e de algumas instituições.

Ao meu orientador, Prof. Nuno Borges Carvalho, um imenso obrigado por todos ensinamentos e valores que me foram transmitidos. Pela motivação, discussões técnicas, apoio e oportunidades proporcionadas.

Ao Prof. José Vieira que me acompanhou no início da jornada e que me apresentou ao mundo da rádio-frequência e por todo o conhecimento que me transmitiu.

Ao Instituto de Telecomunicações por me ter acolhido ao longo destes anos e por me ter proporcionado um ambiente de trabalho fenomenal.

A todos os meus amigos e companheiros, pelos momentos de descontração, pelos ensinamentos, pelo acompanhamento e por todo o carinho.

Aos meus pais por todos os valores transmitidos, pela educação e todo o apoio incondicional para que nada faltasse nesta jornada.

Ao meu irmão e Ana por me terem atribuído a responsabilidade de ser padrinho da Teresa, que muitos sorrisos e muito encanto me tem dado.

À Ju, a minha companheira, melhor amiga e confidente, por toda a força, amizade, carinho, conforto, compreensão e apoio que sempre teve ao longo destes anos. Foram muitos os sacrifícios e muita distância, mas tudo se consegue.

A todos, MUITO OBRIGADO!

Palavras-Chave: Comunicação backscatter, transferência de energia sem fios, sensor passivo, eficiência de conversão RF-DC, circuito integrado de microondas monolítico

Resumo

Atualmente, as redes de sensores sem fios dependem da duração da bateria e,deste modo, existe um interesse renovado em criar um esquema de rede de sensores passivos na área de internet das coisas e sistemas de redes de sensores sem fios relacionados com o espaço. Os desafios do futuro das comunicações de rádio têm uma dupla evolução, sendo um o baixo consumo de energia e, outro, a adaptação e o uso inteligente dos recursos disponíveis. Rádios diferentes dos convencionais devem ser usados para reduzir o consumo de energia e devem adaptar-se ao ambiente de forma inteligente e eficiente, de modo a que este use a menor quantidade de energia possível para estabelecer a comunicação. Esta tese incide sobre o desenvolvimento de sensores passivos baseados em comunicação de baixo consumo energético (backscatter) com recurso a transmissão de energia sem fios de modo a que possam ser usados em diferentes aplicações inseridas na internet das coisas. Nesse sentido, várias modulações de alta ordem para a comunicação backscatter serão exploradas e propostas com o objectivo de aumentar a taxa de transmissão de dados. Além disso, os sensores precisam de ser reduzidos em tamanho e económicos de modo a serem incorporados em outras tecnologias ou dispositivos. Consequentemente, o front-end de rádio frequência dos sensores será projetado e implementado em circuito integrado de microondas monolítico.

Keywords: Backscatter communication, wireless power transmission, passive sensor, RF-DC conversion efficiency, monolithic microwave integrated circuit.

Abstract

Nowadays, the Wireless Sensor Networks (WSNs) depend on the battery duration of the sensors and there is a renewed interest in creating a passive sensor network scheme in the area of Internet of Things (IoT) and space oriented WSN systems. The challenges for the future of radio communications have a twofold evolution, one being the low power consumption and, another, the adaptability and intelligent use of the available resources. Specially designed radios should be used to reduce power consumption, and adapt to the environment in a smart and efficient way. This thesis will focus on the development of passive sensors based on low power communication (backscatter) with Wireless Power Transfer (WPT) capabilities used in IoT applications. In that sense, several high order modulations for the communication will be explored and proposed in order to increase the data rate. Moreover, the sensors need to be small and cost effective in order to be embedded in other technologies or devices. Consequently, the RF front-end of the sensors will be designed and implemented in Monolithic Microwave Integrated Circuit (MMIC).

Contents

Contents i

List of Figures v

List of Tables xiii

List of Acronyms xiv

1 Introduction 1
- 1.1 Background and motivation . . . 1
- 1.2 The Problem . . . 3
- 1.3 The Thesis . . . 6
- 1.4 Original Contributions . . . 7
- 1.5 Publications . . . 8
- 1.6 Document Organization . . . 10

2 State of the Art 12
- 2.1 Backscatter communication . . . 12
  - 2.1.1 History . . . 12
- 2.2 Wireless Power Transmission . . . 14
  - 2.2.1 History . . . 14
  - 2.2.2 RF-DC Converter . . . 17
- 2.3 Different combinations in Backscatter communication . . . 22
  - 2.3.1 Backscatter communication with WPT capabilities . . . 22
  - 2.3.2 Backscatter communication with high order modulation . . . 23
  - 2.3.3 Ambient Backscatter communication . . . 24
  - 2.3.4 Backscatter existing standards . . . 25
  - 2.3.5 Augmented Backscatter radio communication range . . . 27
- 2.4 Monolithic Microwave Integrated Circuit . . . 28
  - 2.4.1 History of MMIC . . . 29

3 Backscatter modulation **31**
3.1 Analysis of Backscatter-Radio Link Budgets . . . 31
3.2 Backscatter Modulation for Wearable Devices . . . 41
3.2.1 Design strategy . . . 41
3.2.2 DUT Performance in Wearable Applications . . . 43
3.3 Conclusions . . . 46

4 Backscatter modulation with WPT capabilities **47**
4.1 Backscatter WPT . . . 47
4.1.1 Backscatter design . . . 48
4.1.2 WPT RF-DC dual band design . . . 48
4.1.3 Integrating Backscatter solution with WPT solution . . . 50
4.1.4 Results . . . 52
4.1.5 Backscatter Design . . . 52
4.1.6 WPT RF-DC dual band design . . . 53
4.1.7 Integrating Backscatter solution with WPT solution . . . 55
4.2 Passive Sensor with Over the Air validation . . . 63
4.2.1 WPT and Backscatter Techniques . . . 63
4.2.2 RF Front End Design and Optimization . . . 64
4.2.3 Sensing and Processing Elements . . . 66
4.2.4 Measurements and Results . . . 69
4.3 Single Transistor Passive Backscatter Sensor . . . 75
4.3.1 Circuit description . . . 75
4.3.2 Experimental results . . . 77
4.4 Conclusions . . . 80

5 High Order backscatter modulation **81**
5.1 QAM backscatter modulation design strategy . . . 81
5.1.1 Constellation Diagram Impedance Generation . . . 85
5.1.2 QAM Backscatter Implementation . . . 89
5.1.3 Results . . . 89
5.2 Dual-Band High Order Modulator . . . 96
5.2.1 Circuit description . . . 96
5.2.2 Results . . . 99
5.3 4-PAM Modulation of Ambient FM Backscattering for Spectrally Efficient Low Power Applications . . . 103
5.3.1 Sensor Node/Tag Design . . . 105
5.3.2 Ambient FM 4-PAM Modulation . . . 109
5.3.3 Receiver . . . 109

5.3.4 Measurement Results . . . 112
5.4 High order QAM modulator with WPT capabilites . . . 114
5.4.1 Backscatter modulator and rectifier implementation . . . 115
5.4.2 System characterization and evaluation . . . 116
5.5 High Order Backscatter Modulation for IoT Applications: Channel Evaluation and Implementation . . . 118
5.5.1 Circuits description . . . 119
5.5.2 Setup Analysis and Description . . . 120
5.5.3 Measurements and Results . . . 125
5.6 Conclusions . . . 129

6 MMIC QAM modulator **131**
6.1 Overview and description of the QAM modulator . . . 131
6.2 Simulations and design of the QAM modulator . . . 132
6.3 Plans for the experimental measurement setup . . . 140
6.4 Conclusions . . . 142

7 Conclusions and Future Work **143**
7.1 Conclusions . . . 143
7.2 Main achievements in the scope of this thesis . . . 144
7.3 Future Work . . . 144

Bibliography **147**

A Chirp Based Backscatter Modulation **163**

List of Figures

1.1 Estimates for associated manufacturing energy and the waste of the IoT related batteries. a) Battery powered IoT devices, b) Annual battery consumption, c) Energy for battery manufacturing. 4

1.2 Wireless sensors power subsystem. a) Simulated wireless sensor with commercial components [1]. b) Optimized wireless sensor with commercial components [1]. c) Sensor with RF backscatter communication [2]. 5

2.1 History of RFID and backscatter communication. 13

2.2 History of radio transmission and wireless power transfer. 16

2.3 State of the art in RF-DC converters, with different topologies, from 450 MHz to 94 GHz. 18

2.4 Different rectifier topologies. (a) Series diode rectifier. (b) Shunt diode rectifier. (c) Shunt diode with $\lambda/4$ stub. (d) N-stage Dickson voltage multiplier. . 20

2.5 A typical Schottky diode I-V curve with respective operating regions. 21

2.6 History of MMIC. 30

3.1 Passive RFID system overview 32

3.2 Data exchange between an RFID reader and a tag. 33

3.3 Equivalent circuit of an RFID tag 34

3.4 Reader to Tag and Tag to Reader communication. 35

3.5 ASK and PSK tag modulation effects. 36

3.6 Different configurations of the antennas in backscatter link. (a) Monostatic. (b) Bistatic Collocated. (c) Bistatic Dislocated. 38

3.7 Average power delivered to the tag and the modulated power backscattered by the tag received by the reader in the monostatic configuration. 39

3.8 Average power delivered to the tag and the modulated power backscattered by the tag received by the reader in the monostatic configuration, considering four different approaches: The tag operating with ASK modulation (passive); The tag operating with PSK modulation (semi-passive); The tag operating at two different frequencies (adding 400 MHz to supply the tag); The tag operating at two different frequencies (adding 1.7 GHz to supply the tag). 40
3.9 Photograph of the developed backscatter modulator. Element values are L1 = 22 nH, L2 = 27 nH. Substrate for the transmission lines is Astra MT77, thickness = 0.762 mm, ε_r = 3.0, tan δ = 0.0017. 41
3.10 Simulations of backscatter modulator. On the left the proposed circuit developed in ADS. On the right the results obtained for the S11 from the simulated circuit with two different voltages at the gate of transistor (0 V and 0.8 V). . . 42
3.11 Measured S_{11} of the tunned chip antenna. 42
3.12 Block diagram of a battery-free wearable device. 43
3.13 Backscatter modulator embedded into the watch. 44
3.14 Laboratorial measurement setup. 44
3.15 Two different scenarios to measure the backscatter modulator embedded into the watch. On the left the person is placed in front of the setup. On the right the person is turning his back to the setup. 45
3.16 Power received by the spectrum analyzer at 916 MHz. 45
3.17 Measurement results with the person placed at 4 m from the transmitter/receiver. On the left the person is placed in front of the setup. On the right the person is turning his back to the setup. 46

4.1 Block diagram of proposed system based on backscattering with WPT. 48
4.2 (a) Configuration of proposed backscatter circuit. (b) Photograph of the backscatter circuit. Element values are L1 = 28.9 mm, W1 = 0.4 mm, L2 = 1 mm, W2 = 1.8 mm, L3 = 13.5 mm, W3 = 1.5 mm, L4 = 16.3 mm, W4 = 0.7 mm, L5 = 1.3 mm, W5 = 0.6 mm, R1 = 50 Ω, C1 = 47 pF. Substrate for the transmission lines is Astra MT77, thickness = 0.762 mm, ε_r = 3.0, tan δ = 0.0017. 49
4.3 Block diagram of dual band rectifier circuit. 49
4.4 (a) Configuration of proposed dual band rectifier. (b) Photograph of the dual band rectifier. Element values are L1 = 4.7 mm, W1 = 0.7 mm, L2 = 7.9 mm, W2 = 2 mm, L3 = 7 mm, W3 = 2 mm, L4 = 5.4 mm, W4 = 0.4 mm. Substrate for the transmission lines is Astra MT77, thickness = 0.762 mm, ε_r = 3.0, tan δ = 0.0017. 50
4.5 Different modes of operation with different frequencies (a) $V_{Gate} = 0$ V for 1.8 GHz (b) $V_{Gate} = 0.6$ V for 1.8 GHz. (c) $V_{Gate} = 0$ V for 2.45 GHz. (d) $V_{Gate} = 0.6$ V for 2.45 GHz. 51

4.6 (a) Configuration of proposed backscatter modulator and dual band rectifier circuit. (b) Photograph of the backscatter modulator and dual band rectifier. Element values are L1 = 1 mm, W1 = 1.6 mm, L2 = 6.3 mm, W2 = 0.8 mm, L3 = 6.5 mm, W3 = 0.5 mm, L4 = 1 mm, W4 = 1.9 mm, L5 = 4 mm, W5 = 1.2 mm. Substrate for the transmission lines is Astra MT77, thickness = 0.762 mm, ε_r = 3.0, tan δ = 0.0017. 52
4.7 S_{11} parameter as function of frequency for two different values of transistor's gate voltage. (a) $V_{Gate} = 0$ V. (b) $V_{Gate} = 0.6$V. 53
4.8 Simulated and experimental results of output power of dual band rectifier as function of input power per tone. 55
4.9 Simulated and experimental results for output power of backscatter modulator and dual band rectifier as function of input power per tone. (a) $V_{Gate} = 0$ V. (b) $V_{Gate} = 0.6$ V. 56
4.10 Simulated S_{11} parameter as function of frequency and input power for two different values of gate voltage. 57
4.11 Simulated and experimental results for DC Vout voltage of backscatter modulator and dual band rectifier as function of input power per tone. (a) $V_{Gate} =$ 0V. (b) $V_{Gate} = 0.6$V. 59
4.12 Measured S_{11} parameter as function of frequency and input power for two different values of gate voltage. 60
4.13 Experimental results of the reflected waves (a) Pin = -12 dBm. (b) Pin = 0 dBm. (c) Pin = 2 dBm. (d) Two tones (1.7 and 2.35 GHz) for different input powers. 61
4.14 Photograph of the measurement setup. 62
4.15 Block diagram of the measurement setup. 62
4.16 Block diagram of the implemented system. 64
4.17 Photograph of implemented system with backscatter modulator combined with Wireless Power Transmission (WPT). Element values are L1 = 21.2 mm, W1 = 1.87 mm, L2 = 15.1 mm, W2 = 1.0 mm, L3 = 21.9 mm, W3 = 0.8 mm, L4 = 11.3 mm, W4 = 1.87 mm, L5 = 17.1 mm, W5 = 1.2 mm, L6 = 6.7 mm, W6 = 1.1 mm, L7 = 18.6 mm, W7 = 0.7 mm, R1 = 50 , and C1 = 47 pF. Substrate for the transmission lines is Astra MT77, thickness = 0.762 mm, ε_r = 3.0, tan δ = 0.0017. 65
4.18 Developed Printed Circuit Board (PCB) 67
4.19 Code diagram. 68
4.20 Message with tag ID, sensor ID, measured temperature, and correction bits. . 69
4.21 Measurements setup. 70
4.22 Dual-band antenna used on the tag. a) Photograph of the dual-band antenna. b) S_{11} parameter of the dual-band antenna. 70

4.23 Two patch antennas used on the reader. a) S_{11} parameter of the WPT patch antenna. b) S_{11} parameter of the backscatter communication patch antenna. c) Photograph of both antennas used on the reader. 71
4.24 Output voltage as function of input power. 73
4.25 WPT at distance of 300 cm. 74
4.26 Distance as function of transmitted power in active mode of sensor. a) Backscatter communication on active mode,considering a receiver sensitivity of -85 dBm. b) WPT that enables active mode. 74
4.27 Block diagram of proposed system 75
4.28 Design of the circuit which includes the rectifier and modulator. a) Photograph. b) Circuit schematic. 76
4.29 Simulated and measured S_{11} parameter for $P_{in} = 10$ dBm. 77
4.30 Simulated and measured results for efficiency as function of input power for Freq. = 2.45 GHz. (a) Simulated efficiency. (b) Measured efficiency. 78
4.31 Measured S_{11} parameter as function of input power at 2.45 GHz for different values of gate voltage. (a) $P_{in} = -10$ dBm. (b) $P_{in} = 0$ dBm. (c) $P_{in} = 10$ dBm. (d) $P_{in} = 20$ dBm. 79

5.1 Three types of design for two different backscatter modulation schemes. a) Amplitude Shift Keying (ASK) backscatter modulation scheme; b) Four-state Quadrature Amplitude Modulation (4-QAM) backscatter modulation scheme without the possibility to increase the modulation order; c) Our proposed scheme for 4-QAM backscatter modulation with the possibility to increase the modulation order. 83
5.2 Photograph of the 4-QAM backscatter circuit. 84
5.3 Model of the QAM solution. 84
5.4 Simulation of the model for 4-QAM solution. 85
5.5 Simulation of the model for 16-QAM solution. 86
5.6 Block diagram for different impedance terminations. 86
5.7 Model for the characterization. a) Design of the circuit. b) Photograph of the proposed characterization circuit. 87
5.8 Simulated, measured and selected measured S11 for different voltage levels at the gate of transistor for 2.45 GHz at 0 dBm. 88
5.9 Simulated S_{11} for different voltage levels (from 0 V to 0.6 V with a step of 0.01V) at the gate of each transistor for 2.45 GHz at 0 dBm. 88
5.10 16-QAM backscatter modulation scheme. a) Design of 16-QAM backscatter modulator. b) Photograph of the 16-QAM backscatter circuit. 89
5.11 Photograph of the measurement setup. 90

5.12 Simulated and measured S_{11} for different voltage levels at the gate of each transistor for 2.45 GHz at 0 dBm. 90

5.13 Measurement setup for demodulation and achievable data rates. a) Block diagram. b) Photograph. 92

5.14 Received 16-QAM constellation for a center frequency of 2.45 GHz for different bit rates. (a) 4 Mb/s with 8.19% of EVM and 21.74 dB of SNR. (b) 40 Mb/s with 10.96% of EVM and 19.20 dB of SNR. (c) 120 Mb/s with 16.76% of EVM and 15.52 dB of SNR. 92

5.15 Measured EVM of the 16-QAM with a varying data rate. 93

5.16 Eye diagrams of received demodulated data for varying data rates. (a) 256 kb/s. (b) 2.4 Mb/s. (c) 4 Mb/s. (d) 120 Mb/s. 94

5.17 Sensitivity of the modulator. a) With 1% of variation on each gate transistor. b) With 5% of variation on each gate transistor. The red marker indicates the limit that is possible to achieve by calibration of the voltages. 95

5.18 Measured EVM of the 16-QAM modulator as function of input power for different data rates. 95

5.19 Block diagram of passive sensor composed by dual-band antenna, M-QAM high order modulator and a solar panel. 97

5.20 Dual-band Wilkinson power divider with scheme and values used. 97

5.21 Simulated results of the dual-band Wilkinson power divider. 98

5.22 Photograph of the implemented circuit, dual-band M-QAM backscatter modulator. 98

5.23 Simulated reflections coefficients by varying the voltage at each gate of transistor from 0 V to 0.6 V with a step of 0.01 V. a) Frequency = 900 MHz. b) Frequency = 2.45 GHz. 99

5.24 Measured results of 4-QAM backscatter modulator for both frequencies 900 MHz and 2.45 GHz with -20 dBm of input power. 100

5.25 Photogrpah of the measurement setup. 100

5.26 Measurement setup used for high data rate validation. a) Block diagram. b) Photograph. 101

5.27 Eye diagrams of received demodulated data for varying data rates. (a) 400 kb/s at 900 MHz. (b) 400 kb/s at 2.35 GHz. (c) 4 Mb/s at 900 MHz. (d) 4 Mb/s at 2.35 GHz. (e) 40 Mb/s at 900 MHz. (f) 40 Mb/s at 2.35 GHz. 102

5.28 FM ambient backscatter communication scheme. An example application could be the identification of clothes in a mall using tablets and low cost SDRs. 103

5.29 Backscatter radio principle: An RF transistor alternates the termination loads Z_i of the antenna corresponding to different reflection coefficients Γ_i. Four reflection coefficients ($n = 4$) could create a four pulse amplitude modulation (4-PAM). 104
5.30 Schematic of Proof-of-concept tag. A low power micro-controller reads the sensors and controls the RF front-end circuit. 106
5.31 Digital-to-Analog Converter output voltage versus the tag power consumption. The tag was measured at 1.8 V when the ADC was turned off. 106
5.32 The fabricated tag prototype with the RF front-end board. The tags is powered by a solar panel. 107
5.33 Smith Chart with measured reflection coefficient values for 4 different voltage levels at the gate of transistor. The *Pin* was fixed at -20 dBm for frequencies $87.5 - 108$ MHz. 108
5.34 An oscilloscope measurement of the sending packet. Voltage levels correspond to the 4-PAM symbols at the gate of the transistor are presented. 109
5.35 Flowchart of the receiver algorithm implemented in MATLAB software. . . . 110
5.36 Received packet signal. a) Signal after squared absolute operation and b) signal after matched filtering for $T_{\text{symbol}} = 5.4$ ms. 110
5.37 Received packet without the preamble after matched filtering. The respective symbols can be decided using three thresholds. 111
5.38 Schematic of the experimental setup in the anechoic chamber. The transmitter-to-tag distance and the tag-to-reader distance were 1.5 m. 112
5.39 Experimental Bit Error Rate (BER) versus the transmitted power at the generator. The bit rate was 345 bps and the distances transmitter-to-tag, tag-to-reader were 1.5 m. 113
5.40 Comparison of wireless technology average consumption and data rates. . . . 114
5.41 Photograph of the proposed system, composed by a 16-QAM modulator and a rectifier. Substrate for the transmission lines is Astra MT77, thickness = 0.762 mm, $\varepsilon_r = 3.0$, $\tan\delta = 0.0017$. 115
5.42 Photograph of the measurement setup used for demodulation. 116
5.43 Received constellations with EVM and energy per bit consumption as function of input power for different data rates. (a) 4 Mb/s. (b) 100 Mb/s. (c) 480 Mb/s. (d) 960 Mb/s. 117
5.44 DC output voltage and efficiency as function of input power at 1.7 GHz with unbiased gate of each E-pHEMT. 117
5.45 DC power consumption of the 16-QAM backscatter modulator over a range of data rates. 118
5.46 Backscatter modulator working at 2.45 GHz (circuit 1). 119

5.47 Dual band backscatter modulator working at 900 MHz and 2.45 GHz (circuit 2).120
5.48 Block diagram of cable test backscatter modulation measurement setup. . . . 121
5.49 Photograph of cable test backscatter modulation measurement setup. 121
5.50 Block diagram of OTA backscatter modulation measurement setup with antennas. 122
5.51 Photograph of OTA backscatter modulation measurement setup with antennas.122
5.52 LabVIEW application to perform backscatter modulation characterization. . . 123
5.53 Flowchart of LabVIEW application. 124
5.54 Algorithm process example to detect M-QAM points, where initial and centered constellations are presented, from backscatter modulator (circuit 1). . . 125
5.55 Cable test and OTA measurement results using circuit 2. 126
5.56 16-QAM, 32-QAM and 64-QAM constellation for backscatter modulator (circuit 1), with corresponding EVM values. 127

6.1 Application example for the MMIC QAM backscatter modulation. 132
6.2 Different drain impedance of the transistor as function of width, length and number of gates. 133
6.3 Layout of the selected transistor. The transistor presents 10 gates, 100μm of width and 130 nm of length. 133
6.4 Schematic of the QAM modulator optimized for a frequency of 24 GHz. . . . 134
6.5 Simulated S_{11} parameter with -10 dBm of input power and variations at the gate of each transistor from 0 V to 1 V with a step of 0.01 V. 134
6.6 Inductor layout simulation. 135
6.7 Inductor layout simulated results. a) Q factor obtained. b) Inductor value obtained. 136
6.8 MMIC QAM layout modulator designed in ADS. The element values are: C1 = 385.117 fF, C2 = 30.012 fF, R = 100 Ohm. 136
6.9 Simulated MMIC QAM layout modulator. The simulation was performed in ADS at 24 GHz from -40 dBm to 10 dBm of input power with a step of 1 dBm. 137
6.10 Simulated MMIC QAM layout modulator. The simulation was performed in ADS at 24 GHz with -10 dBm of input power and varying each gate of transistor from 0 V to 1 V with a step of 0.01 V. 137
6.11 MMIC QAM layout behavior modulator with -10 dBm of input power for different frequencies, from 20 GHz to 30 GHz. a) 20 GHz. b) 21 GHz. c) 22 GHz. d) 23 GHz. e) 24 GHz. f) 25 GHz. g) 26 GHz. h) 27 GHz. i) 28 GHz. j) 29 GHz. k) 30 GHz. 138
6.12 Scheme of the QAM modulator designed with Virtuoso. 139
6.13 Layout of the modulator designed with Vituoso. (a) Layout complete with ground plane. (b) Layout without ground plane 139

6.14 MMIC QAM modulator measurement setup for S_{11} parameter analysis. . . . 140
6.15 MMIC QAM modulator measurement setup for data rate and modulation order evaluation. . . . 141
6.16 MMIC QAM modulator system integration. . . . 141

7.1 Possible solution of multiband EH combined with FM ambient backscatter modulation. . . . 145

List of Tables

2.1 Performance summary and comparison 24
2.2 Ambient Backscatter Communications Systems 26
2.3 Overview of Reflection Amplifiers 27

4.1 Simulated results of system impedance as function of transistor's gate voltage and frequency. 54
4.2 Experimental results of system impedance as function of transistor's gate voltage and frequency 54
4.3 Dual band rectifier simulated results of dc output voltage as function of input power per tone 54
4.4 Dual band rectifier experimental results of dc output voltage as function of input power per tone 55
4.5 Corresponding code from the measured temperature. 68

5.1 Simulated and measured S_{11} for different levels at the gate of transistors (M1 and M2). 91
5.2 Measured S_{11} for different levels at the gate of transistors (V1 and V2). 100
5.3 4-PAM Modulation Parameters 105
5.4 High order Modulation vs Power Consumption vs Bit Rate 113
5.5 Optimum points and voltages for backscatter modulator (circuit 1) for a 16-QAM modulation considering cable test measurement. 127
5.6 EVM results from backscatter modulator (circuit 1) for several power values at the input considering a cable test measurement. 128
5.7 EVM results from backscatter modulator (circuit 2) for several power values at the input considering a cable test measurement. 128
5.8 EVM results from backscatter modulator (circuit 2) for different distances, considering OTA measurement scenario. 128

List of Acronyms

ADS	Advanced Design System
ASK	Amplitude Shift Keying
BER	Bit Error Rate
BiCMOS	Bipolar Complementary Metal-Oxide-Semiconductor
BLE	Bluetooth Low Energy
BPSK	Binary Phase Shift Keying
CW	Continuous Wave
CMOS	Complementary Metal-Oxide-Semiconductor
DAC	Digital-to-Analog Converter
EAS	Electronic Article Surveillance
EH	Energy Harvesting
ERP	Effective Radiated Power
ETSI	European Telecommunications Standards Institute
FET	Field Effect Transistor
FPGA	Field-Programmable Gate Array
GaAs	Gallium Arsenide
GaN	Gallium Nitride
HBT	Heterojunction Bipolar Transistor
HEMT	High-Electron-Mobility Transistor
IC	Integrated Circuit

IoT	Internet of Things
InP	Indium Phosphide
IPV	Instantaneous Power Variance
IZ	Interrogation Zone
LoRa	Long Range
LSSP	Large Signal S-Parameter
MESFET	Metal Semiconductor Field Effect Transistor
MMIC	Monolithic Microwave Integrated Circuit
PAM	Pulse Amplitude Modulation
PAPR	Peak-to-Average Power Ratio
PLL	Phase-locked Loop
PNA	Performance Network Analyzer
POW	Power-optimized Waveforms
PSK	Phase Shift Keying
QAM	Quadrature Amplitude Modulation
RAPM	Retrodirective Array Phase Modulator
RCS	Radar Cross-section
RF	Radio Frequency
RFIC	Radio Frequency Integrated Circuit
RFID	Radio Frequency Identification
SDR	Software Defined Radio
Si	Silicon
SiGe	Silicon Germanium
SNR	Signal-to-noise Ratio
SPCC	Staggered-Pattern Charge Collector

SPS	Solar-Power Satellite
SSP	Space Solar Power
UHF	Ultra High Frequency
UWB	Ultra-wideband
WET	Wireless Energy Transfer
WoR	Wake-on Radio
WPT	Wireless Power Transfer
WSN	Wireless Sensor Network
4-QAM	Four-state Quadrature Amplitude Modulation

Chapter 1

Introduction

Outline

This chapter starts by providing the scope and the main motivation for this work. Then, the thesis main contributions are presented and finally, the chapter is concluded with the presentation of the document organization.

1.1 Background and motivation

The so called IoT is progressively becoming a normal thing in everyones daily lives. The desire of connecting everyday objects to the internet and to each other, to interact with other users and machines, is increasingly becoming a reality. The number of applications that IoT can provide is endless. It can be in wearables, cars, highways, smart homes, smart cities, smart workspaces and one of the most important, the emergency systems. As the number of uses increases largely, it seems reasonable that the number of users will also be astronomic, because of that, it is estimated that this technology will connect 50 billion of devices using the internet around 2020 [3].

As the IoT devices continues to increase and evolve, all that concerns the communications go in the same direction, which leads to higher data rate communications and data services. Thus, it becomes easy to understand that in order to IoT succeed, a scalable and robust communications system is essential [4]. Currently, the IoT devices typically use the already existing wired and wireless network infrastructures, however, because of all the reasons said before, those existing networks will become increasingly congested, mainly in the underserved regions of the globe. As it was described, the massive deployment of IoT sensors for either catastrophic scenarios, agriculture, oil pipe monitoring, railway line, and power lines is of fundamental interest for the overall monitoring of these structures in a controlled and condensed form, which will actually reduce significantly the cost of maintenance and the revenue of most of these companies. Nevertheless, these structures are significantly

large in dimensions, which imposes that a more convenient radio communication is available for monitoring those. Unfortunately, the need of power and energy supply to those sensors is similar to traditional IoT solutions. It is expected that these sensors are able to live (be active) for several years, ideally spanning for 20 or more years, which imposes that some alternatives to power up and/or supply those sensors with alternative energy sources, are of fundamental need for correct operation.

The rapid increase in the progress and development of wireless communications and identification made it possible to track and sense some materials wirelessly. The use of Radio Frequency Identification (RFID) technology as an effective and reliable way for tracking and sensing has gain a lot of importance in recent years. The RFID technology is a short range wireless communication system that comprises a tag, reader, data transfer, and processing subsystems. This technology has been applied in many areas, such as industrial and automation, transportation control management, and access control, and has an enormous potential for future applications (structural health monitoring, human health monitoring, and so on). Some potential scenarios for the optimization of power are the passive sensors where the sensing needs more power than in the normal situation. Passive tags are very cheap, small, and low maintenance, and are already used in various applications [5]. Passive or battery-free RFID tags are an attractive option for WSNs and RFID applications, because they do not need any maintenance requirements. This is due to the fact that passive RFIDs do not use a battery for power storage, since energy is harvested from several sources. Examples of these sources are solar [6], motion or vibration [7], ambient RF [8], or an RF signal generated by the RFID reader. The main difference between passive and active RFID wireless transceivers is the backscatter modulation [9] for the uplink, which consist in reflecting and modulating an incident radio signal. An energy harvester and power management circuitry are responsible for collecting sufficient energy to power the tag and any additional sensor. As previously mentioned, this energy can come from a variety of sources but is typically reader-delivered RF power. Over the last years, RF Energy Harvesting (EH), which is the capability of converting RF signals into electricity, has gained a lot of interest [10]. This renewed interest for the area already resulted in the first commercial solutions. With the growth of portable applications, many companies, such as eCoupled, WiPower, and Powermat, have developed solutions for the commercial market of Wireless Energy Transfer (WET). Thus, there is a strong motivation to enable a WSN with WPT, which could be capable to afford all the operational costs. The new paradigm should be able to communicate and to enhance the power to the sensor by using only electromagnetic waveforms transmitted over the air. This gave rise to important concepts as backscatter radio solutions [11–14] but also to WPT approaches [15–17] that when combined can actually be a solution to build up totally passive WSN [18]. In most RFID systems and passive sensors, the reader to tag communication is an ASK or Phase Shift Keying (PSK) that modulates either the amplitude, or both the ampli-

tude and phase, of the readers transmitted RF carrier. However, some recent works [19–22] have shown that modulated backscatter can be extended to include higher order modulation schemes.

In conclusion, the importance of developing this thesis concerns the following research lines:

- WPT to overcome the limitations related with battery maintenance and lifetime of sensors.
- Backscatter communication - one of the key challenges for IoT is the limited network lifetime due to massive IoT devices being powered with batteries. The low-power and low-complexity backscatter communication has emerged to be a promising technology to overcome this challenge.
- High order backscatter communication to increase the data rate of the sensors.
- Ambient backscatter communication to simplify the network sensor, eliminating the need of dedicated RF transmitters.
- Synthesize Long Range (LoRa) signals, in order to use the already developed receivers, with very low sensitivities.
- MMIC to minimize the costs and size and to enable the possibility of embedding the technology into other devices.

1.2 The Problem

As pointed out in the 1.1, the massive growing of IoT sensors will enable the deployment of the WSNs which will led to the increase of the number of batteries per device. In [23], the associated manufacturing energy and the waste of the IoT related batteries was explored. Considering that in 2025 there will be approximately 80 billion of connected devices, the study in [23] estimated the number of the battery powered IoT devices without the passive devices and all mobile devices and ended up with an estimate of 23 billion battery powered devices in 2025. Figure 1.1(a) presents the results obtained for the battery powered IoT devices.

Moreover, in the study [23] they assumed one battery per IoT device, and each was replaced every second year. Thus, they could estimate the number of annual batteries consumed, which it is presented in Fig. 1.1(b). In 2025, 12 billion of batteries will be needed for powering the IoT devices.

The same study [23] explored the energy needed to manufacture the 12 billion of batteries, assuming that a battery requires 100 times the energy capacity of it and considering a

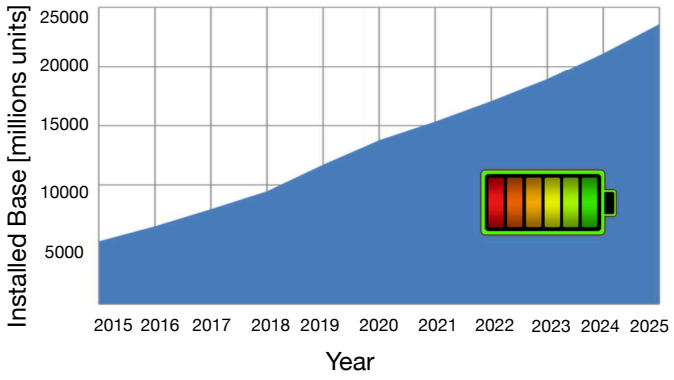

(a)

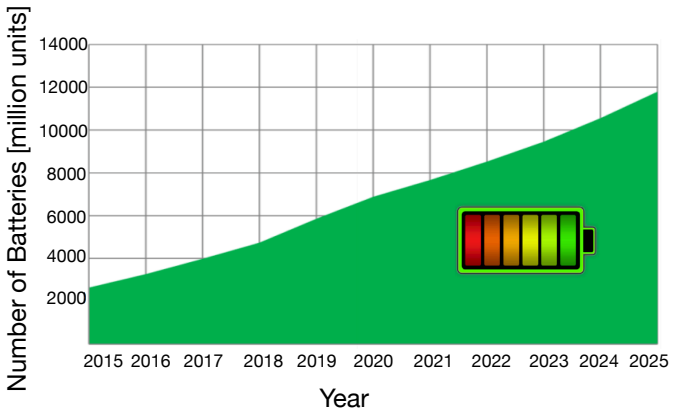

(b)

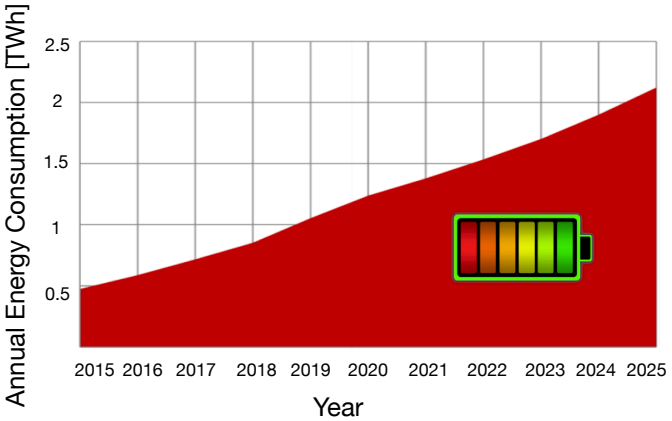

(c)

Figure 1.1: Estimates for associated manufacturing energy and the waste of the IoT related batteries. a) Battery powered IoT devices, b) Annual battery consumption, c) Energy for battery manufacturing.

typical AAA alkaline battery with a capacity of 1.8 Wh (1.2 Ah, 1.5 V). Figure 1.1(c) presents an estimate for worldwide energy consumption for IoT battery manufacturing, and in 2025 the manufacture of these IoT batteries is expected to add approximately 2 TWh of energy consumption.

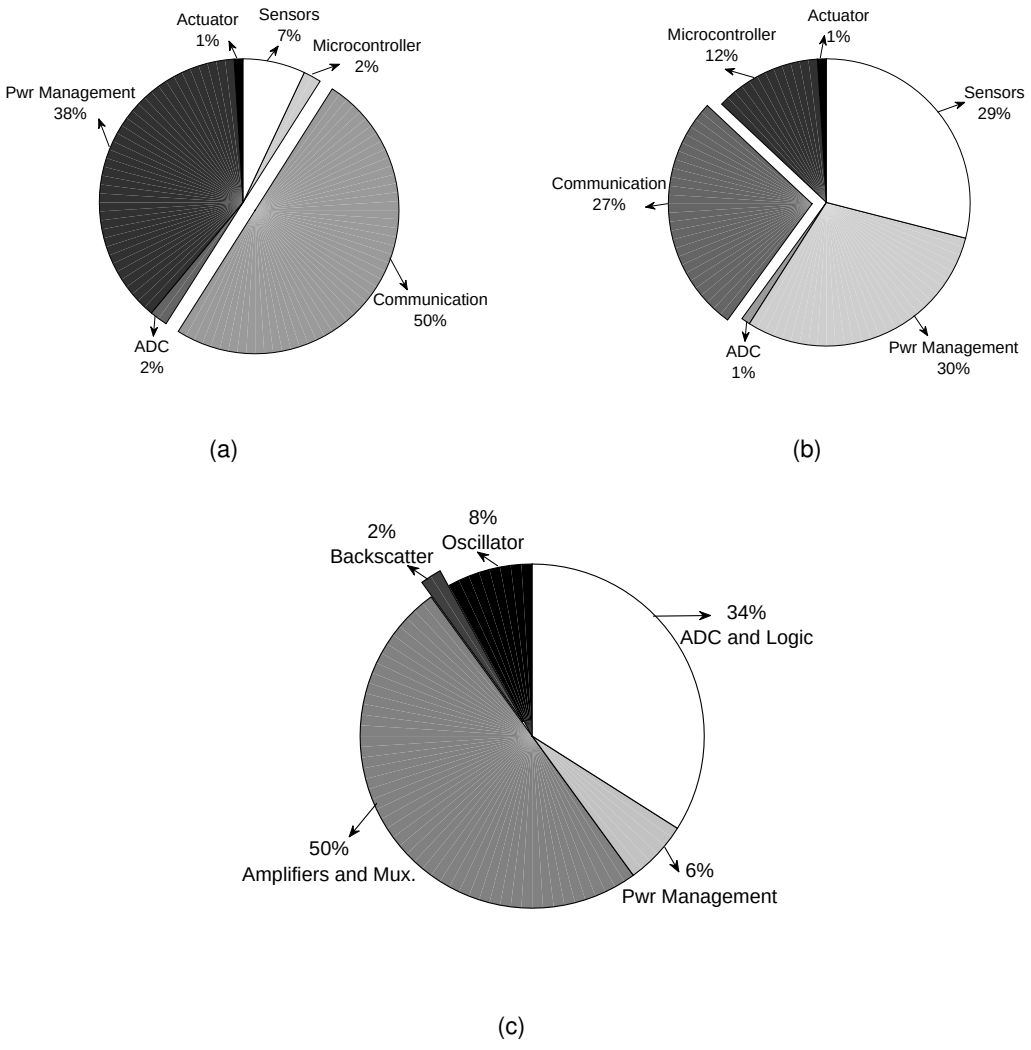

Figure 1.2: Wireless sensors power subsystem. a) Simulated wireless sensor with commercial components [1]. b) Optimized wireless sensor with commercial components [1]. c) Sensor with RF backscatter communication [2].

Through the presented studies, one can be said that the major problem of these devices is the battery. Thus, one of the focus of this thesis will be the exploration of WPT to replace the batteries.

Another challenge that we want to overcome in this thesis, is to reduce the power consumed while the sensors are communicating. In most of the sensors, the power consumed by the wireless link will be the most significant part of the total system power. When refer-

ring to low power sensors and devices, careful power management and power conservation are critical for the device lifetime and effectiveness. Some wireless sensors power subsystem examples were taken from the state of the art and are presented in Fig. 1.2. In Fig. 1.2(a) the radio consumption is 50% [1]. In [1] the authors simulated an optimized sensor for low powering operation by reducing the power management circuitry, the ADC and radio blocks during the active modes. However the radio consumption is 27%, Fig. 1.2(b). In [2] the authors refer to a backscatter based sensor and it can be seen in Fig. 1.2(c), that the radio consumption reduced to 2%. Through this analysis one can be said that the power of the sensors can be reduced by using different approaches in the communication, namely backscatter.

A key challenge of this thesis will be the combination of the two proposed solutions, the WPT to replace the batteries and the backscatter communication to decrease the radio power consumption of the sensor.

1.3 The Thesis

The purpose of this PhD is to study innovative and disruptive ways to improve the design of suitable passive sensors regarding the efficiency of RF-DC converters to maximize energy collection, power optimization, reduce operational costs, increase the communication performance and reduce size of sensors. Within the framework of this work, the focus will be to obtain cost-effective MMIC passive sensors capable of combining WPT with backscatter modulation (from ASK to Quadrature Amplitude Modulation (QAM)).

As referred in the 1.1, the main objective of this thesis is the design of wireless passive sensors that use low power communication (backscatter) that can be combined with WPT. In that sense the approach that will be followed can be divided into several objectives.

The first objective of this thesis is to evaluate the most appropriate configurations of the rectifiers to be used in the WPT (number of stages & Schottky diodes) and the most suitable configurations for the backscatter modulator (Transistor / RF switch / PIN diode).

The second objective is to propose and design a prototype for the passive low power communication (backscatter radio) and to increase the modulation order from ASK to QAM, in order to increase the transmission bit rate and the distance of the communication.

The third objective is to develop prototypes of IoT sensors (temperature, humidity, air quality, soil humidity, accelerometer) that use backscatter radio communication and at the same time are supplied by wireless power transfer.

Design of the IoT sensor using MMIC approaches will be followed, to reduce the size of the radio front-end.

The main goals of this PhD are to study, characterize, implement and design suitable passive sensors that can be deployed in the IoT context. Among the different requirements,

the following will guide our work: increase efficiency of the rectifier, maximize the power optimization, reduce the power consumption of sensors, increase the communication performance and reduce the sensors area.

1.4 Original Contributions

The concept of backscatter radio communication is being pointed out as a promising architecture to cope with the foreseen challenging requirements of the future generations of sensors communication, due to its low power consumption. This Ph.D. work aims precisely in addressing some of the current limitations of such concept, by proposing and implementing innovative designs combining different technologies to improve power consumption, data rate, size and range of communication of the sensors.

This manuscript is based on work presented in papers published in top journals and conferences in the field of this thesis and containing original contributions to the state of-the-art. In particular, one can highlight the following ones:

- The development of a fully-passive sensor which consisted in combining two different technologies, backscatter communication and WPT by using two different frequencies. The sensor was tested and validated with very promising results.

- The design of an RF front-end with only one transistor and behaves as a RF-DC rectifier and a backscatter modulator, depending on the gate transistors' voltage. The solution demonstrated very promising results in terms of the rectifier efficiency and modulation.

- The design of a high order backscatter modulator with very high data rates and a reduced number of active components. It was demonstrated that this modulator can achieve different orders of modulation by varying the gate bias of two transistors.

- The development of a dual-band high order backscatter modulator that will enable the development of sensors that backscatter ambient signals instead of using a CW generator. The proposed modulator presented high data rates for two different frequencies.

- The implementation of a wireless tag that utilizes 4-PAM technique to modulate the amplitude backscattered FM signals in order to send data to a nearby reader.

- The design of a high order backscatter modulator combined with WPT. The solution presented was combined with WPT for ultra low-power wireless applications that require high bandwidth communications. The solution demonstrated the highest reported bit rate with a limited amount of RF power.

1.5 Publications

In the scope of this PhD the following developed work was already presented and/or published:

Patents:

- WO 2018/104865 Al "Passive sensor system powered by wireless energy transmission", **Ricardo Correia** and Nuno Borges Carvalho, Universidade de Aveiro e Instituto de Telecomunicações.

Book Chapters:

- N. B. Carvalho, **R. Correia**, A. Boaventura, R. Gonçalves, and D. Belo, "Far-Field Wireless Power Transmission For Low Power Applications" Chapter 6 in, Frontiers of Research and Development of Wireless Power Transfer, CMC Books, Tokyo, 2016.
- **R. Correia**, D. Belo and N. B. Carvalho, "Internet of Things", Chapter 8 in, Recent Wireless Power Transfer Technologies via Radio Waves, Naoki Shinohara, Kyoto University, Japan, April 2018.

Journals:

- **R. Correia**, D. Belo, F. Pereira, M. Jordo and N. B. Carvalho, "Backscatter Modulation for Wearable Devices: A Backscatter Modulator, Consisting of an Antenna and a 1-MHz Binary Backscatter Modulator Operating at a Carrier Frequency of 915 MHz," in IEEE Microwave Magazine, vol. 20, no. 1, pp. 78-84, Jan. 2019.
- S. N. Daskalakis, **R. Correia**, G. Goussetis, M. M. Tentzeris, N. B. Carvalho and A. Georgiadis, "Four-PAM Modulation of Ambient FM Backscattering for Spectrally Efficient Low-Power Applications," in IEEE Transactions on Microwave Theory and Techniques, vol. 66, no. 12, pp. 5909-5921, Dec. 2018.
- **R. Correia**, P. Pinho and N. B. Carvalho, "Backscatter radio communication for IoT applications." i-ETC: ISEL Academic Journal of Electronics Telecommunications and Computers, vol. 4, no. 1, 2018.
- M. Jordão, **R. Correia** and N. B. Carvalho, "Multi-sine channel optimization for RF-to-dc performance characterization," in URSI Radio Science Bulletin, vol. 2018, no. 364, pp. 39-11, March 2018.
- F. Alimenti, V. Palazzi, C. Mariotti, P. Mezzanotte, **R. Correia**, N. B. Carvalho, L. Roselli, "Smart Hardware for Smart Objects: Microwave Electronic Circuits to Make Objects Smart," in IEEE Microwave Magazine, vol. 19, no. 6, pp. 48-68, Sept.-Oct. 2018.

- **R. Correia** and N. B. Carvalho, "Ultrafast Backscatter Modulator With Low-Power Consumption and Wireless Power Transmission Capabilities" in IEEE Microwave and Wireless Components Letters, vol. 27, no. 12, pp. 1152-1154, Dec. 2017.
- F. Pereira, **R. Correia**, and N. Carvalho, "Passive Sensors for Long Duration Internet of Things Networks" Sensors, vol. 17, no. 10, p. 2268, Oct 2017.
- **R. Correia**, A. Boaventura, and N. Borges Carvalho, "Quadrature Amplitude Backscatter Modulator for Passive Wireless Sensors in IoT Applications" in IEEE Transactions on Microwave Theory and Techniques, vol. 65, no. 4, pp. 1103-1110, Apr 2017.
- **R. Correia**, N. B. Carvalho, and S. Kawasaki, "Continuously Power Delivering for Passive Backscatter Wireless Sensor Networks" in IEEE Transactions on Microwave Theory and Techniques, vol. 64, no. 11, pp. 3723-3731, Nov. 2016.

International Conferences:

- **R. Correia** and N. B. Carvalho, "OFDM-like High Order Backscatter Modulation," 2018 IEEE MTT-S International Microwave Workshop Series on 5G Hardware and System Technologies (IMWS-5G), Dublin, 2018, pp. 1-3.
- **R. Correia** and N. B. Carvalho, "Dual-Band High Order Modulation Ambient Backscatter" 2018 IEEE/MTT-S International Microwave Symposium - IMS, Philadelphia, PA, 2018, pp. 270-273.
- S. Daskalakis, **R. Correia**, G. Goussetis, M. Tentzeris, N. B. Carvalho and A. Georgiadis, "Spectrally Efficient 4-PAM Ambient FM Backscattering for Wireless Sensing and RFID Applications" 2018 IEEE/MTT-S International Microwave Symposium - IMS, Philadelphia, PA, 2018, pp. 266-269.
- F. Pereira, **R. Correia**, and N. Carvalho, "Comparison of active and passive sensors for IoT applications" 2018 IEEE Wireless Power Transfer Conference (WPTC), Jun 2018 (**accepted**).
- M. Jordão, **R. Correia** and N. B. Carvalho, "High order modulation backscatter systems characterization" 2018 IEEE Topical Conference on Wireless Sensors and Sensor Networks (WiSNet), Anaheim, CA, 2018, pp. 44-46.
- **R. Correia** and N. B. Carvalho, "HEMT based RF to DC converter efficiency enhancement using special designed waveforms" in 2017 IEEE MTT-S International Microwave Symposium (IMS), Jun 2017, pp. 609612.
- **R. Correia** and N. B. Carvalho, "Single transistor passive backscatter sensor" in 2017 IEEE MTT-S International Microwave Symposium (IMS), Jun 2017, pp. 820823.

- D. Belo, **R. Correia**, P. Pinho, and N. B. Carvalho, "Enabling a constant and efficient flow of wireless energy for IoT sensors" in 2017 IEEE MTT-S International Microwave Symposium (IMS), Jun 2017, pp. 13421344.

- D. Belo, **R. Correia**, F. Pereira and N. B. Carvalho, "Dual band wireless power and data transfer for space-based sensors" 2017 Topical Workshop on Internet of Space (TWIOS), Phoenix, AZ, 2017, pp. 1-4.

- **R. Correia** and N. B. Carvalho, "Design of high order modulation backscatter wireless sensor for passive IoT solutions" 2016 IEEE Wireless Power Transfer Conference (WPTC), Aveiro, 2016, pp. 1-3.

- M. Jordão, **R. Correia**, D. Ribeiro, P. Cruz, and N. B. Carvalho, "RF to-DC and backscatter load modulator characterization" 2016 87th ARFTG Microwave Measurement Conference (ARFTG), San Francisco, CA, 2016, pp. 1-4.

- **R. Correia**, N. B. D. Carvalho, G. Fukuda, A. Miyaji, and S. Kawasaki, "Backscatter Wireless Sensor Network with WPT Capabilities" in IEEE MTT-S International Microwave Symposium (IMS), 2015, pp. 14.

- **R. Correia**, N. B. Carvalho, and S. Kawasaki, "Backscatter radio coverage enhancements using improved WPT signal waveform" in 2015 IEEE Wireless Power Transfer Conference (WPTC), May 2015, pp. 13.

1.6 Document Organization

The thesis document was organized in eight main chapters as follows:

- **Chapter I - Introduction**: The first chapter presents the background and motivation of this Ph.D. thesis. Then, presents the problem's description that underlies the thesis, as well as the general objectives and the structure of this document;

- **Chapter II - State-of-the-art**: In this chapter an overview of the history on the backscatter communication and IoT is presented. Hence, it is shown how these two concepts are related in order to provide fully passive sensors. High order modulation in the backscatter communication is explored and a combination with WPT is described;

- **Chapter III - Backscatter modulation**: In this chapter an analysis on the link budget of the backscatter radio communication will be performed as well as the concepts behind this technology. An example of application based on the backscatter modulation will be presented and its application on wearable devices.;

- **Chapter IV - Backscatter modulation with WPT capabilities**: In this chapter the combination of WPT with backscatter modulation will be demonstrated and explained. Some pratical examples will be shown, the sensor itself working on two different frequencies (one for performing backscatter communication and the other for WPT) and distances achieved for communication and supply the sensor. Moreover a passive solution for a sensor using only one transistor will be presented and analysed. ;

- **Chapter V - High order backscatter modulation**: This chapter introduces a solution for developing a high order backscatter modulator. Different orders of modulation will be shown, as well as different data rates obtained. Moreover a dual-band high order backscatter modulator that can perform a QAM modulation in two different bands will be analysed. In this chapter a high order backscatter modulator using ambient FM radio waves will be shown. Finally, a high order backscatter modulator combined with WPT will be demonstrated.;

- **Chapter VI - MMIC QAM modulator**: This chapter will provide a description and the plan for an initial characterization of a single-chip QAM backscatter modulator designed for 24 GHz. The simulations and layout design will be shown as well as the plans for the characterization of the chip. The developed design was fabricated on 0.13 μm SiGe technology.;

- **Chapter VII - Conclusions and Future Work**: The last chapter concludes this thesis document and gives some insights regarding potential future work in this field from the author's point of view.

Chapter 2

State of the Art

Outline

Considering that the focus of this work is on the passive backscatter sensors with WPT capabilities, the history and an overview of some concepts need to be addressed. In this chapter the history of the backscatter communication, WPT and MMIC will be explored. Moreover, the state of the art of different rectifiers and different approaches of backscatter communication will also be presented.

2.1 Backscatter communication

2.1.1 History

The concept of communication by scattering dates back to 1880, where the photophone was discovered by Alexander Graham Bell [24]. This system consisted in performing speech communication on a beam of light. The sound waves were projected through an instrument toward a mirror, and through the vibration in the mirror, a modulation was caused in the reflected beam of light. The receiver could demodulate the incident modulated light beam, which resulted in the reproduction of the transmitted signal. In the experiments, they could transmit speech over 213 meters. In 1945, Leon Theremin developed a very advanced modulated backscatter device that contained a passive listening device [25]. This device consisted in a replica of the Great Seal of the United States and was used by the Soviet Union to spy on the US embassy in Moscow. The device consisted of a monopole antenna connected to a resonant cavity with a flexible sound-sensitive conductive membrane. The changes of the membrane modified the resonant frequency of the cavity and the antennas load. Thus, when the device was radiated by an outside RF Continuous Wave (CW) signal, the antenna would reflect a modulated signal originated by the voices of those present in the room.

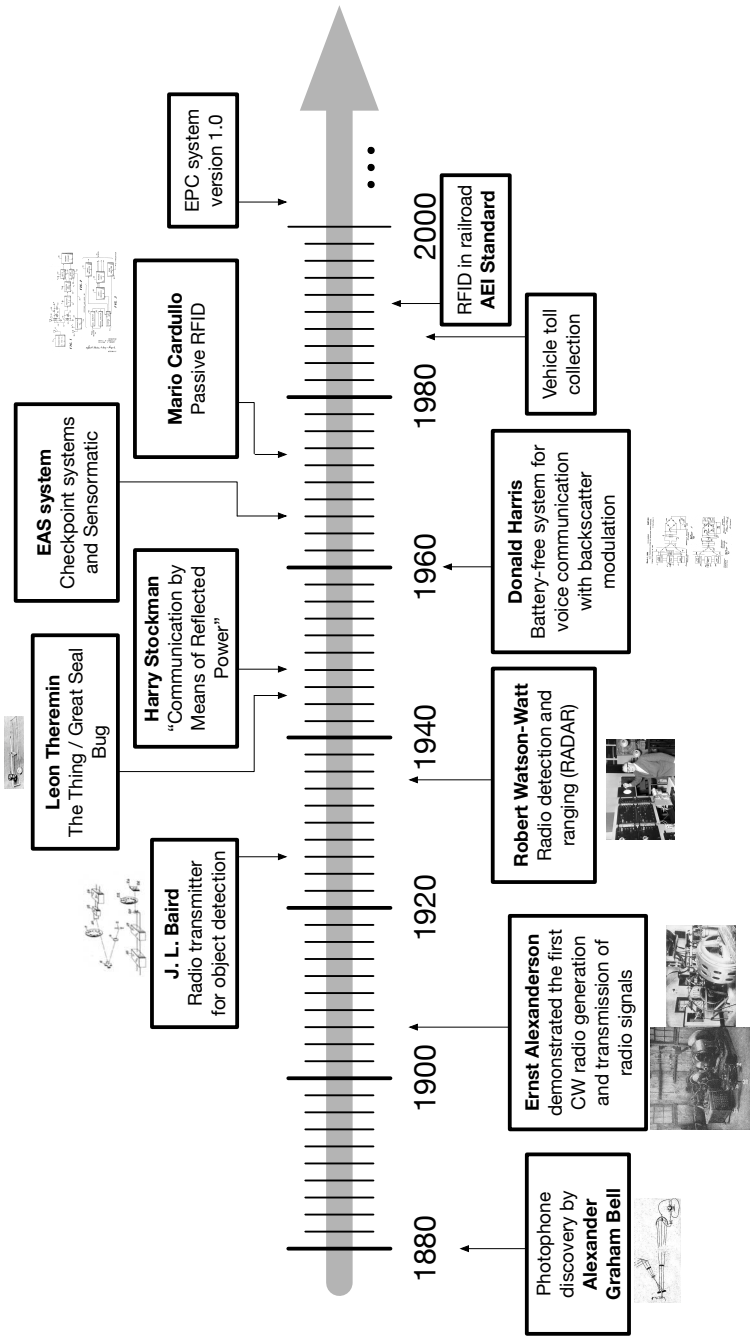

Figure 2.1: History of RFID and backscatter communication.

In 1948, Harry Stockman reported a method to communicate with the use of reflections generated by mechanical devices, which included audio transfer over microwave frequencies [26]. Nowadays, the modern tags use similar modulated backscatter operating principles. These concepts contributed to the evolution of commercial applications based on backscatter communication. Donald B. Harris was the first inventor of the combination of

this technique with WPT, by proposing a battery free system for voice communication with backscatter modulation in 1960 [27]. From this date, the RFID technology started to grow and has evolved into systems with different applications.

In this decade, the companies began commercializing anti-theft systems that used radio waves to determine whether an item had been paid for or not. The 1-bit Electronic Article Surveillance (EAS) tags were used for counter-theft and were the first large scale use of RFID concept [28].

The first application was automated tolling systems where cars are assigned RFID tags that can be interrogated and read by a reader infrastructure implemented in toll booths. Some other commercial applications used the technology for inventory management, for the automotive industry, for the location of livestock and wildlife, for anti-theft in the retail trade, for keys and electronic documents, and in agriculture and nature reserves [5]. Figure 2.1 presents the major milestones of RFID technology.

2.2 Wireless Power Transmission

2.2.1 History

A process that occurs in any system where electrical energy is transmitted from a power source to a load without the connection of electrical conductors is, by definition, WPT. In the late 19th century, Nikola Tesla described the freedom to transfer energy between two points without the need for a physical connection to a power source as of ”all-surpassing importance to man [29]”. While several methods of wireless power have been introduced since Tesla's work, including near-field magnetic resonance and inductive coupling, laser-based optical power transmission, and far-field RF/microwave energy transmission, only RF/microwave and laser-based systems are truly long-range methods.

Interest in microwave-power transfer began to spark again in 1968 after an article by Peter Glaser introducing a concept known as Space Solar Power (SSP) or Solar-Power Satellite (SPS) [30]. He envisioned placing massive solar panel farms in space and then beaming the power down to earth as an effort to reduce fossil fuel consumption and meet energy demand. Many systems-level engineering challenges for the SSP system were addressed in this work, most relevantly the investigation of more appropriate semiconductor diodes. Much of this work collimated in 1975 with the demonstration of a one-mile-long WPT system demonstration with a DC to DC efficiency of 54% (RF-DC efficiency of 82.5% at 2.45 GHz) with a DC output power of 30 kW [31].

In 1975, William Brown demonstrated the WPT long distance coverage when he transmitted a microwave beam converted to DC power by an RF-DC converter at a distance of 1.6 km (Radiated microwave power transmission system efficiency measurements). The concept of a rectenna has been initially proposed by William Brown. The rectenna is a simple

device which has a rectifier attached directly to an antenna. In this manner, DC power could be readily obtained from Radio Frequency (RF) signals incident on the antenna. As a solution to the low-power handling capacity of the rectenna, Brown and the Purdue professors developed a rectenna array. This array consisted of many rectennas linked together across a common load. Thus, the DC power provided was the sum of the power from all the rectennas. One of the first semiconductor rectenna arrays used much lower power than Brown's previous designs at 8 W, but still had an efficiency of 50%, much higher reliability, and lower weight. Brown continued to develop this technology and in 1964, he demonstrated a more efficient microwave-powered helicopter outfitted with a 2.4 GHz rectenna array that could fly 60 feet above an antenna for a sustained period [32]. In the 1990's and 2000's, there was a large amount of work exploring higher frequencies for WPT for SSP applications as well as lower frequencies for RFID and WSN applications. The challenge for the SSP community has been to create the most efficient and economic manner to transfer microwave energy. Thus, a trend to higher frequencies where smaller aperture sizes would be possible has been a focus. Additionally, there has been work by several researchers working on WPT for RFID applications. These applications tend to have a significantly lower power density available, which makes EH a challenge.

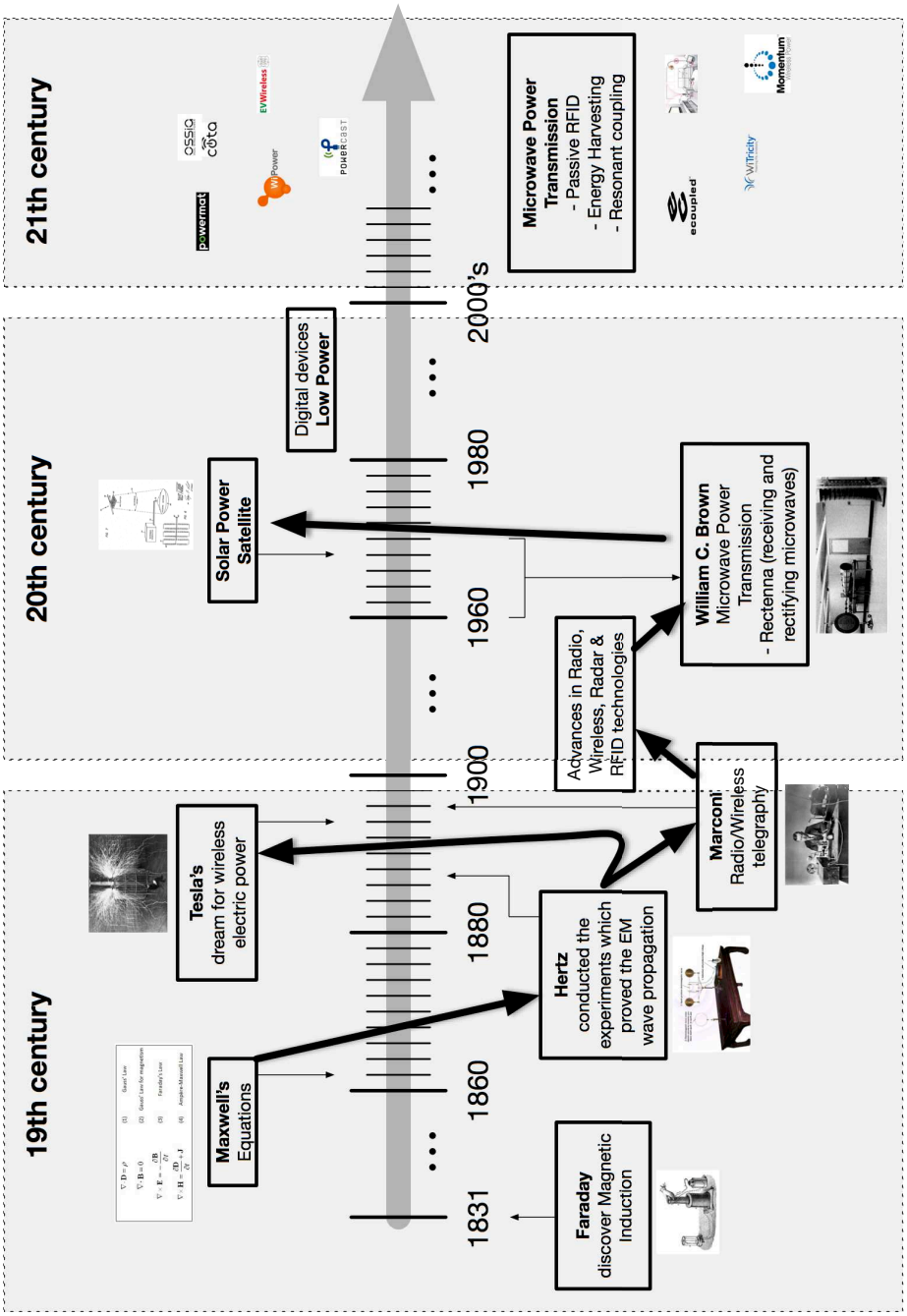

Figure 2.2: History of radio transmission and wireless power transfer.

While there are too many projects to name individually, Naoki Shinohara [33–35] and Kai Chang [36–38] have been among the most recognized names working on WPT focusing on SSP. There has been a progression from high powers at low frequencies to lower powers at higher frequencies. Nowadays, there is a lot of interest in this area in order to develop solutions for the commercial market of WPT. This has also been explored in space, where

one of the main problems, power connectors, constitute a very important component for the success of every space mission. These missions require crucial connector attention in order to perform successful operations. In the far field electromagnetic WPT, the choice of wireless, saves the cost of deploying long wires in harsh environment, issues related of rotating connectors in the case of solar panels, limit the mobility of portable devices and the payloads of spacecraft. Technologies enabling the development of compact systems for WPT through RF waves is thus very important for future space based systems.

Two major communities have made significant contributions towards fulfilling Tesla's dream of wireless power: SSP or SPS and RFID. Though still in the experimental stage, researchers working in SPS have made advancements in energy conversion at great distances and high powers (greater than 1 W) to enable electricity to be shared via radio waves, namely collecting solar energy in orbital stations around earth and beaming it to ground stations via microwave power transfer [30, 33, 39]. Meanwhile the RFID community has focused on the ultra-low power harvesting (usually much less than 1 W) necessary to provide energy for wireless, batteryless RFID tags and backscatter sensors [40]. Future development in WPT will certainly leverage the work of both SPS and RFID researchers and lead to the deployment of efficient, far-field, wireless power systems.

Figure 2.2 presents the major milestones of WPT.

2.2.2 RF-DC Converter

The EH concept relies on the same fundamentals of WPT, where both are composed by RF-DC converters. Nevertheless, the WPT system has a dedicated transmitter source, which radiates high amount of energy, instead of EH systems that do not need any dedicated source, since they use the available power generated by radio communications. The EH system is composed by a matching network (to allow the maximum power transference), a non-linear rectifying device, a low-pass filter and a DC load. Usually, the non-linear rectifying device is a Schottky diode, due to their low voltage threshold and low junction capacitance, which results in a more efficient operation at low powers and increases the maximum operation frequency, respectively.

Figure 2.3 presents the RF-DC conversion efficiency of different rectifiers with different topologies from 450 MHz to 94 GHz, based on [41–43] and with some more work recently reported. Besides the single-band converters which are presented in most of the references presented in the Fig. 2.3, dual-band converters, to harvest in two different sources, are presented in [38, 44–46], as a triple-band converter in [47]. Some works presented the combination of different sources, such as light, heat, electromagnetic waves, vibration and other [17, 48, 49].

Most of traditional rectifiers can only exhibit reasonable RF-DC conversion efficiency with a narrow input power range. The efficiency declines very quickly when the input

power deviates from the operating range, limiting the wireless charging applications with considerable variations of input power. Thus, it is necessary to implement and design rectifiers with a wide operating input power range [50–52]. The authors, in [53] designed an adaptive rectifier for WPT, which could adapt the configuration of the rectifier to the input power level.

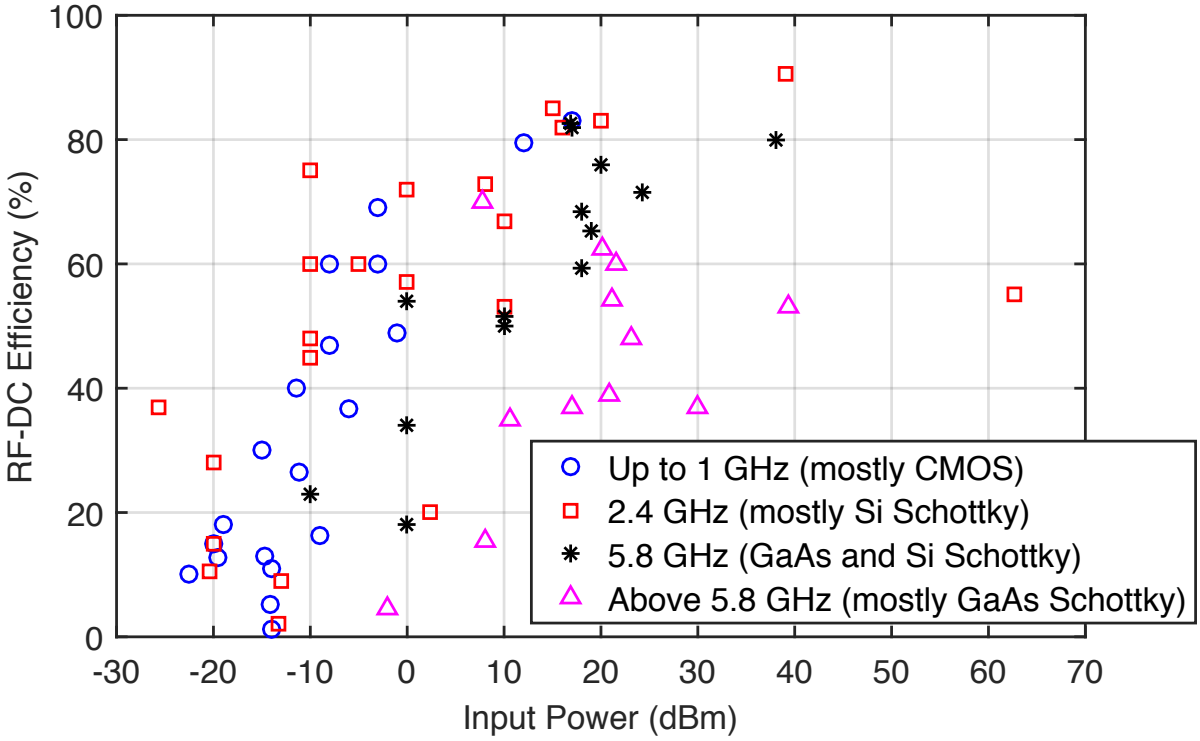

Figure 2.3: State of the art in RF-DC converters, with different topologies, from 450 MHz to 94 GHz.

In Fig. 2.4 different topologies of rectifiers are presented. The charge pumps (voltage multiplier) are the rectifiers more used in RFID applications, since they require a considerable DC voltage to power electronics. The charge pump rectifier (Fig. 2.4(d))can be explained in the following way: It is a single-stage voltage multiplier that ideally produces a voltage which will be twice the peak voltage (V_p) of the input signal. In the negative semi-cycles of the input signal, the diode D2 charges the capacitor C2 with the peak voltage of the input signal ($-V_p$) . When the input signal switches for its positive semi-cycle, the pre-charged capacitor C2 behaves like voltage source in series with the input signal (V_p) thereby doubling the voltage of the signal that finally will be rectified by diode D1. This circuit produces more DC output voltage than single diode rectifiers but its efficiency is lower for low input signal because there is an additional diode that influences its performance. The charge

pump behaves similarly, and the maximum output voltage of a N-stage multiplier is given by $(2N-1)(V_p-2V_D)$, where N is the number of the stages, V_p is the peak amplitude of the AC signal and V_D the voltage drop of diode. The main conclusions that can be taken from simulations and experimental works are:

- The efficiency of the rectifier decreases with the increase of the diodes (increasing the number of diodes means increasing the parasitics, less diodes means minimum amount of input power to switch on the rectifying devices);
- Increasing the number of stages will increase the output voltage.

In this thesis, the focus will be on N-stage Dickson voltage multipliers to boost the output DC voltage to a level compliant with passive tags.

Diodes are typically modeled in the small signal and the I-V characteristics can be represented by the semiphysical exponential model:

$$I_D(V_D) = I_S(e^{\frac{qV_D}{nkT}} - 1), \tag{2.1}$$

where I_S is the diode saturation current, k is the Boltzmann constant ($1.381 \times 10^{-23} \frac{m^2 kg}{s^2 K}$), T is the junction temperature (considering room temperature of $298K$), q is the electronic charge ($1.602 \times 10^{-19} C$), and n is an empirical ideality factor, used for modeling imperfections in the junction. The I-V curve presented in Fig. 2.1 is characterized by three major regions. The voltages V_{br} and V_T give respect to the breakdown and turn-on voltage, respectively. For low voltages, below the V_{br}, the diode is reverse biased and conducts in the reverse direction (breakdown region). Between V_{br} and V_T, the diode is off and only a small amount of leakage current flows (off region) and the total diode current approximates a constant value equal to $-I_S$. Above V_T, the diode is forward biased and the current flows normally (turn-on region).

Nowadays, the scenario of energy management is fundamental for the new applications, the concepts of EH and WPT assume a fundamental role to extend the duration of sensors and electrical circuits in terms of energy capabilities.
Most of the circuits for these type of applications are based on diode solutions and optimized for low power RF signals [41], which in certain cases are not the objective to achieve, but the main objective is the use of these RF-DC converters in very high power configurations, some of them include powering electrical cars, powering space probes, powering large home electrical utensils.

The efficiencies of these systems are very low for lower input powers, thus it is of paramount importance to evaluate this type of technology for other power values as well. Some alternatives to explore and maximize RF-DC conversion efficiency should be discussed and studied in order to overcome the problem derived from propagation scenarios or reduced transmitted power. Some authors have adressed this problem in diode based solutions, those include

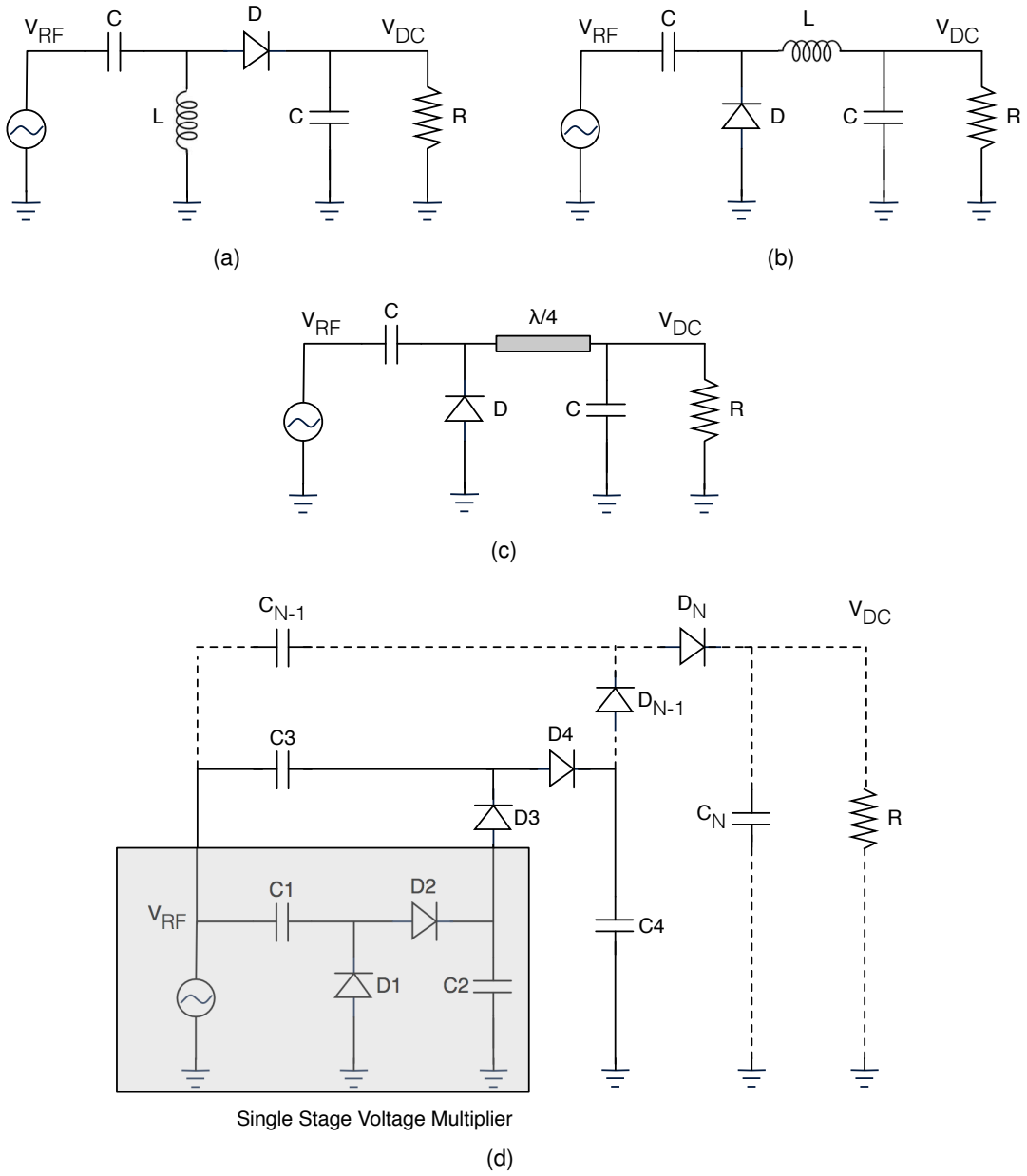

Figure 2.4: Different rectifier topologies. (a) Series diode rectifier. (b) Shunt diode rectifier. (c) Shunt diode with $\lambda/4$ stub. (d) N-stage Dickson voltage multiplier.

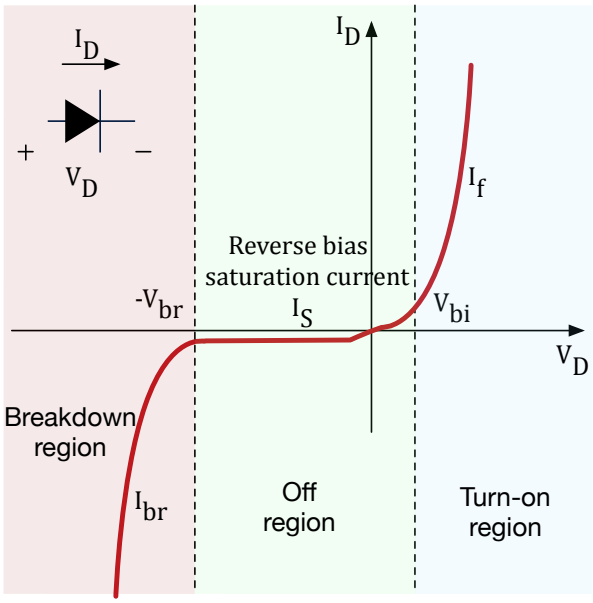

Figure 2.5: A typical Schottky diode I-V curve with respective operating regions.

---

[54] that shown that the RF-DC conversion efficiency can be improved by selecting the appropriate excitation signal. In [55] the use of multitone signals was proposed to increase the efficiency in RF-DC converters with Schottky diodes approach. In [56] the use of chaotic signals was proposed in order to increase RF-DC conversion efficiency for EH systems as well as for WPT. The authors in [56] used the Schottky diode approach to implement the rectifier. The use of high Peak-to-Average Power Ratio (PAPR) waveforms (intermittent CW signals by varying the duty-cycle, UWB signals, Power-optimized Waveforms (POW), chaotic signals, white noise, modulated signals and multi-carrier signals) to increase and improve the WPT efficiency has been demonstrated in [54–62]. Some more recent work focuses in the model to enable an analysis of the multisine-based WPT system focusing on the bandwidth of the signal and the rectifier [63]. The authors in [64] demonstrated the use of modulated signals to improve the RF-DC converter efficiency. Nonetheless, they proposed Instantaneous Power Variance (IPV) to describe, more accurately than PAPR, the variation of the instantaneous power and the occurence of signals peaks that affect directly the RF-DC converter efficiency.

Another application of the rectifiers is their usage on Wake-on Radio (WoR) applications [65–69]. Since one of the focus of this thesis is the low power communication of the sensors it is important to explore the WoR concept. Most of the studies used a single stage rectifier to design the WoR, to increase the sensitivity of the receiver. The WoR architectures use two radios: a main radio responsible for the uplink and a second low-power WoR which is used to continuously listen to the transmission medium for a wakeup signal. When the wakeup

signal is validated, the main radio is woken up and establishes the communication.

2.3 Different combinations in Backscatter communication

2.3.1 Backscatter communication with WPT capabilities

Passive RFID tags use the RF power, from the reader, to energize the digital part of the tag, which is responsible for the modulation of the incoming wave. To enable the possibility of having a totally passive RFID tag with data logging and advanced computing, a more careful and detailed WPTs should be designed and optimized to power the intelligent tags. This integration of passive RFID, passive sensing and increased computing capabilities have enabled the interest in the concept of passive wireless sensors. The concept of having passive wireless sensors with data logging and advanced computing capabilities will play an important role in the IoT context, where a lot of sensors can be connected, deployed anywhere, and give information about environment without the need of batteries. Nonetheless, the increase of IoT sensors will imply the heighten of batteries to be deployed, which will have a negative ambient impact. As it was mentioned previously, battery-powered tags can improve the distance of communication but have some limitations when referring to the battery cost and its replacement. Thus, the alternatives to the battery systems are based on EH technology or other different sources (solar [6], motion or vibration [7], ambient RF [8]). To overcome the drawbacks employed from the EH and batteries, the concept of WPT was explored to supply the tags with power.

In [70], a solution using inductive WPT and Ultra High Frequency (UHF) RFID was presented. The work proves that combining the inductive WPT with the UHF RFID increments the tag sensitivity in 21 dB, which increases the Interrogation Zone (IZ). However, the use of inductive WPT requires proximity between the tag and the power source. Regarding electromagnetic WPT, a comparison between different rectifier topologies and different stage levels was presented in [71]. The obtained results show a high dependence between the received power and the most efficient topology. A structure with a two-tone signal at 1.8 GHz and 2.4 GHz was shown in [72]. The results present a voltage output 20% higher in average when comparing with a single-tone input. The work in reference [73] begins with a reader that is configured to transmit power in CW. After rectification, the power charges the storage capacitor to 5.5 V. The storage capacitor, once charged, powers the tag that performs sensing and communication, reflecting the carrier wave. This entire process occurs at a distance of 1 m between the reader and tag. The same principle was used in [74]. The work in [18, 75] presents a solution using dual band wireless power and data transfer. One frequency is exclusively used to transmit energy to the sensor, and the other is fully dedicated to communication through backscatter. A similar approach, using different frequencies for transmitted energy and communication was presented in [76]. In that work, a differentiated circuit for

the RF-DC conversion is used for each frequency. The work in [77] used two different bands for RF communication and for WPT. The authors used 5.8 GHz to power up a portion of radio that is connected to a battery with an RF-DC converter. This path is only to turn the battery ON for the main transceiver as a WoR, and the link for the power up is no longer needed once the main transceiver is turned ON. The system is not passive and uses the WPT link to activate the main transceiver. Nevertheless, despite of having passive systems for communication, it is utmost important to improve the data rate in order to reduce on-chip power consumption and extend read range.

2.3.2 Backscatter communication with high order modulation

In most RFID systems and passive sensors, the reader to tag communication is an ASK or PSK that modulates either the amplitude, or both the amplitude and phase, of the reader's transmitted RF carrier. The use of this technology entails a number of advantages over bar-code technologies such as tracking people, items, and equipment in real time, non-line of sight requirement, long reading range, and standing harsh environment. However, the work [19] has shown that modulated backscatter can be extended to include higher order modulation schemes, such as 4-QAM. While ASK and PSK transmit 1 bit of data per symbol period, 4-QAM based can transmit 2 bits per symbol period, thus increasing the data rate and leading to reduced on-chip power consumption and extended read range. The work presented in [19,20] refers to a 4-QAM backscatter in semipassive systems, by using a coin cell battery as a power source for the modulator and a microcontroller that needs 3 V of supply. This way, the authors proved the Quadrature Phase Shift Keying (QPSK) modulator and battery powered system, by using an approach with a four lumped impedances connected to a RF switch that is controlled by a microcontroller. The same authors developed a 16-QAM modulator for UHF backscatter communication with a consumption of 1.49 mW at a rate of 96 Mbps only in the modulator (not the overall system with data generation logic feeding the modulator) [21]. This modulator was implemented with 5 switches with lumped terminations as a 16-to-1 multiplexer to modulate the load between 16 different states.

In [78], the authors presented an I/Q backscatter modulator that use bias currents to change the impedance of two PIN diodes. The circuit comprises a Wilkinson power divider, two filters (low pass and high pass) to guarantee symmetrical paths on the board, one in each branch, and one PIN diode for each branch. The bias consumption of the circuit is 80 mW (excluding Digital-to-Analog Converters (DACs) and Field-Programmable Gate Array (FPGA) logic), which imposes high power consumption and data rate limitations. The use of this circuit for a low power sensor is not feasible. Another approach that uses the PIN diodes was presented in [79]. Pozar presented a reflection type phase shifter using a quadrature hybrid and two PIN diodes. By biasing the diodes to the ON and OFF state it was possible to change the total path length for both reflected waves, producing a phase shift

Table 2.1: Performance summary and comparison

Reference	[82]	[19]	[21]	[78]	[83]	[84]	[85]
Technology	Integrated circuit	Discrete components	Discrete components	Discrete components	Integrated circuit	Discrete components	Integrated circuit
Frequency	5.8 GHz	900 MHz	900 MHz	868 MHz	2.9 GHz	2.45 GHz	10 GHz to 11.1 GHz
Modulation	32-QAM	4-QAM	16-QAM	QAM	BPSK	16-QAM	BPSK
Data rate	2.5 Mb/s	400 kb/s	96 Mb/s	-	330 Mb/s	960 Mb/s	10 Mb/s
Power consumption	113 uW	115 nW	1.4 mW	80 mW	0.12 mW	59 uW	-
Energy p/bit	45.2 pJ/bit	0.29 pJ/bit	15.5 pJ/bit	-	0.36 pJ/bit	61.5 fJ/bit	-

at the output. However, the consumption of the PIN diodes is not suitable for low power sensors.

One different solution to obtain a Binary Phase Shift Keying (BPSK) modulation was presented in [80]. The authors presented a phase-shift modulator with two switches that are connected to each other by a 90°delay line or 0°delay line. The phase-shift modulator was implemented as a two-port device that selectively delays the signal by 90°between port 1 and port 2, or passes the signal from port 1 to port 2 with no delay, achieving a BPSK modulation.

In [81], two multi-antenna technologies were used. The authors presented an energy harvester (Staggered-Pattern Charge Collector (SPCC)) that has two independent antenna arrays and harvests power to supply a microcontroller. They also present a Retrodirective Array Phase Modulator (RAPM) that backscatters the signal from the reader to the reader. The RAPM comprises two switches that are controlled by a microcontroller. The four switching states are connected through coplanar waveguides of different wavelengths, each separated by 90°. The RAPM can be used for QPSK modulation by calibrating the phase offsets in the switches. To increase the range of communication of backscattering systems, a 32-QAM [82] was developed at 5.8 GHz. These systems proved to be very suitable for low power communications due to the low energy per bit consumption and the achievable data rates. The authors in [83] presented a BPSK modulator with 330 Mb/s of data rate at 2.9 GHz.

Table 2.1 compares the modulators results from the provided state of the art references.

2.3.3 Ambient Backscatter communication

One of the key challenges for practical IoT and WSNs is the delivering autonomy to a massive number of devices which conventionally need to be powered with batteries. Moreover, ensuring low cost is an equally important parameter pertaining to the viability of such systems. Low-power and low-complexity backscatter communications have emerged as a promising paradigm to address aforementioned challenges. This technology delivers ultra-low-cost and ultra-low-power wireless communications by modulating the reflection of incident RF carrier signals.

In recent works, existing ambient RF signals have been proposed for backscatter communication instead of a CW emitter signal [86, 87]. This approach simplifies the complexity

and cost of the system and its deployment. In [88], broadcast frequency modulated (FM) signals have been used to power the tag and enable effective communication between tag and reader. The initial implementations were able to communicate over distances of several feet, even in cases where transmission towers were up to many kilometers away. In [89], a tag capable of transmitting FM reflections to a computer or a tablet through a low-cost software defined radio (SDR) reader was demonstrated. Moreover, Table 2.2 provides the summary of ambient backscatter communication systems.

To conclude, the main advantages of using this technique are:

- There is no need to develop additional dedicated RF sources, since it already uses available RF sources and can be traduced in lower costs and power consumption;
- Do not require dedicated frequency spectrum which is scarce and expensive;
- The backscatter tag can transmit data anytime without initiation from receivers, being on the presence of ambient sources.

2.3.4 Backscatter existing standards

Some recent works demonstrate the ability to synthesize transmissions compatible with WiFi (802.11 b) [107], Bluetooth Low Energy (BLE) [108, 109], Zigbee [110, 111], LoRa [104, 112] at μWs of power using backscatter transmissions. Through these systems it is possible to increase existing IoT networks with additional sensing without changing the existing deployment. In [107], the authors create IEEE 802.11 b packets using backscatter and receive the packets on WiFi chipsets, while consuming 4-5 orders of magnitude lower power than existing WiFi chipsets. In [109] the authors presented a prototype that produces a band-pass Frequency Shift Keying (FSK) modulation at 1Mb/s, which enabled the compability with conventional BLE advertising channels. The advertising channels are used for uni-directional (broadcast) communication, including device discovery and sensor beacons. In [112] the authors developed an hybrid analog-digital backscatter that can synthesize LoRa symbols and be decoded at the receiver below -135 dBm signal strength. Thus, it will avoid the build of a custom reader, since the backscattered signal can be decoded with available LoRa decoders. In most of these works, the authors use a carrier generator to enable the backscatter communication. An alternative solution, that do not need any external or complementary device, relies on the radio test mode present in many IoT radio transceivers to generate an unmodulated carrier that is necessary for the backscatter communication [111]. Moreover, all the prototypes presented suffer from low data rates and are limited in terms of scalability for other applications. Thus, it enables the possibility to implement an hybrid backscatter modulator that can synthesize all the presented standards.

Table 2.2: Ambient Backscatter Communications Systems

Reference	Objective	Ambient RF source	Results
[90]	Increase communication range and bitrate (theoretical analysis, experiment and prototype)	TV tower 539 MHz	1 Mbps at distances from 1.2 m to 2.1 m and 1 kbps at a distance of 24 m.
[91]	Reduce energy consumption of backscatter transmitters (experiment and prototype)	FM tower 91.5 MHz	11.7 uW at transmitter.
[92]	Increase the communication range and bitrate (theoretical analysis, experiment and prototype)	Wi-Fi AP 2.4 GHz	5 Mbps at a range of 1 m and 1 Mbps at a range of 5 m.
[93]	Improve BER performance and reduce the complexity of detectors (theoretical analysis and simulation)	N. A.	Reduce complexity maintaining BER performance as good.
[94]	Reduce phase cancellation problem (theoretical analysis, simulation, experiment and prototype)	Signal generator 915 MHz	Reduce phase cancellation problem. Increase the communication range.
[95]	Minimize BER (theoretical analysis and simulation)	N. A.	10ˆ-1 and 10ˆ-2 BER with 5 dB and 30 dB of transmit SNR.
[96]	Increase communication range (theoretical analysis)	TV tower 626-632 MHz	1 kbps at a range of 100 m.
[97]	Increase communication range and bitrate (experiment and prototype)	Wi-Fi AP 2.4 GHz	50 kbps at a range of 3.6 m with 10ˆ-3 BER.
[98]	Increase bitrate (theoretical analysis and simulation)	N. A.	Increase bitrate while reducing robustness.
[99]	Improve communication range, bitrate, BER, reliability and energy consumption	TV tower 920 MHz	Backscatter transmitter consumes 0.25 uW for TX and 0.54 uW for RX.
[100]	Improve BER performance (theoretical analysis and simulation)	N. A.	10ˆ-3 BER with 15 dB of transmit SNR and 10ˆ-1 bits/s/Hz with 20 dB of transmit SNR.
[101]	Reduce energy consumption of backscatter transmitters (experiment and prototype)	Wi-Fi AP 2.4 GHz	14.5 uW at 1 Mbps and 59.2 uW at 11 Mbps.
[102]	Multiple access problem (theoretical analysis and simulation)	N. A.	Up to 8 backscatter transmitters.
[103]	Increase bitrate (simulation)	TV tower 539 MHz	2 kbps between the backscatter transmitter and the relay node and 1 kbps between the relay node and backscatter receiver.
[104]	Simplify LoRa system topologies (experiment and prototype)	LoRa transmission	tag can backscatter an ambient LoRa transmission sent from a nearby LoRa node (20 cm away) to a gateway up to 1.1 km (220 μW power consumption)
[105]	Simplify wireless system topologies (experiment and prototype)	FM station	5 m tag-reader distance with 2.5 kb/s - energy per packet of 36.9 uJ.
[106]	Increase bit rate PAM modulation (experiment and prototype)	FM station	1 m tag-reader distance with 345 b/s - power consumption of 27 μW. 34.5 km from the FM station.

Table 2.3: Overview of Reflection Amplifiers

Reference	Year	Device Type	DC Bias Power (mW)	Gain (dB)	RF Input (dBm)	Frequency (GHz)
[122]	2017	tunnel diode	0.045	40	-75	5.8
			0.039	29	-84	
[123]			0.178	13	-30	0.915
[124]			0.2	17		0.890
[125]	2015		0.029	41.4	-92	5.8
[126]			0.045	34.4	-70	5.45
[113]	2014	bipolar transistor	0.325	10.2	-50	0.920
[114]	2013		2	13	-55	5.25
[115]		MESFET	18	10.2	-	4.5
[116]		Josephson junction	-	30	-145	2.7
[117]	2012	MOSFET	0.120	22.3	-71.9	4
[118]	2011	pHEMT	6.3	11.5	-	5.8
[119]	2008		209.3	14	-75	21.2
[120]	2006		330		-45	
[121]	2003		-	8.1	-	6.26

2.3.5 Augmented Backscatter radio communication range

The backscatter radio links are a very interesting topic to explore since most of the tags, when are establishing the communication with the reader, have no power storage available. As it is known, the passive tags collect power from the transmitter which limits their usage for short range applications. The forward link is limited by the minimum signal strength required for the tag to power up (tag sensitivity) and the return link is limited by the reader sensitivity. Thus, it is utmost important to improve the link ranges. This can be done by improving the reader sensitivity or on the tag power requirements. Some recent studies have suggested the use of reflection amplifiers to improve the communication range of RFIDs. The reflection amplifiers are defined by a negative load impedance and can amplify the backscattered RF signal with a certain amount of biasing power. There are two approaches referred in the literature, one by using Field Effect Transistors (FETs) [113–121] and the other based on tunneling effects from tunnel diodes [122–126]. Table 2.3 presents an overview of the existing reflection amplifiers. The tunnel diodes prove to be a very good solution to improve the communication range of the passive tags. Nonetheless, all the prototypes developed refer to ASK/PSK backscatter modulation leaving the possibility of using a tunnel diode to boost the backscatter communication range with high order modulation.

2.4 Monolithic Microwave Integrated Circuit

The MMIC is a microwave circuit composed by active and passive components which are fabricated on the same semiconductor substrate. This is the main characteristic of MMIC and is implicit in its name, since the word monolithic (from the Greek) means "as a single stone".

MMICs are utilized in most applications that comprise transmitting and receiving microwave signals and can be divided into three main areas: military, space and civil applications. Military and space applications are the ones that have pushed and helped to advance the development of technology. Some examples of military applications are the phased-array radar, smart munitions, passive millimetre-wave imaging, instrumentation, etc.. The satellite communications, radiometers, remote sensing and low earth orbit mobile systems are some examples of MMIC applications in space. There are some other applications as mobile phones, global positioning, high speed internet access, automotive industry within autotolling, vehicle identification, road-traffic information, cruise-control systems, Bluetooth and similar wireless systems that serve as example of civil applications.

There are two main features of MMICs that are utmost suited for almost every application previously mentioned, which are their small dimensions and low weight. They can be cheap, if fabricated in large quantities, and very reliable.

With the availability of high resistivity Gallium Arsenide (GaAs) substrates, MMICs were developed, where all active and passive RF components, and conducting paths are embedded in different metal layers on a single substrate. After some time, when these devices were integrated on a silicon substrate, it came to known as a Radio Frequency Integrated Circuit (RFIC) and sometimes MMIC interchangeably. RFICs are more used to operate at lower frequencies than MMICs.

There are two main differentiating factors between RFIC and MMIC technologies.

- The first is process technology – RFICs tend to be built with mainstream mixed signal Complementary Metal-Oxide-Semiconductor (CMOS), Bipolar, or Bipolar Complementary Metal-Oxide-Semiconductor (BiCMOS) flows, where MMICs tend to be built with alternate materials such as III-V compounds, SOS, or graphene.

- The second is the design methodology – RFICs tend to be designed and their resulting products specified in the time domain using traditional analog/mixed signal tools, and MMICs tend to be designed and specified using S parameters in the frequency domain [127].

MMICs have been dominated by III-V technologies particularly in their early era. High-Electron-Mobility Transistors (HEMTs) based on Indium Phosphide (InP) are known for their superior high-frequency properties but a high fabrication cost of InP based MMICs make

them less suitable for mass production. Traditionally, GaAs and Silicon (Si) have been the most popular semiconductor materials used for the design of RF components - especially power amplifiers. Albeit Si devices are typically more cheaper than GaAs, one must say that they do not work as well as GaAs for most high-frequency or for high-power applications. GaAs metamorphic HEMT (mHEMT) process technologies have shown performances close to InP devices [128, 129]. Gallium Nitride (GaN) HEMT technologies are more suitable for high power applications below the mm-wave spectrum, still there are some designs above 30 GHz [130, 131]. Si technologies have emerged during the last years, due to their low-cost in mass production and the possibility of monolithic integration of analog and digital circuits on the same substrate. Both Silicon Germanium (SiGe) based Heterojunction Bipolar Transistors (HBTs) and CMOS FETs have been used in mm-wave circuits and systems [132, 133].

Nevertheless, SiGe devices can exceed the performance of GaAs, though only in low-power, high-frequency applications, such as in the front-end design of mobile phones. The performance of the SiGe BiCMOS processes is approaching that of III-V technologies [134, 135]. Furthermore, with the advancement of SiGe processes with maximum oscillation frequencies of 500 GHz [136] and combined with the lower cost of silicon manufacturing, has made it more popular in recent years.

2.4.1 History of MMIC

The first step which contributed to the development of monolithic circuits was made by Jan Czochralski who invented the Czochralski process, which is used for growing single crystals and in the production of semiconductor wafers [137]. Nevertheless, the change in the electronic industry from vacuum-valve to solid-state technology was only possible when in 1947 Bell Telephone Laboratories invented the transistor [138]. Later on, in 1959, Jack Kilby from Texas Instruments patented the IC [139–141]. This discovery enabled a large number of components to be printed onto the surface of a single part of semiconductor material and the first ICs were made of germanium (Ge). Robert Noyce of Fairchild Semiconductor, some years later, in 1961, patented a complex unitary circuit made of silicon [142]. In 1967 Please Optoelectronics and Microwave Ltd. fabricated a 4 um gate length GaAs Metal Semiconductor Field Effect Transistor (MESFET) at 1 GHz and it become the world first commercial GaAs MESFET - GAT1. One year later, become the first publication of simple monolithic microwave GaAs circuits using diodes and microstrip lines [143, 144]. The major events in the history of MMIC and the consequent development of new designs during and after these years are presented in Fig. 2.6.

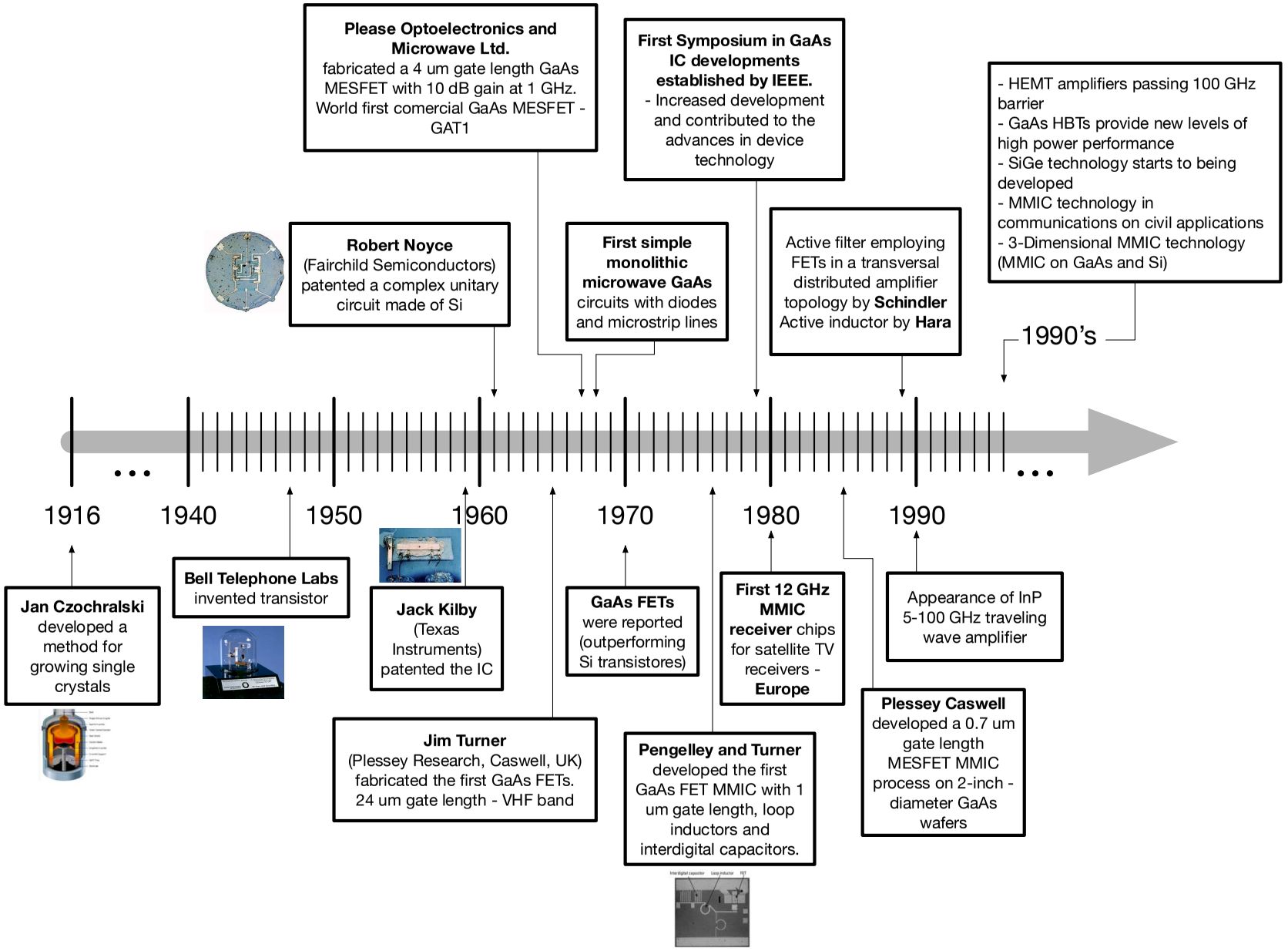

Figure 2.6: History of MMIC.

Chapter 3

Backscatter modulation

Outline

In the IoT context, where billions of connected objects are expected to be ubiquitously deployed worldwide, the frequent battery maintenance of ubiquitous wireless nodes is undesirable or even impossible. The growth of the devices will be made possible only if the sensors battery needs are eliminated or reduced significantly. For low power sensors and devices, careful power management and power conservation are critical to device lifetime and effectiveness. One of the possible solutions is to change completely the paradigm of the radio transceivers in the wireless nodes of the IoT system.

This chapter provides an analysis on the link budget of backscatter radio communication and on the concepts that support this technology. Moreover, a pratical implementation of a backscatter modulator will be presented.

3.1 Analysis of Backscatter-Radio Link Budgets

RFID is a kind of the contactless automatic identification technology via radio frequency signal, and it is one of the most developed rapidly technologies in automatic identification technology field. It uses RF to identify the target and collect data via non-contact radio communication. With the operating frequency of RFID system increasing, for passive RFID systems working at the UHF and microwave bands and on the basis of backscattering modulation principle to work, it becomes very important to research on response model of electromagnetic field and calculation of the read distance. To modulate the backscattered signal, the RFID chip switches its input impedance between two states (amplitude modulation). In order to improve the reading range, the tag's antenna is generally matched to the impedance of the chip. The matching is obtained in special conditions, at a given frequency and usually for tag placed in free space. The impedance of the chip is a function of frequency and received power and the impedance of the antenna is highly dependent on the support on which the

tag is placed. Figure 3.1 illustrates the operation of a modern passive RFID system that includes an RFID reader and an RFID tag, composed of an antenna and an Integrated Circuit (IC) chip. The reader signal alternates between a CW and modulated transmissions. The tag sends data during one of the CW periods by switching its input impedance between two states, effectively changing its Radar Cross-section (RCS) and thus modulating the backscattered field. The RCS of a scattering target is defined by the equivalent area of the target based on the target scattering the incident power isotropically [145]. By knowing the transmitting energy, wavelength and antenna's gains, the RCS of an object can be used to predict the reflected power (backscatter) or identify the object based on RCS characteristics. There are some studies that explored the decrease of RCS, in order to avoid the detection from radar systems [146, 147]. The objective in this thesis is the opposite, since the goal is to control or modulate the RCS. The variations in time of the RCS can be understand as the message to be decoded. Considering two different impedances on the tag, one states is usually high and another is low to provide a significant difference in the backscattered signal. Data exchange between RFID reader and tag can employ various modulation and coding schemes (amplitude modulation and Manchester coding). The signal transmitted on the forward link (reader to tag) contains both CW and modulated commands as shown in Fig. 3.2. On the reverse link (tag to reader), the data is sent back during one of CW periods when the tag impedance modulates the backscattered signal. If the receiver is non-coherent, it can only register a magnitude difference between two scalar RCS values (scalar differential RCS). If the receiver is coherent (such as an RFID reader where transmitter and receiver are phase locked), it detects both amplitude and phase of the signal and can register a vector difference between two RCS values (vector differential RCS). This difference depends on relative phases of the field scattered in different chip impedance states, that is a difference of two scalar RCS values. Two chip impedances can result in the same scalar RCS values for the tag but produce nonzero modulated backscattered power [148].

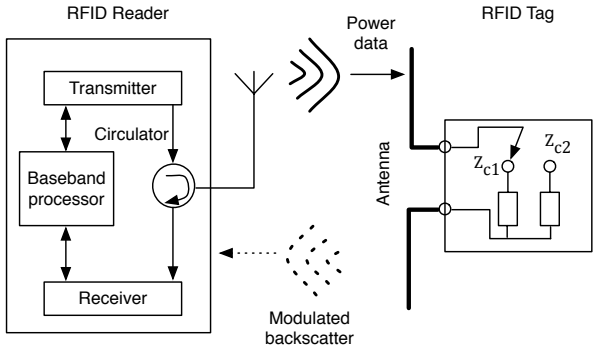

Figure 3.1: Passive RFID system overview

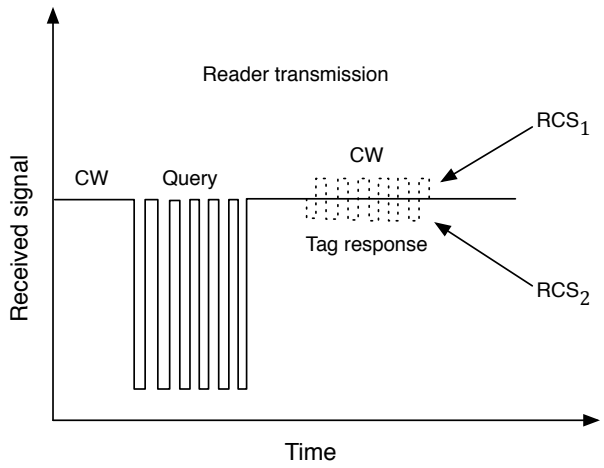

Figure 3.2: Data exchange between an RFID reader and a tag.

The operation of a typical passive backscatter RFID system includes an RFID reader and a passive RFID tag, shown in Fig. 3.1. The chip obtains power and data from the RF signal transmitted by the RFID reader. The tag sends data back by switching its input impedance between two states Z_{c1} and Z_{c2} and thus modulating the backscattered signal. At each impedance state the tag presents a certain RCS. One of the impedance states is generally high RCS_1 and another is low RCS_2 to provide a significant difference in the backscattered signal. The impedance match between the antenna and the chip is very important in RFID, since it influences directly the RFID system performance characteristics such as the range of a tag (the maximum distance that the reader can read or write data to the tag).

In Fig. 3.3 it is demonstrated the equivalent circuit of an RFID tag, where the antenna is represented with its Thevenin equivalent. In the Fig. 3.3 the complex antenna impedance is represented by $Z_a = R_a + jX_a$ and the complex chip (load) impedance is represented by $Z_c = R_c + jX_c$. The antenna impedance is typically matched to the high impedance state of the chip in order to maximize the collected power. The variation of the chip impedance with power and frequency can affect the performance of the tag. Nevertheless, in order to maximize the tag range, the antenna impedance is matched to the chip impedance at low power levels that are required for the chip to work. In most tag application scenarios the tag continues to operate when brought closer to the RFID reader antenna where the power incident on the tag is higher. Nevertheless, it is possible to have a situation where a significant variation of the chip impedance with a higher input power results in a several tag impedance mismatch and causes dead spots within operational range of the tag.

The information transferred between reader and tag can employ various modulation and coding schemes. The signal transmitted on the uplink (reader to tag) contains both CW and modulated commands. On the downlink (tag to reader) the data is sent back during one of

CW periods when the tag impedance modulates the backscattered signal [149]. One of the major problems of a passive backscatter RFID system is the read ability that is limited by the overall efficiency of the system. The antenna characteristics have a radical effect on the read ability of RFID system.

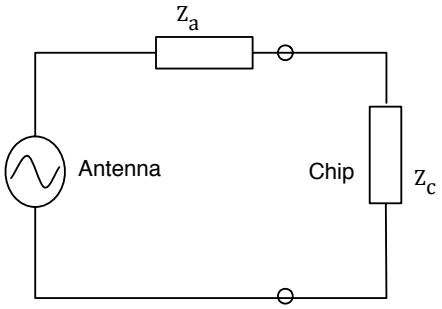

Figure 3.3: Equivalent circuit of an RFID tag

The power scattered back from a loaded antenna can be divided into two parts. The first is the structural mode and is due to currents induced on the antenna when it is terminated with the complex conjugate impedance (due to the interaction between the incident field and the antenna structure). The second is the antenna mode and is due to the mismatch between the antenna impedance and the load impedance [150–152].

The total backscattered field can be written as the field scattered by the open-circuited antenna plus the re-radiated field [153]. The re-radiated power can be obtained from the equivalent circuit shown in Fig. 3.3, which is the approach used in [148]. The power density of an electromagnetic wave incident to the RFID tag antenna in free space is given by

$$S = \frac{P_{T_X} G_{T_X}}{4\pi r^2}, \tag{3.1}$$

where P_{T_X} is the transmitted power, G_{T_X} is the gain of the reader transmitting antenna, and r the distance to the tag, as can be seen in Fig. 3.4. The power P_{Tag} collected by the tag antenna is by definition the maximum power that can be delivered to the complex conjugate matched load:

$$P_{Tag} = SA_e = \frac{P_{T_X} G_{T_X}}{4\pi r^2} A_e, \tag{3.2}$$

where A_e is the effective area of the antenna and considering the Friis formula is given by ($A_e = \frac{\lambda^2}{4\pi} G_{Tag}$). The power reflected by the tag and received by the reader is given by the radar equation [19]:

$$P_{R_X} = \frac{P_{Tag} G_{Tag} G_{R_X} \lambda^2}{(4\pi r)^2} = \sigma \frac{P_{T_X} G_{T_X} G_{R_X} \lambda^2}{(4\pi)^3 r^4}, \tag{3.3}$$

where G_{R_X} is the gain of the reader receiving antenna, λ is the radiation wavelength and σ

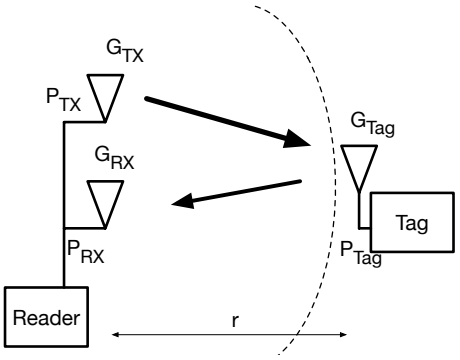

Figure 3.4: Reader to Tag and Tag to Reader communication.

---

represents the RCS of tag antenna which is the amount of reflected power. The effective area (A_e) and the RCS (σ) of an antenna loaded by an impedance Z_c are given by [79]:

$$A_e = \frac{G_{Tag}\lambda^2}{4\pi}(1 - |\rho_c|^2), \tag{3.4}$$

$$\sigma = \frac{\lambda^2}{4\pi}G_{Tag}^2|A_s - \rho_c|^2, \tag{3.5}$$

where G_{Tag} is the gain of tag antenna and ρ_c is the reflection coefficient defined by 3.6. A_s is a complex vector that represents the structural component, due to the fact that any conducting object will scatter electromagnetic waves [154]. On equation 3.4 the term $1 - |\rho_c|^2$ refers to the transmission coefficient and when the load is matched ($\rho_c = 0$), the effective area is given by the Friis formula.

$$\rho_c = \frac{Z_c - Z_a^*}{Z_c + Z_a}, \tag{3.6}$$

The ASK/PSK backscatter modulation requires two different and distinct load impedance states, therefore equation 3.7 shows the variation of ρ_c between two load impedances (Z_1 and Z_2) which modulate the antenna reflection coefficient and consequently the RCS.

$$\rho_{1,2} = \frac{Z_{1,2} - Z_a^*}{Z_{1,2} + Z_a}, \tag{3.7}$$

The modulation factor is an important parameter that should be defined to design an appropriate and efficient backscatter circuit. The power reflection achieves its maximum when the reflection coefficients are equal to 1 and -1, meaning that no power is absorbed. The RF tags use ASK modulation and switch between a matched load and a short, to guarantee balanced power in the tag, Fig. 3.5.

Through 3.4 and 3.5, it is possible to conclude that minimizing the mismatch between the

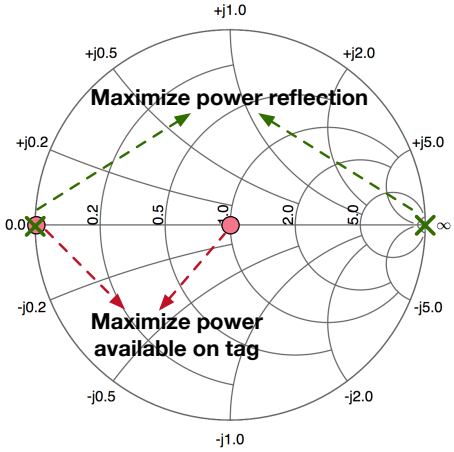

Figure 3.5: ASK and PSK tag modulation effects.

---

antenna and load ($\rho_c = 0$) will produce best results. Nonetheless, to transfer information on backscatter communication there are needed at least two different load impedances, thus it is utmost important to consider differential RCS given by 3.9.

In order to determine the actual data transfer in the uplink it is necessary to take into account the modulation between two impedances (Z_1 and Z_2) or the reflection coefficients (ρ_1 and ρ_2). In [155] a 50% duty-cycle square wave modulation between two impedances was assumed, which gave rise to the effect of load modulation on 3.4 and 3.5:

$$A_{e_m} = \frac{G_{Tag}\lambda^2}{4\pi}(1 - \frac{1}{2}(|\rho_1|^2 + |\rho_2|^2)), \tag{3.8}$$

$$\Delta\sigma_m = \frac{\lambda^2}{4\pi}G_{Tag}^2|\rho_1 - \rho_2|^2, \tag{3.9}$$

where m means the the modulation. By substituting 3.8 on 3.2 and 3.9 in 3.3, it is possible to determine the average power delivered to the tag and the modulated power backscattered by the tag received by the reader, respectively.

$$P_{Tag_m} = G_{T_X}P_{T_X}G_{Tag}(\frac{\lambda}{4\pi r})^2(1 - \frac{1}{2}(|\rho_1|^2 + |\rho_2|^2)), \tag{3.10}$$

$$P_{R_{X_m}} = G_{T_X}P_{T_X}G_{R_X}G_{Tag}^2(\frac{\lambda}{4\pi r})^4\frac{1}{4}|\rho_1 - \rho_2|^2. \tag{3.11}$$

Taking into account the polarization mismatch and multipath fade margins on 3.10 and 3.11:

$$P_{Tag_m} = \frac{G_{T_X}P_{T_X}G_{Tag}\lambda^2 X}{(4\pi r)^2 F_f}(1 - \frac{1}{2}(|\rho_1|^2 + |\rho_2|^2)), \tag{3.12}$$

$$P_{R_{X_m}} = \frac{G_{T_X} P_{T_X} G_{R_X} G_{Tag}^2 \lambda^4 X_f X_b}{(4\pi r)^4 F} \frac{1}{4} |\rho_1 - \rho_2|^2, \tag{3.13}$$

where X represents the polarization mismatch (X_f the forward-link and X_b the reverse-link polarization mismatch), F represents the backscatter link budget fade margin and F_f forward fade margin.

Depending on the configurations of the receiving and transmitting reader antennas 3.6, the equations 3.12 and 3.13 can be slightly different. In the monostatic configuration, where the receiving and transmitting reader antennas are the same, the distance in the forward and backscatter links are the same and represented as r. The bistatic configuration uses two different antennas in the reader, and they can be closely spaced (bistatic collocated) or widely spaced (bistatic dislocated). The distances in the forward link and in the backscatter link can be different between them, so the average power delivered to the tag and the modulated power backscattered by the tag received by the reader in the bistatic configuration, are given by:

$$P_{Tag_m} = \frac{G_{T_X} P_{T_X} G_{Tag} \lambda^2 X}{(4\pi r_f)^2 F_f} (1 - \frac{1}{2}(|\rho_1|^2 + |\rho_2|^2)), \tag{3.14}$$

$$P_{R_{X_m}} = \frac{G_{T_X} P_{T_X} G_{R_X} G_{Tag}^2 \lambda^4 X_f X_b}{(4\pi)^4 r_f^2 r_b^2 F} \frac{1}{4} |\rho_1 - \rho_2|^2, \tag{3.15}$$

Considering an example of an RFID tag, it is possible to calculate the power delivered to the tag from the reader and the modulated power backscattered by the tag which was received from the reader. The following parameters were taken into account:

- Frequency = 866 MHz
- G_{Tag} = 2 dBi
- $G_{T_X} = G_{R_X}$ = 6 dBi
- P_{T_X} = 30 dBm
- Reader Sensitivity$\rightarrow -80$ dBm to -90 dBm
- Tag Sensitivity$\rightarrow -15$ dBm to -20 dBm

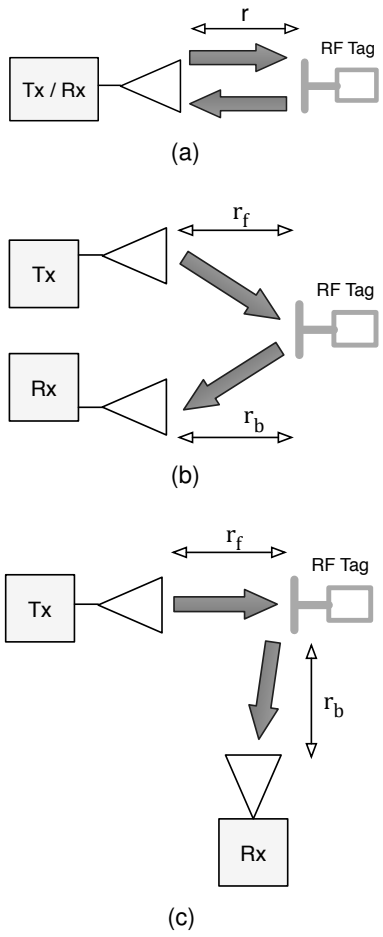

Figure 3.6: Different configurations of the antennas in backscatter link. (a) Monostatic. (b) Bistatic Collocated. (c) Bistatic Dislocated.

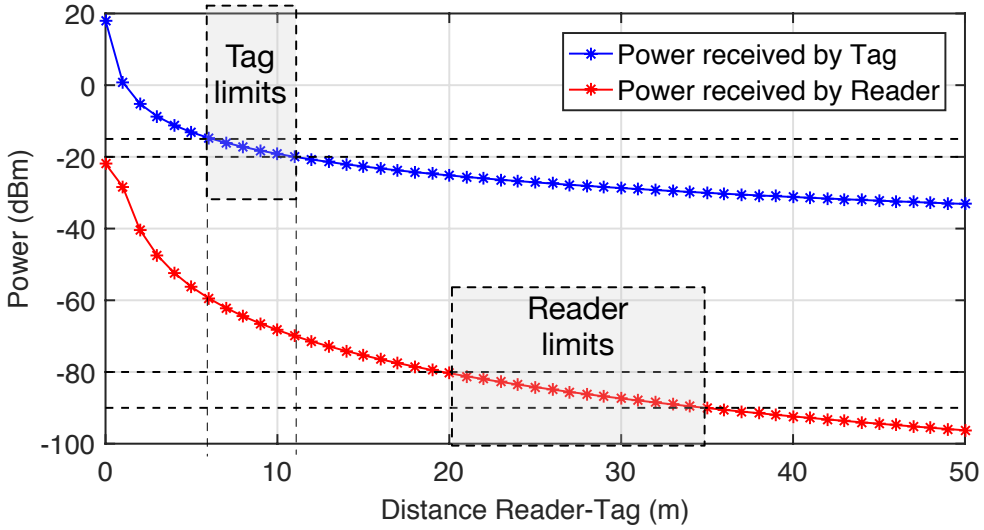

Figure 3.7: Average power delivered to the tag and the modulated power backscattered by the tag received by the reader in the monostatic configuration.

Since the reader antennas are circularly polarized and the tag antenna is linear polarized, a 3 dB polarization mismatch is considered. In order to simplify calculations, it was considered a dominant direct line-of-sight (F = 0 dB). In this example, the non-zero input impedance in one state of the tag will not be considered. This non-zero state is directly related to the incapability of the FET to provide a true short circuit. As it was mentioned, the RFID tag switch between a match load and a short ($\rho_1 = 0$ and $\rho_2 = -1$) which results in a modulation factor of M = 0.25. Considering all these parameters and the equations 3.12 and 3.13 it is possible to obtain the Fig. 3.7. The presented results allow the understanding of the propagation mechanisms that influence the tag received power and the backscatter communication. These calculations are useful for predicting bacskatter radio system performance. Moreover, it enables to define properly the states of modulation in a backscatter system. If the backscatter sweeps between short and open (reflection coefficient of -1 and 1) the power reflection is maximized but the power available on the tag is penalized. From the Fig. 3.7 it can be observed that the major limitation is related to the tag sensitivity, which limits the distance that is possible to power up the tag (6 m to 11 m). On the other hand, the reader sensitivity allows the backscatter communication from 20 m to 34 m.

As it was said previously, the PSK modulation will maximize the power reflected from the tag and the ASK modulation will maximize the power available on the tag, which means that a semi-passive tag will communicate at a larger distance than a passive tag, as can be seen in Fig. 3.8. Moreover, in Fig. 3.8 we demonstrate a possible solution to overcome the limitation imposed by the tag sensitivity, which consist in adding a different tone to supply the tag. Two different tones were added (one at 400 MHz and other at 1.7 GHz) to power the

tag, meaning that the sensor could continuously be powered with one frequency (400 MHz or 1.7 GHz) and communicate at the other (866 MHz).

Adding one tone at 1.7 GHz with 0.5 W will improve the distance that is possible to power up the tag (7 m to 12 m), but the significant improve was verified when a tone at 400 MHz with 0.5 W was added. The distance to power the tag increased from 11 m to 20 m. The equation 3.16 was used to compute different sensitivities of the tag with the added extra tone.

$$P_{TotalTag_m} = \frac{G_{T_X} P_{T_X} G_{Tag} \lambda^2 X}{(4\pi r)^2 F_f} (1 - \frac{1}{2}(|\rho_1|^2 + |\rho_2|^2)) + \frac{G_{T_{X2}} P_{T_{X2}} G_{Tag} \lambda_2^2 X_2}{(4\pi r)^2 F_{f2}}, \tag{3.16}$$

On the other hand, the reader sensitivity allows the backscatter communication from 28 m to 50 m, by using a tag with PSK modulation.

In chapter 4, different tag approaches which operate in two different frequencies (one for backscatter communication and the other for the WPT link), are studied, designed and discussed.

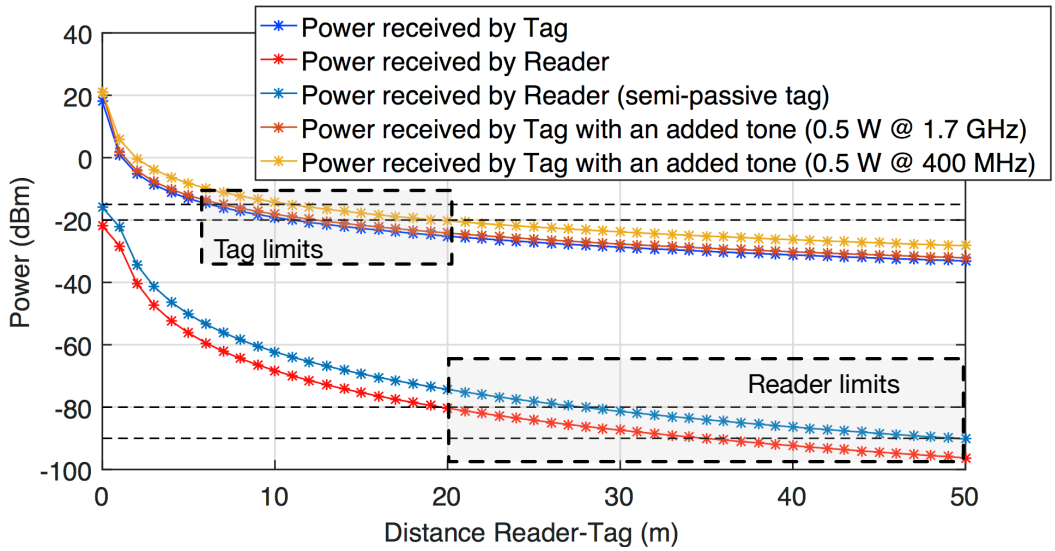

Figure 3.8: Average power delivered to the tag and the modulated power backscattered by the tag received by the reader in the monostatic configuration, considering four different approaches: The tag operating with ASK modulation (passive); The tag operating with PSK modulation (semi-passive); The tag operating at two different frequencies (adding 400 MHz to supply the tag); The tag operating at two different frequencies (adding 1.7 GHz to supply the tag).

3.2 Backscatter Modulation for Wearable Devices

In this section, a BPSK backscatter modulator working at 915 MHz will be designed and experimentally validated. Moreover, the modulator will be evaluated as a potential use case on wearable applications.

3.2.1 Design strategy

The developed BPSK backscatter modulator is presented in Fig. 3.9. The circuit is composed by a surface mount ceramic chip antenna (VJ5601M915MXBSR from Vishay) designed to operate at 915 MHz, the antenna tuning circuit with two inductors and the E-pHEMT (ATF54143 from Broadcom, chosen for its low gate-source drive capacitance) that is responsible for the ON and OFF switching. By changing the voltage presented to the gate of the transistor between 0 V and 0.8 V it is possible to change the phase of the reflection coefficient. The BPSK modulation was used in order to maximize the reflected power. The overall dimension of the circuit is 1.8 cm x 2 cm with a weight of 1.6 g.

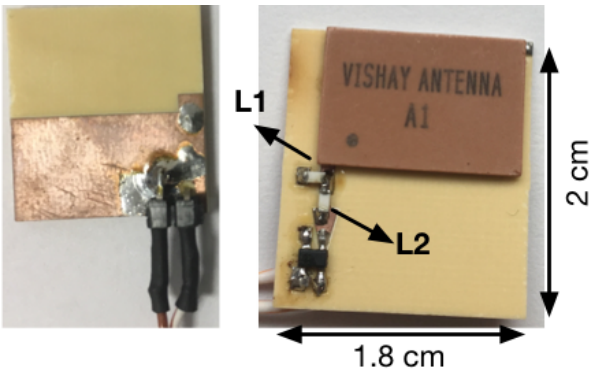

Figure 3.9: Photograph of the developed backscatter modulator. Element values are L1 = 22 nH, L2 = 27 nH. Substrate for the transmission lines is Astra MT77, thickness = 0.762 mm, ε_r = 3.0, tan δ = 0.0017.

In order to implement this circuit, several simulations were conducted. Figure 3.10 (on the right) presents the reflection coefficient (S_{11}) simulated results when the voltage presented to the gate of the transistor varies from 0 V up to 0.8 V, for a 915 MHz operating frequency. These results were performed with a variation from -30 dBm to 0 dBm of input power, in order to understand the behavior of the modulator at lower values of input power. As shown in Fig. 3.10, it is possible to achieve 180°phase shift by simply switching the voltage at the gate of transistor from 0 V to 0.8 V. The simulations were performed with Advanced Design System (ADS) and the schematic developed is presented in Fig. 3.10 (on the left).

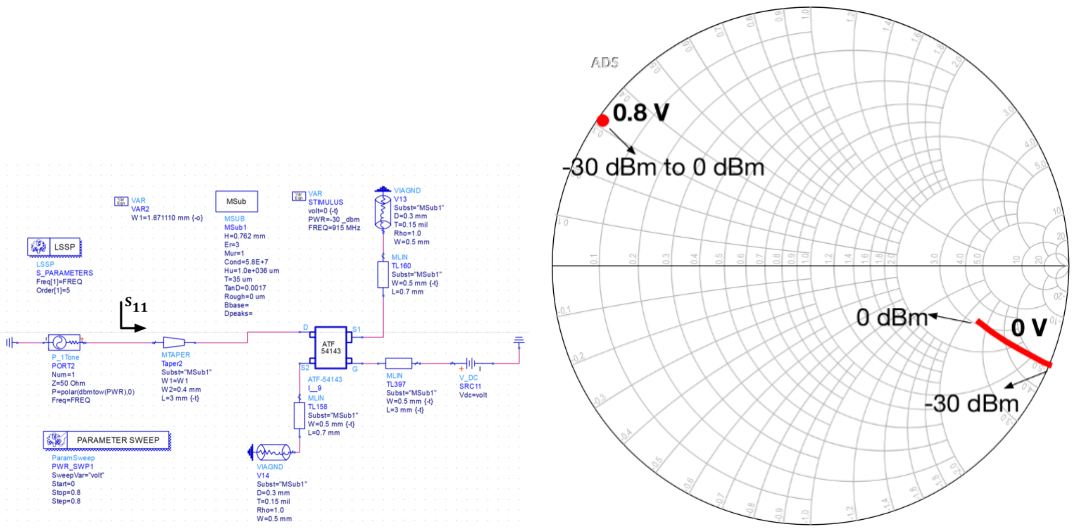

(a) (b)

Figure 3.10: Simulations of backscatter modulator. On the left the proposed circuit developed in ADS. On the right the results obtained for the S11 from the simulated circuit with two different voltages at the gate of transistor (0 V and 0.8 V).

After theoretically validating the transistor behaviour, it was necessary to measure the antenna with the tuning circuit to guarantee matching at 915 MHz. A simple PCB was developed, containing two inductors, the antenna and an SMA connector. A Performance Network Analyzer (E8361C from Agilent Technologies) was used to measure the reflection coefficient (S_{11}) and the results obtained are presented in Fig. 3.11, showing a reasonable match at the operating frequency.

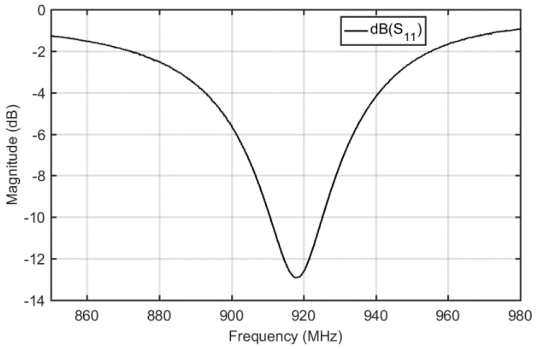

Figure 3.11: Measured S_{11} of the tunned chip antenna.

After these validations, the solution developed is presented in Fig. 3.9. Backscatter communication technology can facilitate the use of wearable devices, and when combined with WPT, can increase the number of possible applications. In Fig. 3.12 we present a possible

block diagram of a wearable device that can have sensing capabilities without requiring batteries. In order to power the microcontroller and the sensors, a rectifier (RF-DC converter) must be developed to convert the RF signals into DC energy.

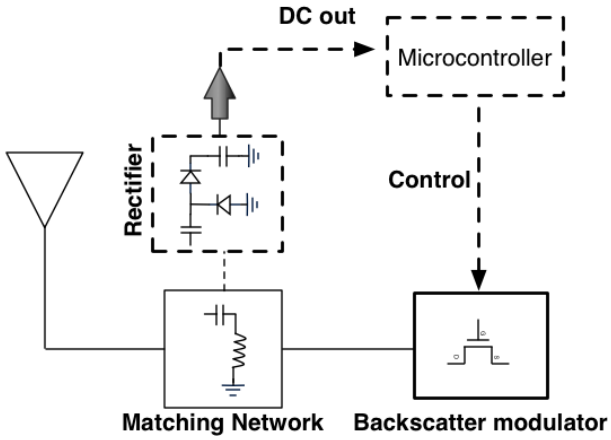

Figure 3.12: Block diagram of a battery-free wearable device.

3.2.2 DUT Performance in Wearable Applications

In order to evaluate the behavior of the backscatter modulator as a wearable device, we inserted the developed circuit presented in Fig. 3.9 into a wristwatch, as can be seen in Fig. 3.13. The two wires coming out from the wristwatch will connect to the waveform generator, which produces an 0.8 Vpp, 1.0 MHz square wave signal. In a real scenario, this modulating signal would be replaced by the bit stream generated by the microcontroller which will contain the desired sensing information.

The setup used for the experimental measurements can be seen in Fig. 3.14. It is composed of two commercial antennas (ALR-8610-AC from Alien), a signal generator (SMW200A from Rohde & Schwarz) to generate the CW at 915 MHz, a spectrum analyzer (FSW8 from Rohde & Schwarz) to obtain the reflected wave at 915 ± 1 MHz and a low frequency waveform generator (33250A from Agilent Technologies) to generate the 1.0 MHz square wave signal.

In order to evaluate the proposed wristwatch presented in Fig. 3.13, we conducted two different scenarios, which are shown in Fig. 3.17. The wristwatch with the backscatter modulator inside was attached to the wrist of a person and several measurements were taken while the person was moving. Two different scenarios were taken into account. First, the person was moving away from the antennas with its back turned to them. Second, the person was moving towards the antennas while facing them. The power transmitted from the signal generator at 915 MHz was 22 dBm. Considering the losses introduced by the antenna

Figure 3.13: Backscatter modulator embedded into the watch.

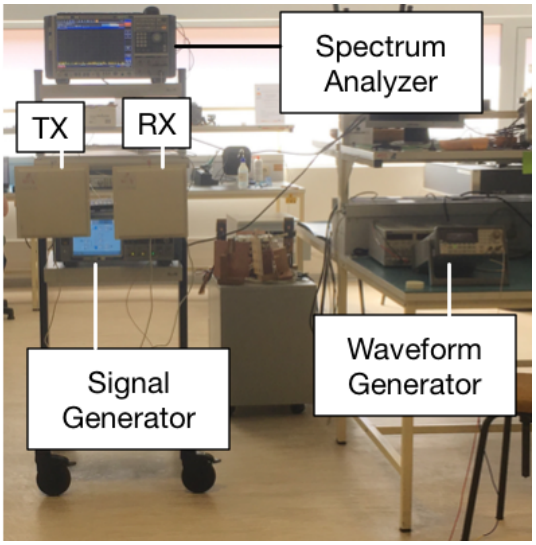

Figure 3.14: Laboratorial measurement setup.

cables (3 dB) and the gain of the antenna (estimated at 5.5 dBi without cable and 4 dBi with cable) the Equivalent Isotropic Radiated Power (EIRP) was estimated to be 23 dBm (the antenna was used with cable). The power obtained at the modulation frequency (916 MHz) in the spectrum analyzer for the two different scenarios is presented in Fig. 3.16. In Fig. 3.17 we present two obtained results, for a distance of 4 m in both scenarios (front and back).

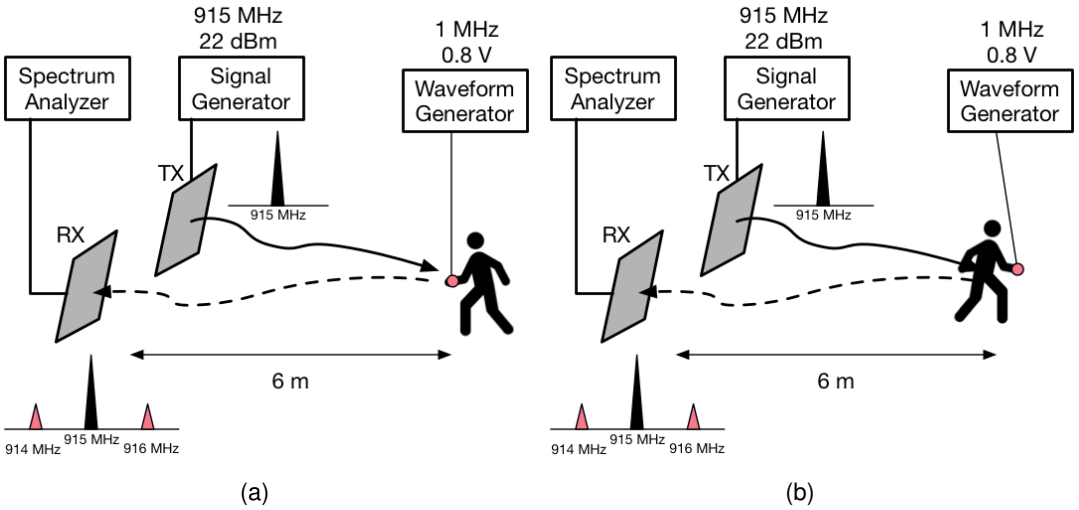

Figure 3.15: Two different scenarios to measure the backscatter modulator embedded into the watch. On the left the person is placed in front of the setup. On the right the person is turning his back to the setup.

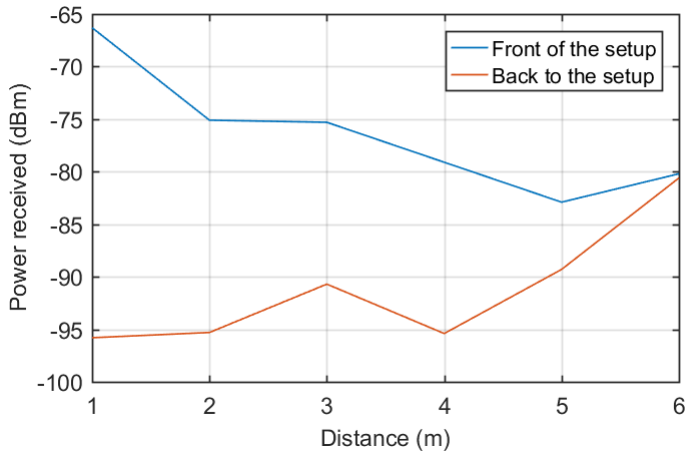

Figure 3.16: Power received by the spectrum analyzer at 916 MHz.

Since BPSK modulation is being used and the bandwidth needed to transfer such low bit rate is very small, all the signal powers that are being received can be decoded by any general purpose receiver. By analyzing Fig. 3.16 it can be seen that as the distance increases, the

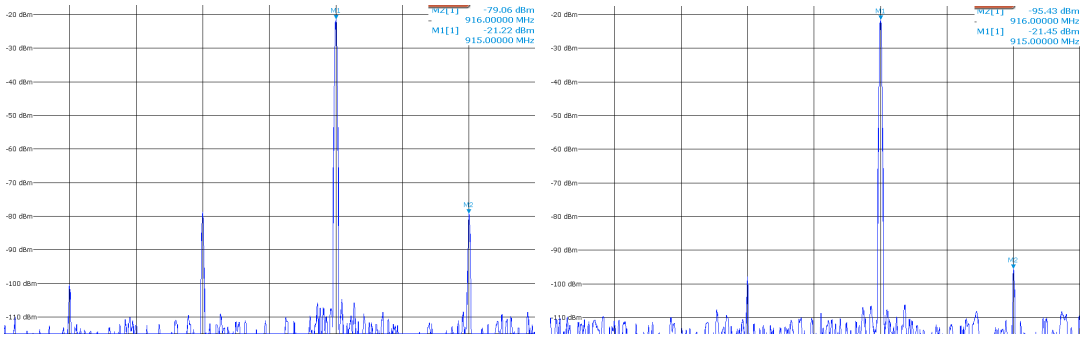

(a) (b)

Figure 3.17: Measurement results with the person placed at 4 m from the transmitter/receiver. On the left the person is placed in front of the setup. On the right the person is turning his back to the setup.

power received at the modulation frequency decreases. Comparing the received values for the two scenarios described previously, when the person is with its back turned to the reader, the power received is lower due to some body blockage. Moreover, at higher distances the received power is similar in both scenarios mainly due to the multipath effects.

3.3 Conclusions

- The tag modulation states must be properly chosen in order to maximize the power absorbed by the tag while maximizing the power reflected from the tag. As it was seen in Fig. 3.8 the PSK modulation (with reflection coefficients of -1 and 1) maximizes the power reflected from the tag but penalizes the power transferred to the tag. In other hand, by adding one more tone to supply the tag, the distance to power the tag was improved. In the next chapter a more carefully analysis will be conducted.

- The BPSK backscatter modulator presents a light, compact and efficient design, which can be used in wearable devices. Although, tests were performed in a laboratory environment, the device was used in a real scenario application, inside a wristwatch. These results are a proof of the concept, demonstrating that the technology can be implemented in real wearable devices, where their use is increasing day by day. This approach has the advantage of extending the wearable devices battery. This kind of communication consumes less power than any other. Besides that, this technology can also be combined with WPT techniques allowing to have battery-less devices. By using this approach, a considerable distance between the reader and the device was achieved, with conventional values for the transmitted power and sensitivity. The distance could be enhanced by increasing the transmitted power or antenna gain (bellow the values of regulation).

Chapter 4

Backscatter modulation with WPT capabilities

Outline

Nowadays WSNs depend on the battery duration and there is a lot of interest in creating a passive sensor network scheme in the area of IoT and space oriented WSN systems. RF EH enables the control and the delivery of wireless power to RF devices. All the devices made with this technology can be sealed, embedded with these structures, or made mobile, so they can be battery independent.

In this chapter, a complete passive WSN, that can potentiate the IoT area and space craft sensing will be presented. This WSN should be capable of receiving a continuous flow of energy, so that the sensing mechanisms can be continuously powered, as it was previously demonstrated in the previous chapter. For this, a combination of backscatter modulation with WPT, using the same diode based approach as in a traditional RFID circuit is proposed. This way the cost is maintained low, but the amount of gathered energy is maximized during the backscatter communication. Moreover, in this chapter the steps to implement the passive sensor will be explained and experimentally validated.

4.1 Backscatter WPT

Our proposed system is based on Fig. 4.1 and it was firstly evaluated with another configuration in [156]. It is composed by two matching networks, a backscatter modulator and a dual band rectifier. The goal is to harvest electrical energy with one tone (1.8 GHz) and with the other tone (2.45 GHz) transfer data by backscatter means. The RF power harvester employs a receiving antenna, an impedance matching network, DC power conditioning and the sensor to be powered. The backscatter modulator employs the receiving antenna, an

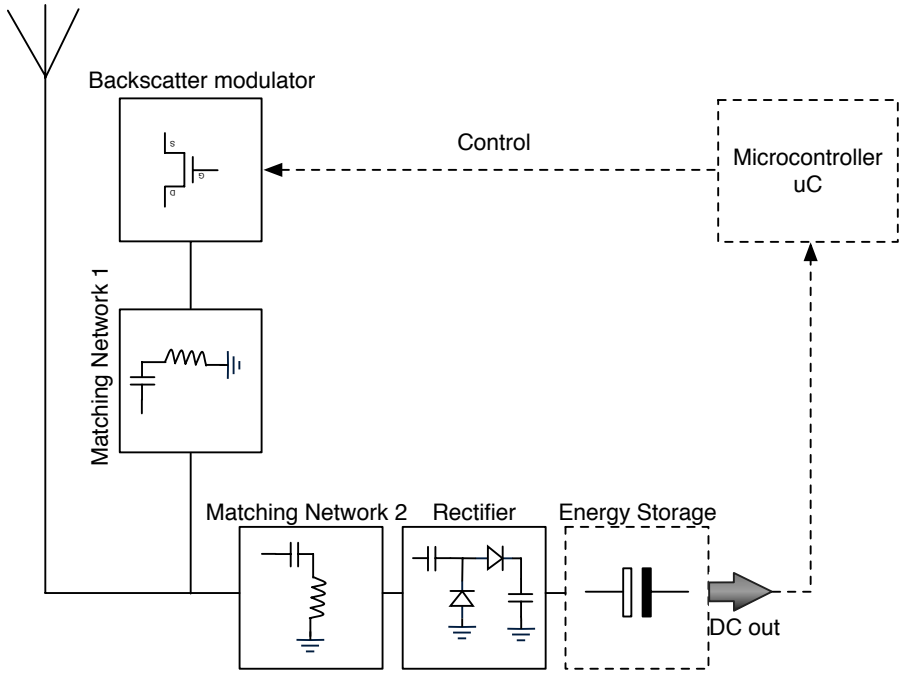

Figure 4.1: Block diagram of proposed system based on backscattering with WPT.

impedance matching network and a semiconductor device to control the reflection coefficient.

4.1.1 Backscatter design

In this section an implementation of a stand-alone circuit for backscatter modulation is presented. The proposed system is shown in Fig. 4.2 and includes a switch (Broadcom ATF-54143) that modulates the impedance of the antenna and causes a change in the amount of energy reflected by the antenna. The signal at the gate of the transistor is a sequence of one and zero bits. In common backscatter modulators, when the switching transistor is in the ON-state, the incoming carrier signal is reflected by the antenna and scattered back to the reader with ideally π phase-difference. During the OFF-state of the switching transistor, the received signal is reflected back to the reader with ideally zero phase.

4.1.2 WPT RF-DC dual band design

Due to the need of having autonomous devices for IoT, the EH and WPT technologies are of interest in scientific as well as industrial areas. Since ambient EH is available in low levels, there is a need to design efficient energy harvesters that can collect ambient energy from different frequency bands. The proposal in this paper uses a dual band rectifier coping with backscatter. In this section the configuration for the dual band rectifier is shown. The

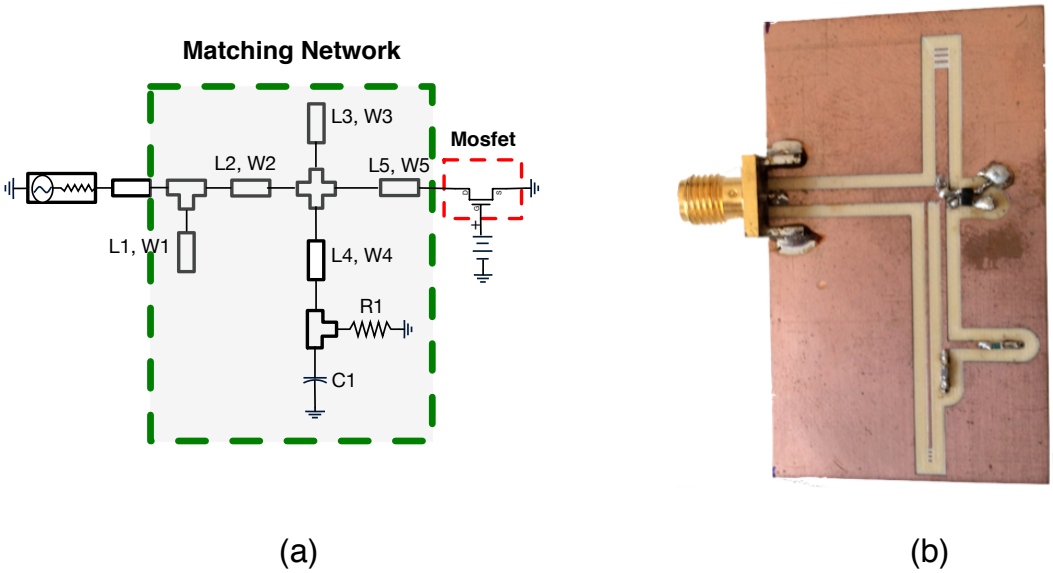

Figure 4.2: (a) Configuration of proposed backscatter circuit. (b) Photograph of the backscatter circuit. Element values are L1 = 28.9 mm, W1 = 0.4 mm, L2 = 1 mm, W2 = 1.8 mm, L3 = 13.5 mm, W3 = 1.5 mm, L4 = 16.3 mm, W4 = 0.7 mm, L5 = 1.3 mm, W5 = 0.6 mm, R1 = 50 Ω, C1 = 47 pF. Substrate for the transmission lines is Astra MT77, thickness = 0.762 mm, ε_r = 3.0, tan δ = 0.0017.

---

configuration used is based on the principle shown in [157] due to the simplicity of the design, and it is presented in Fig. 4.3.

Some work on dual band operation has been developed in many different configurations. In [158] a microstrip printed dual frequency rectifier that operates at 1.8 GHz and 2.4 GHz by using a cross-shaped match stub was presented. In [49] a dual band (915 MHz / 2.45 GHz) rectifier based on resistance compression networks was designed in order to improve the performance.

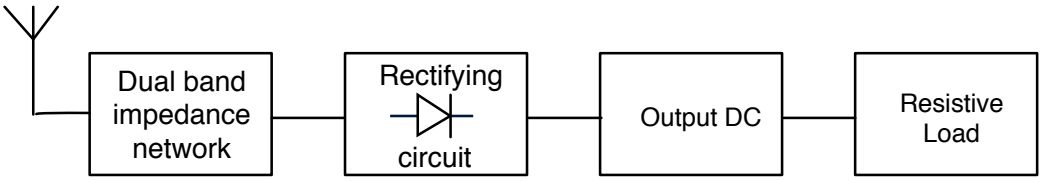

Figure 4.3: Block diagram of dual band rectifier circuit.

In [159] the authors designed a dual band rectifier based on discrete elements for the frequencies of 915 MHz and 2.45 GHz. In [160] a dual band two-section 1/3-wavelength transformer that operates at the fundamental frequency and its first harmonic was developed.

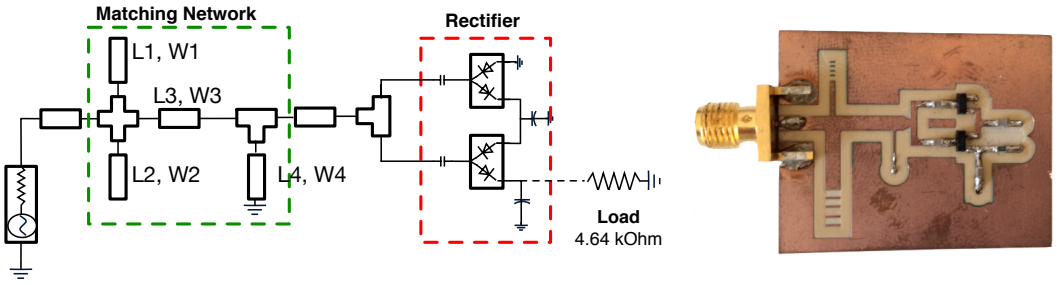

(a) (b)

Figure 4.4: (a) Configuration of proposed dual band rectifier. (b) Photograph of the dual band rectifier. Element values are L1 = 4.7 mm, W1 = 0.7 mm, L2 = 7.9 mm, W2 = 2 mm, L3 = 7 mm, W3 = 2 mm, L4 = 5.4 mm, W4 = 0.4 mm. Substrate for the transmission lines is Astra MT77, thickness = 0.762 mm, ε_r = 3.0, tan δ = 0.0017.

Monzon [161] showed a novel and elementary two-section impedance transformer, capable of dual band operation under restricted load and frequency conditions. In [162], Giannini and Scucchia presented a class of distributed element matching networks that was able to guarantee the required impedance values at fundamental frequency and its second and third harmonics. Chang [157] presented a modified shunt-stub dual band impedance transformer that contained four different configurations, each of which consisted of dual two-section transmission lines. In our approach the dual band matching network is developed to match the two different impedances. The dual band rectifier, including the matching network and output DC has been designed and simulated using harmonic balance in ADS and it was optimized for 2 dBm in order to achieve better efficiency in the frequencies of 1.8 GHz (for the WPT) and 2.45 GHz (for the implementation of backscatter scheme). A two-stage Dickson multiplier was designed and the diodes used were RF Schottky diodes (Skyworks SMS7630-006LF), in order to provide stronger current drive ability, with the penalty that the capacitors in parallel have to withstand the full DC voltage developed along the chain. A matching network is essential in providing the maximum power transfer from the antenna to the rectifier circuit. This matching network was designed and optimized in order to maximize the efficiency of the rectifier for both frequencies at 1.8 GHz and 2.45 GHz. Fig. 4.4 shows the final prototype.

4.1.3 Integrating Backscatter solution with WPT solution

Figure 4.5 illustrates the two different states of the transistor gate voltage for two different frequency tones. Since the backscatter design is the same as the one explained in section 4.1.1, and the dual band rectifier the same as the one in section 4.1.2, the combination of these two circuits can be explained by the example in Fig. 4.5.

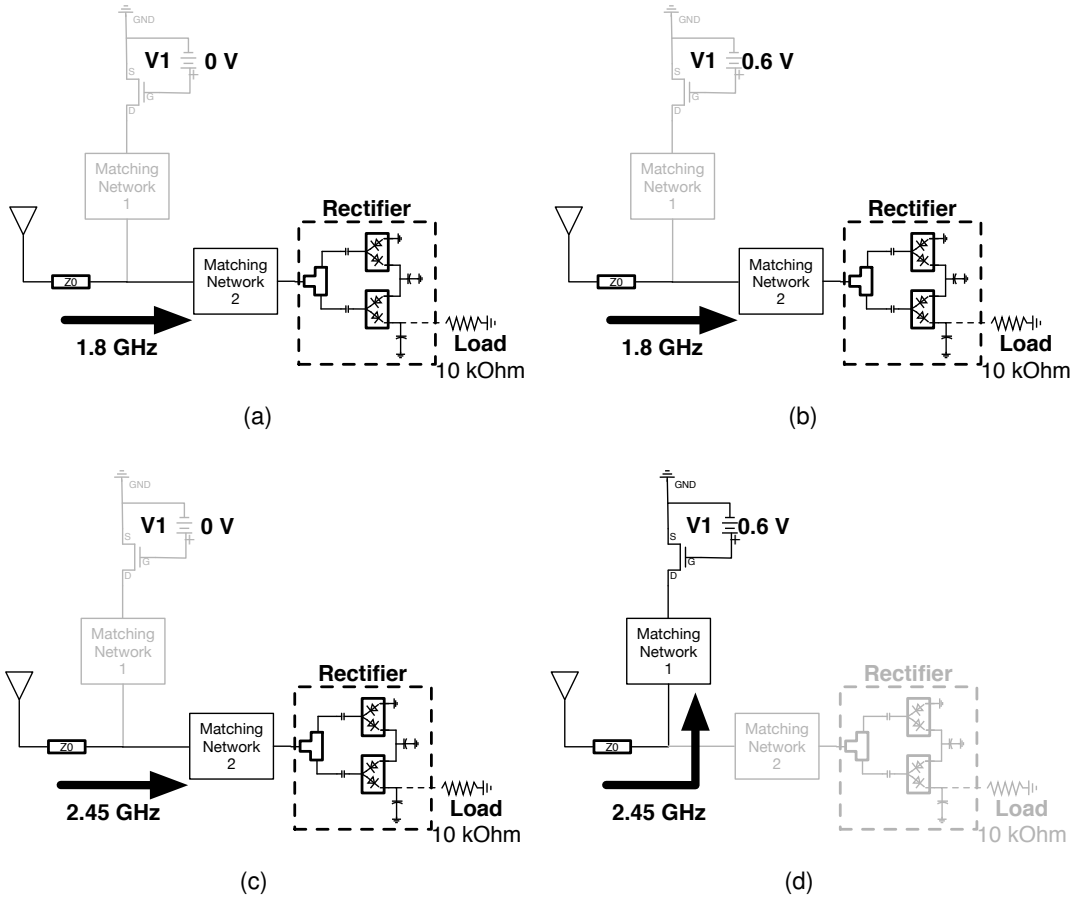

Figure 4.5: Different modes of operation with different frequencies (a) $V_{Gate} = 0$ V for 1.8 GHz (b) $V_{Gate} = 0.6$ V for 1.8 GHz. (c) $V_{Gate} = 0$ V for 2.45 GHz. (d) $V_{Gate} = 0.6$ V for 2.45 GHz.

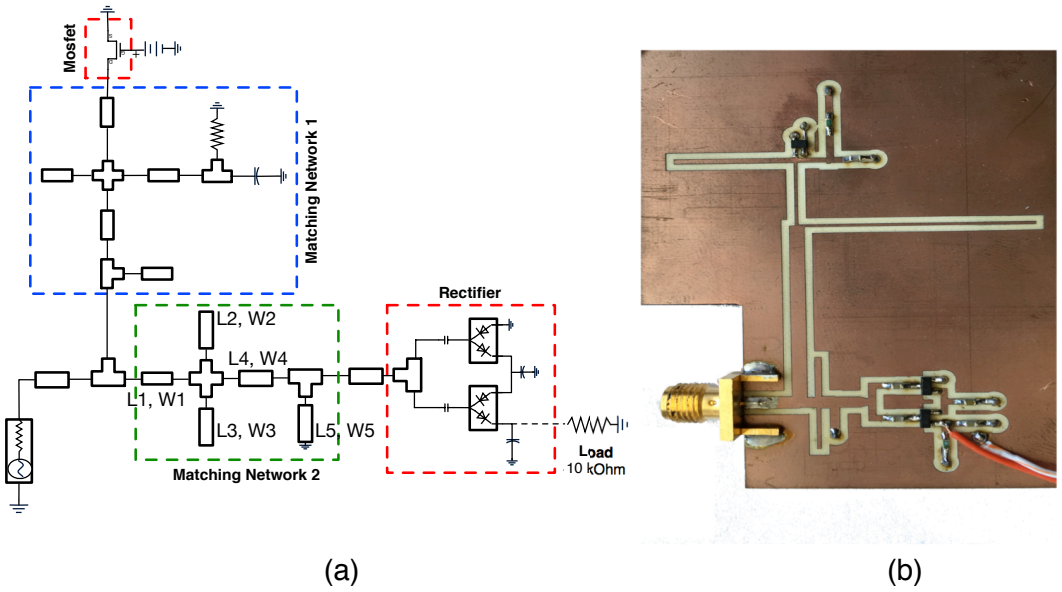

Figure 4.6: (a) Configuration of proposed backscatter modulator and dual band rectifier circuit. (b) Photograph of the backscatter modulator and dual band rectifier. Element values are L1 = 1 mm, W1 = 1.6 mm, L2 = 6.3 mm, W2 = 0.8 mm, L3 = 6.5 mm, W3 = 0.5 mm, L4 = 1 mm, W4 = 1.9 mm, L5 = 4 mm, W5 = 1.2 mm. Substrate for the transmission lines is Astra MT77, thickness = 0.762 mm, ε_r = 3.0, tan δ = 0.0017.

During the OFF-state and ON-state of the switching transistor at 1.8 GHz, the circuit was designed to have almost zero reflection coefficient, as shown in Fig. 4.5(a) and Fig. 4.5(b). The same reflection coefficient is achieved during the OFF-state of the switching transistor when the frequency is 2.45 GHz, as shown in Fig. 4.5(c). During the ON-state of the switching transistor at 2.45 GHz, the circuit was designed to have the reflection coefficient different from 0 (ideally equal to 1), as illustrated in Fig. 4.5(d).

In Fig. 4.1 the block diagram of a backscatter modulator with dual band rectifier design is presented, and the main goal is to combine backscattering with WPT. The objective is to obtain, for different states of the transistor (0 V and 0.6 V at gate) and for two different frequencies (1.8 GHz and 2.45 GHz), modulation combined with WPT. Figure 4.6 shows the prototype designed that includes the transistor which modulates the impedance of the antenna and the two-stage Dickson multiplier.

4.1.4 Results

4.1.5 Backscatter Design

In this implementation, the backscatter modulator was designed for two different frequencies and the goal was to achieve zero-phase when the switching transistor is at OFF-

state (0 V at the gate of transistor) at 1.8 GHz and 2.45 GHz and when the transistor is at ON-state (0.6 V at the gate of transistor) at 1.8 GHz. At 2.45 GHz when the transistor is at the ON-state we intended to achieve π phase-difference. These results can be seen in Fig. 4.7 and the impedances obtained are shown in table 4.2 and can be compared with the simulated results shown in table 4.1. The circuit in Fig. 4.2 was optimised to achieve two reflection coefficients (-1 and 1) which correspond respectively to a short circuit and an open circuit. The designed backscatter works at 2.45 GHz, since the reflection coefficient varies from 1 to -1 as the gate voltage of the transistor is switched from 0 to 0.6 V, as can be seen in Fig. 4.7. At 1.8 GHz the reflection coefficient is always 1 (open circuit) as it was intended. In 4.1 and 4.2 the values of the impedances for two different frequencies (1.8 GHz and 2.45 GHz) at two different states of the gate voltage of the transistor (0 V and 0.6 V) are shown. The values of the impedances at 1.8 GHz are very high (ideally infinite) in both states of the transistor. At 2.45 GHz when the gate voltage is 0 V the impedance is very high (ideally infinite) and with 0.6 V at the gate of transistor the value of the impedance is very low (ideally zero).

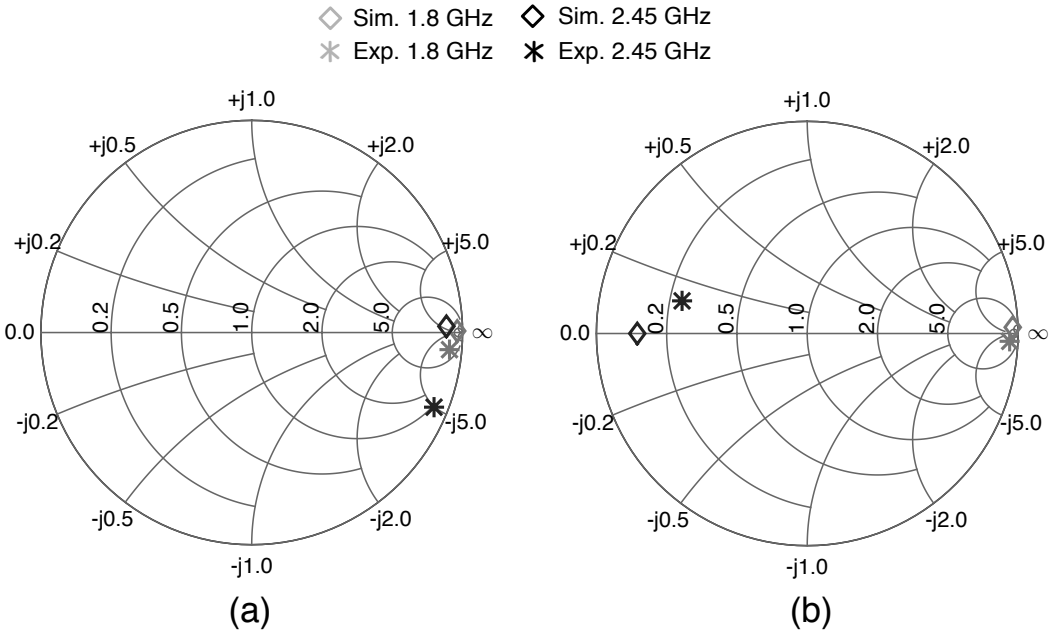

Figure 4.7: S_{11} parameter as function of frequency for two different values of transistor's gate voltage. (a) $V_{Gate} = 0$ V. (b) $V_{Gate} = 0.6$V.

4.1.6 WPT RF-DC dual band design

Fig. 4.8 presents the output power achieved, measured and simulated, for both frequencies, 1.8 GHz and 2.45 GHz, for different input powers. Fig. 4.8 shows the agreement between experimental and simulated results, except for 2.45 GHz. For 1.8 GHz, at 2 dBm of

Table 4.1: Simulated results of system impedance as function of transistor's gate voltage and frequency.

$\mathbf{V_{Gate}(V)}$	$\mathbf{Z(\Omega)}$ 1.8 GHz	$\mathbf{Z(\Omega)}$ 2.45 GHz
0	$3.40\text{E}3 + j609.68$	$1.01\text{E}3 + j687.28$
0.6	$1.50\text{E}3 + j2.12\text{E}3$	$4.46 - j0.83$

Table 4.2: Experimental results of system impedance as function of transistor's gate voltage and frequency

$\mathbf{V_{Gate}(V)}$	$\mathbf{Z(\Omega)}$ 1.8 GHz	$\mathbf{Z(\Omega)}$ 2.45 GHz
0	$531.84 - j808.03$	$46.35 - j245.27$
0.6	$1.38\text{E}3 - j1.27\text{E}3$	$12.20 + j5.97$

Table 4.3: Dual band rectifier simulated results of dc output voltage as function of input power per tone

Power (dBm)	**DC voltage (V)** 1.8 GHz	**DC voltage (V)** 2.45 GHz	**DC voltage (V)** 1.8 GHz + 2.45 GHz
-10	0.297	0.296	0.503
-8	0.422	0.421	0.686
-6	0.586	0.587	0.925
-4	0.800	0.802	1.233
-2	1.076	1.080	1.627
0	1.430	1.437	2.128
2	1.881	1.896	2.605
4	2.454	2.473	2.877

input power, the output power achieved is 0.76 mW and 0.82 mW in respectively, simulated and experimental results. For 2.45 GHz, at 2 dBm of input power, the output power obtained is 0.77 mW and 0.61 mW in respectively, simulated and experimental results. Using two tones at the input of the system, 1.8 GHz and 2.45 GHz, the output power obtained at 2 dBm is 1.46 mW and 1.51 mW in respectively, simulated and experimental results. The addition of another tone increases the output power, since the design is a dual band rectifier. In table 4.4 and table 4.3 is shown, respectively, experimental and simulated results of the voltage at the output as function of input power for different frequencies. The power that is in the axis of Fig. 4.8 and in the tables 4.3 and 4.4 for the two tones, is the power used for backscatter communication (2.45 GHz tone) and not the overall power. The other tone (1.8 GHz) is used to increase the dc output voltage.

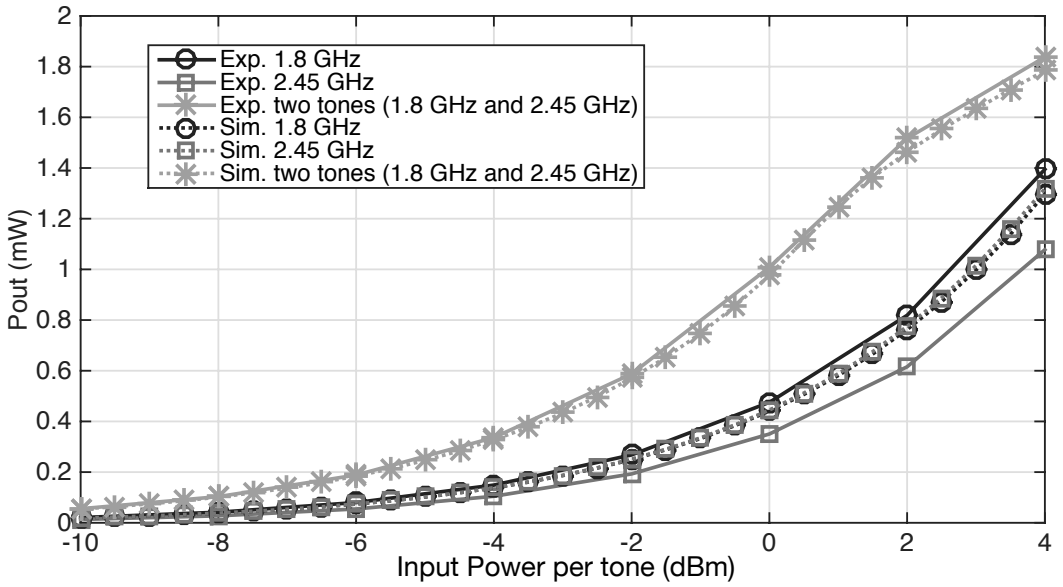

Figure 4.8: Simulated and experimental results of output power of dual band rectifier as function of input power per tone.

Table 4.4: Dual band rectifier experimental results of dc output voltage as function of input power per tone

Power (dBm)	**DC voltage (V)** 1.8 GHz	**DC voltage (V)** 2.45 GHz	**DC voltage (V)** 1.8 GHz + 2.45 GHz
-10	0.310	0.247	0.507
-8	0.440	0.357	0.692
-6	0.609	0.503	0.935
-4	0.831	0.697	1.249
-2	1.115	0.946	1.651
0	1.485	1.275	2.162
2	1.949	1.690	2.653
4	2.544	2.236	2.920

4.1.7 Integrating Backscatter solution with WPT solution

At 1.8 GHz for both states of the transistor, we intended to achieve the highest output power at 2 dBm and to match the impedance of the system as it can be seen, respectively in Fig. 4.9 and Fig. 4.10. At 2.45 GHz it was intended to obtain two different results, with 0 V at the gate of transistor, the output power should be the maximum possible and the impedance of the system should be matched as well. With 0.6 V at the gate of the transistor the goal was to obtain the mismatch of the system impedance. In Fig. 4.9 and Fig. 4.10 the results for these goals can be seen.

In Fig. 4.11 the DC output voltage obtained for the different states of transistor for two different frequencies for both simulated and experimental results is demonstrated. It was

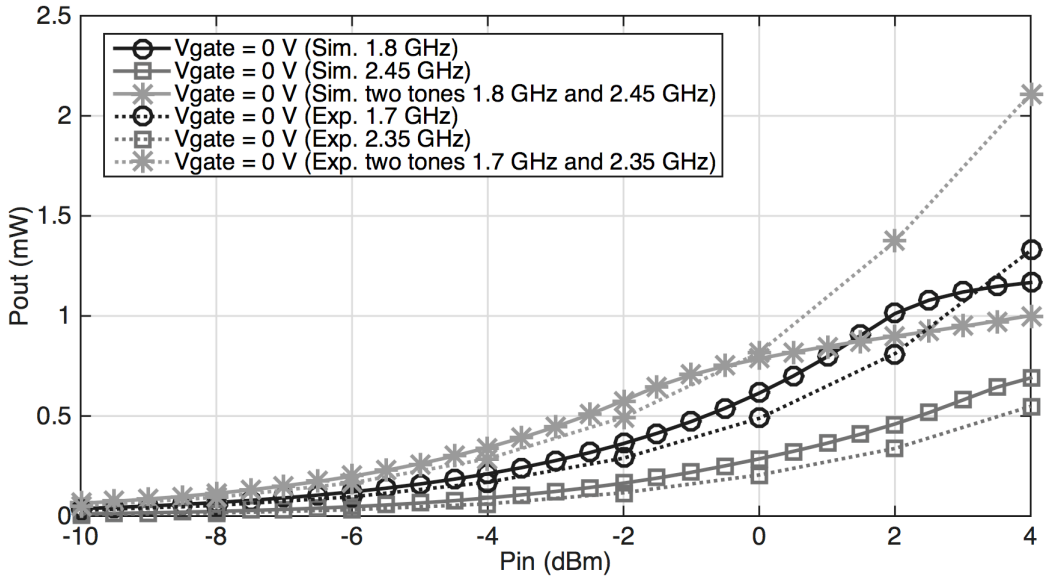

(a)

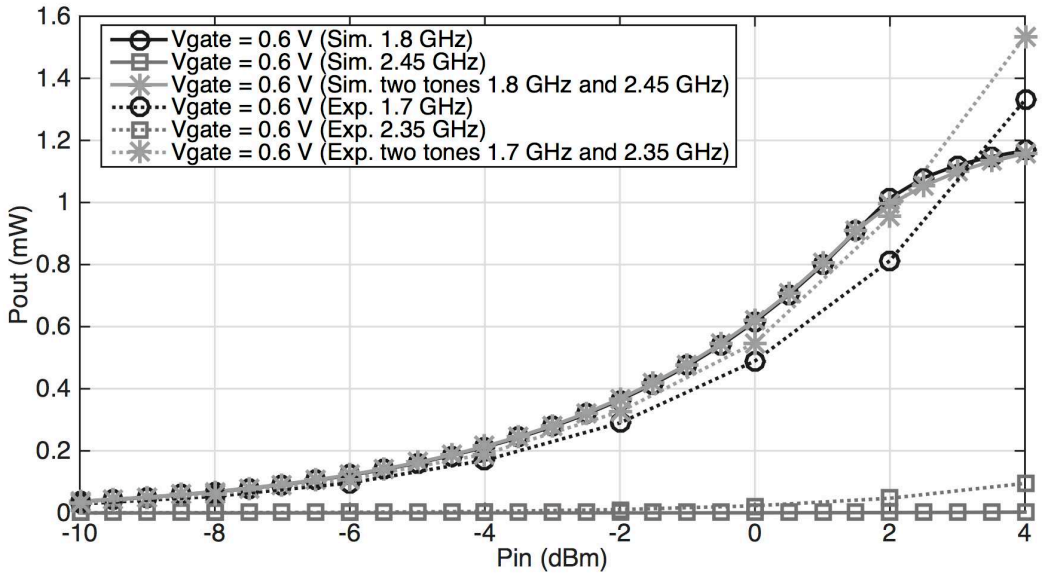

(b)

Figure 4.9: Simulated and experimental results for output power of backscatter modulator and dual band rectifier as function of input power per tone. (a) $V_{Gate} = 0$ V. (b) $V_{Gate} = 0.6$ V.

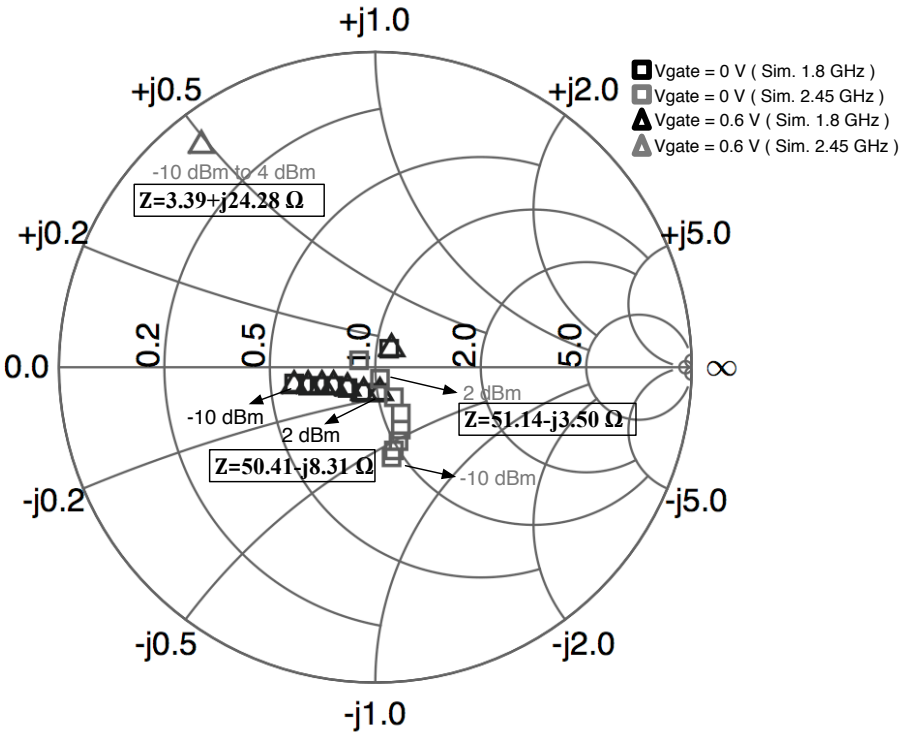

Figure 4.10: Simulated S_{11} parameter as function of frequency and input power for two different values of gate voltage.

expected that this system could be capable to supply a microcontroller that needs 1.5 V of supply.

By measuring the S_{11} parameter at 2 dBm we concluded that the circuit was matched for the frequencies 1.7 GHz and 2.35 GHz. We measured the DC output voltage for these two frequencies and compared with 1.8 GHz and 2.45 GHz. For 1.7 GHz at 2 dBm of input power with 0 V at gate, the DC output voltage measured was 2.9 V (0.35 V below the simulated value) and 1.8 V at 2.35 GHz (0.35 V below the simulated value), as shown in Fig. 4.11(a). Switching the gate voltage to 0.6 V, with 2 dBm of input power, the DC output voltage measured at 1.7 GHz was 2.9 V (0.35 V below the simulated value) and 0.75 V at 2.35 GHz (0.65 V above the simulated value), as illustrated in Fig. 4.11(b).

The main purpose of this work was to validate both matching networks, for the backscatter modulation and for the dual band rectifier, in order to design a system with the capability to be fully passive with a continuous power delivering. Input power for the single tone is different from the dual tone, but in these figures (Figs. 4.9 and 4.11) we intended to show the increase of output power and DC voltage obtained when adding an extra tone. In terms of application, this extra tone is the same as adding a fixed wireless power transmitter. We should be aware that in the backscatter frequency (2.45 GHz) the signal will be modulated as an ASK, thus the power delivered to the sensor will be lower in certain periods of the modulation envelope. In our approach the delivering of power is constant, as can bee seen by Figs. 4.9 and 4.11, thus the sensor will be continuously powered.

The use of a second tone to increase the dc output voltage is shown in Fig. 4.11 with simulated and measured results. For 0 V voltage at gate, the simulated dc output voltage obtained is 3.0 V and the measured one is 3.75 V, as illustrated in Fig. 4.11(a). Switching the gate of transistor to 0.6 V the simulated DC output voltage is 3.15 V and the measured one is 3.10 V, as shown in Fig. 4.11(b).

Figure 4.12 shows the measured results of S_{11} parameter as function of frequency and input power for two different voltage values at the gate of transistor. It can be seen that comparing this figure with Fig. 4.10, there are some differences on the loads and frequencies between simulated and measured results. We believe this deviation is due to the models used for the diode and transistor and at higher frequencies due to the serious parasitic effects arisen from via holes and soldering. The integration of backscatter with WPT solution was designed in order to modulate data by backscatter means and supply the wireless sensors with WPT by using two different tones at the input. The simulated results presented in Fig. 4.10, prove the capability of supplying the wireless sensor by WPT at 1.8 GHz and modulate data at 2.45 GHz. The measured results presented in Fig. 4.12, evidence the capacity of supplying the wireless sensor by WPT at 1.7 GHz and modulate data as a traditional backscatter at 2.35 GHz.

Figure 4.14 shows the photograph of the measurement setup used to acquire the re-

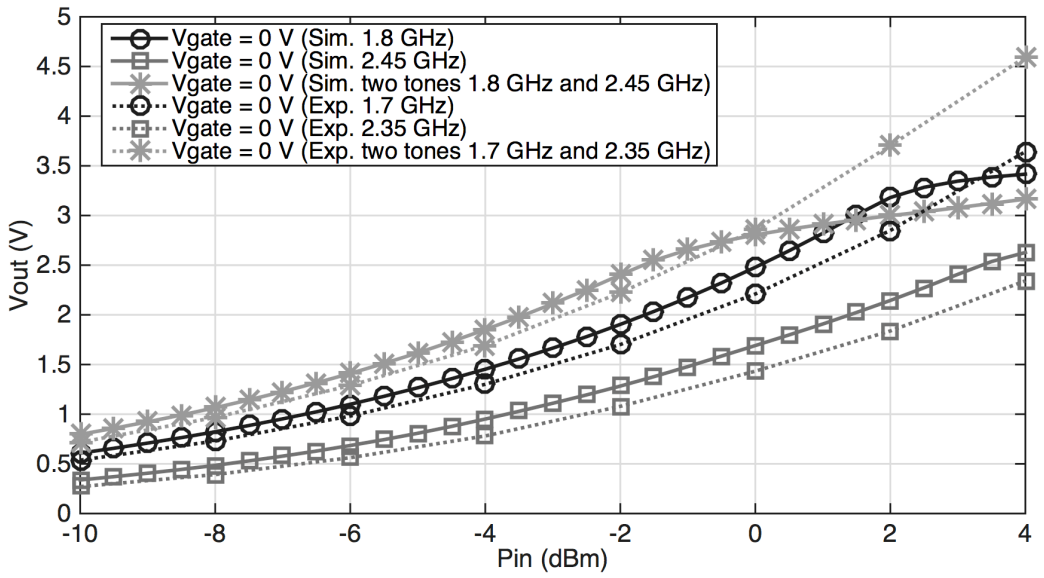

(a)

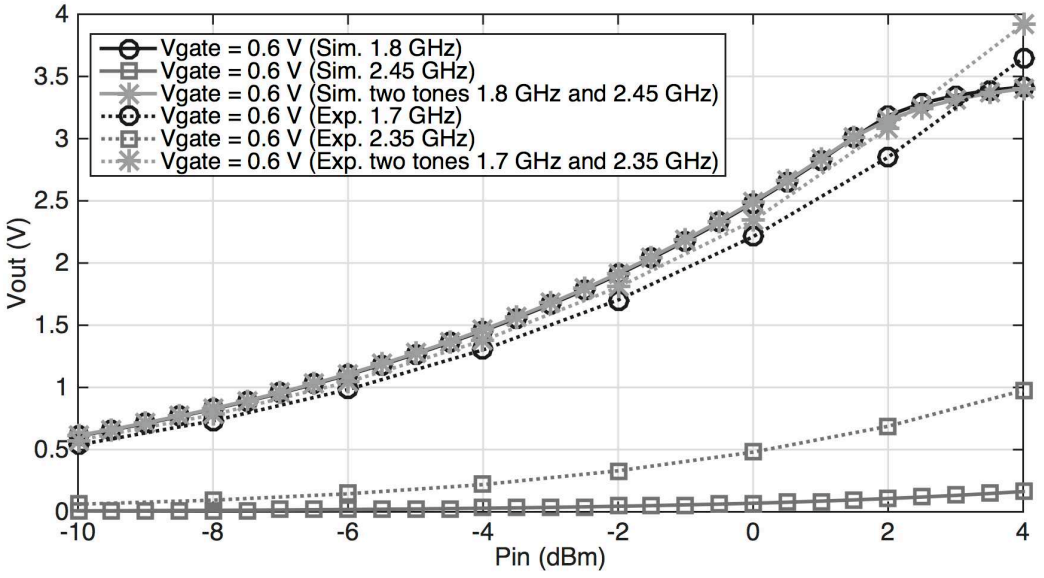

(b)

Figure 4.11: Simulated and experimental results for DC Vout voltage of backscatter modulator and dual band rectifier as function of input power per tone. (a) $V_{Gate} = 0$V. (b) $V_{Gate} = 0.6$V.

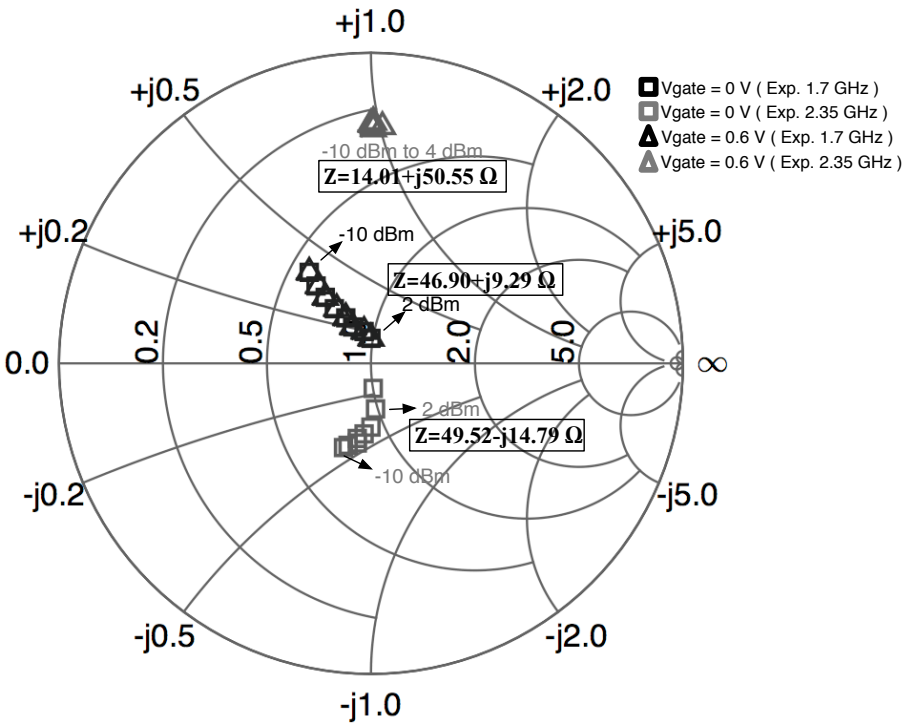

Figure 4.12: Measured S_{11} parameter as function of frequency and input power for two different values of gate voltage.

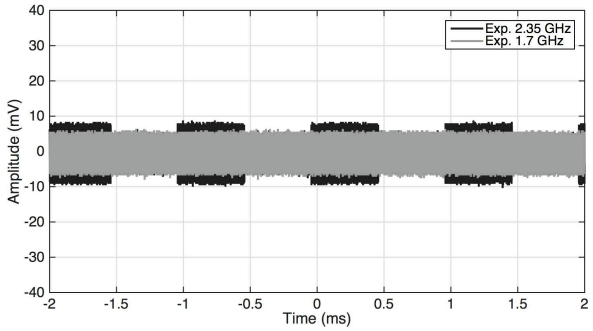

(a)

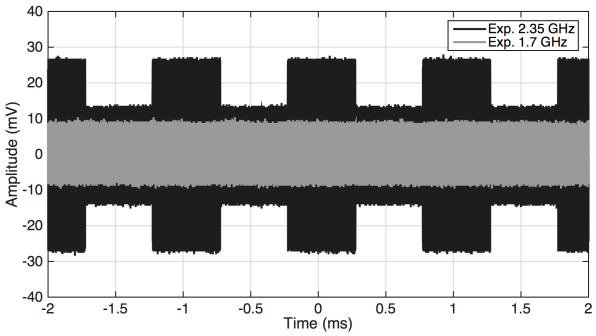

(b)

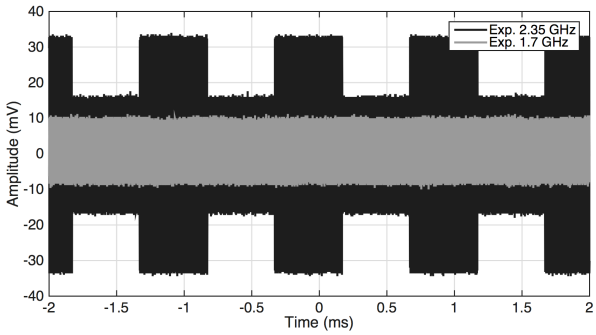

(c)

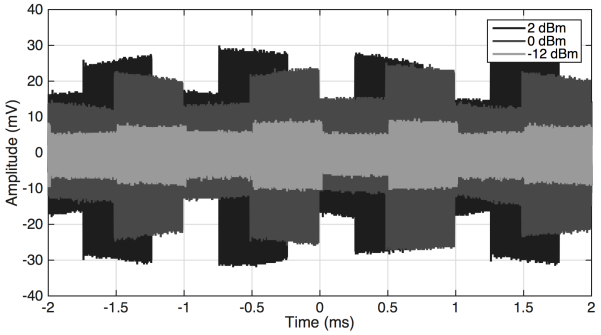

(d)

Figure 4.13: Experimental results of the reflected waves (a) Pin = -12 dBm. (b) Pin = 0 dBm. (c) Pin = 2 dBm. (d) Two tones (1.7 and 2.35 GHz) for different input powers.

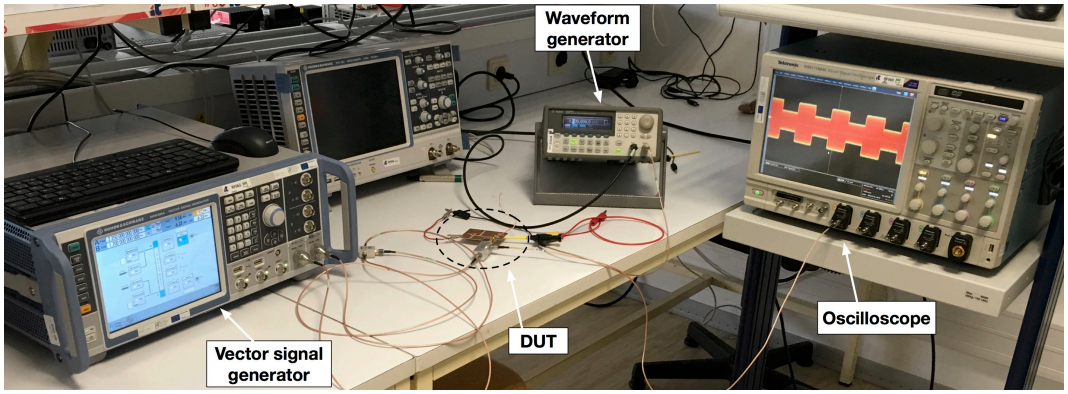

Figure 4.14: Photograph of the measurement setup.

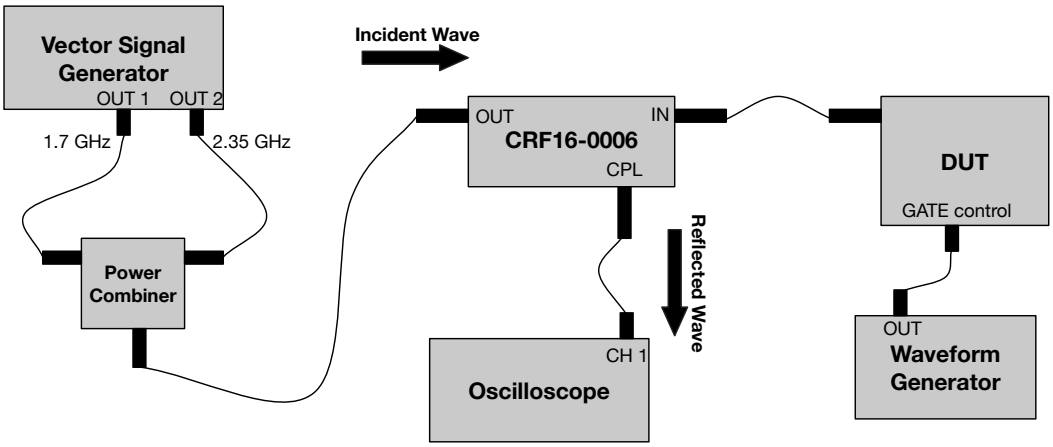

Figure 4.15: Block diagram of the measurement setup.

flection wave from the circuit shown in Fig. 4.6b. We used a vector signal generator (ROHDE&SCHWARZ, SMW200A) to generate 1.7 GHz and 2.35 GHz. A waveform generator (Agilent, 3325OA) was used to change the state of the transistor gate, continuously. At the output of the vector signal generator we used a power combiner (Mini-Circuits, ZFRSC-183-S+) to combine 1.7 GHz and 2.35 GHz to the input of our circuit. A coupler (Marki, CBR16-0012) was used to measure the reflected waves from the circuit, by an oscilloscope (Tektronix, MSO 71604C). Before acquiring the reflected waves, we calibrated the input power by using a power meter (Agilent, N1913A). Figure 4.15 presents the block diagram of the measurement setup.

Figures 4.13(a), 4.13(b) and 4.13(c) show the acquisitions for -12 dBm, 0 dBm and 2 dBm at the input power, respectively. The acquisitions were obtained with only one frequency band turned on at each time. Figure 4.13(d) presents three different acquisitions with two frequency bands combined, with different input powers. By analyzing Figs. 4.13(a), 4.13(b) and 4.13(c) it is possible to observe that at 1.7 GHz the amplitude level does not change, since the circuit is matched, so the reflected wave is reduced and does not change with the transistor gate variation. At 2.35 GHz it is visible that the amplitude level is changing as the state of the voltage gate varies. In this way, it is proven that it is possible at 1.7 GHz to supply the wireless sensor by WPT and at 2.35 GHz to modulate the information by backscattering means.

4.2 Passive Sensor with Over the Air validation

In this section, a temperature/accelerometer passive sensor will be designed and tested. To implement this sensor, we followed the same architecture explained in the previous section, which consists in three different concepts. The sensor was supplied by WPT. Communication between the sensor and reader is established by a backscatter, and to ensure minimum energy consumption, low power techniques are used. In a simplistic way, the process starts by the transmission of two different waves by the reader to the sensor, one of which is used in power transmission and the other of which is used to communicate. Once the sensor is powered, the monitoring process starts. From the monitoring state, results from after processing are used to modulate the incoming wave, which is the information that is sent back from the reader to the tag. This new combination of technologies enables the possibility of using sensors without any cables or batteries to operate 340 cm from the reader. The developed prototype measures acceleration and temperature. However, it is scalable.

4.2.1 WPT and Backscatter Techniques

To implement the combination of these two technologies, the approach used in reference [18] was followed. In this approach, two different transmitter frequencies are used, one to

supply the sensor and the other to communicate via backscatter.

Figure 4.16 shows a block diagram of the proposed combined technologies. Two main blocks are presented. The first, the RF harvesting circuit, is responsible for converting RF signals into DC energy to supply the microcontroller and modulate the information acquired by the sensors. The modulation is provided by switching the transistor ON and OFF, which is part of the backscatter modulator block. This process is known as Modulated Scattering Technique (MST) [163–165], resulting in this case in an ASK modulation.

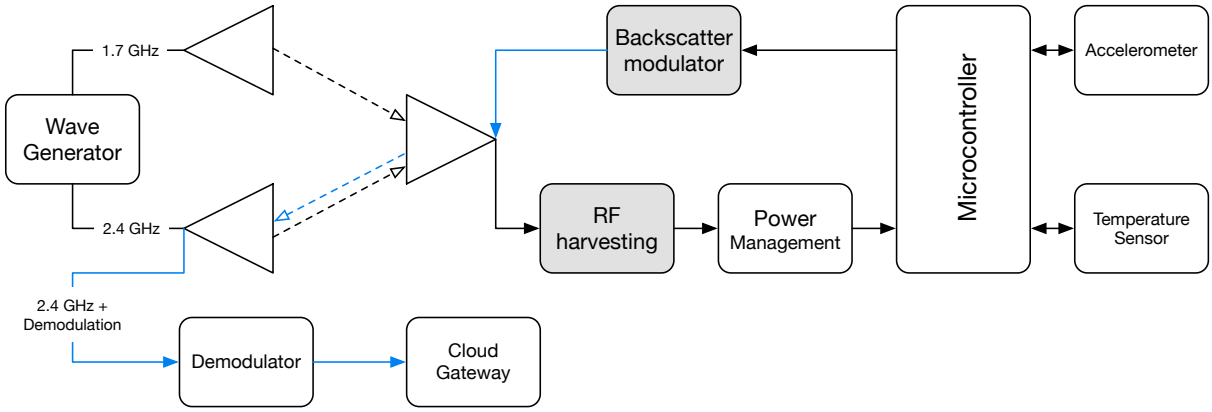

Figure 4.16: Block diagram of the implemented system.

4.2.2 RF Front End Design and Optimization

The RF circuit is shown in Fig. 4.17. It is divided into three main sections: the backscatter modulator, which is composed of a switch transistor that modulates the impedance of the antenna; the matching network, which was designed to provide backscatter load modulation at one frequency and continuous flow of WPT at other frequency; and, the five-stage Dickson multiplier, which allows for RF-DC conversion to provide sufficient DC power to supply the microcontroller.

The main differences from the works presented in references [18,44] consist of the design and the optimization of the matching network to provide enough DC power to supply the digital processing unit. Once all of the lower frequency circuits within the sensor node were designed, the sleep current consumption that resulted from the sum of all of the quiescent currents was taken into consideration to model the load for the energy harvester, which was designed to mimic the real load that the harvester sees while the sensor node is sleeping. Out of all of the circuitry downstream from the output of the energy harvester, only the large storage capacitor and Schottky diode that precedes it were included into the simulation model of the load. All of the other circuits were replaced by an ideal current source that

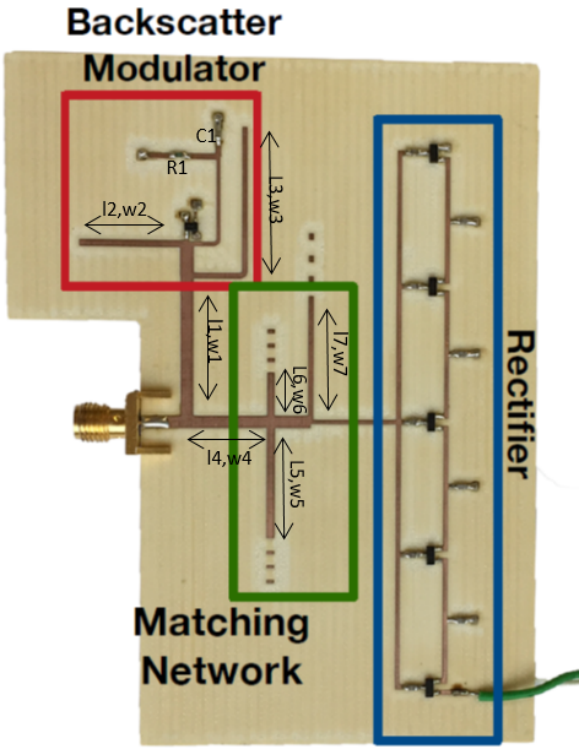

Figure 4.17: Photograph of implemented system with backscatter modulator combined with Wireless Power Transmission (WPT). Element values are L1 = 21.2 mm, W1 = 1.87 mm, L2 = 15.1 mm, W2 = 1.0 mm, L3 = 21.9 mm, W3 = 0.8 mm, L4 = 11.3 mm, W4 = 1.87 mm, L5 = 17.1 mm, W5 = 1.2 mm, L6 = 6.7 mm, W6 = 1.1 mm, L7 = 18.6 mm, W7 = 0.7 mm, R1 = 50 , and C1 = 47 pF. Substrate for the transmission lines is Astra MT77, thickness = 0.762 mm, ε_r = 3.0, tan δ = 0.0017.

was placed in parallel with the storage capacitor with a value set equal to the estimated maximum sleep current consumption (that is, 5 μA). A harmonic balance simulation was performed in ADS to tune the matching network for the maximum conversion efficiency and DC output with the ideal current. In references [18,44], simulations were performed for a fixed load value, without any consideration of the digital processing unit consumption.

To provide both backscatter communication and wireless power transfer, a Large Signal S-Parameter (LSSP) simulation was performed with the objectives of matching the circuit in both states of the transistor at 1.7 GHz, matching the system at 2.4 GHz in one state and mismatching at the other state. This change of the antenna's impedance at 2.4 GHz provides the backscatter communication. Regarding the RF transmission, three patch antennas were used. Two of them were connected to the wave generator, matched at 1.7 GHz and 2.4 GHz, respectively, and the third connected to the sensor, matched at both frequencies (dual-band). The patch antennas were chosen due to their high directivity.

4.2.3 Sensing and Processing Elements

The sensing part of the system is composed of a temperature sensor and an accelerometer, both of which were chosen carefully to have low power consumption and reliable measurements. Texas Instruments LM94021 was the temperature sensor that was selected. In addition to its low power consumption (12 μA) and precise calibration, the sensor has a simple calibration process and temperature range from 50°to 150°[166]. Since the measurements performed during the tests were at ambient temperatures, the sensor was calibrated to operate between 0 and 40°, allowing for a better output resolution. The second sensor was added to prove that the system can work with multiple sensors. Accelerometers were chosen due to their low power consumption, human interaction factor, and a wide range of possible applications. The accelerometer chosen was Analog Devices ADXL362, which consumes 1.8 μA at 100 Hz in operation mode and 10 nA in standby mode [167]. To acquire and process all of the data that come from the sensors, a processing unit is necessary. The chosen microcontroller was MSP430F2132 from Texas Instruments. This microcontroller only consumes 2 μA in active mode and 0.3 μA in sleep mode. It also contains I/O ports, an Analog-to-Digital Converter (ADC), timers, and communications protocols [168]. The only feature missing for the microcontroller with regard to the final application was a DAC unit. This unit was added to the system as an external component. The sensing and processing elements were supplied by the RF-DC converter. The voltage delivery from the RF-DC converter depends on the distance from the reader as well as many other factors, such as wave reflections. Different levels of voltage create different behaviors in the components, and stable conditions are important for performing sensing activities. To solve this problem, a voltage regulator circuit was placed between the RF-DC circuit and sensing and processing units. The voltage regulator output was 1.8 V. In Fig. 4.18, the PCB with the sensing and processing elements is

shown.

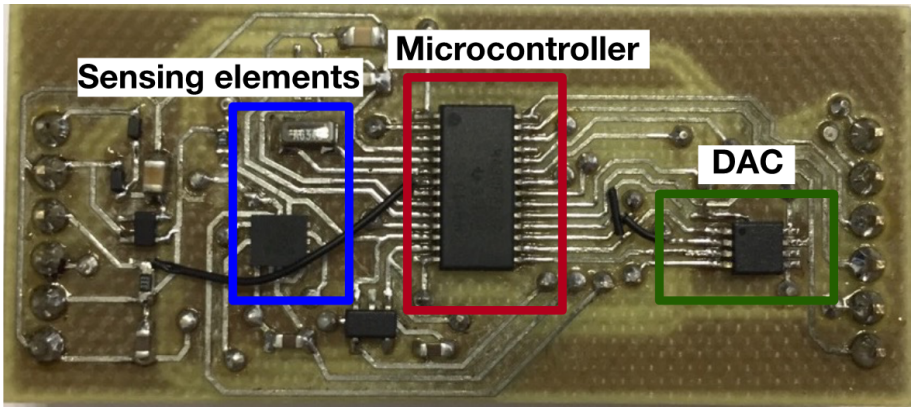

Figure 4.18: Developed Printed Circuit Board (PCB)

As important as choosing low power components is in the software development, they should also be efficient to ensure that the components are only in active mode when they are actually needed. These techniques allow for a reduction of the system power consumption. The first software operation is the configuration of all of the elements, clocks, I/O ports, timers, ADC, DAC, and sleep modes. After configurations, the software processes the sensing block, reading the temperature and acceleration. The measured data need to be processed since misleading measurement errors can occur. A message is then produced to be delivered to the DAC. At this point, the DAC is responsible for controlling the system impedance by varying the voltage. When the message bit is a zero, the DAC output voltage is 0.0 V, which means that the system is adapted and, consequently, that there is no reflection. By contrast, when the message bit is one, the DAC output voltage is 0.6 V, which means that the impedance of the system is mismatched, which occurs with the reflection of the carrier wave. After sending each bit, the microcontroller enters sleep mode for a short period of time. When it sends the complete message, the microcontroller enters a longer period of sleep. Figure 4.19 illustrates the process described.

All of the message and sleep periods are defined by a simple variable on the code. The same is done with the output voltage delivered by the DAC. This gives the system the ability to easily modify the parameters for different applications. The message frame is composed of a total of 11 bits: 3 bits to identify the tag ID, 2 bits to identify the sensor, 4 bits for the measurement, and 2 bits to detect errors in the message. The following Table 4.2.3 exemplifies the message frame with the coding resulting from the measured temperature:

The power consumption of the tag is defined by the bit period and sleep period. Long sleep periods result in low power consumption. The bit period is related to the frequency of the reflected wave, which defines the deviation of the modulated message from the carrier. Having a good deviation from the carrier wave is crucial to isolate the wave modulated by

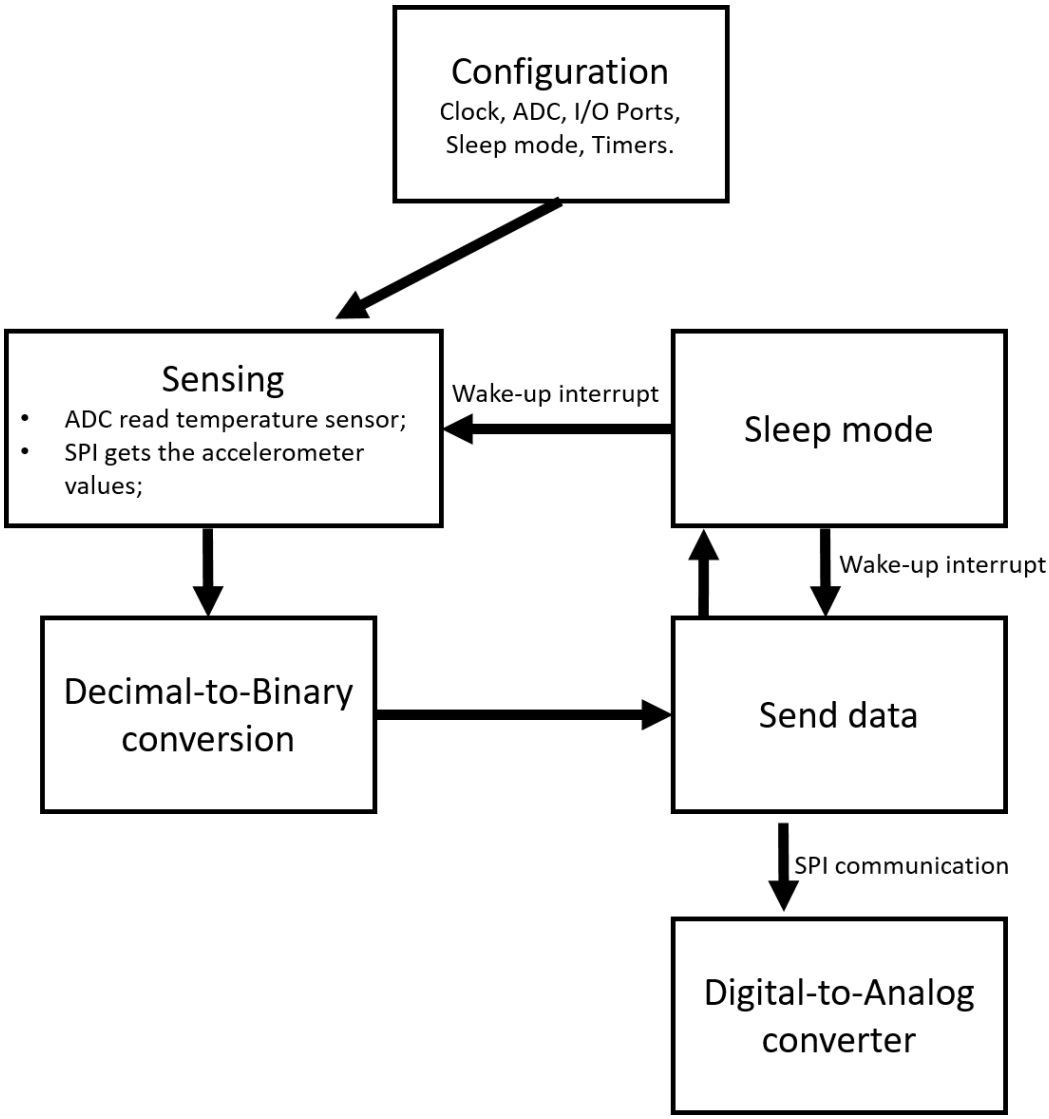

Figure 4.19: Code diagram.

Table 4.5: Corresponding code from the measured temperature.

Temperature (Celsius)	**Code (bits)**
0.0 - 2.5	101-00-0001-11
2.5 - 5.0	101-00-0010-11
5.0 - 7.5	101-00-0011-01
(...)	(...)
37.5 - 40.0	101-00-1111-01

the tag from the carrier wave. Tests were conducted to optimize the periods. Periods of 366 μs for the bit period and 6.312 ms for the sleep period were established. The tag average consumption was 59 μA.

4.2.4 Measurements and Results

The first measurements were to ensure the correct operation of the digital logic. Figure 4.20 shows the DAC output with the code 101-00-1000-11 that corresponds to a temperature between 17.5°and 20°.

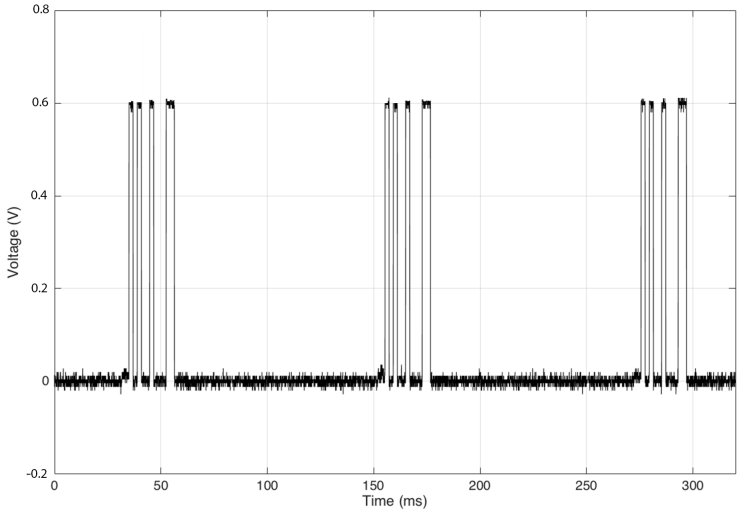

Figure 4.20: Message with tag ID, sensor ID, measured temperature, and correction bits.

As discussed previously, the goal of this work was to develop a passive tag. However, to perform and evaluate measurements, a reader is needed.

The reader is composed of a Vector Signal Generator (SMW200A, Rohde & Schwarz) to generate two signals at different frequencies, one dual band patch antenna and a Spectrum Analyzer (FSP, Rohde & Schwarz) to analyze the signal modulated and reflected by the tag. The tag has a dual band antenna, a board with the RF front-end circuit, and another board with the processing and sensing elements. The RF-DC circuit and processing sensing elements are not on the same board to allow for specific tests for each approach. Figure 4.21 shows the measurements setup.

The first measurement was taken to determine the optimal frequencies for system operation. The S_{11} parameter of the RX and TX antennas was measured and is presented in Fig. 4.22 and Fig. 4.23, respectively with the respective antennas used.

Based on the results, the frequency chosen for WPT was 1.720 GHz and for performing backscatter communication was 2.405 GHz.

Figure 4.21: Measurements setup.

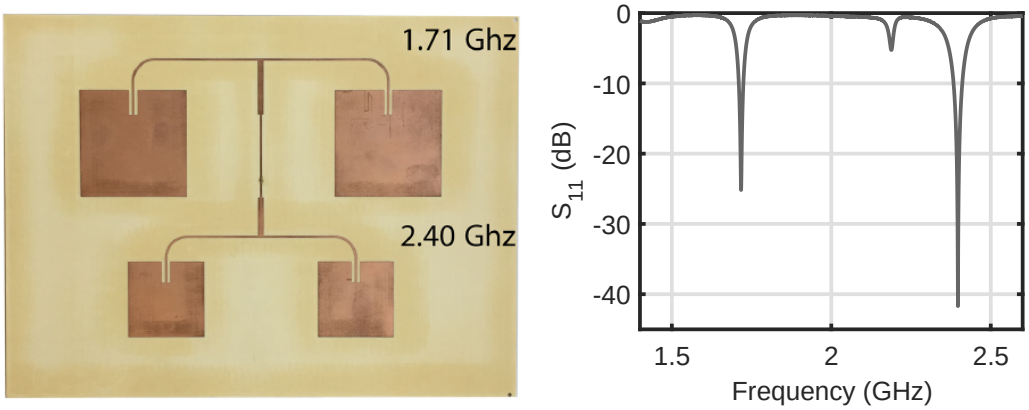

(a) (b)

Figure 4.22: Dual-band antenna used on the tag. a) Photograph of the dual-band antenna. b) S_{11} parameter of the dual-band antenna.

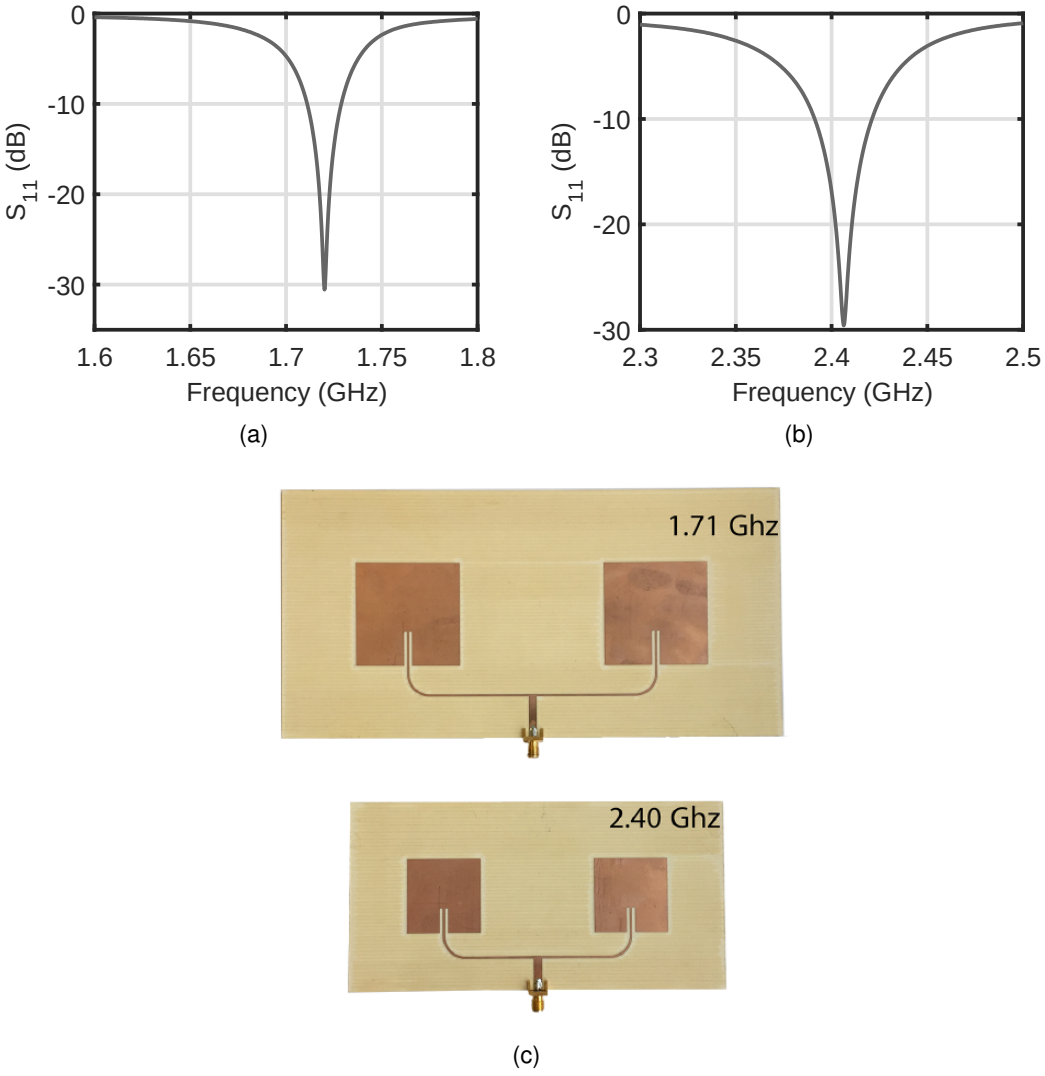

Figure 4.23: Two patch antennas used on the reader. a) S_{11} parameter of the WPT patch antenna. b) S_{11} parameter of the backscatter communication patch antenna. c) Photograph of both antennas used on the reader.

The following measurements were used to evaluate the input power and output voltage after the RF-DC circuit under different test conditions. There are three parameters that changed during the tests: load, tag adaptation, and power delivery. No load means that there is no load attached to the RF-DC circuit, and a load occurs when the sensing and processing board are attached to the RF-DC circuit. Backscatter absorbing is the state at which the DAC output voltage is 0.0 V, meaning that the circuit is at its most adapted point (maximum absorption). In backscatter reflection, the DAC output is 0.6 V, corresponding to a mismatch of the system impedance (maximum reflection). The power delivery to the system varies from -20 dBm to 0 dBm. The results are shown in Fig. 4.24. It can be concluded that the frequency that is exclusively used for WPT is not affected by the backscatter absorption or the reflection state. The figure also shows that the wave with 2.405 GHz generates more DC voltage when the system is adapted than when it is not. Another aspect is that there is a decrease of voltage when a load is present. As is known, maintaining the delivered power and increasing the current makes the voltage drop.

To better understand the reliability of the WPT technique, the reader and tag were placed at a distance of 300 cm from each other. During the test, the power transmitted by the reader was varied from 0 dBm to 30 dBm at both frequencies. By measuring the power received by the tag at both frequencies, its respective output voltage, and the tag state (ON or OFF), it is possible to obtain all of the information about the WPT process. Figure 4.25 presents the results. The transmitted power refers to both frequencies, which means that each tone is increased from 0 dBm to 30 dBm. As it was stated in the previous section, the input power for single tone is different from the dual tone and the main objective was to analyze the behavior of the sensor when an extra tone is added.

Figure 4.25 shows that an increment in the transmitted power results in linear growth of the received power for both frequencies until the tag is OFF. The tag turns ON when the transmitted power is near 26 dBm. At this point, the tag starts performing the backscatter process, changing between reflecting and absorbing states. The ON state of the tag is reflected on the receiver power, at 2.405 GHz, where a decrease is visible on the growing line after that point.

In addition to the previous test, for understanding the characteristics of WPT, another test was conducted to measure the maximum distance at which the reader can supply the tag. The maximum transmitted power, 30 dBm, was defined, and the maximum distance of 430 cm between reader and tag was measured. In this point it is important to refer that European Telecommunications Standards Institute (ETSI) legislates the amount of power that can be transmitted. For an UHF RFID the legal limitation is 33 dBm Effective Radiated Power (ERP).

Even though the maximum distance at which the reader can supply the tag is 430 cm, this does not mean that the complete system can work at that distance. For this system to

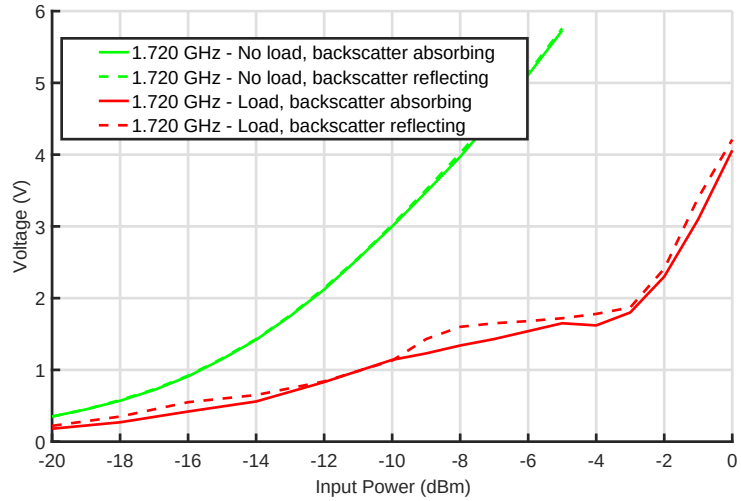

(a)

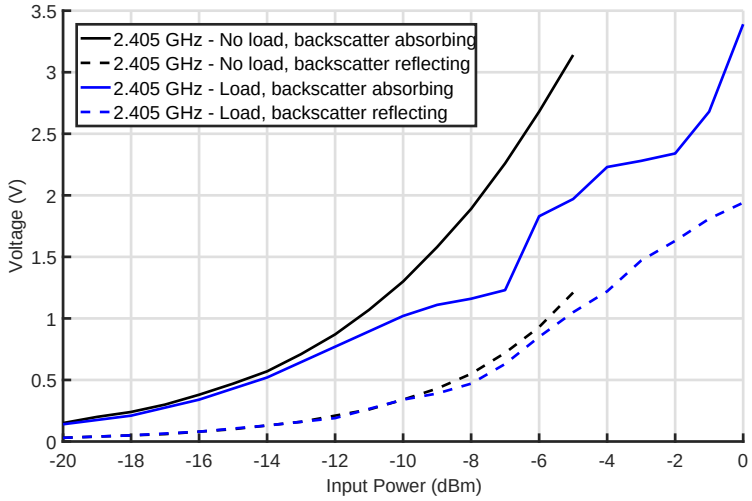

(b)

Figure 4.24: Output voltage as function of input power.

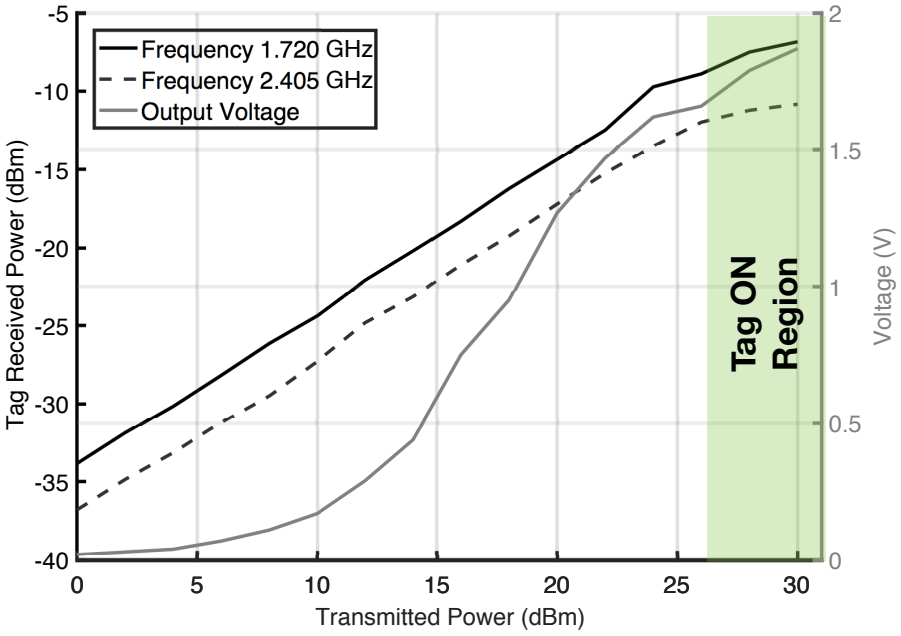

Figure 4.25: WPT at distance of 300 cm.

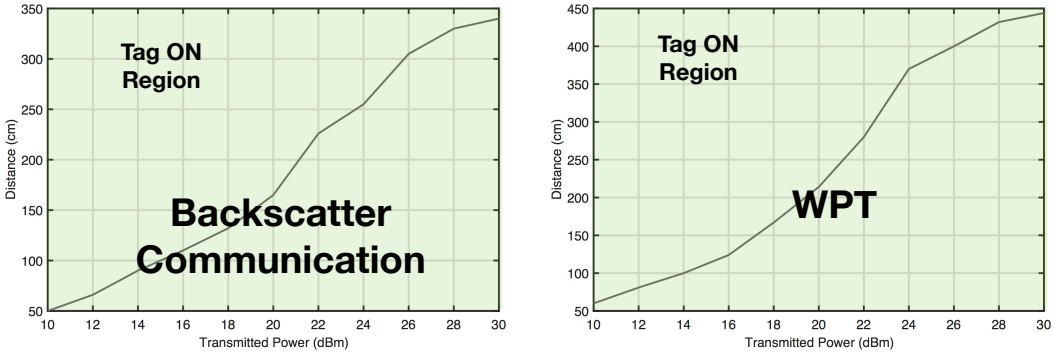

(a) (b)

Figure 4.26: Distance as function of transmitted power in active mode of sensor. a) Backscatter communication on active mode,considering a receiver sensitivity of -85 dBm. b) WPT that enables active mode.

work, the tag needs to modulate the signal and reflect it with enough power so that it can be received by the reader. Figure 4.26 presents the distances obtained as function of transmitted power per tone in active mode of sensor. Considering a reader sensitivity of -85 dBm, the maximum distance obtained was 330 cm.

4.3 Single Transistor Passive Backscatter Sensor

In this section a fully passive wireless sensor based on a single E-pHEMT device is presented. The implemented circuit behaves as a RF-DC rectifier when the gate of E-pHEMT is unbiased and as a modulator when the generated voltage switches to 0.6 V. The sensor achieves 83% efficiency for 16 dBm of input power and it is demonstrated that for higher powers the backscatter modulator has a very good behavior. Through this implementation it is possible to reduce the size and the number of components that composes the sensor.

4.3.1 Circuit description

The circuit was developed over the ATF54143 E-pHEMT device from Broadcom. As the goal of this work focuses on a passive sensor, there are two main blocks that need to be developed such as the RF-DC converter to harvest or collect RF energy to supply a microcontroller and the backscatter modulator which is responsible for the communication. The block diagram of the proposed system is presented in Fig. 4.27 and illustrates the blocks needed to implement a passive sensor that harvest energy and modulate data with one transistor.

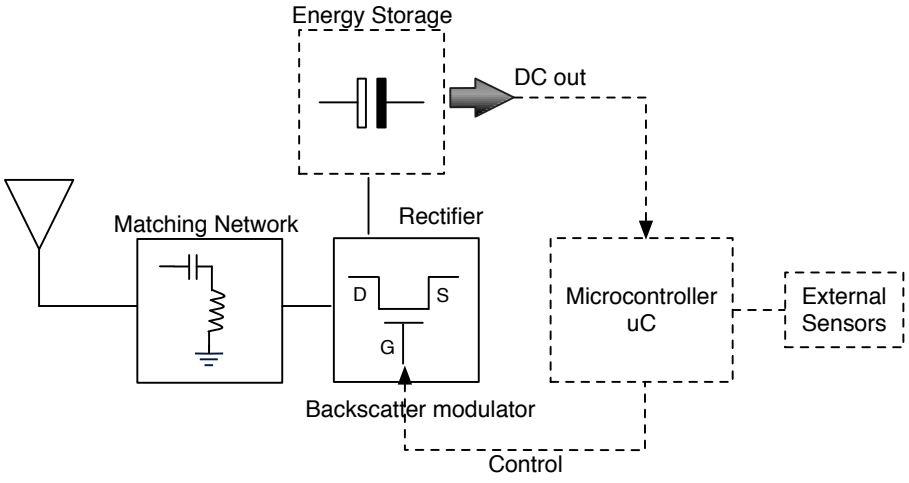

Figure 4.27: Block diagram of proposed system

The circuit was optimized to maximize the input RF signal to the transistor, and also to maximize the conversion efficiency from RF-DC converter. In this case the nonlinear be-

haviour of the HEMT device is used, specially the nonlinear behavior of the drain-source current.

In Fig. 4.28, the schematic and photograph of the implemented circuit is shown. The circuit includes a RF-DC converter that will generate output DC voltage to supply a micro-controller which will change the gate voltage of the transistor, causing a variation in the amount of energy reflected by the antenna.

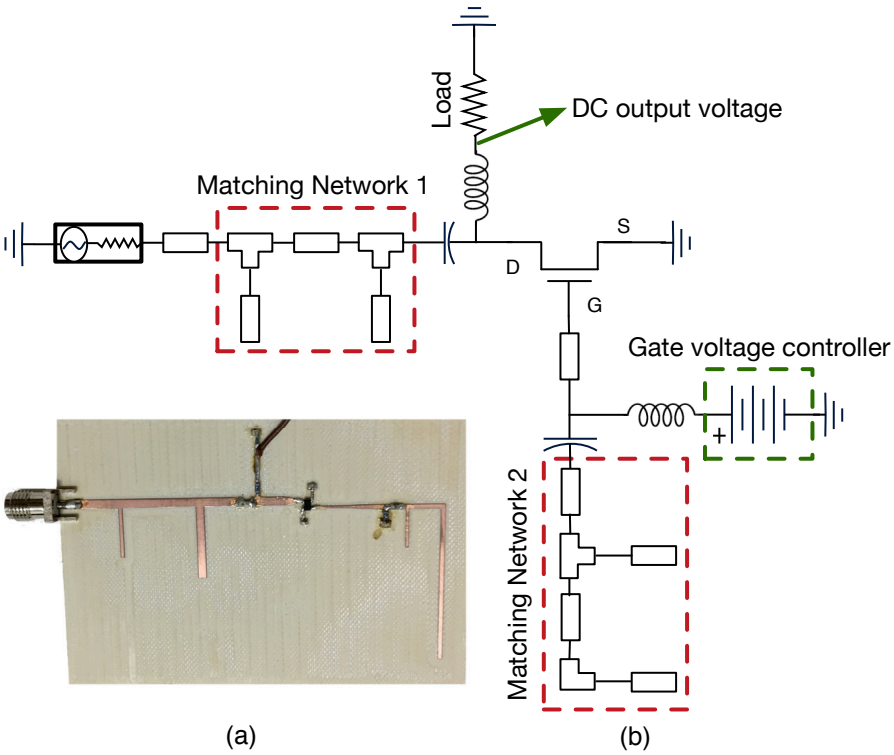

Figure 4.28: Design of the circuit which includes the rectifier and modulator. a) Photograph. b) Circuit schematic.

The matching networks 1 and 2 were designed with two main purposes for the frequency of 2.45 GHz. First was to obtain the maximum efficiency when the gate voltage is 0 V with a perfect matching $S_{11} < -10\,dB$. Second, when the gate voltage is 0.6 V the efficiency should be the minimum as possible with a perfect mismatch in terms of S-parameter. The load used in the output of rectifier was fixed in 308 Ω, in order to increase the RF-DC conversion efficiency for the unbiased gate state. In a real application, with a sensor, a more carefully implementation should be conducted, as it was demonstrated in the previous section.

4.3.2 Experimental results

Figure 5.22 illustrates the rectifier/modulator design implemented. The circuit was optimized to operate at 2.45 GHz and for 10 dBm of average input power using LSSP simulations (Fig. 4.29 shows simulated and measured S_{11} parameter). At 2.45 GHz with unbiased gate the circuit behaves as a rectifier and it is matched. Changing the gate of the E-pHEMT device, it is supposed that the circuit behave as a backscatter modulator with a low S_{11} parameter, meaning that the incoming signal is reflected.

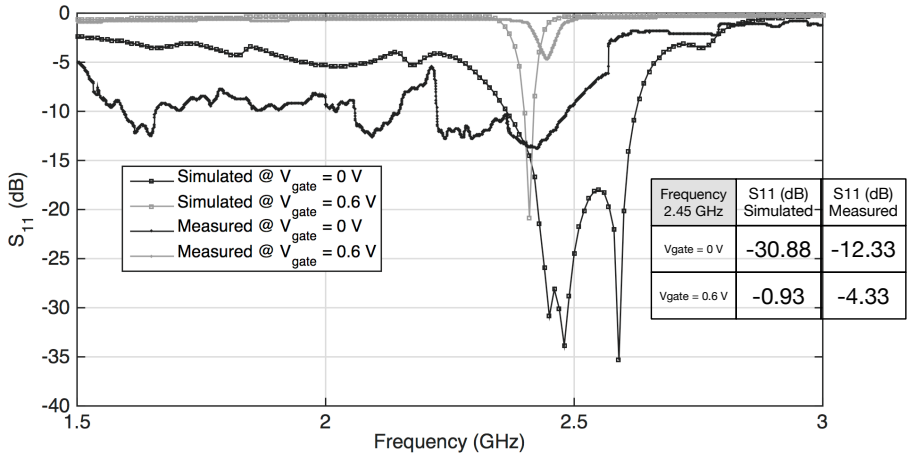

Figure 4.29: Simulated and measured S_{11} parameter for $P_{in} = 10$ dBm.

The simulated and measured results for the efficiency as function of input power can be seen in Fig. 4.30. The first objective was to demonstrate that the efficiency is the maximum as possible with an input power of 10 dBm and with unbiased gate. The small deviations from the simulated results is due to the substrate used and the model for the E-pHEMT nonlinear behavior. Figure 4.30 shows that is possible to maintain a constant efficiency level by varying the gate voltage level of the E-pHEMT device. The circuit can provide an RF-DC conversion efficiency of 40% from -8 dBm to 19 dBm of input power, allowing this way to power up the sensor microcontroller.

In order to validate the backscatter modulator, Fig. 4.31 is presented. This figure present the measured S_{11} parameter as function of input power at 2.45 GHz. As it was previously mentioned, the circuit was optimized for an input power of 10 dBm. The operating mode of the backscatter consists in switching the impedance across the antenna between matched and short states.

Figure 4.31(a) shows that for unbiased gate state the circuit is not perfect matched, since the circuit was matched for high input power. Nevertheless, the behavior of the circuit from 0 dBm to 20 dBm is very good, and acts as a backscatter modulator by switching from unbiased gate to 0.6 V at the E-pHEMT device.

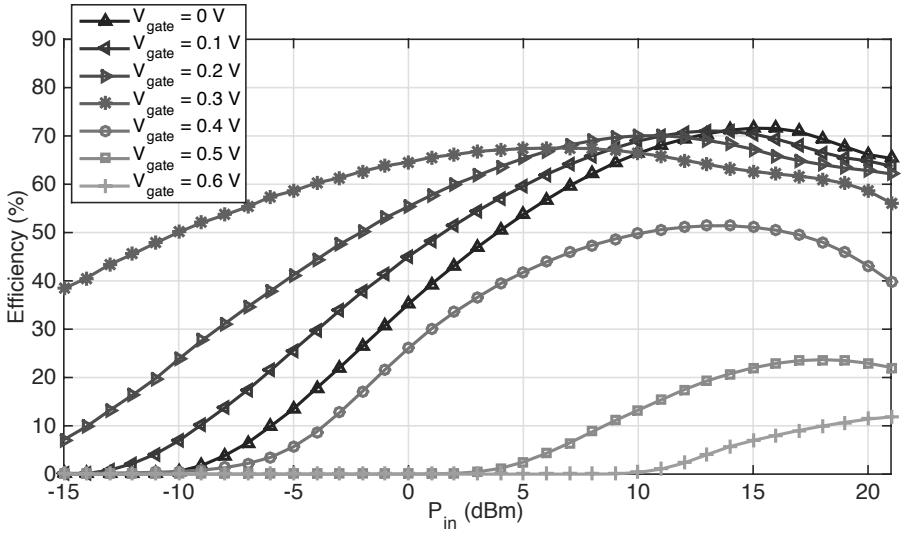

(a)

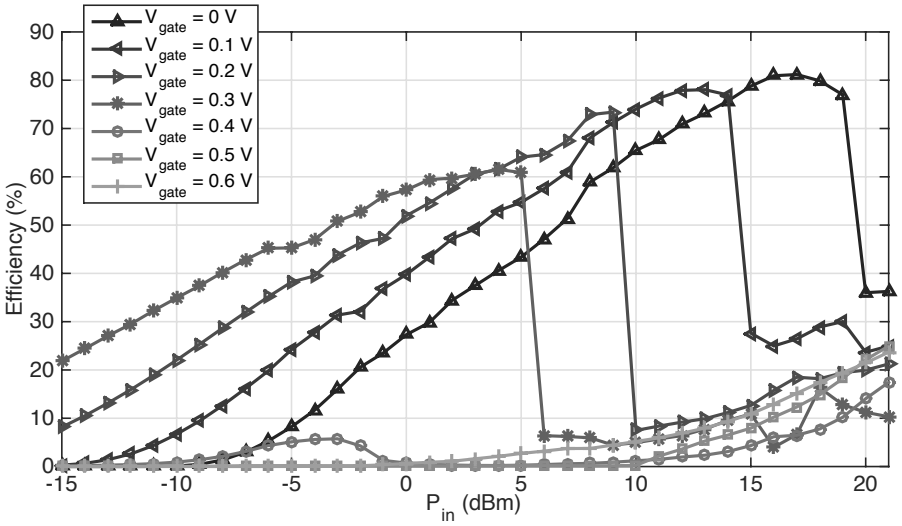

(b)

Figure 4.30: Simulated and measured results for efficiency as function of input power for Freq. = 2.45 GHz. (a) Simulated efficiency. (b) Measured efficiency.

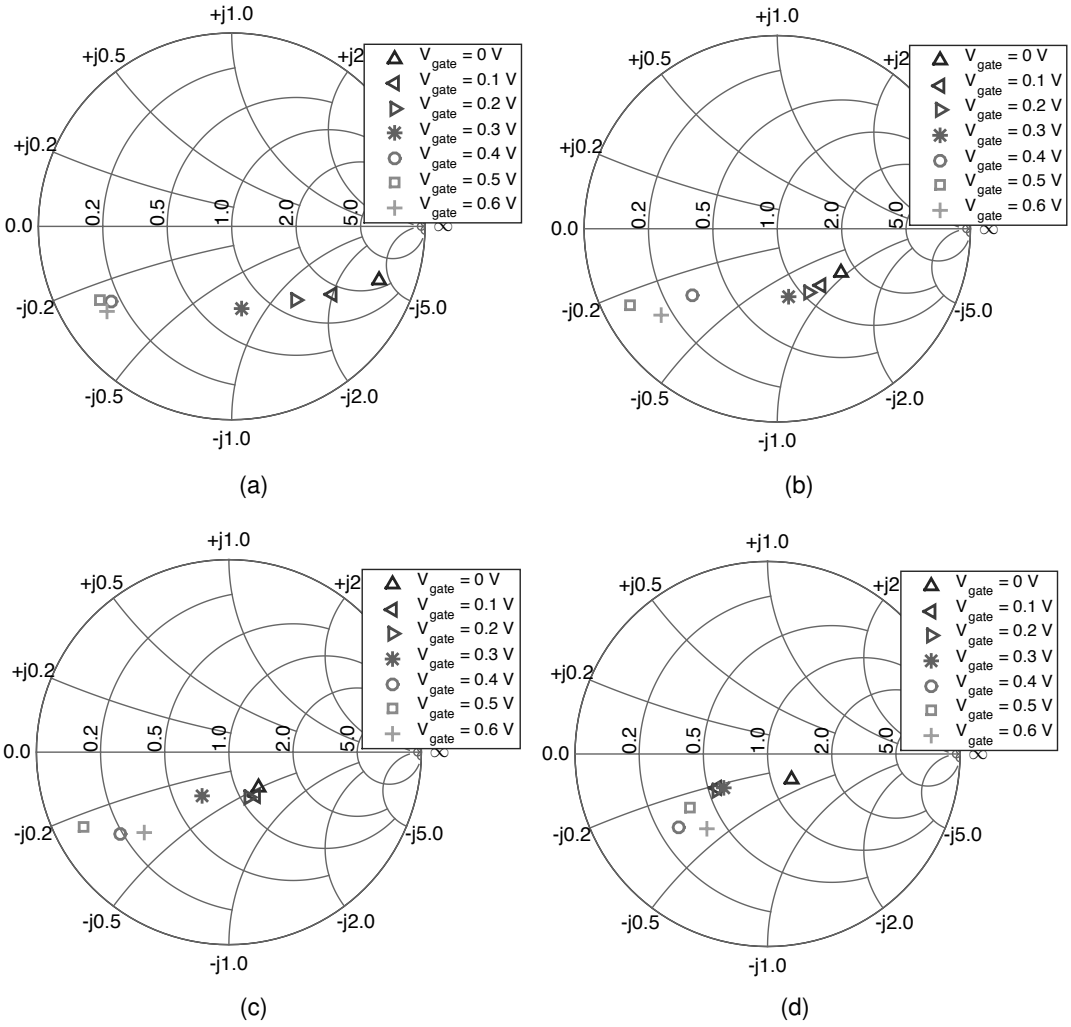

Figure 4.31: Measured S_{11} parameter as function of input power at 2.45 GHz for different values of gate voltage. (a) $P_{in} = -10$ dBm. (b) $P_{in} = 0$ dBm. (c) $P_{in} = 10$ dBm. (d) $P_{in} = 20$ dBm.

4.4 Conclusions

- The developed backscatter design presented a good agreement between the measured and simulated results. It was designed and optimized for two different frequencies (1.8 GHz and 2.45 GHz) at 2 dBm but, as it was required, only modulates the data at one frequency (2.45 GHz). The dual band rectifier design was implemented and optimized to both maximize DC voltage and energy conversion efficiency. Both measured and simulated results shown good matching at the designed frequencies for DC output voltage and output power. By using the dual band rectifier, the major advantage is the gain on output DC voltage when comparing to a single band rectifier. With the proposed scheme it was shown that it is possible to supply a continuous power flow to the wireless sensor with a combination of backscatter communications. This way the sensors can be continuously powered during the operation mode.

- Moreover, a passive tag with sensing and processing elements was presented. The developed tag has two sensing elements: temperature and acceleration. It is important to note that the microcontroller has the capability to incorporate a greater number and different types of sensors. The aim is to use the tag in multiple scenarios, especially situations that do not allow for a physical connection, maintenance and access. Agriculture, space, and smart house applications are good examples for which this technology could be used. In agriculture, sensors need to be underground to measure soil conditions. This scenario is not favorable for battery replacement. In space applications, the monitoring system is usually connected by a large amount of cables. Removing the cables would decrease the ship weight and consequently fuel consumption. In smart house applications, the sensors could be embedded at different locations, making different types of measurements. One of the contributions from this work is the measurement and testing of the technology, which combines WPT and backscatter techniques. This technology enables the use of one frequency exclusively for power transmission and another for communication, which allows for greater distances between the reader and tag. Development of the sensing and processing elements to ensure maximum power efficiency is an important addition. The obtained results shown a very good distance at which it is possible for the sensor to communicate its measurements after they are handled by its processing unit.

- A single E-pHEMT device acting as a rectifier and as a backscatter modulator was demonstrated. The circuit achieved 82% of efficiency for an input power of 16 dBm with unbiased gate and proves consistency acting as a backscatter modulator for higher input powers with generated voltage equal to 0.6 V at the gate of the E-pHEMT. This sensor demonstrated the capability of maintaining the rectifier efficiency equal to 40% from -8 dBm to 19 dBm of input power by varying the gate voltage from 0 V to 0.6 V.

Chapter 5

High Order backscatter modulation

Outline

Fully passive wireless networks are a key-enabling technologies for the IoT. Backscatter radios are a hypothesis to design these passive wireless networks. Backscatter modulation allows a remote device to wirelessly transfer information without requiring a traditional transceiver. Instead, a backscatter device leverages a carrier transmitted by an access point or base station. Nevertheless, the traditional approach is to use ASK or PSK backscatter solutions which limits the data rate of the sensors, since it transfers only one bit per symbol period. In this chapter a novel modulator which employs a Wilkinson power divider with a phase shift in one of the design branch and two transistors acting as switches in order to generate M-QAM backscatter modulation is proposed. The design strategy for high level order backscatter modulations will be explained and a design approach will be presented in this chapter.

This solution can be combined with WPT for ultra low-power wireless applications requiring high bandwidth communications such as remote camera sensors or wireless audio. This work challenges held assumptions concerning the backscatter link that backscatter communication is limited to low bandwidth and binary modulation solutions. In this chapter, the combination of high order backscatter modulation combined with WPT will be presented.

5.1 QAM backscatter modulation design strategy

Backscatter radios are based on the reflected waveform that should switch between a fully matched and short circuit solution built on a switch that is directly connected to the receiving/transmitting antenna of the sensor. For a higher level modulation format, the number of different backscattered waves should change among several states, thus the switch combinations should clearly create a specific impedance for that symbol combination. To determine the most suitable impedances we had to test several implementations with differ-

ent number of transistors (E-PHEMTs). Figure 5.1 presents three different schemes, for ASK (Fig. 5.1a) and 4-QAM (Fig. 5.1b and Fig. 5.1c) backscatter modulation.

Figure 5.1a presents the traditional ASK backscatter, a ON or OFF switch will impose two different reflected waves by changing the impedances. The switch is made using a simple transistor (ATF54143, from Broadcom) and biasing it to obtain an open or a short circuit. Figure 5.1b presents a higher order level backscatter modulation with two transistors. This implementation create a 4-QAM solution with 4 stages in the switches: (ON, ON), (ON, OFF), (OFF, ON) and (OFF, OFF). This particular solution is very difficult to implement since the two states (ON, ON) and (OFF, OFF) are not completely complementary, which imposes that the impedances seen by each of them, from the antenna point of view, are not complementary and create a complex matching network to be designed to achieve the 4-QAM modulation format. To expand this solution into higher order modulations, such as 16-QAM, the complexity would increase and it would be very difficult to implement.

Figure 5.1c presents a solution for 4-QAM, where a four-switch approach was used, [169]. Each branch of each switch is exactly equal and by changing the line and/or the stub in the terminal of each switch, it is possible to achieve the impedance or the scattering parameters required. Figure 5.22 presents the photograph of this solution. Despite the very good results presented in [169], the dimensions of the circuit are very large and even larger if we extend to higher order modulation, such as 16-QAM.

In order to minimize the dimensions of the circuit and to increase the modulation order to a 16-QAM solution, a new implementation was evaluated. Figure 5.3 presents the design for the 16-QAM solution. This model employs a Wilkinson power divider and each branch is terminated with a line and an ideal impedance. The lines present a 45°phase shift respect to each other, so as to allow that the reflected wave from each branch has 90°phase difference from the other. Equation 5.1 shows the reflected wave as a sum of both reflected waves from each branch. Using (5.2) and (5.3) is possible to determine the reflection coefficient of the model for different impedances.

$$b = \frac{b1}{\sqrt{2}} + \frac{b2}{\sqrt{2}} = \frac{a_1\Gamma_1 e^{j\frac{\pi}{2}}}{\sqrt{2}} + \frac{a_2\Gamma_2}{\sqrt{2}} \tag{5.1}$$

$$\Gamma_1 = \frac{R_1 - Z_0}{R_1 + Z_0}; \quad \Gamma_2 = \frac{R_2 - Z_0}{R_2 + Z_0} \tag{5.2}$$

$$\Gamma = \frac{b}{a} = \frac{\Gamma_1 \frac{1}{\sqrt{2}}}{\sqrt{2}} e^{j\frac{\pi}{2}} + \frac{\Gamma_2 \frac{1}{\sqrt{2}}}{\sqrt{2}} \Rightarrow \Gamma = \frac{\Gamma_2}{2} + j\frac{\Gamma_1}{2} \tag{5.3}$$

Considering two different values for each resistance (0 or ∞) we obtain four different combinations with four different reflection coefficients:
$R_1 = 0$ and $R_2 = 0 \Rightarrow \Gamma = -\frac{1}{2} - j\frac{1}{2}$;

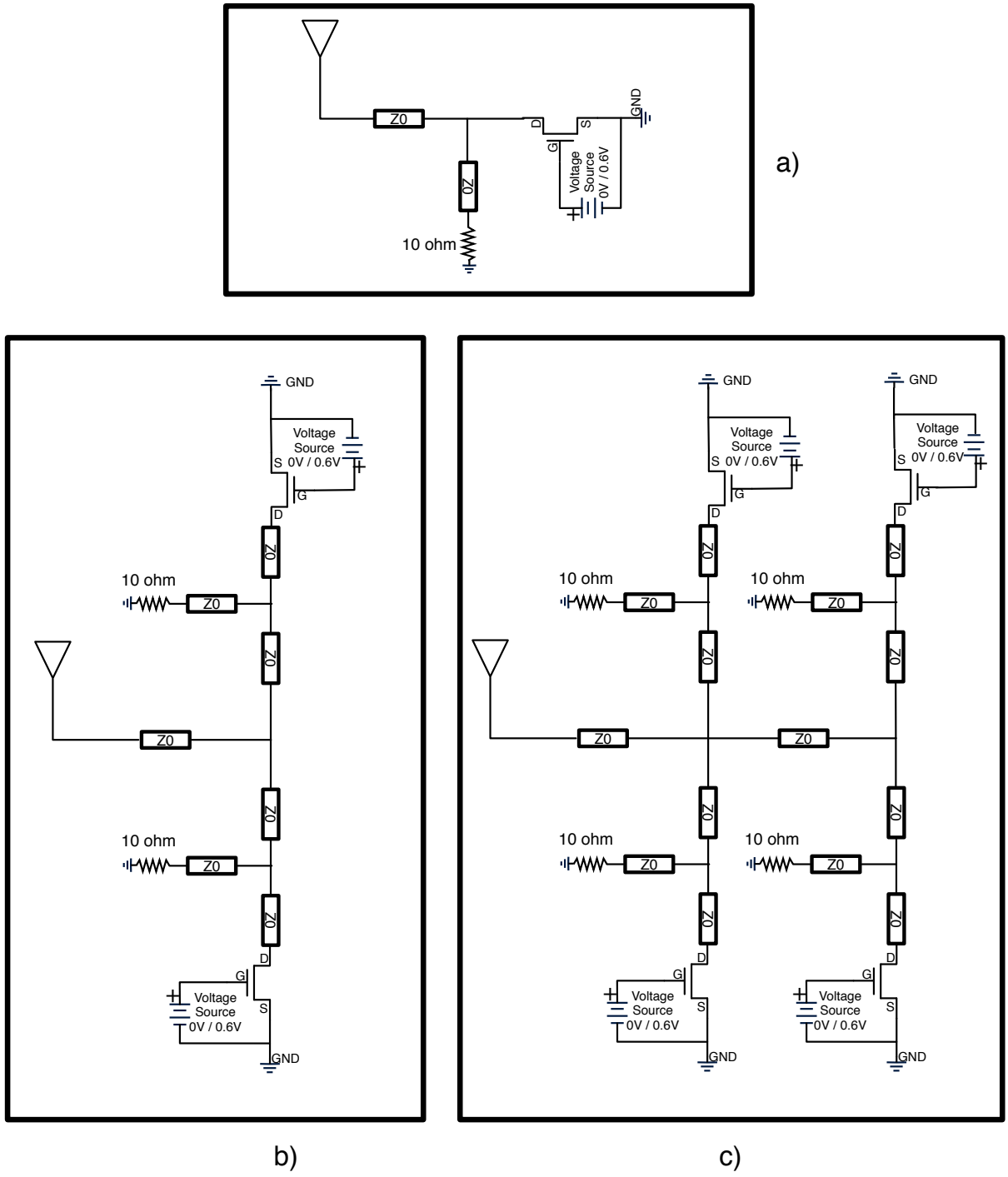

Figure 5.1: Three types of design for two different backscatter modulation schemes. a) ASK backscatter modulation scheme; b) 4-QAM backscatter modulation scheme without the possibility to increase the modulation order; c) Our proposed scheme for 4-QAM backscatter modulation with the possibility to increase the modulation order.

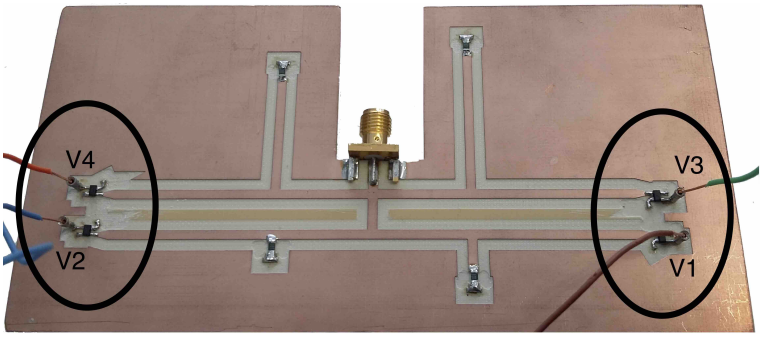

Figure 5.2: Photograph of the 4-QAM backscatter circuit.

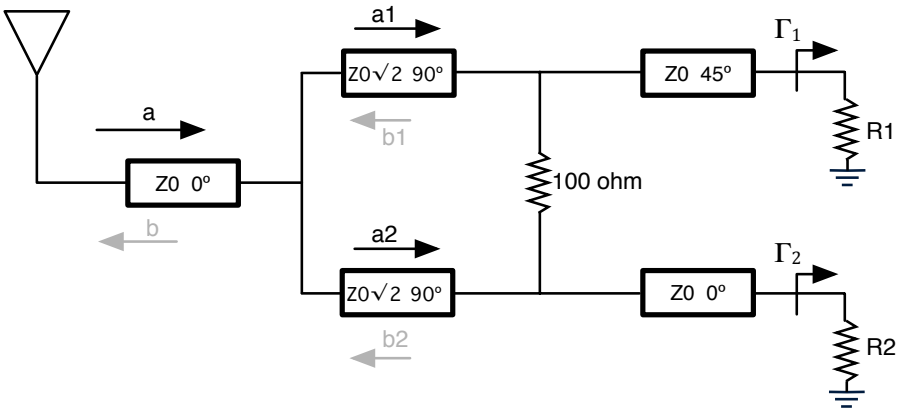

Figure 5.3: Model of the QAM solution.

$R_1 = 0$ and $R_2 = \infty \Rightarrow \Gamma = \frac{1}{2} - j\frac{1}{2}$;
$R_1 = \infty$ and $R_2 = 0 \Rightarrow \Gamma = -\frac{1}{2} + j\frac{1}{2}$;
$R_1 = \infty$ and $R_2 = \infty \Rightarrow \Gamma = \frac{1}{2} + j\frac{1}{2}$.
Figure 5.4 presents the previous reflection coefficients in the Smith chart.

A similar reasoning can be used to create any type of multi-level higher order modulation. In order to do that, arbitrary real impedances could be used, instead of the 0 and ∞ impedance. Thus different impedances are implemented using an active load based on a transistor, one example is presented in Fig. 5.5, where different impedances were used in the scheme presented in Fig. 5.3, the impedances were 0 Ω, 20 Ω, 60 Ω and 200Ω.

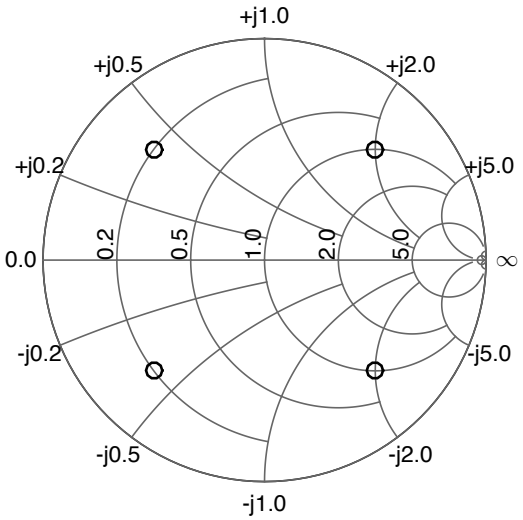

Figure 5.4: Simulation of the model for 4-QAM solution.

In a generalized scheme, the last approach can be extended, where the load presents different impedance values, consider for instance a, b, c and d real impedances. The impedances are then matched with the overall circuit using a two branch approach and a microstrip line scheme, were each branch imposes a specific delay. By combining these two degrees of freedom, several impedance levels can be created. Equation 5.4 was deduced, where R represents the four different impedances in one branch and R represents the four impedances in the other branch. It was based on Fig. 5.6 and presents the sixteen possibilities of impedances.

$$X = R\underline{/\phi} + Q\underline{/\theta} \tag{5.4}$$

5.1.1 Constellation Diagram Impedance Generation

In order to create different impedances for the constellation diagram creation, a transistor was used as an active load, in this case the transistor was matched so that it presents an

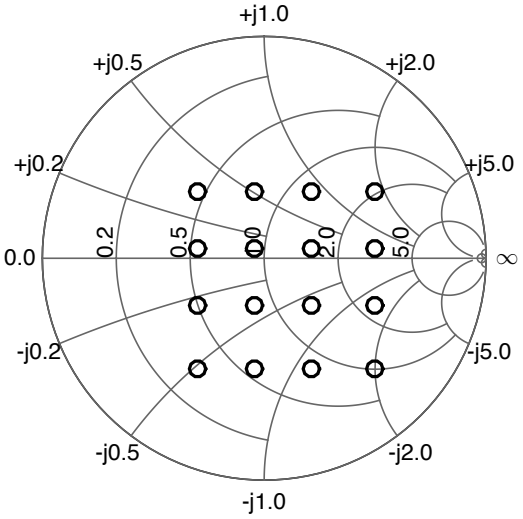

Figure 5.5: Simulation of the model for 16-QAM solution.

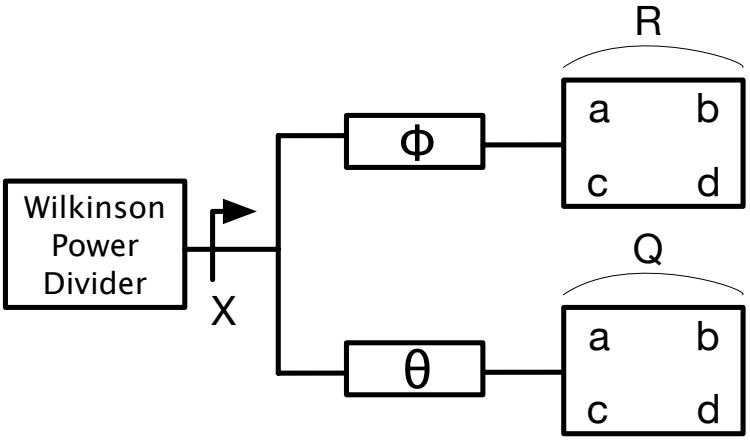

Figure 5.6: Block diagram for different impedance terminations.

impedance for different control voltages. The approach followed in this case was to use a single transistor as is presented in Fig. 5.7(a). The gate voltage in this case can be changed from 0 V to 0.6 V. The matching network was optimized for the extreme cases 0 V and 0.6 V, where the resistive value of the resistor is $4.7 + j0.5\ \Omega$ and $379.6 - j630.8\ \Omega$, respectively. By changing the gate voltage other impedances can be generated as is presented in Fig. 5.8. For this work and in order to create a QAM approach, the selected impedances were $4.7 + j1.4\ \Omega$, $14.9 + j1.8\ \Omega$, $61.0 - j1.2\ \Omega$, $566.6 + j1.4\ \Omega$, as is presented in Fig. 5.8.

In order to validate the system, we implemented and designed a simple circuit with only one transistor and an impedance matching network. The objective in the simulations was to achieve an open circuit when the gate voltage is 0.6 V and a short circuit with 0 V at the gate of transistor. Nevertheless, we added two different voltages at the gate of transistor, 0.2 V and 0.4 V, to characterize the system to 4 different voltage levels. We measured the circuit for 26 voltages levels (from 0 V to 0.6 V) and we selected the levels more approximated with the simulations (Fig. 5.8). Since the sensitivity of the circuit is higher between 0.3 V and 0.5 V, the measurement step selected, within this range, was 0.01 V instead of 0.1 V. Figure 5.7(a) shows the design of the circuit and Fig. 5.7(b) the photograph of the implemented circuit. Figure 5.8 presents the real impedances in the Smith chart. The purpose of the matching network is to achieve real impedances in all levels at the drain of transistor, from 0 V to 0.6 V. Figure 5.9 shows the simulation of total reflection coefficients possibilities of the solution. The voltages at the gate of transistor were chosen from 0 V to 0.6 V with a step of 0.01 V. Using this approach with a two branch network allows the creation of a multitude of impedance arrangements, as can be seen in Fig. 5.9, for several gate voltages. Despite this is a simulation value, it already shows that for a real implementation a calibration procedure is fundamental for the development of a true higher order modulation.

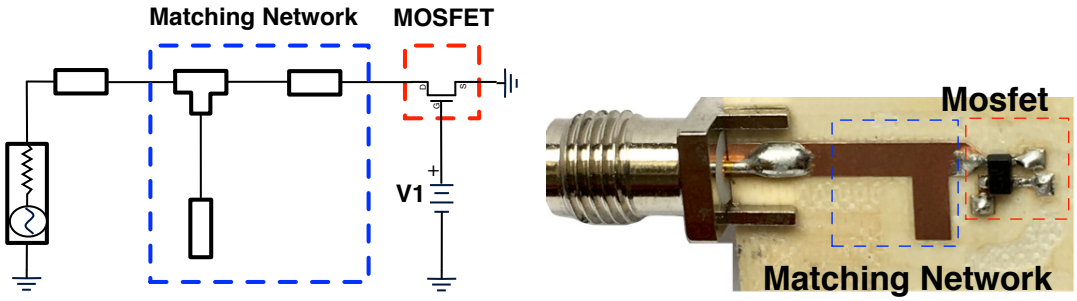

Figure 5.7: Model for the characterization. a) Design of the circuit. b) Photograph of the proposed characterization circuit.

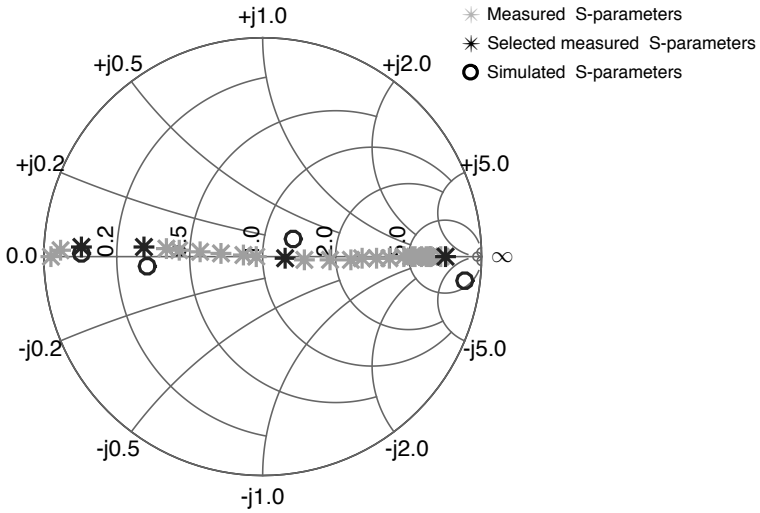

Figure 5.8: Simulated, measured and selected measured S11 for different voltage levels at the gate of transistor for 2.45 GHz at 0 dBm.

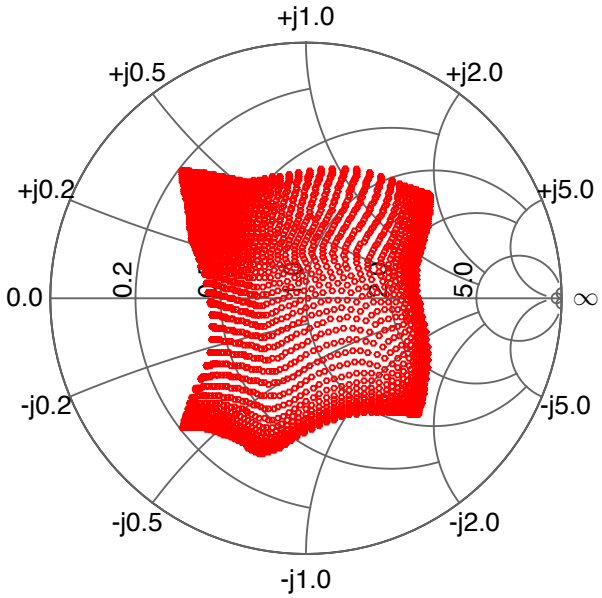

Figure 5.9: Simulated S_{11} for different voltage levels (from 0 V to 0.6 V with a step of 0.01V) at the gate of each transistor for 2.45 GHz at 0 dBm.

5.1.2 QAM Backscatter Implementation

Figure 5.10(a) shows the design of the proposed 16-QAM scheme and Fig. 5.10(b) the prototype implemented that includes the Wilkinson power divider, two matching networks and two transistors. This prototype was optimized for 0 dBm at 2.45 GHz and it was simulated in ADS. In Fig. 5.10(b) is possible to view the difference of line length in each branch, and it is related with the 45°phase shift. As it was previously mentioned we used two transistors, in order to achieve the 16-QAM modulation. Fig. 5.19 presents the block diagram approach to explain the different impedances obtained. With this approach the design illustrated in Fig. 5.10(a) was implemented in order to obtain the 16-QAM modulation. Each transistor is switched for different voltage levels to achieve different reflection coefficients.

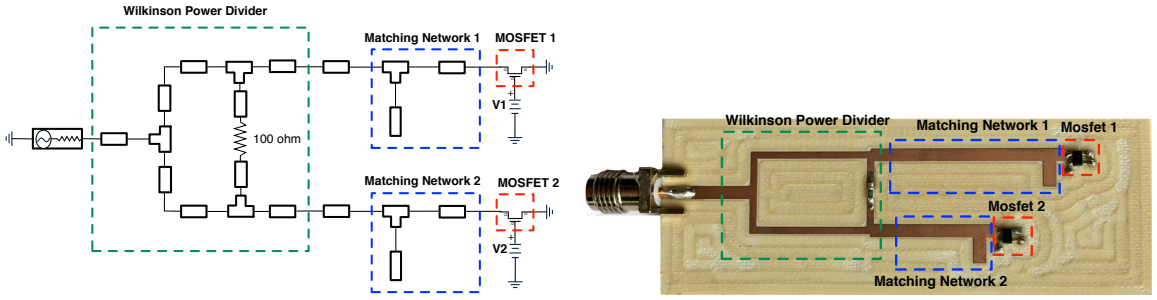

Figure 5.10: 16-QAM backscatter modulation scheme. a) Design of 16-QAM backscatter modulator. b) Photograph of the 16-QAM backscatter circuit.

5.1.3 Results

The measured results were obtained by using a power supply and the Performance Network Analyzer (PNA) (E8361C, from Agilent Technologies) that was calibrated at 0 dBm for the frequencies from 2 GHz to 3 GHz. Figure 5.11 shows the photograph of the measurement setup used to acquire the reflection coefficients from the circuit shown in Fig. 5.10(b). The switches were changed according to the simulated results, by biasing the gate of each transistor. The results of the simulations and measurements are presented in Fig. 5.12 and in Table 5.1 are presented the different reflection coefficients for different voltages at the transistor. Table 5.1 shows also the simulated and experimental voltage levels used to obtain the matching between the reflection coefficients. As can be seen in the Table 5.1, the voltages measured and simulated are different, due to the models used for the transistor. The obtained results clearly showed that the 16-QAM modulation is viable and as it was mentioned previously, the points can be better adjusted in the Smith chart by biasing the gate of each transistor with more precision.

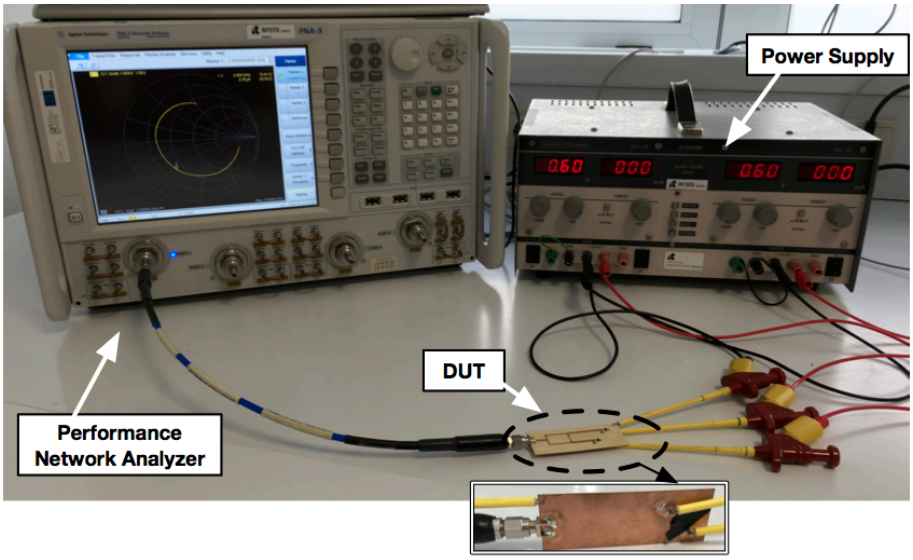

Figure 5.11: Photograph of the measurement setup.

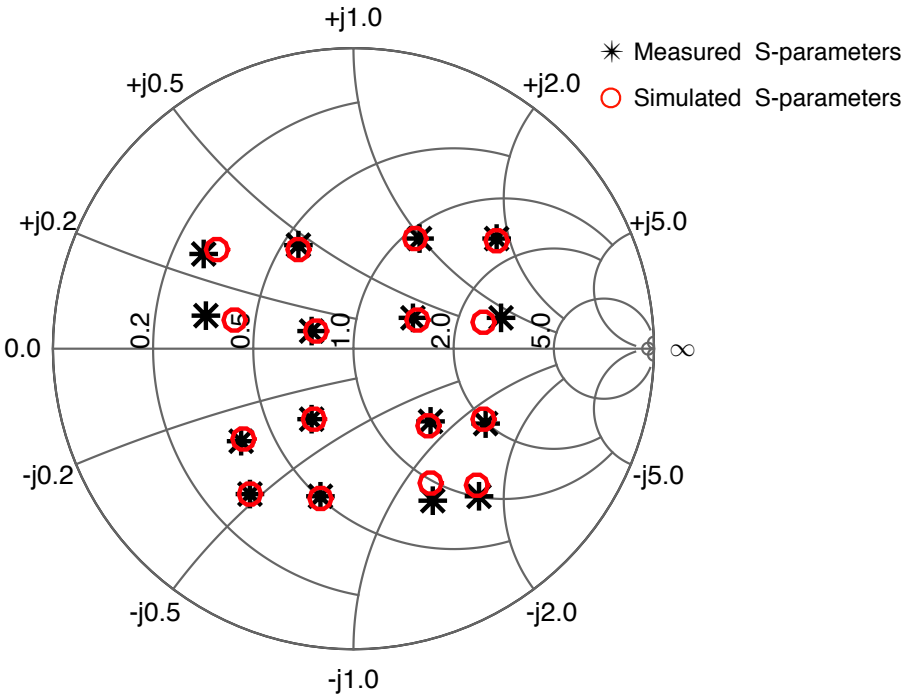

Figure 5.12: Simulated and measured S_{11} for different voltage levels at the gate of each transistor for 2.45 GHz at 0 dBm.

Table 5.1: Simulated and measured S_{11} for different levels at the gate of transistors (M1 and M2).

Measured			***Simulated***		
M1 (V)	**M2 (V)**	**S11**	**M1 (V)**	**M2 (V)**	**S11**
0	0.4	.44 - .25j	0	0.35	.44 - .24j
0	0.6	.42 - .49j	0.13	.52	.41 - .45j
0	0.34	.49 + .1j	0.1	0.44	.43 + .09j
0.4	0	-.18 + .35j	0.43	0.16	-.18 + .33j
0.4	0.4	-.14 - .23j	0.42	0.45	-.13 - .24j
0.6	0	-.5 + .32j	0.57	0.08	-.46 + .33j
0.6	0.4	-.37 - .31j	0.51	0.41	-.36 - .3j
0.6	0.6	-.34 - .49j	0.54	0.6	-.34 - .48j
0.6	0.25	-.49 + .11j	0.6	0.27	-.4 + .1j
0.34	0.34	.19 + .1j	0.35	0.35	.21 + .1j
0.34	0	.22 + .36j	0.33	0.17	.2 + .36j
0	0	.48 + .37j	0	0.2	.47 + .36j
0.25	0.41	.25 - .24j	0.28	0.42	.25 - .25j
0.2	0.6	.26 - .5j	0.28	0.48	.25 - .45j
0.37	0.6	-.11 - .49j	0.42	0.6	-.11 - .5j
0.4	0.33	-.14 + .06j	0.45	0.34	-.12 + .05j

Demodulation and Achievable Data Rates

The maximum data rate of the communication on the modulator link was studied by using the measurement setup presented in Fig. 5.13 to view the received constellation and eye diagrams of the I and Q signals at multiple transmission rates. We used a vector signal generator (ROHDE&SCHWARZ SMJ 100A) to generate the transmitter signal at 2.45 GHz. An arbitrary waveform generator (TEKTRONIX AWG5012C) was used to generate the voltage levels at the gate of each transistor mimicking the modulated data rate. A coupler was used to measure the reflected signal from the circuit, by the spectrum analyzer (ROHDE&SCHWARZ FSW8).

To analyze the achievable data rates, the voltages presented on Table 5.1 were applied to the gate of each transistor, creating 16 reflected impedances or symbols. The received constellations acquired from the signal & spectrum analyzer are shown in Fig. 5.14 for bit rates of 4 Mb/s, 40 Mb/s and 120 Mb/s, respectively. The constellation points lie in the appropriate quadrants, and each point is clearly visible. The constellation presented in Fig. 5.14 is not perfect, but can be calibrated with more precision by adjusting the voltages at the gate of each transistor. The received eye diagrams for varying data rates are shown in Fig. 5.16, and for the data rates of 256 kb/s, 2.4 Mb/s and 4 Mb/s the eye is clearly open and the received signals are clean. For the data rate of 120 Mb/s the received signals appear with some noise and the eye is beginning to close. By analyzing Fig. 5.16(d), it is visible the limit of the

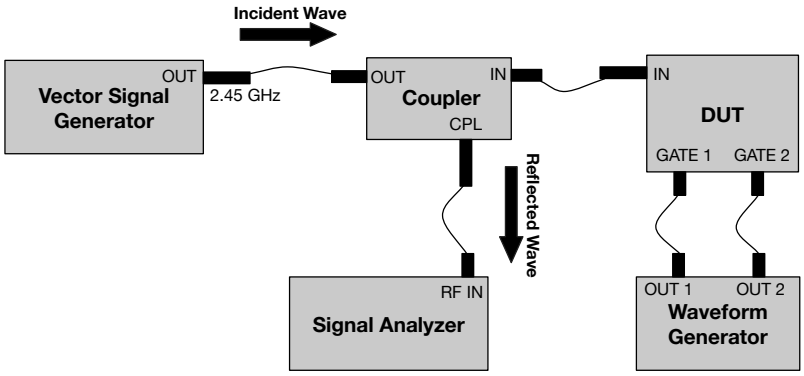

(a)

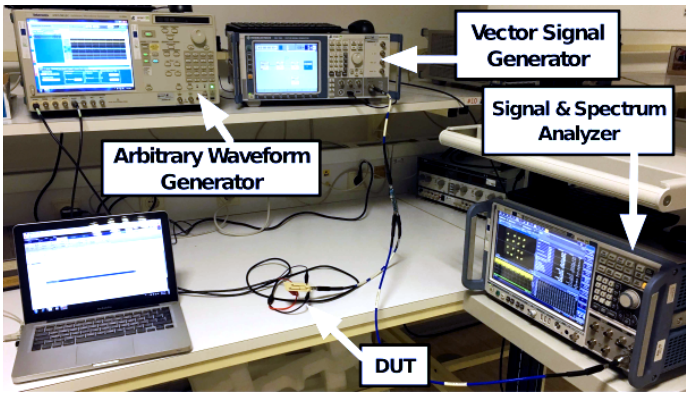

(b)

Figure 5.13: Measurement setup for demodulation and achievable data rates. a) Block diagram. b) Photograph.

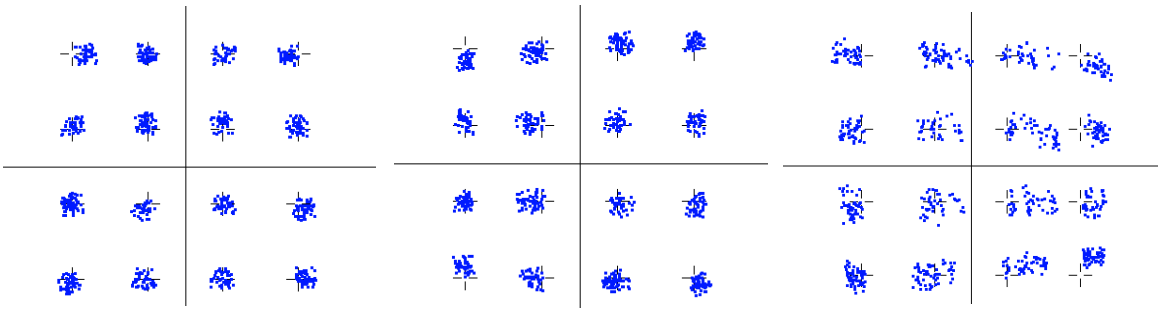

(a) (b) (c)

Figure 5.14: Received 16-QAM constellation for a center frequency of 2.45 GHz for different bit rates. (a) 4 Mb/s with 8.19% of EVM and 21.74 dB of SNR. (b) 40 Mb/s with 10.96% of EVM and 19.20 dB of SNR. (c) 120 Mb/s with 16.76% of EVM and 15.52 dB of SNR.

communication rate. Nevertheless, Fig. 5.14(c) illustrates that it is possible to demodulate at such higher data rate.

Figure 5.15 illustrates the measured EVM for different data rates. As the data rate increases, the measured EVM also increases. Nevertheless and despite the EVM seems high, the process has not passed through any signal processing equalization at the receiver. These results clearly state the viability of the proposed solution for a high bit rate backscatter approach.

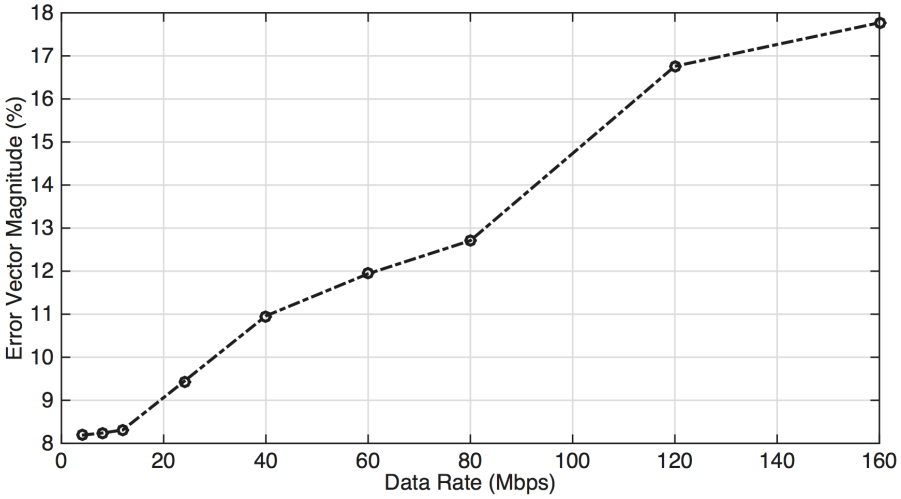

Figure 5.15: Measured EVM of the 16-QAM with a varying data rate.

Sensitivity of Backscatter Modulator

To evaluate the sensitivity of the gate voltage applied to each transistor, a Monte Carlo simulation was performed. A 1% and 5% of variation on each gate voltage were applied and Fig. 5.17 presents the results obtained from the modulator. The red marker in the figure shows the limit of the possible calibration for this modulator. By varying the voltages with 0.01 V it is possible to scale this system to a 64-QAM with adequate calibration.

Power consumption of Backscatter Modulator

In Fig. 5.18, the measured EVM of the 16-QAM modulator as function of input power for different data rates can be seen. Since this device was optimized for a 0 dBm (1 mW) RF input signal, the lowest value of EVM can be seen to be around this RF power. By using different voltage values at each gate of transistor, it is possible to reduce the EVM values at different levels of input power.

As the data rate increases, DC consumption increases following $\frac{1}{2}CV^2f$. The capacitance at the gate of each E-pHEMT is 1.73 pF and the voltage levels used for each transistor vary

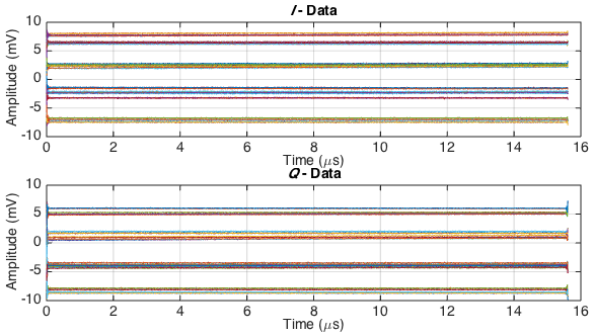

(a)

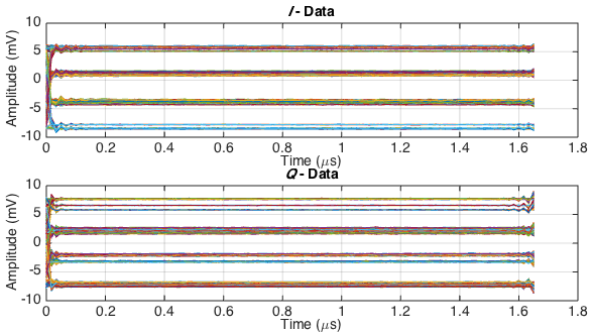

(b)

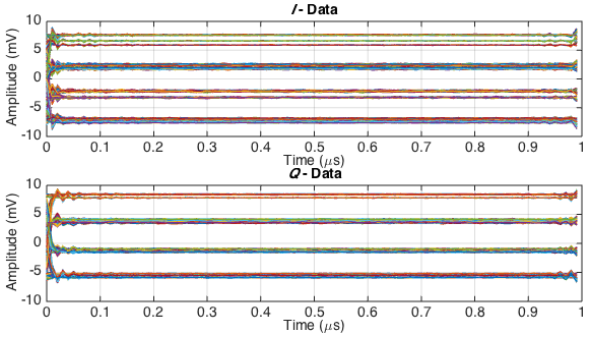

(c)

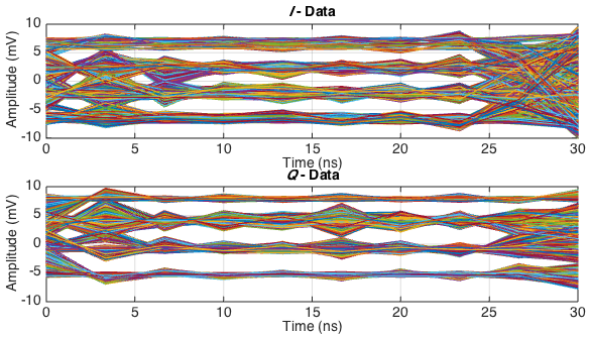

(d)

Figure 5.16: Eye diagrams of received demodulated data for varying data rates. (a) 256 kb/s. (b) 2.4 Mb/s. (c) 4 Mb/s. (d) 120 Mb/s.

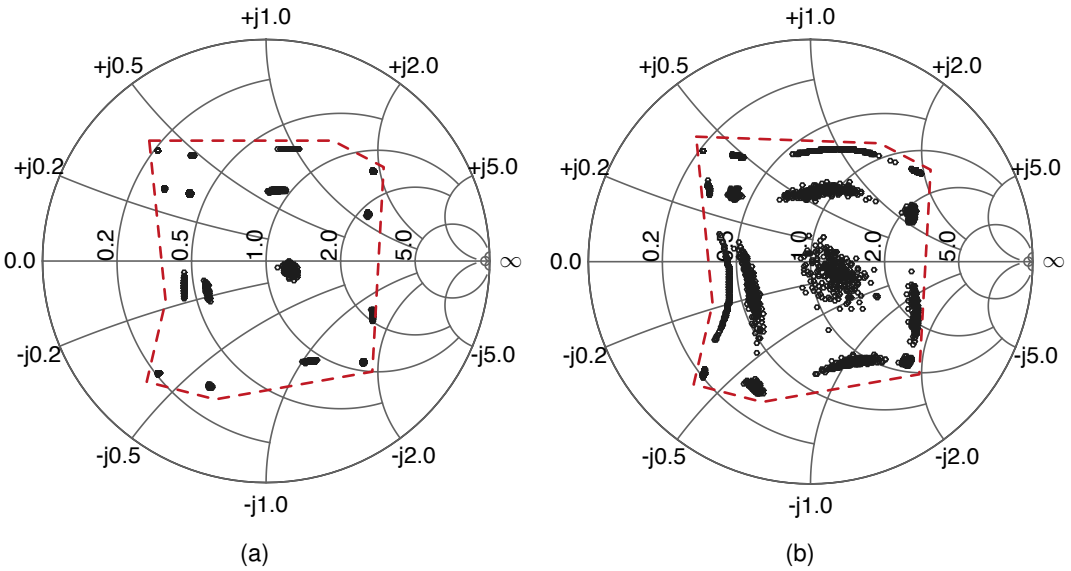

Figure 5.17: Sensitivity of the modulator. a) With 1% of variation on each gate transistor. b) With 5% of variation on each gate transistor. The red marker indicates the limit that is possible to achieve by calibration of the voltages.

---

from 0 V to 0.6 V, so we calculated an average value of all transitions that perform the 4-QAM, which is 0.25 V. Considering a data rate of 120 Mb/s, the power consumption of the 4-QAM backscatter modulator is 6.5 μW. The energy consumption per bit of this modulator is approximately 54 fJ for a data rate of 120 Mb/s.

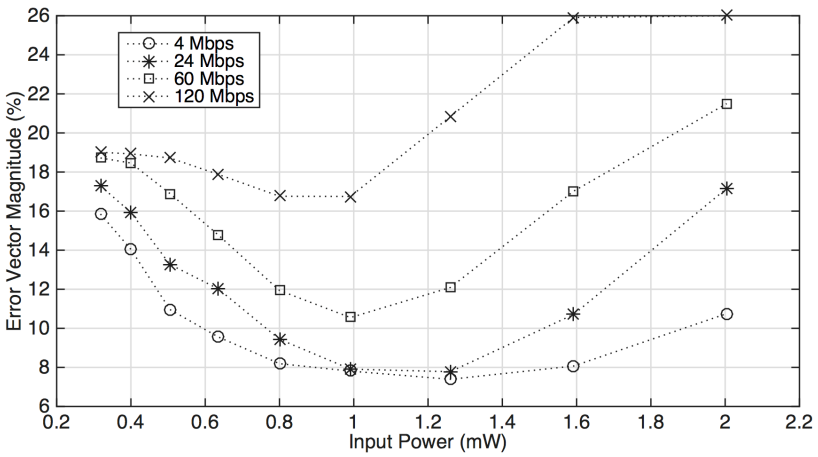

Figure 5.18: Measured EVM of the 16-QAM modulator as function of input power for different data rates.

5.2 Dual-Band High Order Modulator

In this section, a new approach for a dual-band high order modulation backscatter passive radio solutions will be presented. It will be described a modulation technique that enables a high-bandwidth wireless communication while requiring very low power demands. The system is suitable for backscatter communications in two different frequencies, instead of focusing in one single frequency. Moreover, the solution can be combined with a solar panel for ultra low-power wireless applications requiring high bandwidth communications.

5.2.1 Circuit description

There are two main blocks that need to be developed in order to implement a passive sensor: the RF-DC converter to harvest or collect RF energy in both frequencies to supply a microcontroller and the backscatter modulator responsible for the communication modulation. The block diagram of the proposed system is presented in Fig. 5.19 and illustrates the modules needed to implement a passive sensor that harvests energy and modulates data with high order modulation in two different frequencies.

To design a dual-band M-QAM backscatter modulator it was necessary to perform and evaluate a dual-band Wilkinson power divider to follow the approach used in [22], where a M-QAM backscatter modulator was developed with the use of a single band Wilkinson power divider. A dual-band Wilkinson power divider based on the schematic in Fig. 5.20 was simulated with the values presented in the table in Fig. 5.20 and obtained through the following equations:

$$\theta = \frac{\pi}{1 + \frac{f_2}{f_1}}, \tag{5.5}$$

$$Z_2 = \frac{\sqrt{2}Z_0}{k(1 + \tan^2\theta)\sin\theta\cos\theta}, \tag{5.6}$$

$$\frac{Z_2}{Z_c} = \frac{(1 - \frac{1}{k})(1 + \cot^2\theta)}{k(1 + \tan^2\theta)}, \tag{5.7}$$

$$\frac{Z_2}{Z_3} = \tan^2\theta - \frac{1}{k}, \tag{5.8}$$

where

$$k = \frac{Z_1}{Z_2}, \tag{5.9}$$

A value of $k = 2$ was considered. The design of the Wilkinson power divider was based on the approach used in [170] and the main goal was to transfer the drain impedances to the antenna in both frequencies and to isolate one transistor from the other.

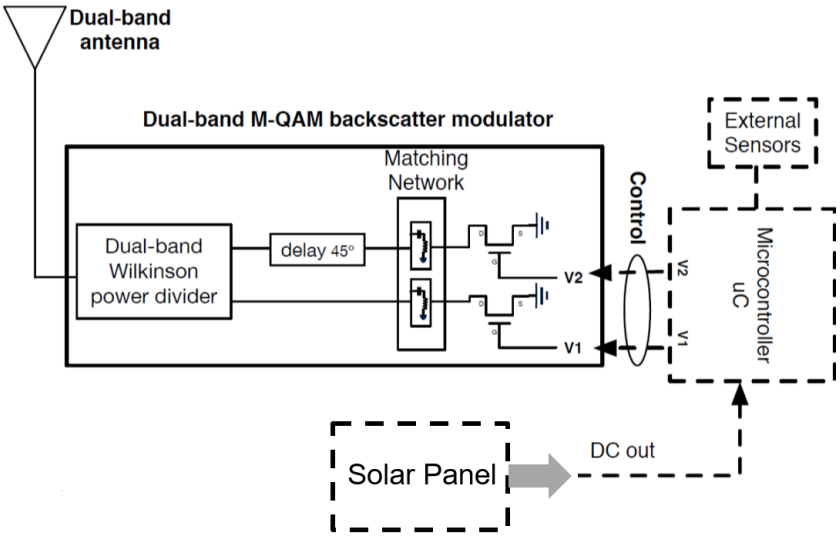

Figure 5.19: Block diagram of passive sensor composed by dual-band antenna, M-QAM high order modulator and a solar panel.

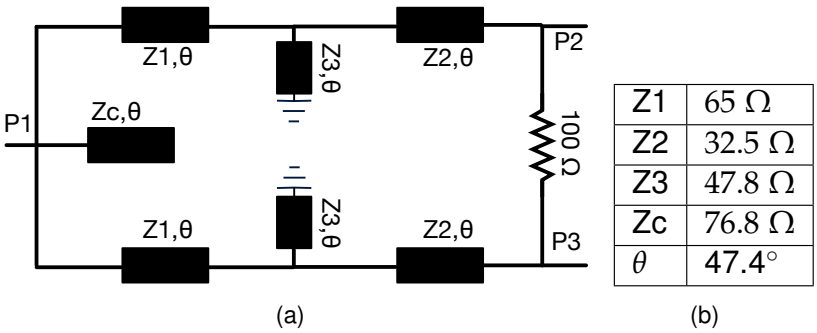

Z1	65 Ω
Z2	32.5 Ω
Z3	47.8 Ω
Zc	76.8 Ω
θ	47.4°

Figure 5.20: Dual-band Wilkinson power divider with scheme and values used.

The results from the simulations presented in Fig. 5.21 validated the first step to design the M-QAM dual-band high order backscatter modulator at 900 MHz and 2.45 GHz.

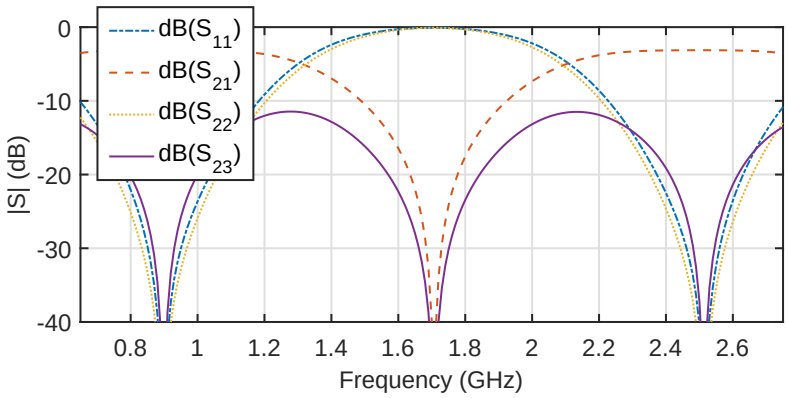

Figure 5.21: Simulated results of the dual-band Wilkinson power divider.

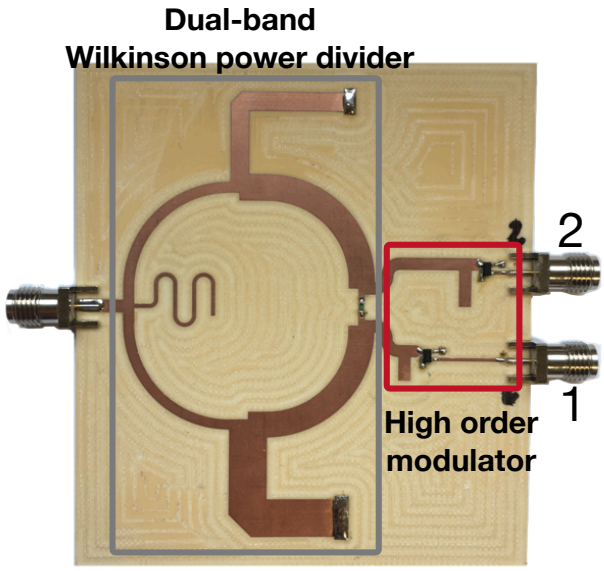

Figure 5.22: Photograph of the implemented circuit, dual-band M-QAM backscatter modulator.

The backscatter modulator is composed of a dual-band Wilkinson power divider, two matching networks, and two E-pHEMT transistors (Broadcom ATF-54143), following the same approach used in [3]. The lines of each branch of the modulator present a 45° phase delay with respect to each other in order to provide a 90° phase in each reflected wave of the branch at both frequencies. The transistors are responsible for changing the drain impedance by varying the voltages at the gate of each transistor from 0 V to 0.6 V. We combined the dual-band Wilkinson power divider with the modulator to obtain the dual-band M-QAM

backscatter modulator. To optmize the design, several simulations were carried out using ADS. The main goal was to optimize the circuit to obtain four different reflection coefficients at 900 MHz and other four at 2.45 GHz with the same voltages at the gate of each transistor, to obtain 4-QAM modulation, reason for which some values of the dual band Wilkinson power divider have changed. Due to multipath effects and line of sight to the sources, it was important to maintain the same coefficient reflections by varying the voltage at the gate of transistors and level of input power.

In Fig. 5.22, the photograph of the implemented circuit is shown. The circuit includes a dual-band Wilkinson power divider and the M-QAM modulator composed by two transistors that create a variation in the amount of energy reflected by the antenna.

5.2.2 Results

Figure 5.23 presents the results obtained from the simulations with variations of voltage from 0 V to 0.6 V with a step of 0.01 V on each transistor in both frequencies (900 MHz and 2.45 GHz). These results were performed with a variation from -90 dBm to 0 dBm of input power. As can be seen in Fig. 5.23 it is possible to achieve at least a 16-QAM modulation in the two bands.

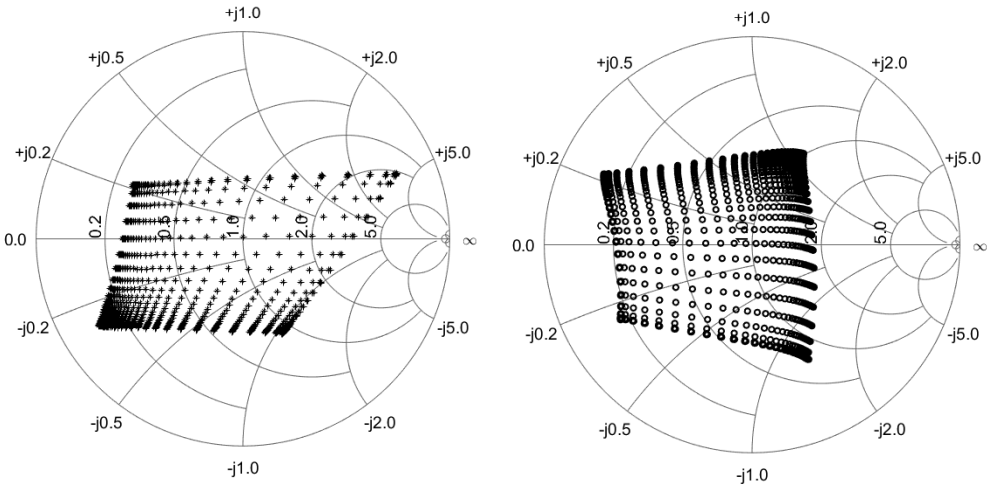

Figure 5.23: Simulated reflections coefficients by varying the voltage at each gate of transistor from 0 V to 0.6 V with a step of 0.01 V. a) Frequency = 900 MHz. b) Frequency = 2.45 GHz.

Figure 5.24 presents the obtained results with the circuit presented in Fig. 5.22. The reflection coefficients corresponding to each applied voltage at the gate of the transistor at each frequency can be observed in the Table 5.2. The setup used to acquire these results can be seen in Fig. 5.25.

Table 5.2: Measured S_{11} for different levels at the gate of transistors (V1 and V2).

Measured			
V1 (V)	**V2 (V)**	**S11 (900 MHz)**	**S11 (2.45 GHz)**
0	0	.77+.29j	-.39-.25j
0	0.47	-.26+.23j	.32-.23j
0.34	0	.35-.33j	-.44+.48j
0.6	0.6	-.62-.41j	.36+.48j

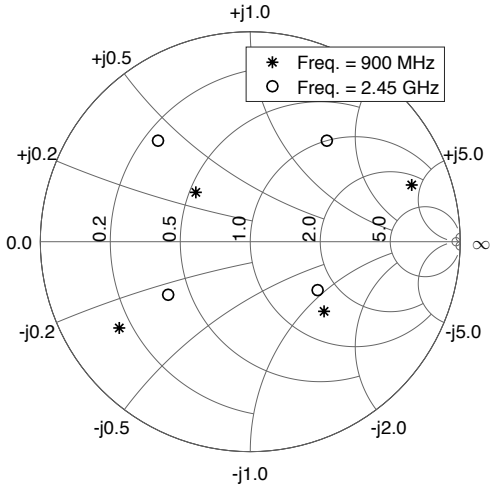

Figure 5.24: Measured results of 4-QAM backscatter modulator for both frequencies 900 MHz and 2.45 GHz with -20 dBm of input power.

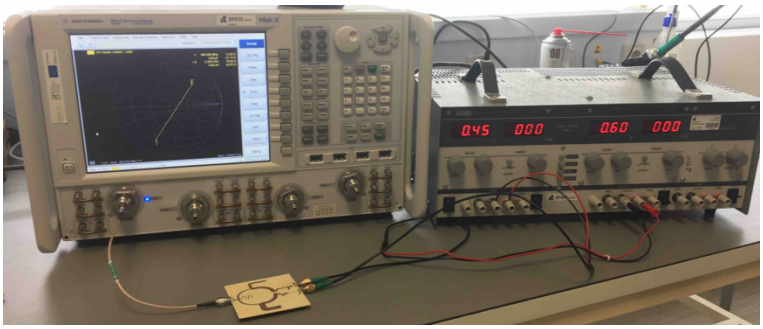

Figure 5.25: Photogrpah of the measurement setup.

The four points represented for each frequency show the limits of the reflection coefficients, which can be concluded that it is possible to increase the modulation order by increasing the number of voltages applied at the gate of each transistor. Nevertheless, the focus of this work was to design a system capable of modulating two different CWs at two

different frequencies with high order modulation (4-QAM).

In order to integrate this system into the emerging technologies of IoT, it is a high requirement the low power consumption of the modulator. The DC power consumption of the modulator was characterized, by including only the power required for each E-pHEMT. As the data rate increases, DC consumption increases following $\frac{1}{2}CV^2f$. The capacitance at the gate of each E-pHEMT is 1.73 pF and the voltage levels used for each transistor vary from 0 V to 0.6 V, so we calculated an average value of all transitions that perform the 4-QAM, which is 0.25 V. Considering a data rate of 500 kbps, the power consumption of dual-band 4-QAM backscatter modulator is 27 nW.

Achievable Data Rates

The maximum data rate of the communication on the modulator link was studied by using the measurement setup presented in Fig. 5.26 to view the eye diagrams of the I and Q signals at multiple transmission rates. We used a vector signal generator (ROHDE&SCHWARZ SMJ 100A) to generate the transmitter signal at 900 MHz 2.35 GHz. An arbitrary waveform generator (TEKTRONIX AWG5012C) was used to generate the voltage levels at the gate of each transistor mimicking the modulated data rate. A coupler was used to measure the reflected signal from the circuit, by the spectrum analyzer (ROHDE&SCHWARZ FSW8).

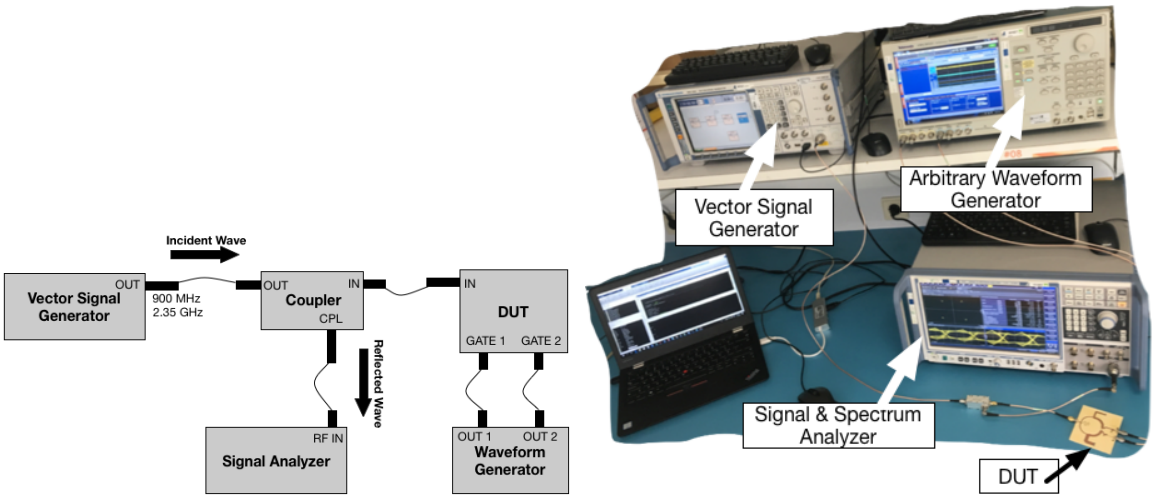

Figure 5.26: Measurement setup used for high data rate validation. a) Block diagram. b) Photograph.

The received eye diagrams for varying data rates are shown in Fig. 5.27, and for the data rates of 400 kb/s, 4 Mb/s and 40 Mb/s the eye is clearly open and the received signals are clean for both frequencies.

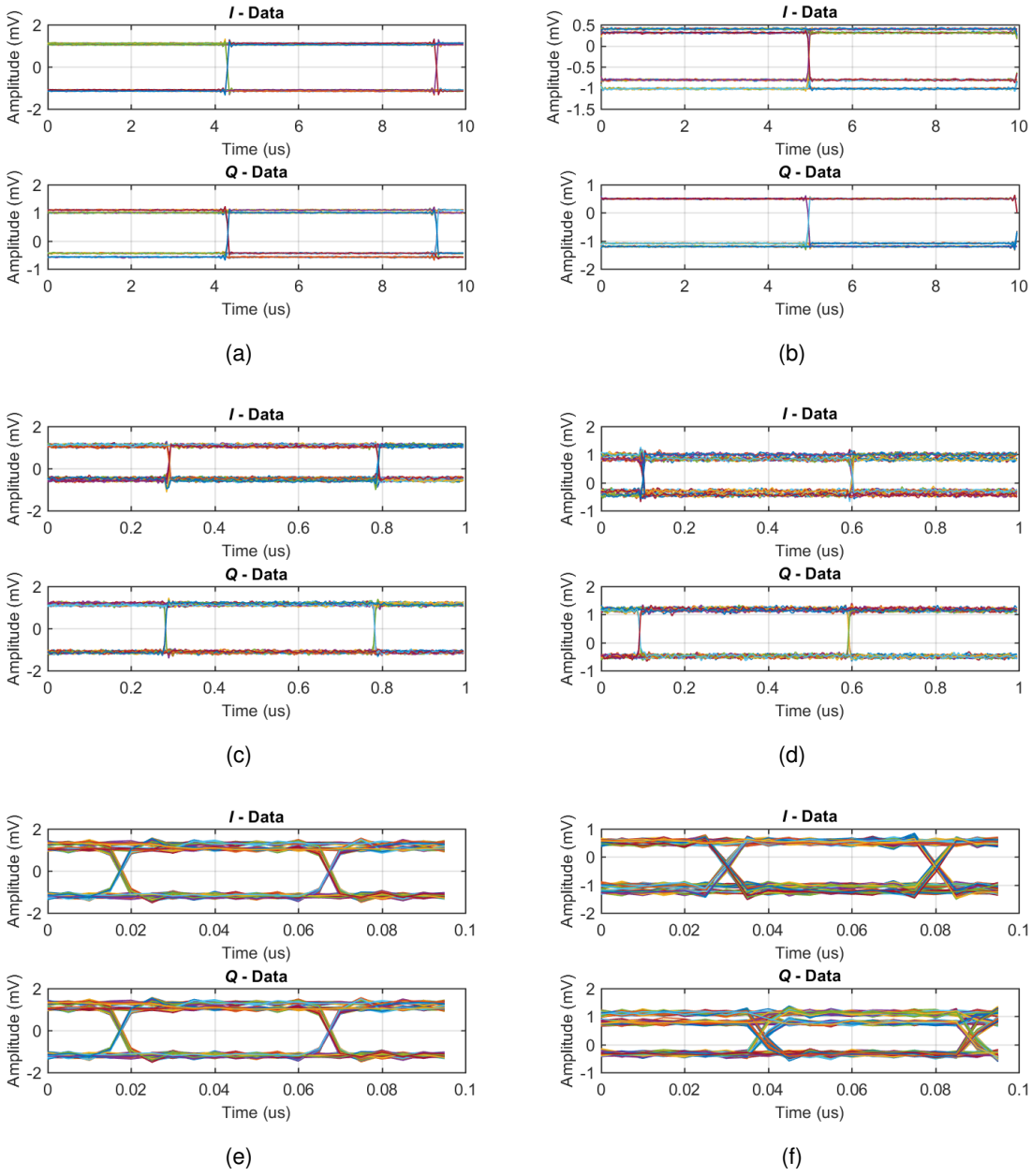

Figure 5.27: Eye diagrams of received demodulated data for varying data rates. (a) 400 kb/s at 900 MHz. (b) 400 kb/s at 2.35 GHz. (c) 4 Mb/s at 900 MHz. (d) 4 Mb/s at 2.35 GHz. (e) 40 Mb/s at 900 MHz. (f) 40 Mb/s at 2.35 GHz.

5.3 4-PAM Modulation of Ambient FM Backscattering for Spectrally Efficient Low Power Applications

Ambient backscatter uses RF signals available in the environment (e.g. radio broadcasting, television or mobile telephony) to transmit data effectively leading to significant energy and cost efficiency increase. In this section a novel wireless tag, which for the first time utilizes 4-pulse amplitude modulation (4-PAM) technique to modulate the ambient backscattered FM signals in order to send data to a nearby low-cost SDR reader is presented. The tag is based on an RF front-end that uses a single transistor controlled by an ultra low-power microcontroller, which includes an ADC for sensing and a DAC for RF front-end control. A proof-of-concept prototype in an indoor environment with the low bit rate of 345 bps will be demonstrated. The prototype tag consumed 27 μW and it operated using an FM station at 34.5 Km away. The value of energy spent in this modulator was 78.2 nJ/bit at 345 bps and 27.7 nJ/bit at 10.2 Kbps.

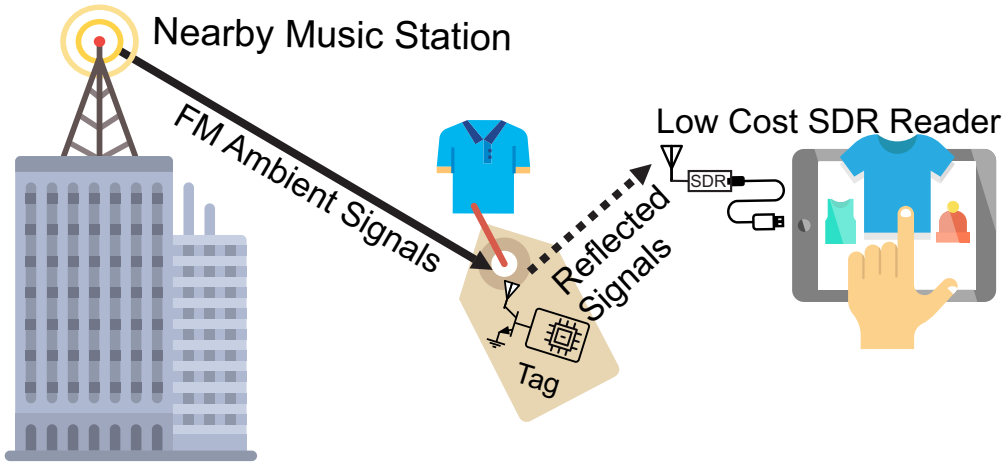

Figure 5.28: FM ambient backscatter communication scheme. An example application could be the identification of clothes in a mall using tablets and low cost SDRs.

Figure 5.28 depicts a possible application of this system. The tag uses ASK binary modulation with FM0 encoding on ambient FM station signals as in commercial RFID systems. The FM transmitter was 34.5 Km away from the measurement setup and a 5 m communication range between the tag and the reader was achieved with 2.5 Kbps bit rate.

In [88], for the first time high-order modulation was introduced for ambient backscattering communications. The authors demonstrated 4 FSK modulation to transmit two bits per symbol over the ambient FM signals with a maximum data rate 3.2 kbps. The work involves simulation of an integrated circuit for the tag, while for the prototype an AWG was used connected with an RF front-end.

In this work we consider high order amplitude modulation and we demonstrate the

first prototype suitable for ambient backscatter communication deployment working with 4-PAM. The 4-PAM modulation is used to double the bit rate, compared to a 2-PAM system. With amplitude modulation the complexity of the receiver and the tag can be drastically simplified as there is no need for a different frequency for each symbol. Tag and receiver are more complex as variation of modulating signal has to be converted and detected from corresponding variation in frequencies. Preliminary results were presented in previous work [171], where 4-PAM scheme was selected due the low hardware complexity and low power consumption. In particular, this tag employs a single low cost transistor and a telescopic antenna achieving communication with low bit rate for reducing power consumption. This work differs from [21,22] since it uses ambient FM signals as the carrier instead of an intentionally transmitted unmodulated CW signal. The use of FM signals on the receiver increases the complexity of selecting the thresholds associated with demodulation. A tag consisting of a microcontroller with a DAC and an ADC is presented. The tag could collect data from sensors through the ADC and process them. The microcontroller creates the modulation pulses internally and controls the RF front-end transistor via the DAC.

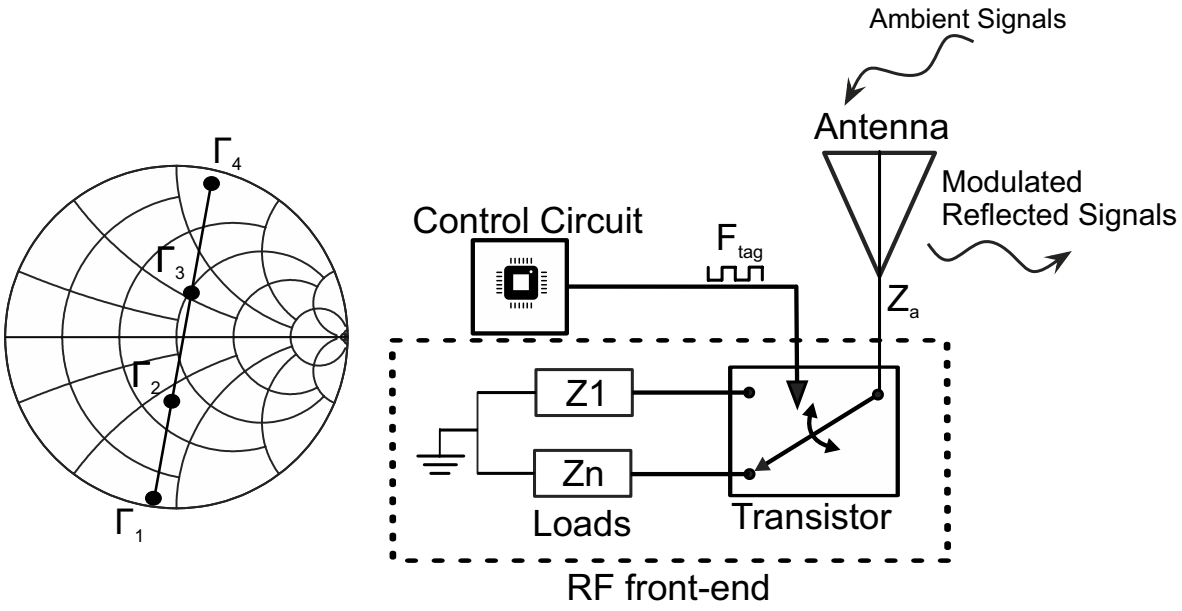

Figure 5.29: Backscatter radio principle: An RF transistor alternates the termination loads Z_i of the antenna corresponding to different reflection coefficients Γ_i. Four reflection coefficients ($n = 4$) could create a four pulse amplitude modulation (4-PAM).

In backscatter communications, the tags do not need to transmit a radio signal, since they reflect signals transmitted by the reader or another ambient radio emitter. A backscattering tag modulates the reflected signal using one or more transistors or RF switches connected to the antenna as it is shown in Fig. 5.29. A binary backscatter communication is based on

a reflected waveform that should switch between a fully matched and a short circuit load terminating the antenna. In [105], an RF switch was directly connected to the RF front-end antenna in order to create the two discrete states. For high order modulations, the number of states have to be increased and the RF circuit must create a specific discrete impedance for each transmitted symbol. For this purpose, a single RF transistor circuit can be used as an active load in order to create different impedances for the PAM constellation [22]. In this work an E-pHEMT transistor was used to implement a circuit compatible with a 4-PAM scheme. The RF circuit presents four distinct impedance values for a four different gate voltages. A given antenna with impedance Z_a connected to a complex load with impedance $Z_i \in \{Z_1, Z_2, Z_3, Z_4\}$, is associated with a reflection coefficient obtained as:

$$\Gamma_i = \frac{Z_i - Z_a^*}{Z_i + Z_a}. \tag{5.10}$$

Typically the antenna impedance is chosen to be 50 Ohm. By changing the gate voltage of the transistor, four distinct reflection coefficients can be achieved corresponding to the four symbols.

Table 5.3: 4-PAM Modulation Parameters

Γ	Symbol	Bits	V_{gate} (mV)
$-0.7245 - j0.6922$	-3	00	0
$-0.3414 - j0.2881$	-1	01	333
$+0.0223 + j0.1779$	$+1$	11	387
$+0.3079 + j0.6334$	$+3$	10	600

The performance of PAM modulation is optimized when the Γ_i values lie equidistantly along a straight line on the Smith Chart (Fig. 5.29, left) [22].

Considering the above, we can select the desired values of the reflection coefficients; an example of four equidistant measured values on the same line is shown in Table 5.3. Using this table and (5.10), the desired voltage values at the transistor gate can be obtained.

5.3.1 Sensor Node/Tag Design

The tag consists of an ultra low power microcontroller connected with an RF front-end as it is depicted in the block diagram of Fig. 5.30. The 8-bit PIC16LF1459 microcontroller from Microchip Inc. was used, which consumes 25 μA/MHz of current at 1.8 V [172]. The clock of the MCU was programmed at 32 KHz in order to minimize the power consumption of the tag. The MCU also has a sleep mode operation with current consumption of 0.6 μA. The MCU includes a 10 bit ADC and collects data from analog sensors on the tag. The 5-bit DAC of the MCU is used in our application to drive the RF front-end transistor with different voltages. The DAC has the ability to supply the gate of the transistor with 2^5 distinct voltage

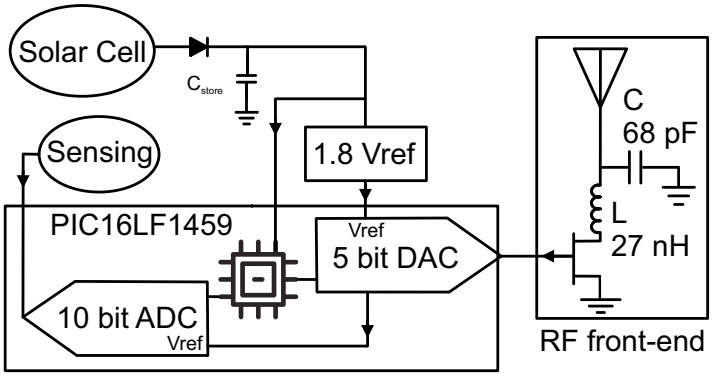

Figure 5.30: Schematic of Proof-of-concept tag. A low power micro-controller reads the sensors and controls the RF front-end circuit.

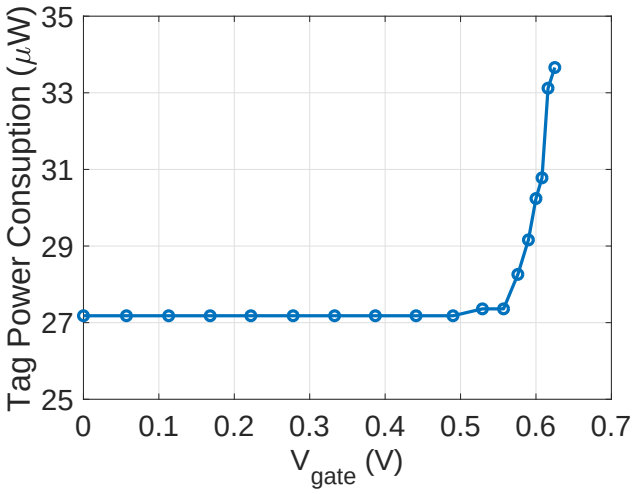

Figure 5.31: Digital-to-Analog Converter output voltage versus the tag power consumption. The tag was measured at 1.8 V when the ADC was turned off.

levels in order to change the antenna load impedance. For our application the maximum gate voltage for the transistor and thus DAC output was 0.6 V. Fig. 5.31 depicts the power consumption for different DAC output voltages when the MCU was supplied by a 1.8 V voltage source.

The tag was powered by the flexible solar panel, SP3-37 provided by PowerFilm Inc. [173]. The solar panel charges a 220 μF tantalum capacitor instead of a battery through a low-voltage-drop Schottky diode. An external voltage reference IC XC6504 [174] was also used to supply the tag with a stable voltage (V_{ref}) 1.8 V. The proposed sensor node do not focus on a specific sensing application or power management system but only on the novel telecommunication part of the system. An RF harvester could be designed in the future to charge the capacitor during the night in combination with solar cell during the day [175].

The RF front-end consists of the ATF52189 E-pHEMT RF transistor from Broadcom and the SRH788 monopole antenna. The maximization of the magnitude of complex reflection coefficient differences between the four states is a main objective for optimized backscatter communication [176]. In this work, a core RF circuit challenge was to achieve the desired change of the drain impedance by varying the voltage at the gate in the range from 0 to 0.6 V. The ADS from Keysight was used for the optimization of the RF front-end circuit. The simulations performed involved the variation of the gate voltage at the transistor from 0 to 0.6 V with a sweep of 0.01 V from 87.5 MHz to 108 MHz. More specifically the LSSP simulation was used to perform the backscatter modulation in order to maximize the distance between the consecutive Γ_i values. Following the aforementioned optimization procedure, the matching network between the transistor and the antenna was composed by a capacitor and an inductor as depicted in the schematic of Fig. 5.30. The optimum component values were found to be 68 pF and 27 nH. The main board of the proof-of-concept tag that integrates the

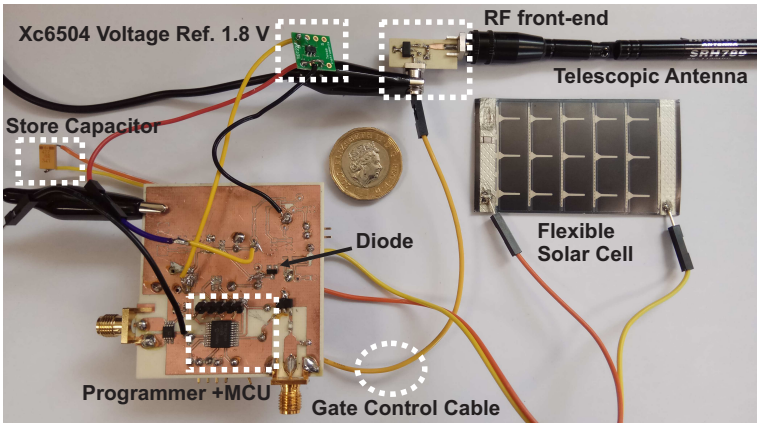

Figure 5.32: The fabricated tag prototype with the RF front-end board. The tags is powered by a solar panel.

microcontroller was fabricated on a Rogers RO4350B substrate. The RF front-end board was

fabricated on Astra MT77 substrate with thickness 0.762 mm, $\epsilon_r = 3.0$ and $tan\delta = 0.0017$. The fabricated prototypes and the solar panel are shown in Fig. 5.32. As mentioned, the output of the DAC was connected to the gate of the transistor on the RF front-end.

The fabricated RF front-end board was measured using a vector network analyser (VNA) with $P_{\text{in}} = -20$ dBm at the frequencies of the FM band, $87.5 - 108$ MHz. The four voltages: 0, 333, 387 and 600 mV were found as the optimum values to supply the gate of the transistor, creating four impedances or symbols for a specific frequency. The reflection coefficients in the FM band are presented in Fig. 5.33. Table 5.3 also shows the resulting Γ, the symbols, the bits and the gate voltages at a fixed frequency of 95.8 MHz. Using the four voltages at the gate of the transistor and sweeping the frequency it is possible to observe that each state corresponds to an "arc" on the Smith Chart. In particular, the set of four states (each line in Fig. 5.33) rotates clockwise as the frequency increases. Equal distances between the symbols were achieved in order to maximize the signal-to-noise ratio (SNR). It is noted that our tag is a semi-passive design where the available capacitor powers the microcontroller during transmission from the tag to the reader.

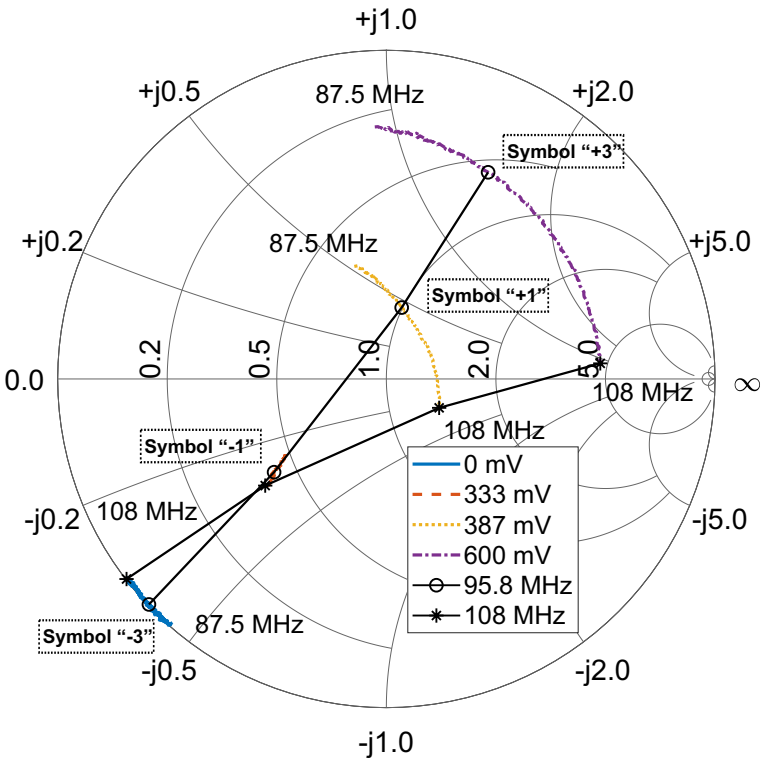

Figure 5.33: Smith Chart with measured reflection coefficient values for 4 different voltage levels at the gate of transistor. The Pin was fixed at -20 dBm for frequencies $87.5 - 108$ MHz.

5.3.2 Ambient FM 4-PAM Modulation

Pulse Amplitude Modulation (PAM) is a method of sending information by scaling a pulse shape with the amplitude of the symbols and duration T_{symbol} [177]. In the 4-PAM there are four symbols and each symbol corresponds to a pair of two bits. Each bit duration is denoted as T_{bit} and the data bit rate is $2/T_{\text{bit}}$ bits per second (bps). According to 4-PAM it is possible to transmit two bits with each symbol/pulse, for example, by associating the amplitudes of `-3,1,+1,+3`, with four bit choices `00`, `01`, `11`, and `10` (Table. 5.3). The bit representation of the symbols is Gray coded [178].

The proof-of-concept tag was set up to send a fixed bitstream packet format. In this work the fixed bit sequence was: `10001000100111-00-01-0111100011` which is translated to symbol sequence: `+3-3+3-3+3-1+1 -3 -1 -1+1+3-3+1`. Transmission of some known preamble data is required at the receiver to identify the beginning of a frame (packet) at the transmission. Here the first seven symbols (14 bits) were added before the message sequence as a preamble. The symbols of the preamble are used also as training symbols as explained below. After the preamble, "Tag Number" bits (2 bits), "Sensor Number" bits (2 bits) and "Sensor Data" bits (10 bits) follow. The "Tag Number" bits were utilized in case that four different tags can be used in a future wireless sensor network. With this allocation, the tag could support up to four sensors and the "Sensor ID" part is used to identify the sensor number. The last 10 bits section is used for transmitting the sensor data. An example of the transmitted packet is depicted in Fig. 5.34 and more bits could be added in order to include extra sensors or tags.

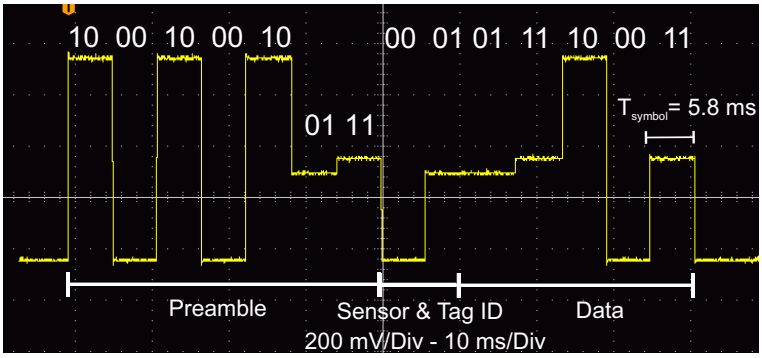

Figure 5.34: An oscilloscope measurement of the sending packet. Voltage levels correspond to the 4-PAM symbols at the gate of the transistor are presented.

5.3.3 Receiver

The flowchart of the 4-PAM receiver is shown in Fig. 5.35. The algorithm captures data in a specific time window equal with $3\times$packet duration and packet duration $= 14 * T_{\text{symbol}}$.

The matched filter is a square pulse signal with T_{symbol} duration and acts as a low-pass

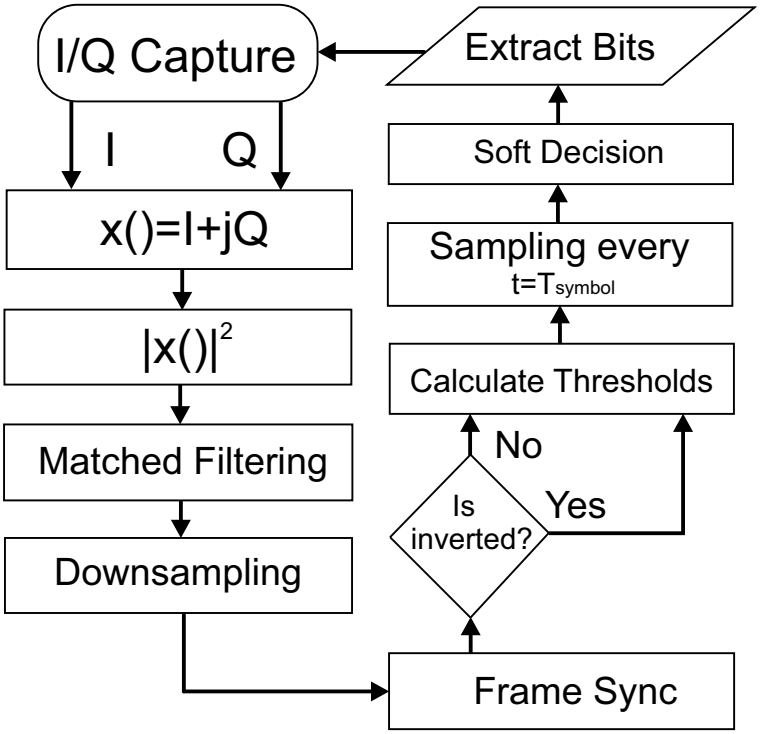

Figure 5.35: Flowchart of the receiver algorithm implemented in MATLAB software.

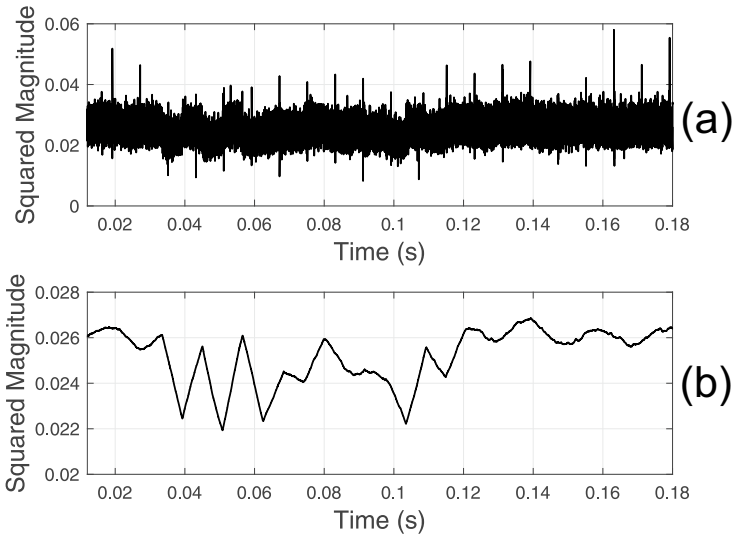

Figure 5.36: Received packet signal. a) Signal after squared absolute operation and b) signal after matched filtering for $T_{\text{symbol}} = 5.4$ ms.

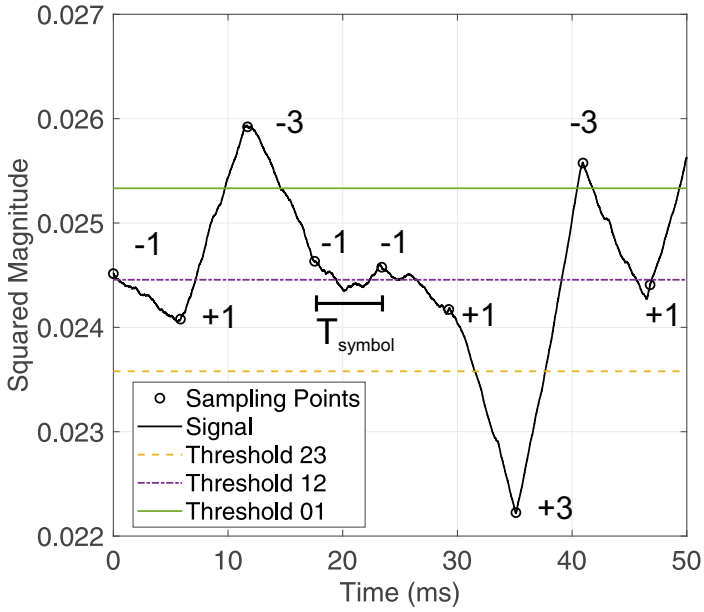

Figure 5.37: Received packet without the preamble after matched filtering. The respective symbols can be decided using three thresholds.

filter that removes out-of-band signals. Fig. 5.36 (a) shows an example of a received packet in time domain after the absolute square operation. The packet after the low-pass filtering is depicted in Fig. 5.36 (b). A downsampling operation by a factor of 585 was applied in order to reduce the computational complexity of the following steps. Proper decoding requires locating where the frame starts and this step is called frame synchronization. Cross-correlation was used for the synchronization with a known preamble sequence `10-00-10-00-10-01-11`. As it is observed the preamble includes all the symbols at least once and in this work, it is used also for training. In particular, the group of training symbols are send prior to the useful data symbols and they are useful for calculation of the thresholds.

During synchronization, it is also detected if the signal is an inverted waveform or not. An inverted waveform (Fig. 5.36) results due to the channel propagation characteristics and this information is required for the next step.

For each packet coming at the receiver it is necessary to calculate different thresholds. In Fig. 5.37, the estimated thresholds for the signal of Fig. 5.36 are depicted.

Next, the algorithm quantizes the received signal based on the three thresholds. Samples every T_{symbol} are taken and compared with threshold(s) to determine the recovered data symbols. A transmitted symbol is determined if the sample corresponds to its specific symbol region. In Fig. 5.37 is depicted the useful signal without the preamble part and a specific symbol/region corresponds to a received sample for a given T_{symbol}. Finally, a quantizer makes the decisions that are then decoded back from symbols to the bits of the message.

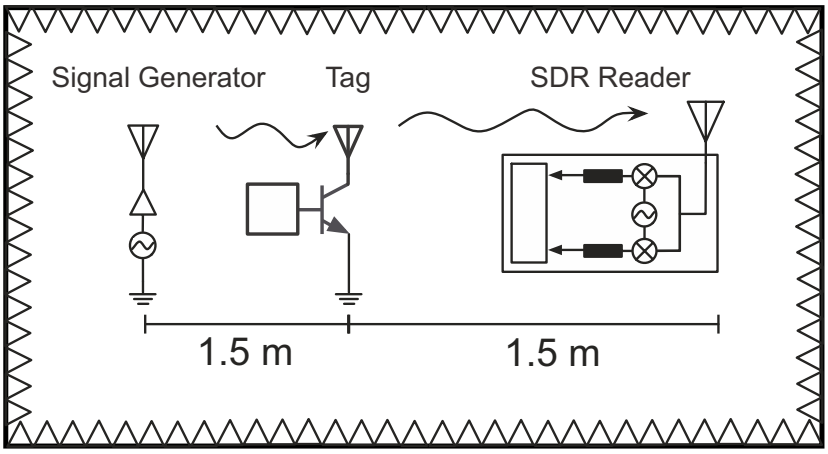

Figure 5.38: Schematic of the experimental setup in the anechoic chamber. The transmitter-to-tag distance and the tag-to-reader distance were 1.5 m.

5.3.4 Measurement Results

In order to evaluate telecommunication measurements for our system, the proof-of-concept tag prototype was programmed to produce a fixed packet bit-stream at the DAC output. The symbol representation of bit-sequence was described above and it is depicted in Fig. 5.34. The figure is an oscilloscope measurement and shows the four voltage levels of the transmitted symbols that are used to drive the transistor. The T_{symbol} was fixed at 5.8 ms and thus the bit rate is calculated at 345 bps. It can be observed that a small variation between the gate voltages corresponding to the states `-1` and `+1` occurs. This variation do not correspond to small variation in Γ_i but leads to the maximum distance between Γ_1 and Γ_2 as it is shown in Fig. 5.33. This is due to the non-linear relationship between the transistor gate voltage and the corresponding Γ_i.

To test the performance of the backscatter communication link we first demonstrated our system in a controlled environment (anechoic chamber). The RF front-end antenna was placed 1.5 m away from the receiver antenna while the FM generator antenna was 1.5 m way from the tag. The generator and the reader use commercial passive FM antennas with gain 2.5 dBi. The bistatic topology schematic is showed in Fig. 5.38 and the signal generator was set at 98.5 MHz. Different transmit power levels were recoded at the generator while the tag was set to send the fixed packet continuously. At the receiver, the bandwidth around the carrier frequency was fixed at 1 MHz. In order to compute the bit error rate (BER), 1200 packets of data were collected for a varying transmit power from -45 to -20 dBm. Each packet contains 28 bits and thus the transmitted bits were 33600. The resulting BER versus the transmit power is shown in Fig. 5.39 and the minimum BER value at -20 dBm was measured to be $8.16 * 10^{-4}$.

As expected, the BER increased as the power at the generator decreases thus the reader

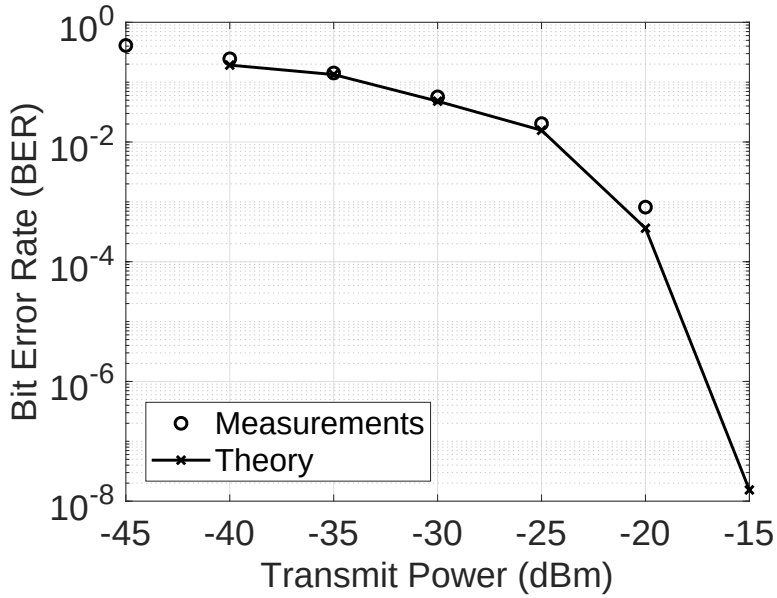

Figure 5.39: Experimental Bit Error Rate (BER) versus the transmitted power at the generator. The bit rate was 345 bps and the distances transmitter-to-tag, tag-to-reader were 1.5 m.

can not decode successfully the packets. In Fig. 5.39 the theoretical BER results are also depicted along with the measurements.

A good agreement between simulation and measurement results can be observed.

Table 5.4: High order Modulation vs Power Consumption vs Bit Rate

Work	Modulation	Backscatter Signal	Power	Part	Bit rate	Energy/bit
This work	4-PAM	Ambient FM	27 μW (Measurement)	Tag+Modulator	345 bps	78.2 nJ/bit
This work	4-PAM	Ambient FM	501 μW (Measurement)	Tag+Modulator	10.2 Kbps	27.7 nJ/bit
[19]	4-QAM	UHF CW	115 nW+6mW (Measurement)	Tag+Modulator	400 kbps	15 nJ/bit
[21]	16-QAM	UHF CW	1.49 mW (Measurement)	Modulator	96 Mbps	15.5 pJ/bit
[22]	16-QAM	UHF CW	1 mW (Measurement)	Modulator	60 Mbps	6.7 pJ/bit
[86]	4-FSK	Ambient FM	11.07 μW (Simulation)	Tag+Modulator	3.2 kbps	3.46 nJ/bit

The power consumption results of this work compared with the referenced work designs, are summarized in Table 5.4. The tag has been measured at low bit rate using ambient FM signals for communication and ensure fair comparison with the other works. As shown, this works represents the lowest power consumption ambient backscatter hardware prototype implementation with high order modulation, reported to date. The energy per bit was calculated at 78 nJ/bit for 345 bps and 27.7 nJ/bit for 10.2 kbps including the energy consumption of the modulator (RF transistor).

5.4 High order QAM modulator with WPT capabilites

Nowadays the wireless sensing devices are growing at a phenomenal rate, with billions of wireless sensors reaching a much larger proportion than the world's population. However, this rapid increase presents two main issues: increased use of batteries and energy consumption. Therefore, there is a significant need to design novel wireless communication techniques to achieve higher data rates while simultaneously minimizing energy consumption.

The existing standards consume much more power in comparison with the one proposed in this section. As shown in Fig. 5.40, power levels are in the range of 800 mW for Wi-Fi, 100 mW for Bluetooth, 50 mW for Zigbee, whereas the sensor presented in this section requires lower power levels of around 59 μW for the modulator. The high data rate and long operating range of Wi-Fi and wireless USB technologies come at an increase in power consumption which is impracticable for low power and remote sensor applications that require high-bandwidth wireless communication.

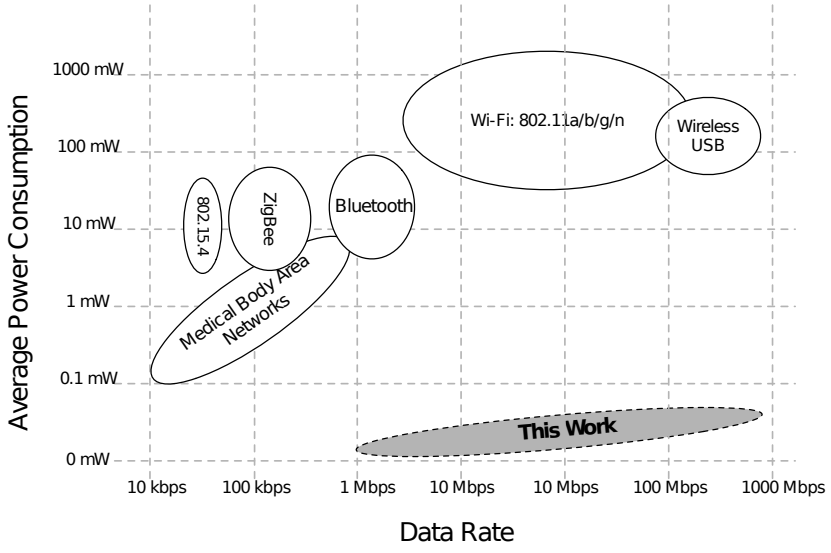

Figure 5.40: Comparison of wireless technology average consumption and data rates.

In order to overcome this issue, RFID backscattering systems are being explored with some advances in the type of modulations used.

In this section a system composed of a backscatter modulator at 2.45 GHz that has a consumption of 61.5 fJ/bit with WPT capabilities at 1.7 GHz is presented. The 16-QAM modulator is shown to provide 960 Mb/s of data rate with an EVM of 8.37%. The demonstrated system enables low power consumption, while maintaining a high modulation bandwidth.

5.4.1 Backscatter modulator and rectifier implementation

The system proposed in this work is divided into two main blocks, the backscatter modulator and a rectifier. Figure 5.41 shows the prototype implemented with these two blocks. The first, which is the backscatter modulator, is composed by a Wilkinson power divider, two matching networks and two E-pHEMT transistors (Broadcom ATF-54143), following the same approach used in [22]. The lines of each branch of the modulator present a 45°phase shift respect to each other in order to provide 90°phase in each reflected wave of the branch. The objective of the transistors is to change the drain impedance by varying the voltage at the gate. With different impedances at the drain of the transistor it is possible to change the reflection coefficient of the modulator providing, in this case, a 16-QAM constellation.

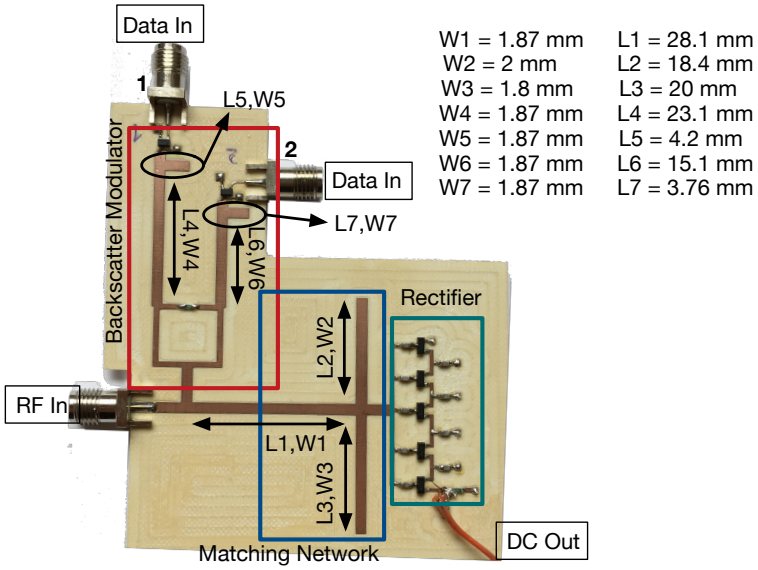

Figure 5.41: Photograph of the proposed system, composed by a 16-QAM modulator and a rectifier. Substrate for the transmission lines is Astra MT77, thickness = 0.762 mm, ε_r = 3.0, tan δ = 0.0017.

A five-stage Dickson multiplier is added to our system to harvest the maximum DC power from the CW of transmitter. In this work, our focus was the design of the RF front end, so we did not designed the digital processing hardware to generate the voltage levels for the modulator. However, with the rectifying circuit the goal was to generate enough DC voltage that could supply a microcontroller (1.8 V). The matching network was optimized to maximize the conversion efficiency at 1.7 GHz and to perform the backscatter communication at 2.45 GHz. The continuous change of voltage levels at the gate of transistor will induce different impedances at the input of rectifier, making it very difficult to design the modulator and the rectifier at the same frequency. Nevertheless, we followed the approach used in [18], by using two different frequencies, one for the backscatter communication and

the other for the WPT. This approach led to 56% of efficiency with 5 dBm of input power at 1.7 GHz with unbiased gate at each E-pHEMT. The added link for WPT with the new input matching network improved the efficiency of the rectifier with unbiased gate at each transistor. When the voltages are changed this will have an impact on the RF-DC conversion efficiency, the worst case scenario is a reduction from 56% to 10%.

5.4.2 System characterization and evaluation

The achievable data rates that are presented in this work were obtained by using the measurement setup presented in Fig. 5.42. Before acquiring the reflected waves or measuring the output DC voltage, we calibrated the input power by using a power meter (Agilent, N1913A).

We used a vector signal generator (ROHDE&SCHWARZ SMJ 100A) to generate the continuous wave at 1.7 GHz and 2.45 GHz. In order to test the input data on each transistor, we used an arbitrary waveform generator (TEKTRONIX AWG5012C) to create the voltage levels needed between 0 V and 0.6 V. These variations on the transistor's gate cause changes on the drain impedance that will originate different reflection coefficients. The reflected waves generated were analyzed by signal & spectrum analyzer (ROHDE&SCHWARZ FSW8) and the received constellations as well as the error vector magnitude (EVM) as function of input power for 4 Mb/s, 100 Mb/s, 480 Mb/s and 960 Mb/s are shown in Fig. 5.43.

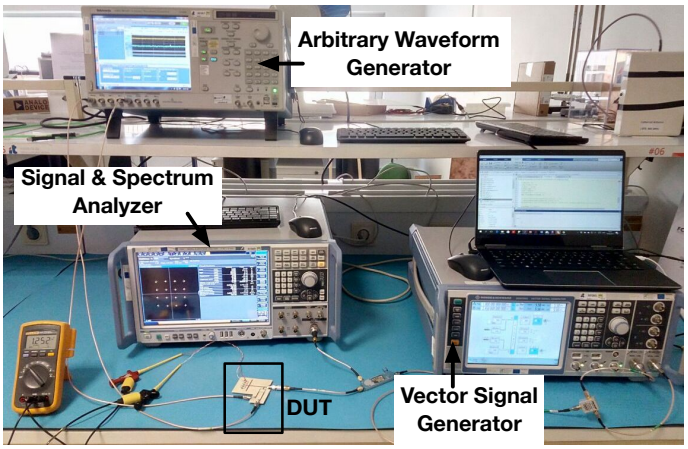

Figure 5.42: Photograph of the measurement setup used for demodulation.

We measured the average DC output voltage and efficiency generated by the system as function of input power for a load of 21.5 kOhm as can be seen in Fig. 5.44. We measured 56% of efficiency with 5 dBm of input power at 1.7 GHz with both E-pHEMT unbiased. The use of a different frequency for WPT is to avoid the large deviations of the impedance at the input of the rectifier.

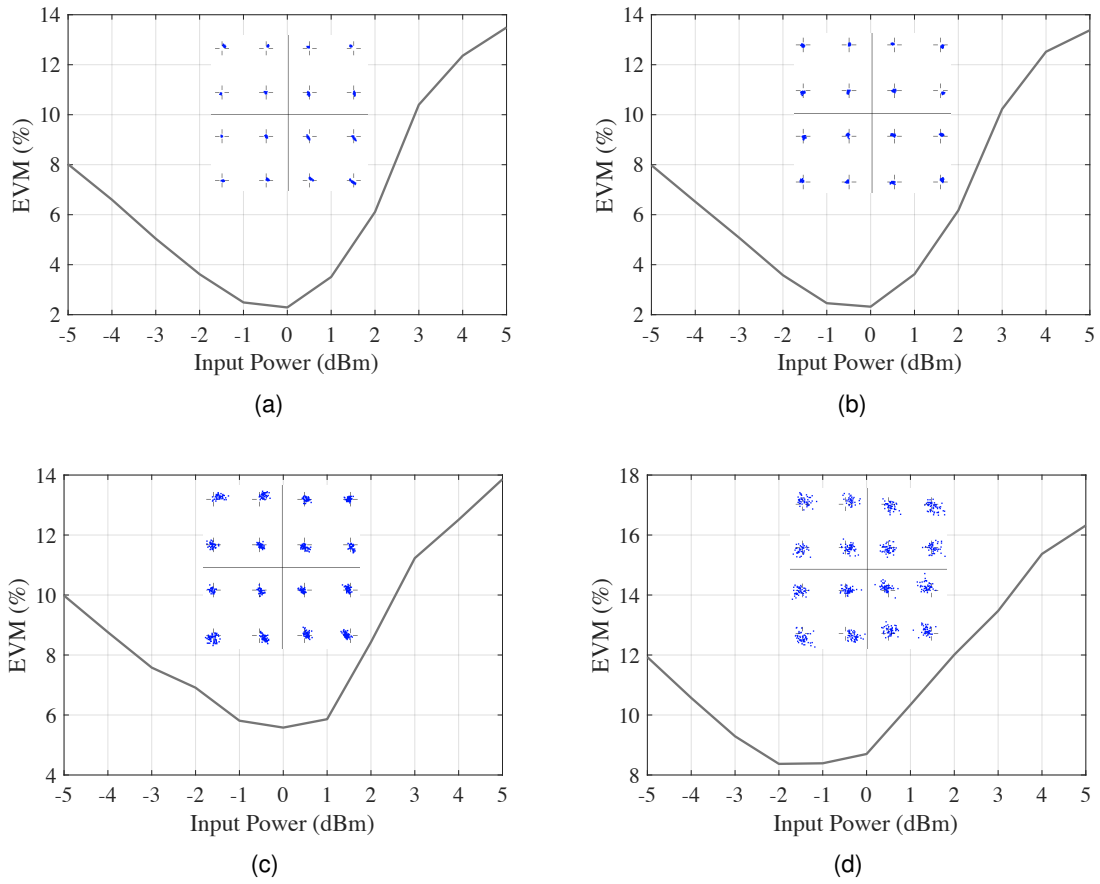

Figure 5.43: Received constellations with EVM and energy per bit consumption as function of input power for different data rates. (a) 4 Mb/s. (b) 100 Mb/s. (c) 480 Mb/s. (d) 960 Mb/s.

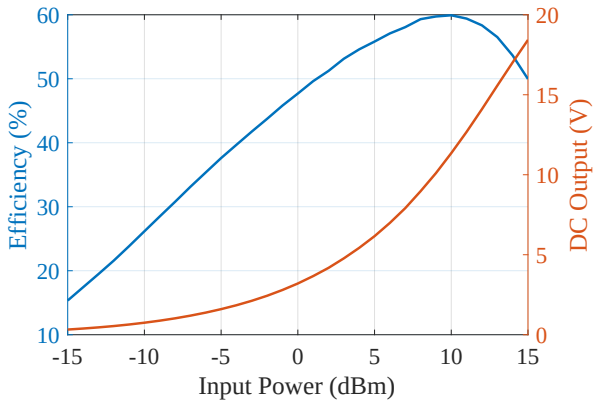

Figure 5.44: DC output voltage and efficiency as function of input power at 1.7 GHz with unbiased gate of each E-pHEMT.

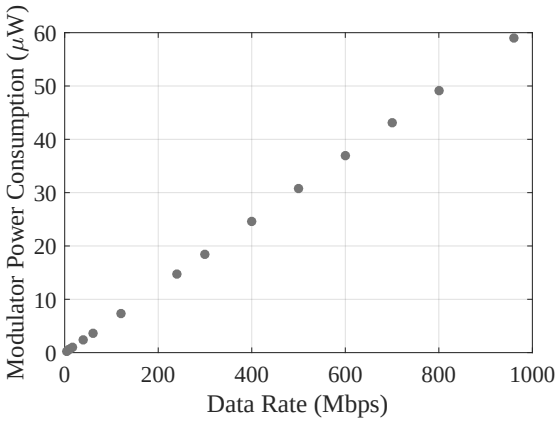

Figure 5.45: DC power consumption of the 16-QAM backscatter modulator over a range of data rates.

Figure 5.43(d) shows an EVM of 8.37% corresponding to 59 uW of energy consumption for a data rate of 960 Mb/s. The EVM can decrease to 2.29% for a data rate of 4 Mb/s with a consumption of 0.25 uW, as can be seen in Fig. 5.43(a). Since the circuit was optimized for an input power of 0 dBm, the levels of voltage were obtained with the same amount of power at the input of circuit. The EVM could be improved for lower values of input power with different levels of voltage.

The DC power consumption of the modulator was characterized, by including only the power required for each E-pHEMT. As the data rate increases, DC consumption increases following $\frac{1}{2}CV^2f$. The measured capacitance at the gate of each E-pHEMT is 1.98 pF and the voltage levels used for each transistor vary from 0 V to 0.6 V, so we calculated an average value of all transitions that perform the 16-QAM, which is 0.35 V. Figure 5.45 presents the DC power consumption of the 16-QAM modulator over a range of data rates.

In section 5.1, 160 Mb/s of data rate with an EVM of 17.8% was achieved, but in this work we improved the data rate, the EVM and decreased the energy per bit consumption. This improvement was possible by using an equalizer in the receiver (signal & spectrum analyzer) and by determining with more precision the levels of voltage to apply in each E-pHEMT, using controlled gate voltages and a VNA for optimization of the ideal impedance matching. Due to these reasons, the data rate had an increase of 6 times higher than in [22].

5.5 High Order Backscatter Modulation for IoT Applications: Channel Evaluation and Implementation

The backscatter modulation has an important role in the IoT, since they use it for transfer information, with a low cost, in terms of energy consumption. Moreover, these devices are

being combined with WPT scenarios, in order to overcome the large number of batteries. With the recent development of backscatter systems for high bit rate communications, the design of calibrated measurement system capable of characterize and calculate the optimum points for M-QAM modulations, is very important. The main objective of this work is to present a channel evaluation of high order backscatter modulators, using over the air calibrated characterization measurement system to evaluate backscatter modulation systems. With this characterization approach, the capability of 64-QAM backscatter modulation in free-space as well as EVM will be validated and computed.

This work is focused on the characterization of high order modulation backscatter systems using a LabVIEW application capable of extracting the optimum points for M-QAM modulations schemes. With this characterization, passive sensors with high order backscatter communication that meet certain EVM restrictions can be evaluated and this modulation scheme can be adapted into the systems referred previously, that take advantage on ambient signals.

5.5.1 Circuits description

The circuits that will be characterized can be seen in Fig. 5.46 and Fig. 5.47 and were explained in 5.4 and 5.2, respectively. The circuit in Fig. 5.46 (circuit 1), as it was stated previously, is composed by by a Wilkinson power divider with two branches, with 45°shift with each other. Each branch is terminated with a transistor, which will change the impedance of the antenna by varying the gate voltage. A five-stage Dickson multiplier block is also presented in the circuit. The modulator presented in Fig. 5.47 (circuit 2) was previously explained in 5.2, designed to work at two different frequencies, 900 MHz and 2.45 GHz and is composed by a dual band Wilkinson power divider.

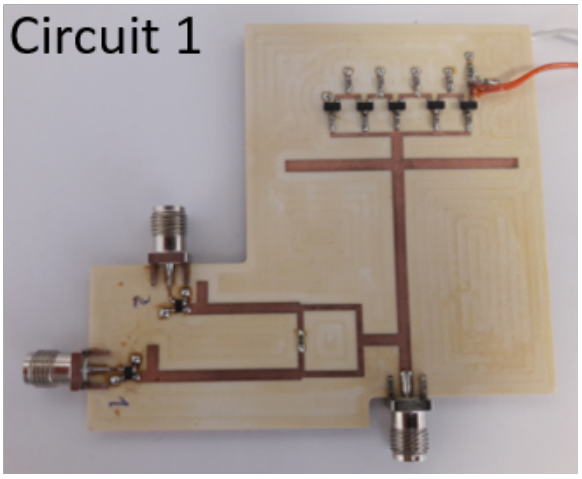

Figure 5.46: Backscatter modulator working at 2.45 GHz (circuit 1).

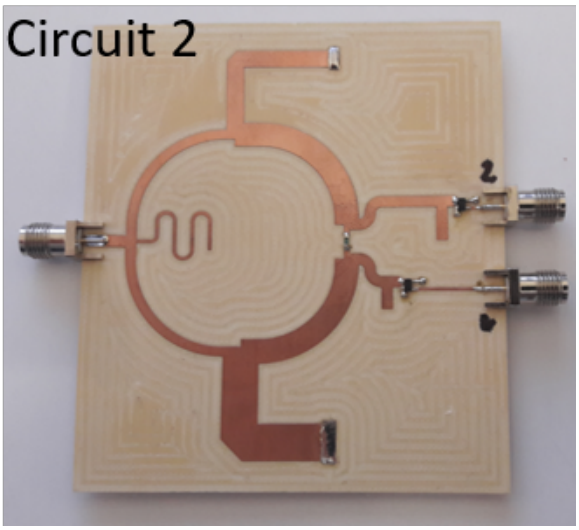

Figure 5.47: Dual band backscatter modulator working at 900 MHz and 2.45 GHz (circuit 2).

5.5.2 Setup Analysis and Description

To measure backscatter modulation circuits, the S_{11} is one of the most important parameter. Due to this fact, a characterization measurement system was built in order to characterize backscatter modulation circuits, to extract the optimum point for M-QAM modulations, in two distinct scenarios: cable test measurement (Fig. 5.48 and Fig. 5.49) and OTA measurement (Fig. 5.50 and Fig. 5.51). For both measurement scenarios, the measurement setup procedure is the same.

In this sense, the measurement setup is performed by sweeping the voltage in the DC ports and then the S_{11} in RF port is measured. The backscatter modulation measurement system is composed by a transmitter (NI 5793), to generate the RF signal, two receivers (NI 5792), to read the incident (a_1) and reflected (b_1) power waves and two power supplies (NI 4138 and NI 4112), to generate the DC voltages. These devices are controlled by PCI eXtensions for Instrumentations (PXI) (PXIe-1085). In addition, the system requires two external couplers (CBR16-006) to obtain a_1 and b_1 power waves, which are connected to the receivers. The block diagrams of the measurement system for the two measurement scenarios are presented in Fig 5.48 and Fig 5.50.

The device under test (DUT), which are the backscatter modulation circuits, are composed by three ports, one RF port, and two DC ports, to switch the transistors gate voltage. To characterize each DUT the transmitter sends a single tone which is a CW with 0 dBm of input power. Then, the transmitter output is connected to the first coupler, where the incident wave (a_1) can be read through the first receiver. From the second coupler the reflected

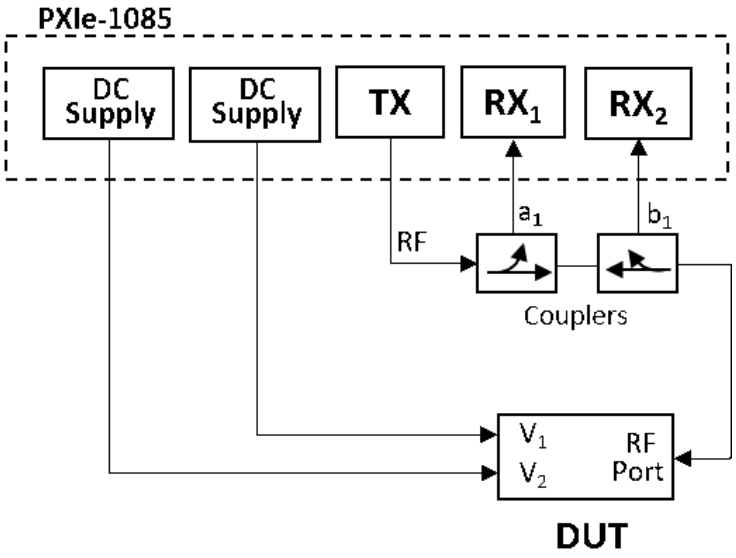

Figure 5.48: Block diagram of cable test backscatter modulation measurement setup.

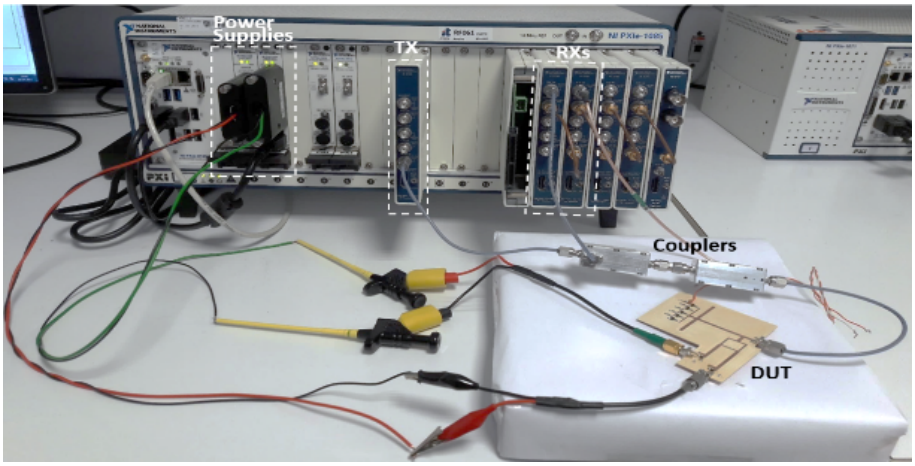

Figure 5.49: Photograph of cable test backscatter modulation measurement setup.

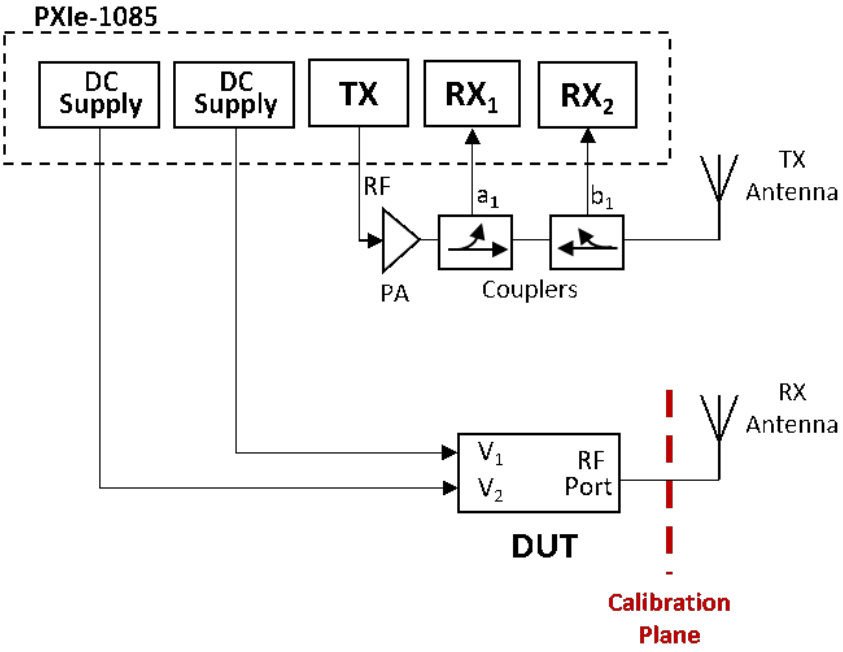

Figure 5.50: Block diagram of OTA backscatter modulation measurement setup with antennas.

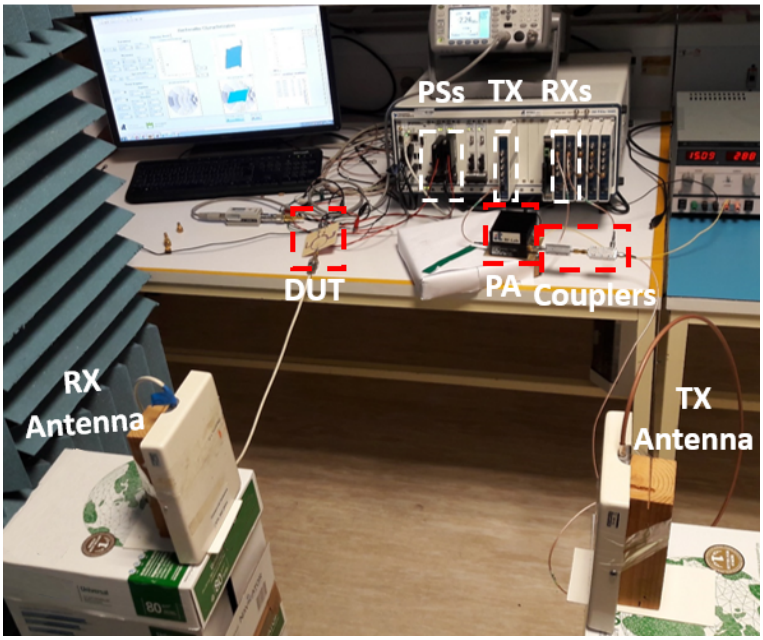

Figure 5.51: Photograph of OTA backscatter modulation measurement setup with antennas.

wave (b_1) can be read through the second receiver. After that, the RF port is connect to DUT RF port. Both power supplies generate the DC voltage and they are connected to the DUT DC ports. Both DC ports are swept from 0.1 V to 0.6 V, with a step of 1 mV. The measurement setup for both measurement scenarios are shown in Fig 5.49 and Fig 5.51.

In the first measurement scenario which correspond to the cable test measurement, the DUT is fully characterized when is directly connected to measurement system. In the second measurement scenario which correspond to the OTA measurement, antennas were introduced to evaluate the DUT OTA in a free space, and for this reason a power amplifier was introduced to increase the transmitted power. In this setup, the calibration plane was place between DUT and the receiving antenna, as shown in Fig 5.50. With the calibration plane in this position, it was possible to include the model of the antennas and channel into the characterization. In the next subsection, the measurement system procedure will be explained in detail.

LabVIEW Application

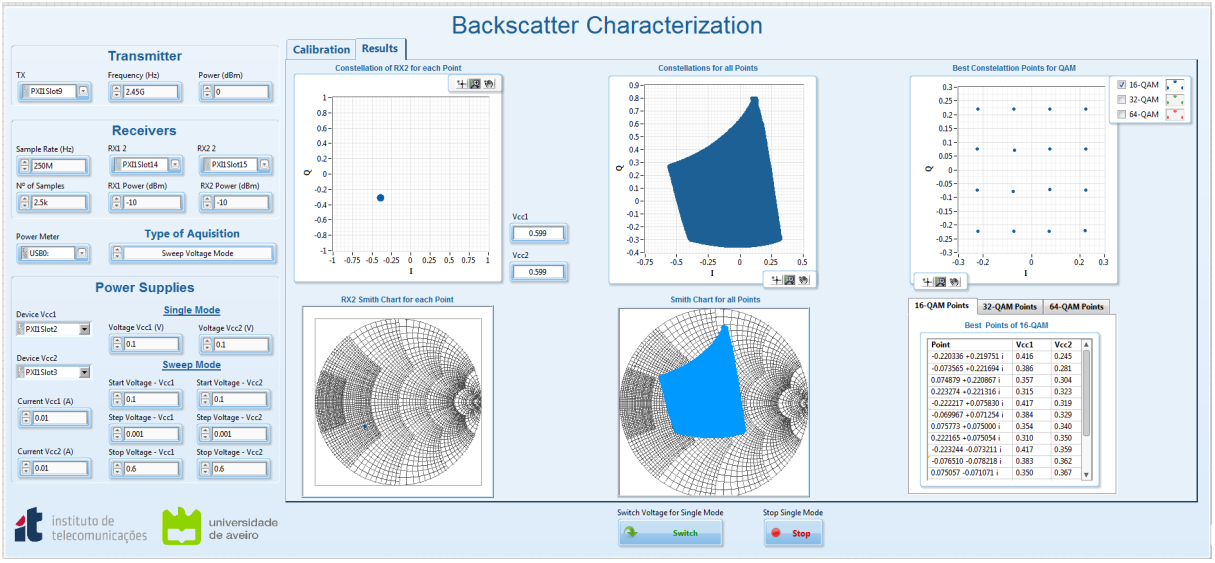

Figure 5.52: LabVIEW application to perform backscatter modulation characterization.

To perform the measurement system, a LabVIEW application was developed in order to control the devices and extract the optimum points for M-QAM constellations, which can be seen in Fig 5.52. The application procedure is illustrated in flowchart of Fig 5.53. First, the voltage values for each DC port are chosen (start, step and stop voltages), as well as the frequency to operate and the power value for transmission. Then, a SOL calibration is applied and saved. Subsequently, when the DC voltages are swept, the constellation points for each

voltage are presented, and the S_{11} is measured. The last application step is to calculate the optimum points to build the M-QAM constellations and the respective voltages for QAM constellations are shown.

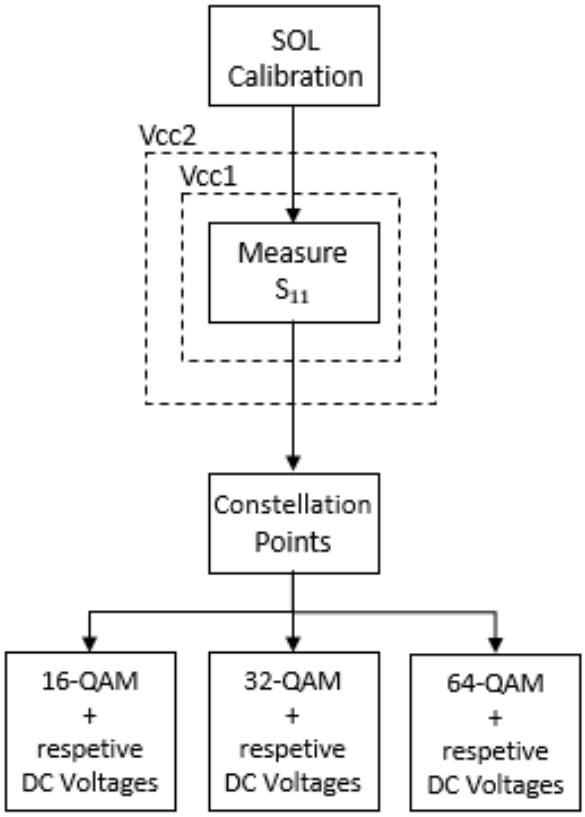

Figure 5.53: Flowchart of LabVIEW application.

Calibration

In this measurement system, it is required to measure the S_{11}, when the backscatter modulator DC ports voltages are switching, which implies to calibrate the RF port. Consequently, a Short, Open and Load (SOL) calibration was used, to calibrate the system and for this purpose, the Agilent 85052D 3.5 mm calibration kit was used. In addition, a power meter (NRP-Z21 from Rohde & Schwarz) to calibrate the power value, in the RF port, was required. After measuring these four terms, the calibration algorithm [179] was applied and the RF port was calibrated.

Algorithm for Constellation Detection

In order to calculate the best points to build a M-QAM constellation, after the transistor gate voltages have been swept, a specific algorithm for this purpose was developed. In Fig. 5.54 (initial constellation graph) an example of the obtained constellation graph with the cable test measurement is shown, using the circuit 1. The figure on the left presents the initial obtained constellation while on the right presents the constellation with some processing to center the square on the graph. For this reason, it is required to calculate the ideal square for M-QAM constellations, in order to find the optimum constellation points for M-QAM modulations. Therefore, the first step in the algorithm is to center the constellation at zero, since the constellation is not centered. To do this, the angle deviation to center the constellation is calculated and then this deviation correction is applied. After that, the constellation points were rotated (Fig. 5.54 constellation centered graph), by calculating the optimum point to rotate the constellation. The final step is to calculate the best optimum points for M-QAM modulation. In this part, the minimum value obtained in each constellation quadrant is calculated to have a valid constellation, which will serve as a reference for the other quadrants. Thus, the M-QAM modulation is achieved.

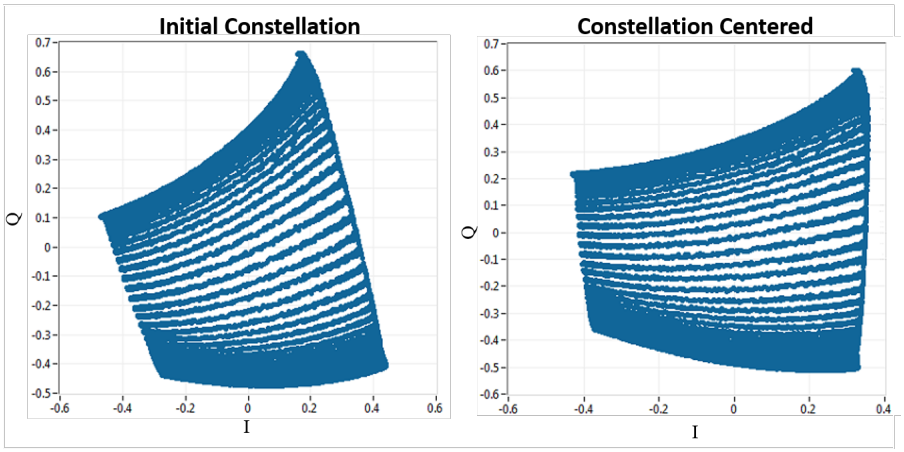

Figure 5.54: Algorithm process example to detect M-QAM points, where initial and centered constellations are presented, from backscatter modulator (circuit 1).

5.5.3 Measurements and Results

This backscatter modulation characterization platform is capable of extracting the 16-QAM, 32-QAM and 64-QAM constellation points. The corresponding voltage values for each constellation point is then obtained and can be saved in the sensor look up table. In this sense, in order to demonstrate the flexibility of the system, two different backscatter circuits were characterized. To validate the results, the EVM was calculated for each QAM

modulation, by using the following equation:

$$EVM(\%) = \sqrt{\frac{P_{error}}{P_{reference}}} \times 100 \tag{5.11}$$

where P_error is the error vector power and $P_{reference}$ is the ideal reference vector power.

Backscatter modulator (circuit 1) characterization

The backscatter modulator (circuit 1) presented in Fig. 5.46, which operates at 2.45 GHz, was characterized using a cable test measurement scenario (Fig. 5.48 and Fig. 5.49). As can be seen in Fig. 5.55, a 16-QAM, 32-QAM and 64-QAM constellation were obtained, for a power value of 0 dBm. For each point of the 16-QAM constellation corresponds two DC values, which are shown in Table 5.5.

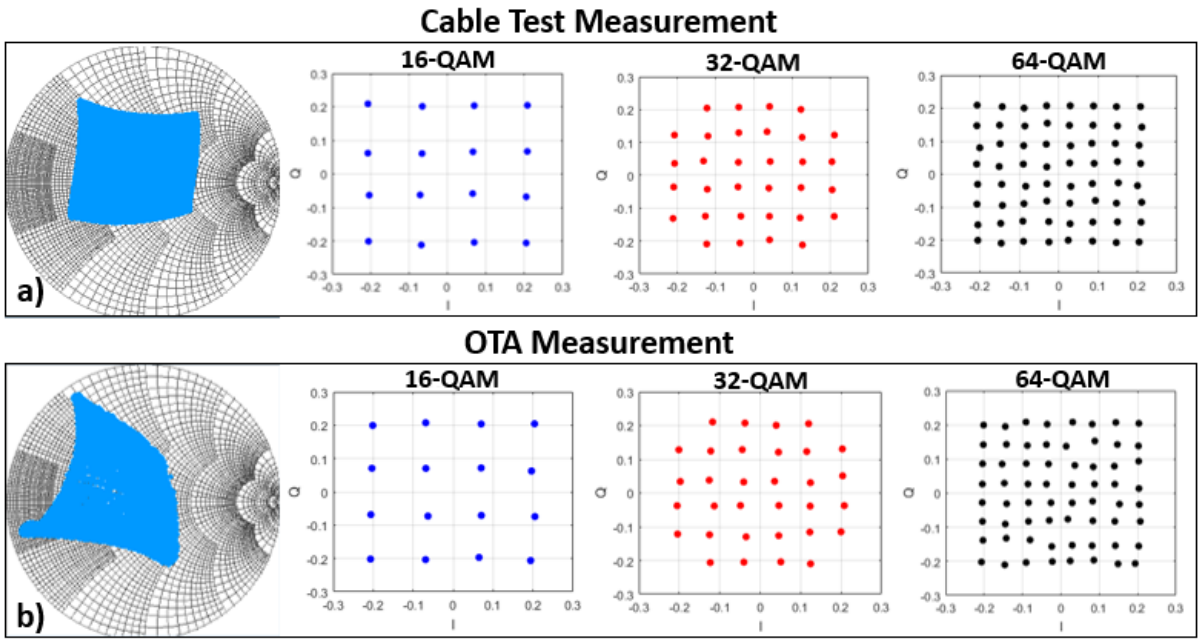

Figure 5.55: Cable test and OTA measurement results using circuit 2.

Analyzing the constellation figures from Fig. 5.56, the EVM results are very similar for each QAM modulation. It is also important to measure the performance of the backscatter circuits for different power values, in order to evaluate their behavior with low input power. For this reason, the backscatter modulator (circuit 1) was characterized for several power values. Table 5.6 shows the EVM results for different power values. It can be seen that the EVM result is getting worse, when power values decrease, as expected, since the circuit was

Table 5.5: Optimum points and voltages for backscatter modulator (circuit 1) for a 16-QAM modulation considering cable test measurement.

Point	Vcc1 (V)	Vcc2 (V)	Point	Vcc1 (V)	Vcc2 (V)
-0.220 + 0.220 i	0.416	0.245	-0.223 + 0.073 i	0.417	0.359
-0.074 + 0.222 i	0.386	0.281	-0.076 - 0.078 i	0.383	0.362
0.075 +0.222 i	0.357	0.304	0.075 - 0.071 i	0.350	0.367
0.223 + 0.221 i	0.315	0.323	0.224 - 0.074 i	0.302	0.374
-0.222 + 0.076 i	0.417	0.319	-0.222 - 0.223 i	0.415	0.395
-0.070 + 0.070 i	0.384	0.329	-0.072 - 0.223 i	0.378	0.304
0.076 + 0.075 i	0.354	0.340	0.073 - 0.224 i	0.344	0.397
0.222 + 0.075 i	0.310	0.350	0.221 - 0.220 i	0.296	0.399

optimized for 0 dBm.

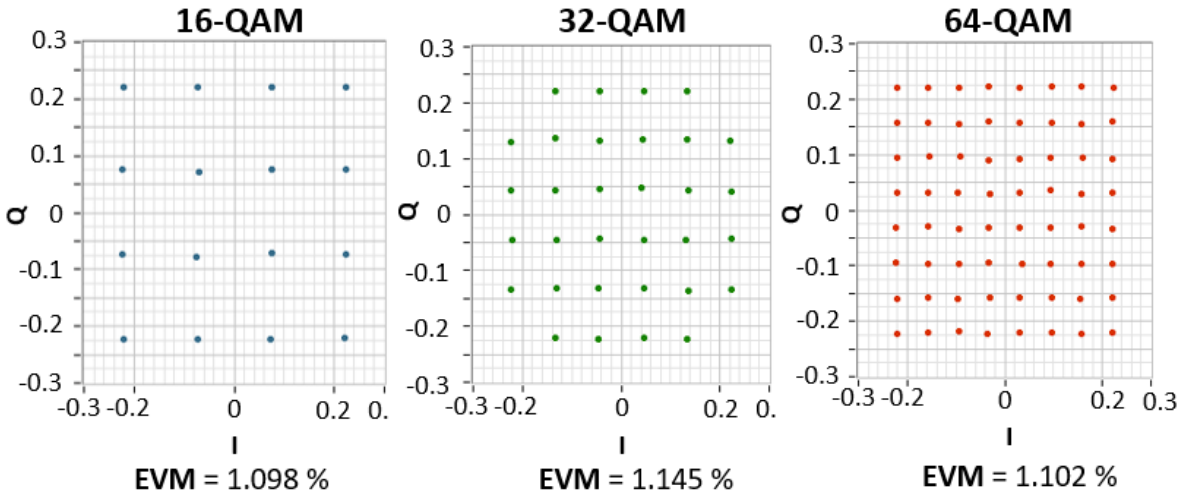

Figure 5.56: 16-QAM, 32-QAM and 64-QAM constellation for backscatter modulator (circuit 1), with corresponding EVM values.

Backscatter modulator (circuit 2) characterization

The backscatter modulator (circuit 2) presented in Fig 5.47 was characterized in the two scenarios, cable test and OTA measurements. This circuit operates in two frequencies, 900 MHz and 2.45 GHz, and it was characterized for different power values at both frequencies, to evaluate the modulation performance. The EVM results at both frequencies, considering a cable test measurement scenario, can be seen in Table 5.7. With this dual band M-QAM backscatter circuit it was possible to demodulate the signal with -40 dBm of input power,

Table 5.6: EVM results from backscatter modulator (circuit 1) for several power values at the input considering a cable test measurement.

Circuit 1 at 2.45 GHz				
Power (dBm)	0	-10	-20	-30
EVM (%) 16-QAM	1.09	1.89	1.80	1.93
EVM (%) 32-QAM	1.15	1.97	1.96	2.70
EVM (%) 64-QAM	1.10	2.12	2.01	2.30

Table 5.7: EVM results from backscatter modulator (circuit 2) for several power values at the input considering a cable test measurement.

Power (dBm)		0	-10	-20	-30	-40
EVM (%) 16-QAM	900 MHz	1.05	1.92	2.01	2.70	2.07
	2.45 GHz	1.69	1.69	2.62	2.50	2.63
EVM (%) 32-QAM	900 MHz	1.25	2.14	2.55	2.52	2.73
	2.45 GHz	2.04	2.13	3.06	2.95	3.60
EVM (%) 64-QAM	900 MHz	1.28	2.17	2.41	2.53	2.74
	2.45 GHz	1.88	2.25	2.72	3.40	3.35

which proved to be a more sensitive modulator than the first. Moreover, the EVM results at both frequencies increased, while reducing the input power, as it was expected.

To understand the behavior of backscatter circuits in a free space scenario, the OTA measurement was performed. Figure 5.55 presents the behavior of backscatter modulator (circuit 2) at 2.45 GHz, for cable test measurement scenario and OTA measurement scenario. Since the antennas used were not perfectly matched for these two different frequencies, the obtained shape with antennas is slightly different from the shape without antennas. Thereafter, the backscatter modulator (circuit 2) was characterized, at both frequencies, for two different distances between TX and RX antennas. Table 5.8 present the results for these measurements. From the results presented on Table 5.8 it is possible to observe that 16-QAM, 32-QAM and 64-QAM backscatter communication can be performed in free-space at two different frequencies. The EVM values increased with the increase of the distance, as it was expected. Nevertheless, the M-QAM communication can be performed as well.

Table 5.8: EVM results from backscatter modulator (circuit 2) for different distances, considering OTA measurement scenario.

Frequency	**Distance (m)**	**EVM (%) 16-QAM**	**EVM (%) 32-QAM**	**EVM (%) 64-QAM**
900 MHz	0.5	3.37	4.09	4.42
	1	5.42	5.52	5.82
2.45 GHz	0.5	2.50	3.70	3.89
	1	5.26	5.62	5.81

5.6 Conclusions

- In this chapter, new approaches for higher order modulation backscatter passive radio solutions were presented. It was described a modulation technique that enables a high-bandwidth wireless communication while requiring very low power demands. The solution that comprises the Wilkinson power divider and the two transistors is actually to our knowledge the one that achieves higher bit rate with a limited amount of RF power and with a low count of active devices. This solution can be combined with WPT for ultra low-power wireless applications requiring high bandwidth communications such as remote camera sensors or wireless audio.

  This work challenges held assumptions concerning the backscatter link that backscatter communication is limited to low bandwidth and binary modulation solutions.

- Moreover, a 16-QAM modulator with WPT capabilities was presented. The circuit works with two different frequencies, one for the WPT and the other to perform the backscatter communication. The energy consumption per bit of this modulator can be as low as 61.5 fJ for a data rate of 960 Mb/s with an EVM of 8.37%. The system, due to the rectifier block has demonstrated some WPT capabilities with 56% of efficiency for an input power of 5 dBm. With all these features this system is suitable for providing high bandwidth for future low power devices.

- A dual band high order backscatter modulator was presented and experimentally validated and showed promising results for the applications that require two different frequencies for the backscatter communication.

- In this chapter, an ultra low power sensor node/tag with ambient FM backscatter and high order modulation capabilities was also demonstrated. The tag can read up to four sensors and modulate the information using 4-PAM modulation instead of the binary 2-PAM. The transmitted bit rate is duplicated and the tag uses the ambient FM signals in order to send the data to a reader. This high order modulation approach is the first demonstration of backscatter 4-PAM modulation on ambient FM signals. It also paves the way for practical deployments for short range, ultra-low-power backscatter sensors such as wearable body area-sensors.

- A backscatter characterization system that gives an overview about the behavior of the backscatter modulators was presented. With this calibration system through a LabVIEW application, it is possible to get the optimum points to find multiples M-QAM modulations. In addition, the performance for different power values in each backscatter circuit was measured to evaluate the behavior of the circuits for different input powers with low values. Two different test scenarios were considered, proving the importance of free space to test IoT devices performance. Finally, this calibration

system demonstrated the possibility of performing high order backscatter communication in free-space for two different frequencies. With this calibration, it will be possible to implement different modulations orders depending only in the different voltages applied to the transistors, which means that high data speed low power sensors will be possible to implement for IoT applications.

Chapter 6

MMIC QAM modulator

Outline

This chapter provides a description of the implementation and plans for an initial characterization of a single-chip QAM backscatter modulator designed for 24 GHz. Results presented here will aid in shaping future design of backscatter systems. The chip is designed to be a customizable integrated backscatter communication. The simulations and layout design will be provided in this chapter as well as the plans for the characterization of the chip. The plans include the measurements of reflection coefficients over varying frequencies and incident RF power levels.

The design developed was based on 0.13 μm SiGe technology from Innovations for High Performance Microelectronics (IHP), from Germany. This technology consists in a high performance BiCMOS with npn-HBTs up to $f_T/f_{max} = 250/340$ GHz, with 3.3 V I/O CMOS and 1.2 V logic CMOS.

Along this chapter, the active devices and the passive components used in the QAM backscatter design will be studied using Virtuoso software, developed by Cadence Design System. Due to high working frequency there is a need to study all components through electromagnetic simulations. This will be done by using Momentum, which is part of ADS software, developed by Agilent Technologies.

6.1 Overview and description of the QAM modulator

As it has been proved along this thesis, backscatter radio have been increasingly used as a low power and low cost implementation of wireless communication, which can contribute with high impact to the sensor networks. Nonetheless, most of backscatter modulators are designed up to 2.45 GHz mainly due to the low transmission line and active components losses. In this chapter a QAM modulator will be designed for a frequency of 24 GHz. In this frequency it is possible to design reduced antennas, contrary to UHF bands, which enables

the integration with wearables for mobile health, sensing, security and the most important short-range ultra high-speed data transmission between mobiles or mobile to a fixed station (kiosk containing files, videos, etc..), as it can be seen in Fig. 6.1.

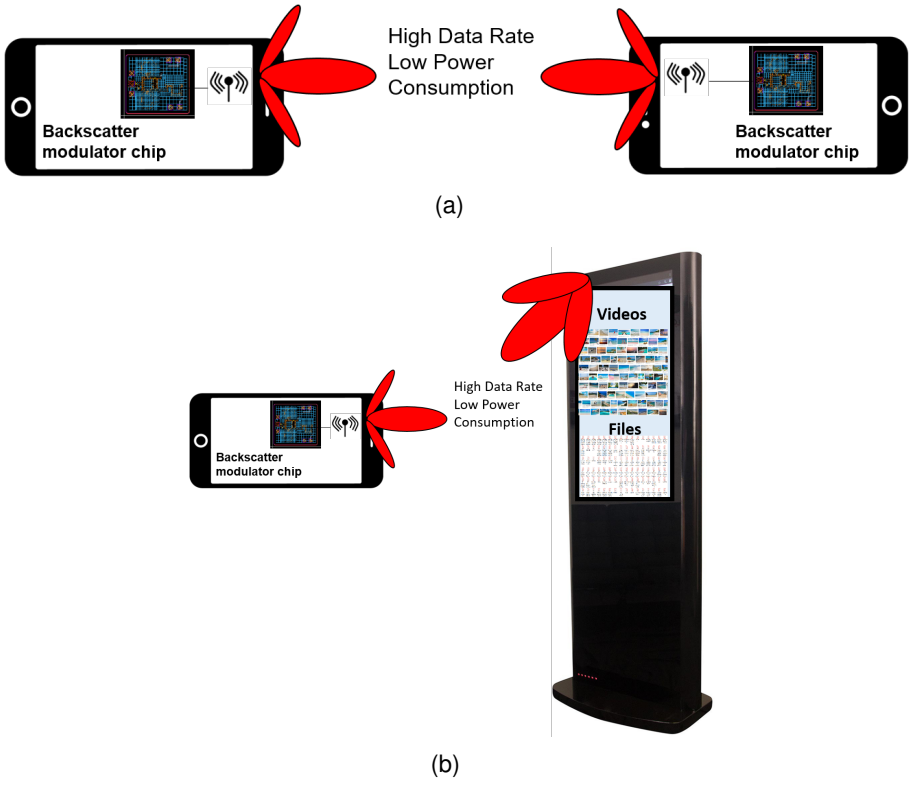

Figure 6.1: Application example for the MMIC QAM backscatter modulation.

6.2 Simulations and design of the QAM modulator

The high frequency QAM modulator designed, followed the same approach explained in chapter 5, composed by a Wilkinson power divider and two branches, each connected to a RF nmos transistor. The lines present a 45°phase shift respect to each other, so as to allow that the reflected wave from each branch has 90°phase difference from the other.

The first steps of this design consisted in determining the number of gates, width and length of the transistor. Thus, it was necessary to determine the drain transistor's impedance at 24 GHz for different gate voltages (from 0 V to 1 V with a step of 0.1 V) and for different number of gates, width and length. Figure 6.2 shows different configurations of the transistor at 24 GHz with -10 dBm of input power. For the design of the modulator, the most appropriate configuration gives respect to a number of gates of 10, 100μm of width and 130 nm of length, since the objective was to select the configuration that presented the greatest variation of drain impedance. Figure 6.3 presents the layout of the transistor selected.

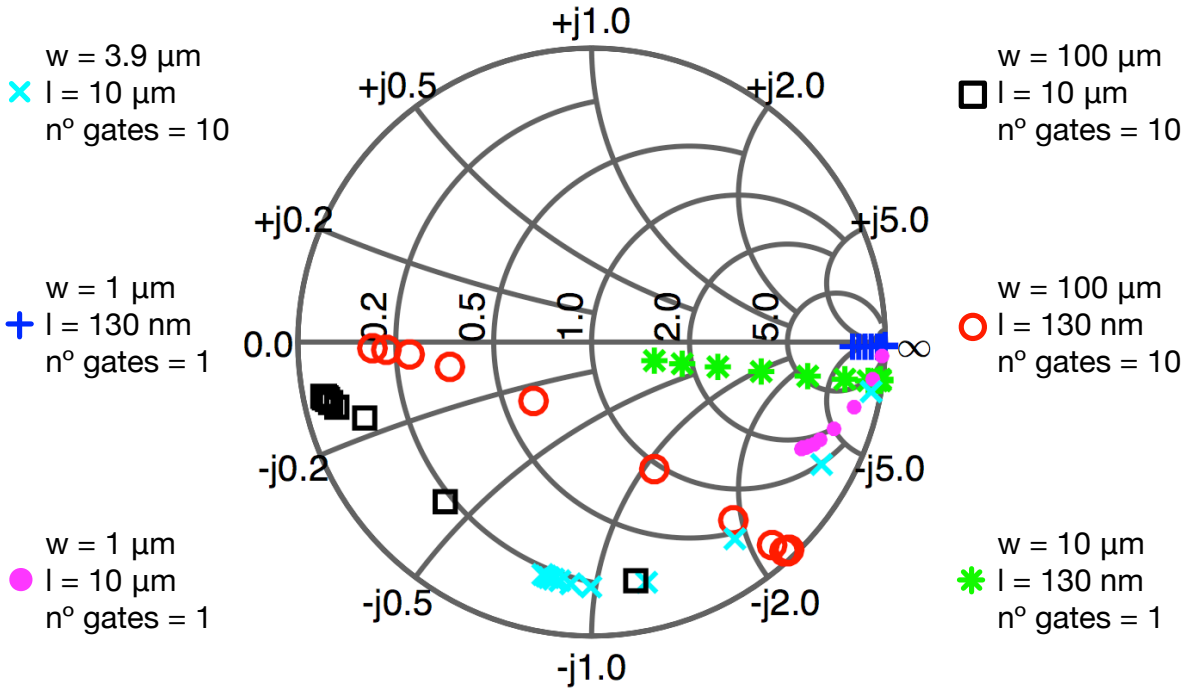

Figure 6.2: Different drain impedance of the transistor as function of width, length and number of gates.

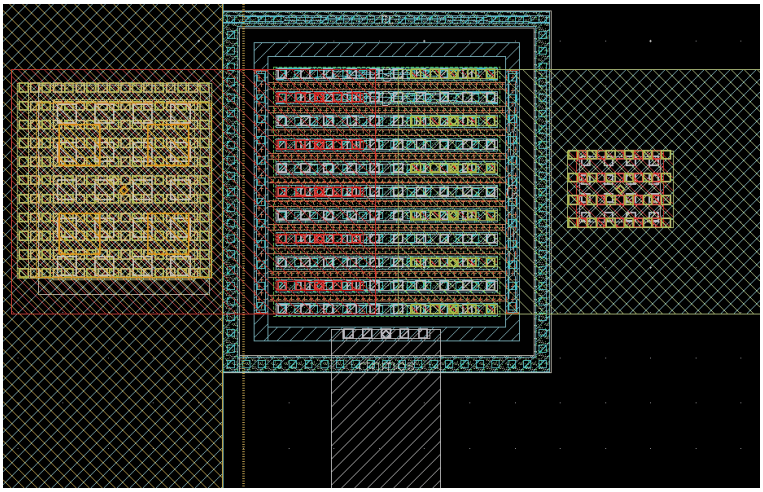

Figure 6.3: Layout of the selected transistor. The transistor presents 10 gates, 100μm of width and 130 nm of length.

After selecting the transistor, the next step consisted in designing the schematic of the QAM modulator using the design kit from IHP. Figure 6.4 presents the schematic of a QAM modulator at 24 GHz. The simulations presented in Fig. 6.5 show the behavior of the modulator at 24 GHz, with -10 dBm of input power and variations at the gate of each transistor from 0 V to 1 V with a step of 0.01 V.

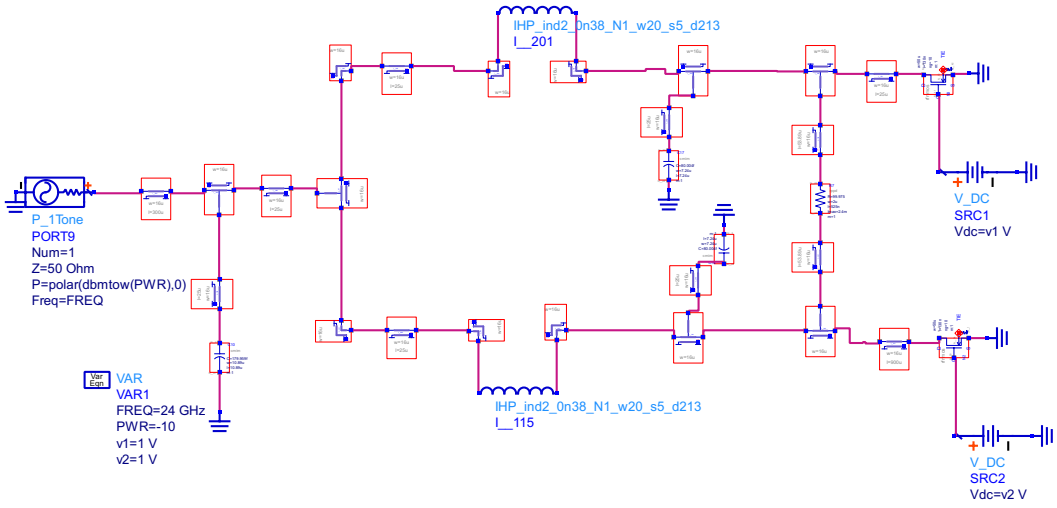

Figure 6.4: Schematic of the QAM modulator optimized for a frequency of 24 GHz.

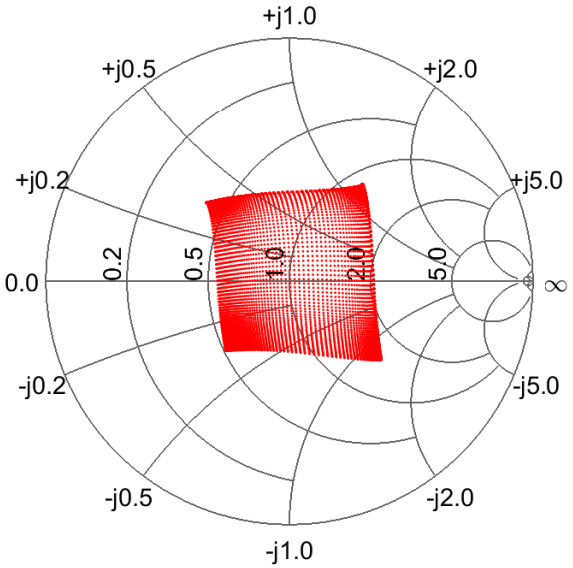

Figure 6.5: Simulated S_{11} parameter with -10 dBm of input power and variations at the gate of each transistor from 0 V to 1 V with a step of 0.01 V.

Subsequently to this step, it was necessary to validate this solution with electromagnetic simulations by using momentum. The differences observed from the schematic to the electromagnetic simulator were large, so we had to simulate each passive component to achieve the desired result. From Fig. 6.6 one can see the layout of the inductor used and through equations 6.1 and 6.2 we obtained the value of the inductor as well as the Q factor of the inductor, Fig. 6.7. As it can be seen, the selected value of the inductor in the layout was 0.3 nH and from the electromagnetic simulations the value decreased to 0.18 nH at 24 GHz with the mesh of metal 1 (ground plane).

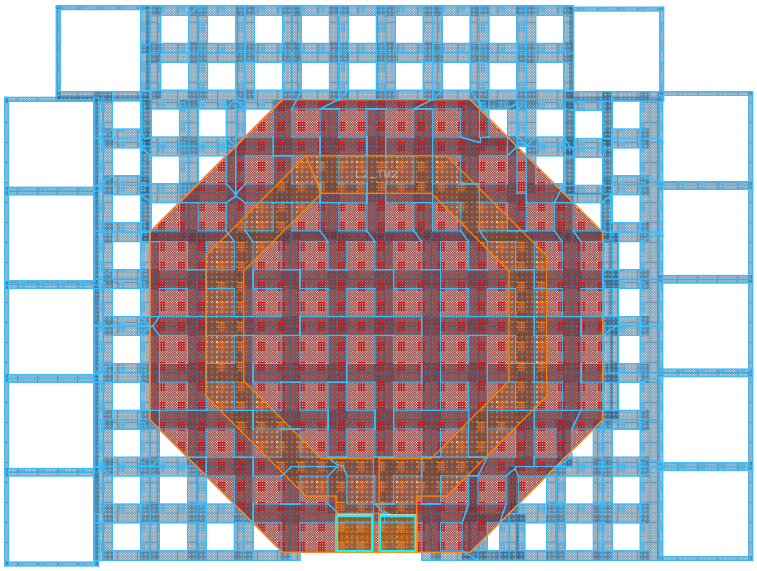

Figure 6.6: Inductor layout simulation.

$$L_S = -\frac{1}{\omega} Imag(\frac{1}{Y_{21}}), \tag{6.1}$$

$$Q = \frac{2Imag(S_{11})}{1 - |S_{11}|^2 - |S_{21}|^2}, \tag{6.2}$$

To design the modulator, all these deviations were taken into account and after some electromagnetic simulations the final layout is shown in Fig. 6.8.

We performed some validations of the layout, one with different input powers (from -40 dBm to 10 dBm with a step of 1 dBm) at 24 GHz, to understand the behavior of modulator, Fig. 6.9. After this validation, it was necessary to understand the capability of this modulator in increasing the modulation order. In Fig. 6.10 we present the impedances of the modulator while biasing the gate of each transistor with voltages from 0 V to 1 V with a step of 0.01 V. In Fig. 6.11 it is shown the behavior of the modulator at different frequencies (from 20 GHz to 30 GHz).

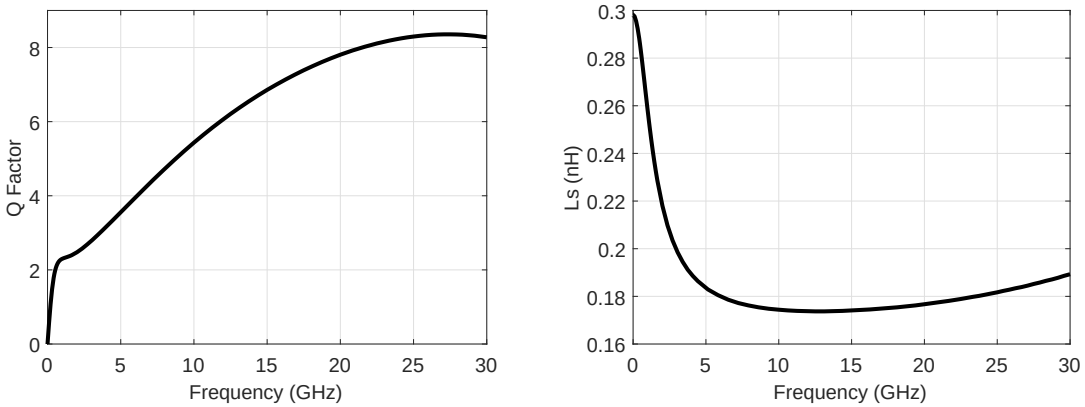

Figure 6.7: Inductor layout simulated results. a) Q factor obtained. b) Inductor value obtained.

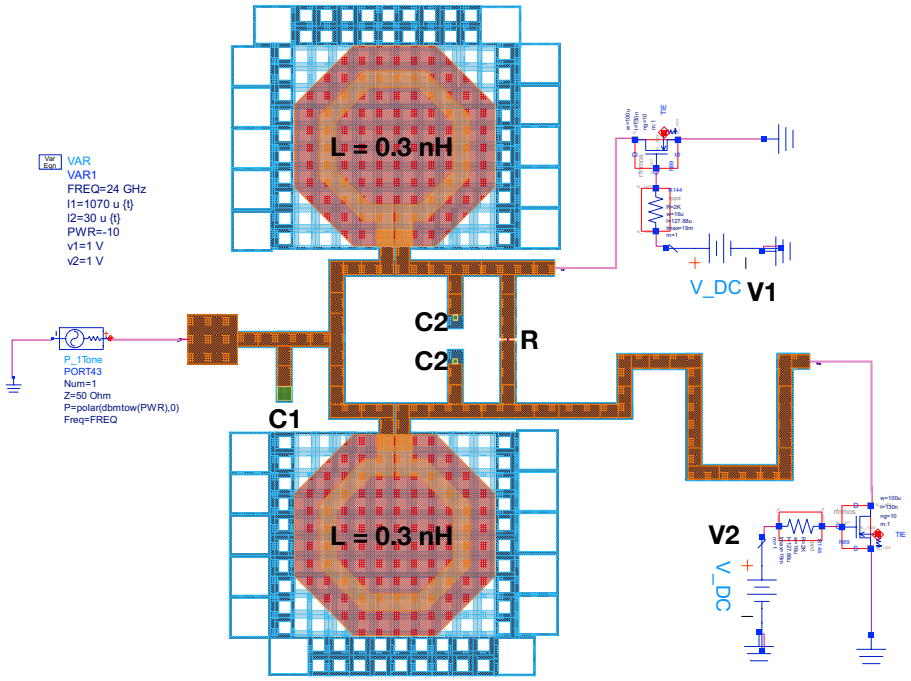

Figure 6.8: MMIC QAM layout modulator designed in ADS. The element values are: C1 = 385.117 fF, C2 = 30.012 fF, R = 100 Ohm.

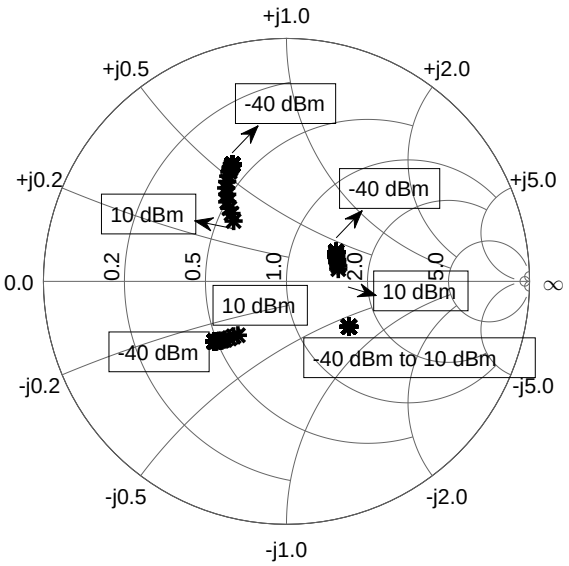

Figure 6.9: Simulated MMIC QAM layout modulator. The simulation was performed in ADS at 24 GHz from -40 dBm to 10 dBm of input power with a step of 1 dBm.

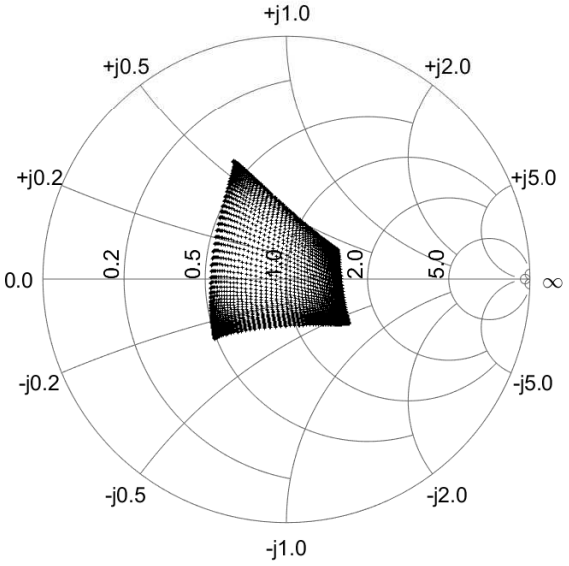

Figure 6.10: Simulated MMIC QAM layout modulator. The simulation was performed in ADS at 24 GHz with -10 dBm of input power and varying each gate of transistor from 0 V to 1 V with a step of 0.01 V.

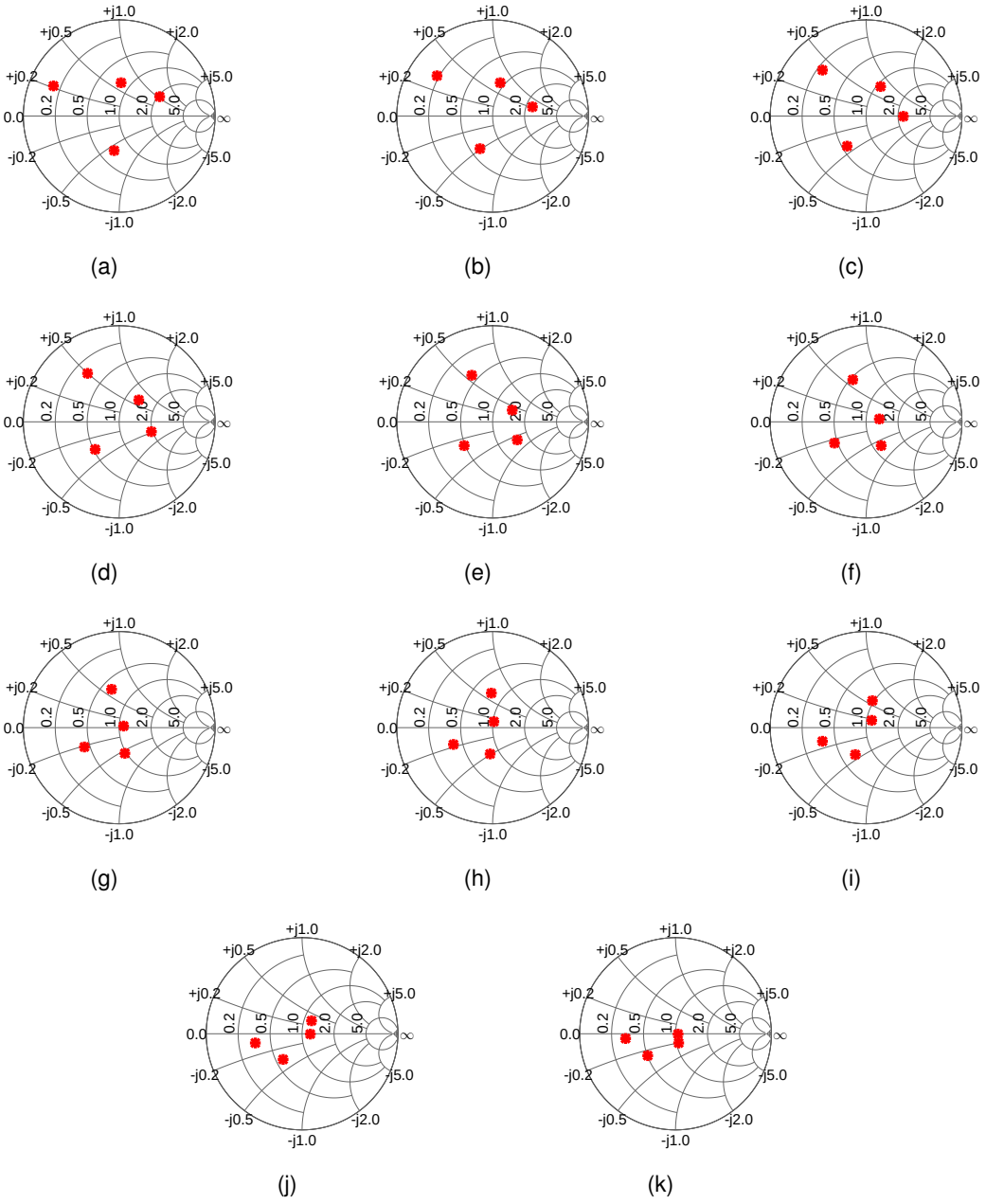

Figure 6.11: MMIC QAM layout behavior modulator with -10 dBm of input power for different frequencies, from 20 GHz to 30 GHz. a) 20 GHz. b) 21 GHz. c) 22 GHz. d) 23 GHz. e) 24 GHz. f) 25 GHz. g) 26 GHz. h) 27 GHz. i) 28 GHz. j) 29 GHz. k) 30 GHz.

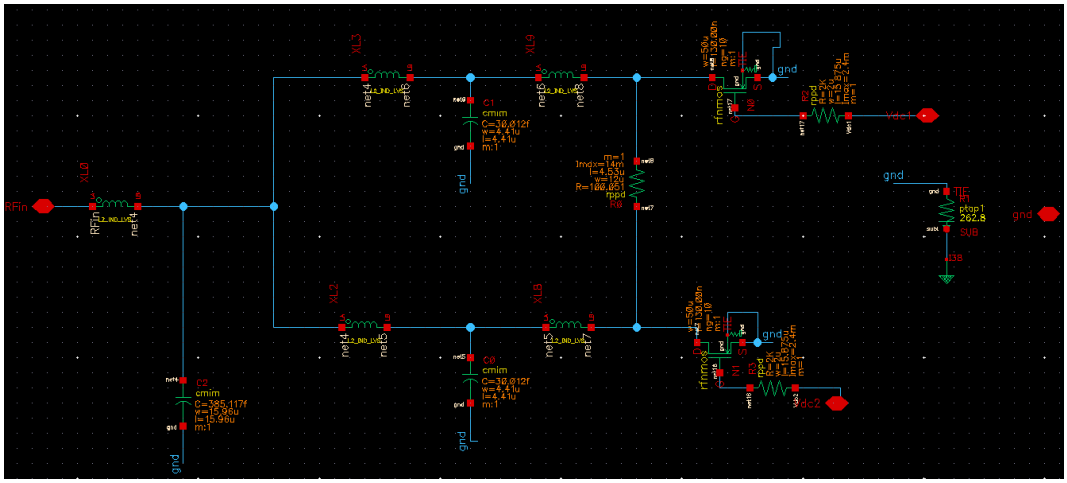

Figure 6.12: Scheme of the QAM modulator designed with Virtuoso.

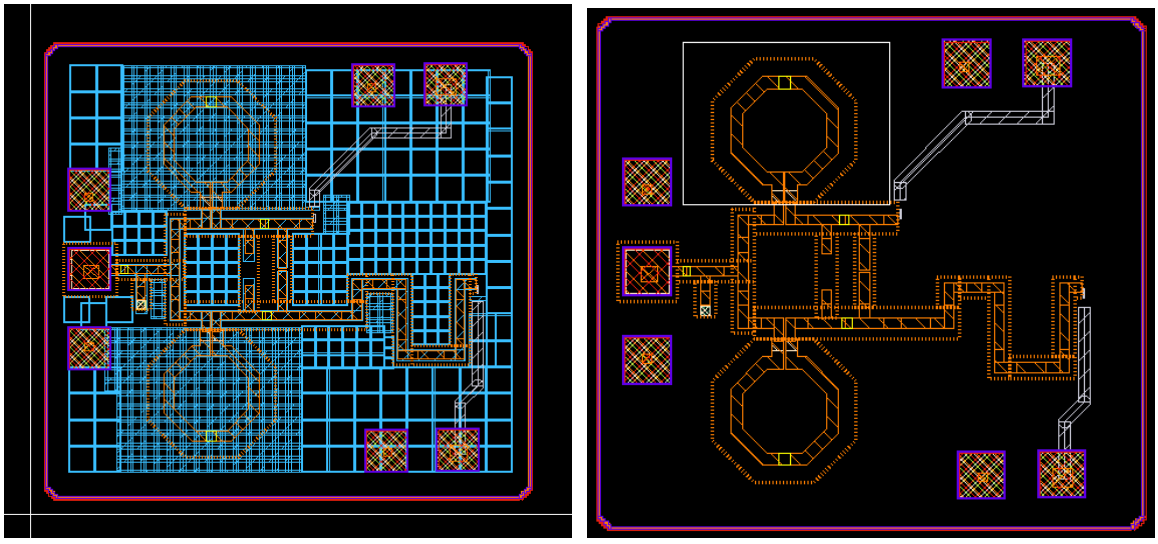

(a) (b)

Figure 6.13: Layout of the modulator designed with Vituoso. (a) Layout complete with ground plane. (b) Layout without ground plane

After the validation of the schematic and layout in ADS, it was necessary to use the Virtuoso to design the schematic and layout to perform the physical verification of the chip. Figure 6.12 presents the schematic and in Fig. 6.13 the final layout with and without ground. We used Design Rule Check (DRC) to check if the layout passes through the rules designed for faultless and then the Layout Versus Schematic (LVS) to compare the connectivities of our layout with that of the schematic. Subsequently to these verifications, it was necessary to generate metal fills for the density rules, so a DRC fill was necessary. Finally, another DRC with all metals filled was necessary to conclude the chip.

6.3 Plans for the experimental measurement setup

The measurements that will be realized consist in two different setups. The first, presented in Fig. 6.14 is composed by PNA, a power supply and the probe station (Cascade Microtech 9000). The main objective of this measurement will rely on the evaluation of the chip S-Parameter. Each gate of the transistor will be biased from 0 V to 1 V and the respective impedances of the modulator will be measured with the PNA over varying input frequency and RF power levels.

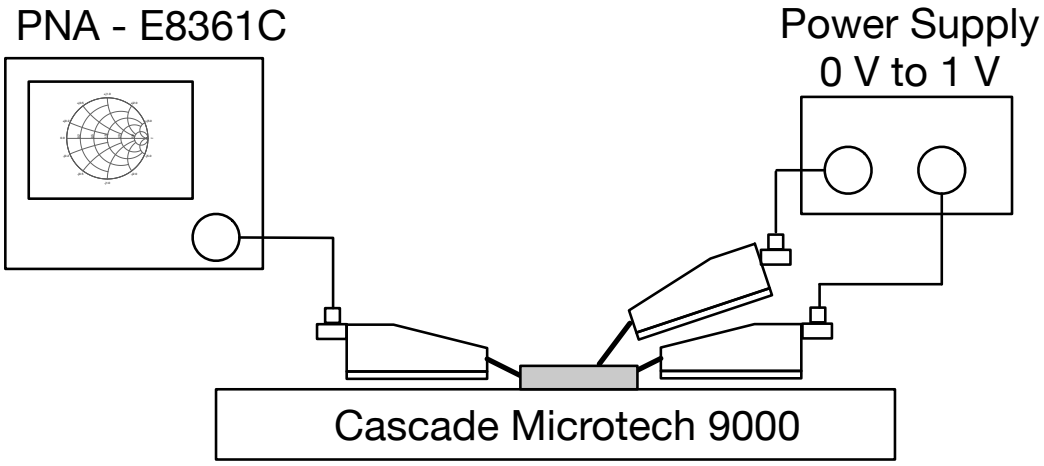

Figure 6.14: MMIC QAM modulator measurement setup for S_{11} parameter analysis.

The second setup, presented in Fig. 6.15, will evaluate the modulator in terms of data rate and different order of modulation. The setup is composed by a signal generator that will generate a CW at 24 GHz, a coupler to acquire the reflected wave from the chip that will be analyzed in the spectrum analyzer. An arbitrary waveform generator will be used to bias the gate of each transistor with different data rates. With this setup it will be possible to determine the maximum modulation order as well as the data rate of the modulator. The outcome of this measurement will be the EVM for different orders of modulation with

respective voltages of each transistor gate.

Finally, an analysis on the power as well as the energy per bit consumption of the chip will be evaluated.

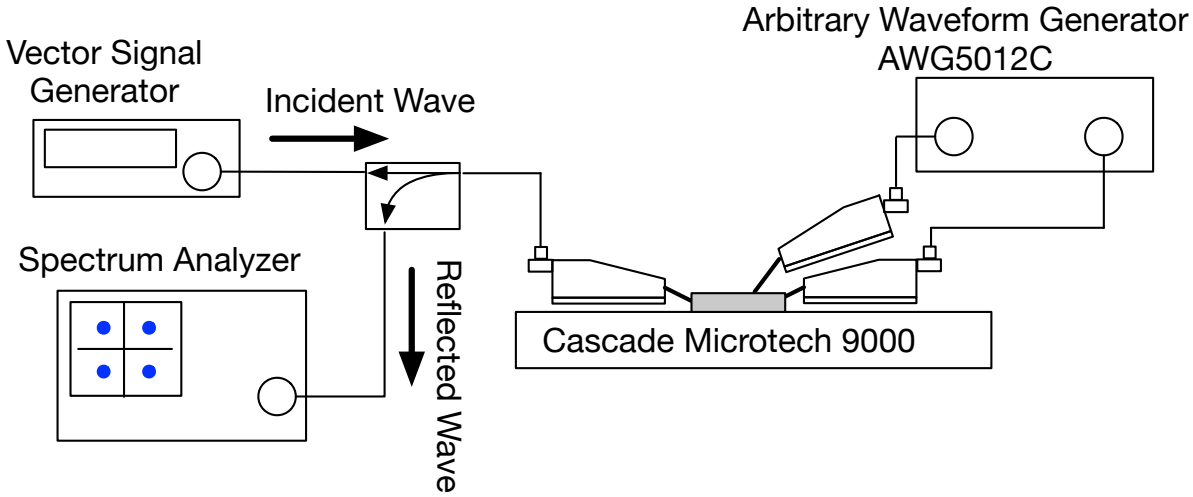

Figure 6.15: MMIC QAM modulator measurement setup for data rate and modulation order evaluation.

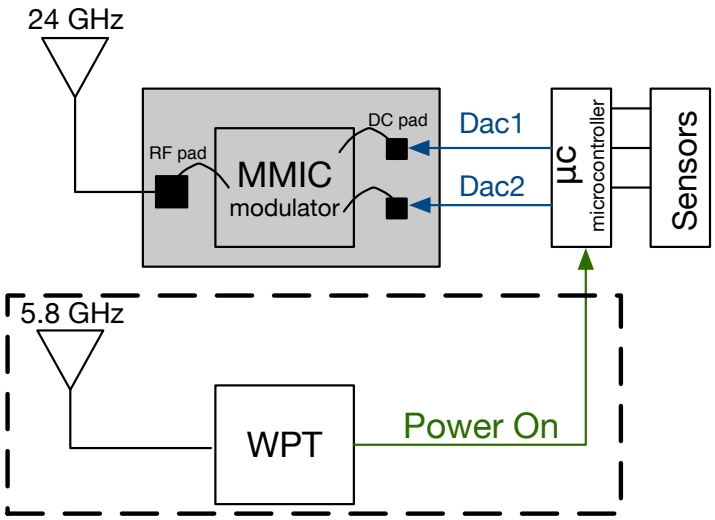

Figure 6.16: MMIC QAM modulator system integration.

Figure 6.16 presents the chip integration with all the blocks that enable a high order backscatter passive sensor. The system is composed by an antenna at 24 GHz, the microcontroller that will generate the voltages for each gate of transistor according to the information

of sensors. The dashed block in the figure presents a possible solution to remove batteries from sensor based on WPT. Solar, vibration or motion could be possible alternative solutions to enable the passive sensor, as it was said previously.

6.4 Conclusions

In this chapter, a single-chip implementation of a QAM backscatter modulator was presented and two plan measurement setups were presented. The performance of the chip will be evaluated through a PNA to model a 50 Ω antenna connected to the modulator input. With spectrum analyzer and AWG, different modulation orders and data rates will be measured.

The implementation of the chip in other existing technologies will be much easier due to its size which will potentiate the use of this technology in most of all IoT applications.

Chapter 7

Conclusions and Future Work

7.1 Conclusions

In recent years, the increasing use of IoT sensors has allowed smart objects to provide major industries with the vital data that they need to track inventory, manage machines, increase efficiency, save costs, and even save lives. In this context, in which billions of connected objects are expected to be placed all over the world, frequent battery maintenance of wireless nodes is undesirable or even impossible. In these scenarios, passive-backscatter radios will play a crucial role due to their low cost, low complexity, and battery-free operation. WPT technology also plays an important role in providing continuous power for these backscatter radios.

This Ph.D. work contributed with several advances in the state of the art that were summarized in this document. This contribution enables a more convenient design of passive backscatter systems.

In this sense, chapter 3 explored the link budgets of the backscatter radio communication and its main concepts. Moreover, a pure BPSK backscatter modulator was designed and measured to prove the technology capabilities and its application on wearable devices.

Chapter 4 reported the first fully passive sensor based on two different frequencies. This sensor enabled a continuous flow of energy by usign a WPT link in one frequency and was capable of backscattering the data in another frequency. This system was experimentally validated in terms of RF-DC converter efficiency, backscatter modulation, distances of communication and power. In addition, a passive solution for a sensor using only one active component was presented and its RF-DC converter efficiency and backscatter modulation was validated.

The chapter 5 presented several relevant approaches for high order backscatter modulation. More precisely, a new design which allows a 64-QAM backscatter modulation was experimentally validated in terms of most important figures of merit, such as EVM, achievable data rate and power consumption. Moreover, this design was improved and combined

with WPT, which presented the highest data rate value in high order backscatter modulation systems, with a very low power consumption. Furthermore, a novel wireless tag that uses 4-PAM technique to modulate ambient backscatter FM signals was shown and validated in an indoor and outdoor environment. The results proved the system viability by using the backscatter technique. Additionally, a new design for dual band high order backscatter modulation was demonstrated with very promising results in terms of power consumption and achievable data rates.

Since the overall objective of this Ph.D. is the exploration and development of passive backscatter sensors it is utmost important to minimize their costs and size. For this purpose, in chapter 6 an MMIC QAM backscatter modulator is designed for a frequency of 24 GHz. Along the chapter, a description of the implementation and plans for an initial characterization of the chip were presented. The major importance of this implementation will be the integration of this technology in wearables for mobile health, sensing, security and the most important short-range ultra high-speed data transmission for mobiles.

At last, one can conclude that this Ph.D. work successfully proposed innovative designs and solutions that surpassed the state of the art in the major research topics on the backscatter radio communications.

7.2 Main achievements in the scope of this thesis

- Finalist of the student paper competition of the IEEE - International Microwave Symposium (IMS 2018).
- First place of the Student Design Competition on ”Backscatter Radio” of the IEEE - International Microwave Symposium (IMS 2018).
- First place of the ANACOM-URSI Portugal prize at 10 Congresso do Comité Português da URSI, 2016, Lisboa.
- First place of the Student Poster Competition at 6th Workshop WIPE (Wireless Power Transmission for Sustainable Electronics), 2016, Aveiro.
- Third place of the Student Paper Competition at IEEE WPTC (Wireless Power Transfer Conference), 2015, Boulder.

7.3 Future Work

In the chapter 4 some passive sensors were referred and experimentally validated with the use of laboratory equipment. Some work on the side of the receiver could be done, more precisely, a low cost implementation based on a raspberry pi and an SDR USB stick.

Moreover, a simple fixed WPT (based on an oscillator and an amplifier) could be designed, so that it would be possible to implement an outdoor network based on passive sensors. All these designed could be combined with a solar panel to be possible to implement a totally passive sensor network.

As it was previously stated, the chapter 5 referred to different approaches on high order backscatter modulation. As a future work, the combination of high order backscatter modulation with the reflection amplifier (tunneling diode based) could be considered as a way to increase the communication range of this technology. Additionally, new modulations can be achieved by synthesizing LoRa symbols and with this it would be possible to use the already developed readers that offer sensitivities of -149 dBm. Some work on this area has already started and can be found in the appendix A. Moreover, and as a future work, an hybrid backscatter modulator could be designed, capable of synthesizing LoRa and Bluetooth symbols and with this could be used in both, indoor and outdoor applications without the need of developing custom readers.

As a future work and related with ambient backscatter can be the combination of the ambient backscatter communication with multiband EH, enabling the communication between the system at very low power in any location. The use case of the possible solution can be seen in Fig. 7.1.

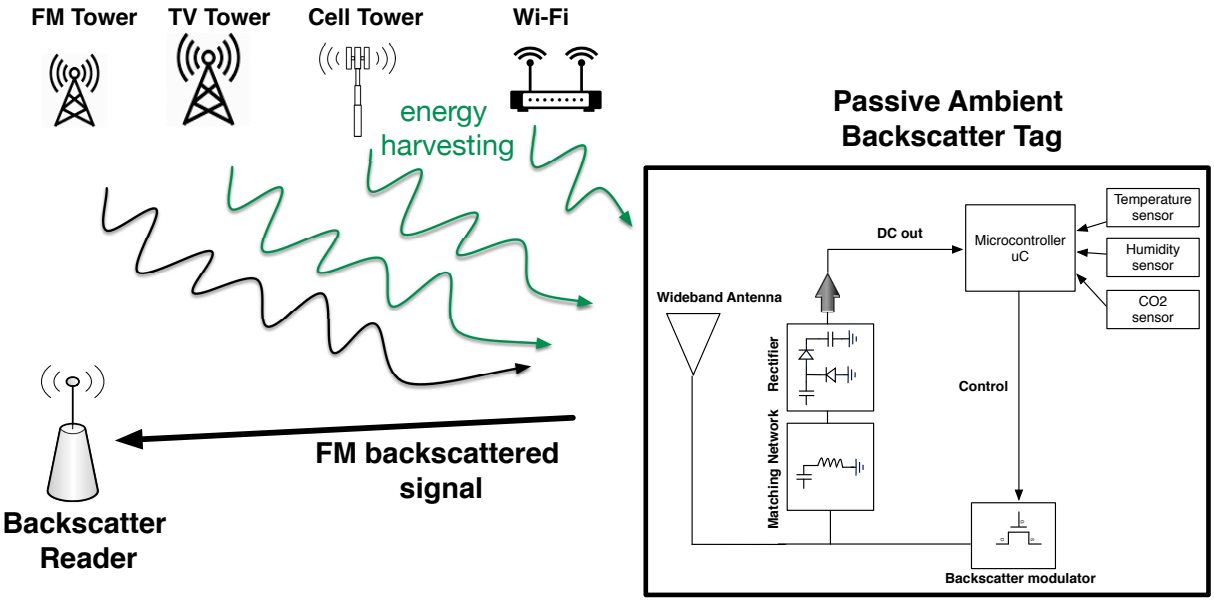

Figure 7.1: Possible solution of multiband EH combined with FM ambient backscatter modulation.

The chapter 6 shown the implementation and plans for measuring an MMIC QAM modulator. As a future work, the measurements should be conducted to evaluate the viability of

including these chips into already developed technologies that are included in the field of IoT.

Bibliography

[1] V. Pop, R. Francisco, H. Pflug, J. Santana, H. Visser, R. Vullers, H. Groot, and B. Gyselinckx, "Human++: Wireless autonomous sensor technology for body area networks," in *16th Asia and South Pacific Design Automation Conference (ASP-DAC)*, 2011.

[2] S. J. Thomas, R. R. Harrison, A. Leonardo, and M. S. Reynolds, "A Battery-Free Multichannel Digital Neural/EMG Telemetry System for Flying Insects," *IEEE Trans. Biomed. Circuits Syst.*, vol. 6, no. 5, pp. 424–436, oct 2012. [Online]. Available: http://ieeexplore.ieee.org/document/6355642/

[3] T. Lee, "Global internet access from space for humanitarian applications," in *Int. Freq. Control Symp.* IEEE, May 2016, pp. 1–3.

[4] A. Marchiori, "Maximizing coverage in low-power wide-area IoT networks," in *Int. Conf. Pervasive Comput. Commun. Work. (PerCom Work.* IEEE, Mar 2017, pp. 467–472.

[5] L. Roselli, *Green RFID Systems*. Cambridge: Cambridge University Press, 2014.

[6] A. P. Sample, J. Braun, A. Parks, and J. R. Smith, "Photovoltaic enhanced UHF RFID tag antennas for dual purpose energy harvesting," *2011 IEEE Int. Conf. RFID, RFID 2011*, pp. 146–153, 2011.

[7] S. Roundy, P. K. Wright, and J. Rabaey, "A study of low level vibrations as a power source for wireless sensor nodes," *Comput. Commun.*, vol. 26, no. 11, pp. 1131–1144, 2003.

[8] A. Sample and J. R. Smith, "Experimental results with two wireless power transfer systems," in *2009 IEEE Radio Wirel. Symp.* IEEE, Jan 2009, pp. 16–18.

[9] F. Fuschini, C. Piersanti, F. Paolazzi, and G. Falciasecca, "Analytical Approach to the Backscattering from UHF RFID Transponder," *IEEE Antennas Wirel. Propag. Lett.*, vol. 7, pp. 33–35, 2008.

[10] H. J. Visser and R. J. M. Vullers, "RF Energy Harvesting and Transport for Wireless Sensor Network Applications: Principles and Requirements," *Proc. IEEE*, vol. 101, no. 6, pp. 1410–1423, Jun 2013.

[11] V. Talla and J. R. Smith, "Hybrid analog-digital backscatter: A new approach for battery-free sensing," in *2013 IEEE Int. Conf. RFID*. IEEE, Apr 2013, pp. 74–81.

[12] G. Vannucci, A. Bletsas, and D. Leigh, "A Software-Defined Radio System for Backscatter Sensor Networks," *IEEE Trans. Wirel. Commun.*, vol. 7, no. 6, pp. 2170–2179, Jun 2008.

[13] S.-N. Daskalakis, S. D. Assimonis, E. Kampianakis, and A. Bletsas, "Soil Moisture Scatter Radio Networking With Low Power," *IEEE Trans. Microw. Theory Tech.*, vol. 64, no. 7, pp. 2338–2346, Jul 2016.

[14] C. Konstantopoulos, E. Koutroulis, N. Mitianoudis, and A. Bletsas, "Converting a Plant to a Battery and Wireless Sensor with Scatter Radio and Ultra-Low Cost," *IEEE Trans. Instrum. Meas.*, vol. 65, no. 2, pp. 388–398, Feb 2016.

[15] Z. Popovic, E. Falkenstein, and R. Zane, "Low-power density wireless powering for battery-less sensors," in *2013 IEEE Radio Wirel. Symp.* IEEE, Jan 2013, pp. 31–33.

[16] Z. Popovic, "Far-field low-power wireless powering for unattended sensors," in *2015 IEEE 16th Annu. Wirel. Microw. Technol. Conf.* IEEE, Apr 2015, pp. 1–4.

[17] N. Borges Carvalho, A. Georgiadis, A. Costanzo, H. Rogier, A. Collado, J. A. Garcia, S. Lucyszyn, P. Mezzanotte, J. Kracek, D. Masotti, A. J. S. Boaventura, M. de las Nieves Ruiz Lavin, M. Pinuela, D. C. Yates, P. D. Mitcheson, M. Mazanek, and V. Pankrac, "Wireless Power Transmission: R&D Activities Within Europe," *IEEE Trans. Microw. Theory Tech.*, vol. 62, no. 4, pp. 1031–1045, Apr 2014.

[18] R. Correia, N. B. Carvalho, and S. Kawasaki, "Continuously Power Delivering for Passive Backscatter Wireless Sensor Networks," *IEEE Trans. Microw. Theory Tech.*, pp. 1–9, 2016.

[19] S. J. Thomas, E. Wheeler, J. Teizer, and M. S. Reynolds, "Quadrature amplitude modulated backscatter in passive and semipassive UHF RFID systems," *IEEE Trans. Microw. Theory Tech.*, vol. 60, no. 4, pp. 1175–1182, 2012.

[20] S. Thomas and M. S. Reynolds, "QAM backscatter for passive UHF RFID tags," in *2010 IEEE Int. Conf. RFID (IEEE RFID 2010)*. IEEE, Apr 2010, pp. 210–214.

[21] S. J. Thomas and M. S. Reynolds, "A 96 Mbit/sec, 15.5 pJ/bit 16-QAM modulator for UHF backscatter communication," in *2012 IEEE Int. Conf. RFID*. IEEE, Apr 2012, pp. 185–190.

[22] R. Correia, A. Boaventura, and N. Borges Carvalho, "Quadrature Amplitude Backscatter Modulator for Passive Wireless Sensors in IoT Applications," *IEEE Trans. Microw. Theory Tech.*, vol. 65, no. 4, pp. 1103–1110, Apr 2017.

[23] E. D. . N. Annex, "Energy Efficiency of the Internet of Things," Tech. Rep., 2016.

[24] A. G. Bell, "The Photophone," *Science (80-.).*, vol. 1, no. 11, pp. 130–134, 1880.

[25] P. Nikitin, "Leon Theremin (Lev Termen)," *IEEE Antennas Propag. Mag.*, vol. 54, no. 5, pp. 252–257, Oct 2012.

[26] H. Stockman, "Communication by Means of Reflected Power," *Proc. IRE*, vol. 36, no. 10, pp. 1196–1204, Oct 1948.

[27] D. B. Harris, "Radio transmission systems with modulatable passive responder," 1960.

[28] K. Finkenzeller, *RFID Handbook*. Chichester, UK: John Wiley & Sons, Ltd, Mar 2003.

[29] N. Tesla, "The transmission of electrical energy without wires as a means for furthering peace," *Electr. World Eng.*, pp. 21–24, 1905.

[30] P. E. Glaser, "Power from the sun: its future." *Science*, vol. 162, no. 3856, pp. 857–861, 1968.

[31] W. C. Brown, "The History of Power Transmission Radio Waves," *IEEE Trans. Microw. Theory Tech.*, vol. 32, no. 9, pp. 1230–1242, 1984.

[32] W. Brown, J. Mims, and N. Heenan, "An experimental microwave-powered helicopter," *IRE Int. Conv. Rec.*, vol. 13, no. October, 1965.

[33] N. Shinohara, "Wireless Power Transmission for Solar Power Satellite (SPS)," Space Solar Power Institute, Tech. Rep., 2000.

[34] K. Takahashi, J. P. Ao, Y. Ikawa, C. Y. Hu, H. Kawai, N. Shinohara, N. Niwa, and Y. Ohno, "GaN schottky diodes for microwave power rectification," *Jpn. J. Appl. Phys.*, vol. 48, no. 4 PART 2, 2009.

[35] K. Nishida, Y. Taniguchi, K. Kawakami, Y. Homma, H. Mizutani, M. Miyazaki, H. Ikematsu, and N. Shinohara, "5.8 GHz high sensitivity rectenna array," in *2011 IEEE MTT-S Int. Microw. Work. Ser. Innov. Wirel. Power Transm. Technol. Syst. Appl.* IEEE, May 2011, pp. 19–22.

[36] T. Yoo and K. Chang, "Theoretical and Experimental Development of 10-GHz and 35-GHz Rectennas," *IEEE Trans. Microw. Theory Tech. Vol. 40, No. 6, June*, vol. 40, no. 6, pp. 1259–1266, 1992.

[37] J. McSpadden, L. F. L. Fan, and K. C. K. Chang, "Design and experiments of a high-conversion-efficiency 5.8-GHz\nrectenna," *IEEE Trans. Microw. Theory Tech.*, vol. 46, no. 12, pp. 2053–2060, 1998.

[38] Y. Suh and K. Chang, "A High-Efficiency Dual-Frequency Rectenna for 2.45- and 5.8-GHz Wireless Power Transmission," *IEEE Trans. Microw. Theory Tech.*, vol. 50, no. 7, pp. 1784–1789, 2002.

[39] R. M. Dickinson, "Power in the sky: Requirements for microwave wireless power beamers for powering high-altitude platforms," *IEEE Microw. Mag.*, vol. 14, no. 2, pp. 36–47, 2013.

[40] D. M. Dobkin and S. M. Weigand, "UHF RFID and Tag Antenna Scattering, Part I: Experimental Results," *Microw. Journal, Euro-Global Ed.*, vol. 49, no. 5, pp. 170–190, 2007.

[41] C. R. Valenta and G. D. Durgin, "Harvesting Wireless Power: Survey of Energy-Harvester Conversion Efficiency in Far-Field, Wireless Power Transfer Systems," *IEEE Microw. Mag.*, vol. 15, no. 4, pp. 108–120, Jun 2014.

[42] H. Liu, X. Li, R. Vaddi, K. Ma, S. Datta, and V. Narayanan, "Tunnel FET RF Rectifier Design for Energy Harvesting Applications," *IEEE J. Emerg. Sel. Top. Circuits Syst.*, vol. 4, no. 4, pp. 400–411, Dec 2014.

[43] E. Falkenstein, M. Roberg, and Z. Popovic, "Low-Power Wireless Power Delivery," *IEEE Trans. Microw. Theory Tech.*, vol. 60, no. 7, pp. 2277–2286, Jul 2012.

[44] D. Belo, R. Correia, F. Pereira, and N. B. De Carvalho, "Dual band wireless power and data transfer for space-based sensors," in *2017 Top. Work. Internet Sp.* IEEE, Jan 2017, pp. 1–4.

[45] R. Correia and N. B. Carvalho, "HEMT based RF to DC converter efficiency enhancement using special designed waveforms," in *2017 IEEE MTT-S Int. Microw. Symp.* IEEE, Jun 2017, pp. 609–612.

[46] R. Scheeler, S. Korhummel, and Z. Popovic, "A Dual-Frequency Ultralow-Power Efficient 0.5-g Rectenna," *IEEE Microw. Mag.*, vol. 15, no. 1, pp. 109–114, Jan 2014.

[47] B. L. Pham and A.-V. Pham, "Triple bands antenna and high efficiency rectifier design for RF energy harvesting at 900, 1900 and 2400 MHz," in *2013 IEEE MTT-S Int. Microw. Symp. Dig.* IEEE, Jun 2013, pp. 1–3.

[48] A. Georgiadis, A. Collado, S. Via, and C. Meneses, "Flexible hybrid solar/EM energy harvester for autonomous sensors," in *2011 IEEE MTT-S Int. Microw. Symp.* IEEE, Jun 2011, pp. 1–4.

[49] K. Niotaki, A. Collado, A. Georgiadis, S. Kim, and M. M. Tentzeris, "Solar/Electromagnetic Energy Harvesting and Wireless Power Transmission," *Proc. IEEE*, vol. 102, no. 11, pp. 1712–1722, Nov 2014.

[50] Z. Zhong, H. Sun, and Y. Guo, "Design of rectifier with extended operating input power range," *Electron. Lett.*, vol. 49, no. 18, pp. 1175–1176, Aug 2013.

[51] R. Correia and N. B. Carvalho, "Single transistor passive backscatter sensor," in *2017 IEEE MTT-S Int. Microw. Symp.* IEEE, Jun 2017, pp. 820–823.

[52] M. N. Ruiz, R. Marante, and J. A. Garcia, "A class E synchronous rectifier based on an E-pHEMT device for wireless powering applications," in *2012 IEEE/MTT-S Int. Microw. Symp. Dig.* IEEE, Jun 2012, pp. 1–3.

[53] H. Sun, Z. Zhong, and Y.-X. Guo, "An Adaptive Reconfigurable Rectifier for Wireless Power Transmission," *IEEE Microw. Wirel. Components Lett.*, vol. 23, no. 9, pp. 492–494, Sep 2013.

[54] M. Trotter, J. Griffin, and G. Durgin, "Power-optimized waveforms for improving the range and reliability of RFID systems," in *2009 IEEE Int. Conf. RFID*. IEEE, Apr 2009, pp. 80–87.

[55] A. S. Boaventura and N. B. Carvalho, "Maximizing DC power in energy harvesting circuits using multisine excitation," in *2011 IEEE MTT-S Int. Microw. Symp.* IEEE, Jun 2011, pp. 1–4.

[56] A. Collado and A. Georgiadis, "Improving wireless power transmission efficiency using chaotic waveforms," in *2012 IEEE/MTT-S Int. Microw. Symp. Dig.* IEEE, Jun 2012, pp. 1–3.

[57] R. Correia, N. B. Carvalho, and S. Kawasaki, "Backscatter radio coverage enhancements using improved WPT signal waveform," in *2015 IEEE Wirel. Power Transf. Conf.* IEEE, May 2015, pp. 1–3.

[58] R. D. Fernandes, A. S. Boaventura, N. B. Carvalho, and J. N. Matos, "Increasing the range of wireless passive sensor nodes using multisines," in *2011 IEEE Int. Conf. RFID-Technologies Appl.* IEEE, Sep 2011, pp. 549–553.

[59] A. S. Boaventura and N. B. Carvalho, "Spatially-combined multisine transmitter for wireless power transmission," in *2013 IEEE Wirel. Power Transf.* IEEE, May 2013, pp. 21–24.

[60] A. Boaventura, D. Belo, R. Fernandes, A. Collado, A. Georgiadis, and N. B. Carvalho, "Boosting the Efficiency: Unconventional Waveform Design for Efficient Wireless Power Transfer," *IEEE Microw. Mag.*, vol. 16, no. 3, pp. 87–96, Apr 2015.

[61] C. R. Valenta and G. D. Durgin, "Rectenna performance under power-optimized waveform excitation," in *2013 IEEE Int. Conf. RFID*. IEEE, Apr 2013, pp. 237–244.

[62] A. Collado and A. Georgiadis, "Optimal Waveforms for Efficient Wireless Power Transmission," *IEEE Microw. Wirel. Components Lett.*, vol. 24, no. 5, pp. 354–356, May 2014.

[63] N. Pan, D. Belo, M. Rajabi, D. Schreurs, N. B. Carvalho, and S. Pollin, "Bandwidth Analysis of RF-DC Converters Under Multisine Excitation," *IEEE Trans. Microw. Theory Tech.*, vol. 66, no. 2, pp. 791–802, Feb 2018.

[64] J. Blanco, F. Bolos, and A. Georgiadis, "Instantaneous power variance and radio frequency to dc conversion efficiency of wireless power transfer systems," *IET Microwaves, Antennas Propag.*, vol. 10, no. 10, pp. 1065–1070, Jul 2016.

[65] A. S. Boaventura and N. B. Carvalho, "A Low-Power Wakeup Radio for Application in WSN-Based Indoor Location Systems," *Int. J. Wirel. Inf. Networks*, vol. 20, no. 1, pp. 67–73, Mar 2013.

[66] M. Magno, N. Jackson, A. Mathewson, L. Benini, and E. Popovic, "Combination of hybrid energy harvesters with MEMS piezoelectric and nano-Watt radio wake up to extend lifetime of system for wireless sensor nodes," in *26th Int. Conf. Archit. Comput. Syst.*, 2013.

[67] M. Magno and L. Benini, "An ultra low power high sensitivity wake-up radio receiver with addressing capability," in *10th Int. Conf. Wirel. Mob. Comput. Netw. Commun.* IEEE, Oct 2014, pp. 92–99.

[68] P. Kamalinejad, K. Keikhosravy, M. Magno, S. Mirabbasi, V. C. Leung, and L. Benini, "A high-sensitivity fully passive wake-up radio front-end for wireless sensor nodes," in *Int. Conf. Consum. Electron.* IEEE, Jan 2014, pp. 209–210.

[69] M. Del Prete, D. Masotti, A. Costanzo, M. Magno, and L. Benini, "A dual-band wake-up radio for ultra-low power Wireless Sensor Networks," in *Top. Conf. Wirel. Sensors Sens. Networks*. IEEE, Jan 2016, pp. 81–84.

[70] J. Kracek, M. Svanda, M. Mazanek, and J. Machac, "Implantable Semi-Active UHF RFID Tag With Inductive Wireless Power Transfer," *IEEE Antennas Wirel. Propag. Lett.*, vol. 15, pp. 1657–1660, 2016.

[71] F. J. Velez, N. Barroca, L. M. Borges, R. Chávez-Santiago, and I. Balasingham, "Radio-frequency energy harvesting for wearable sensors," *Healthc. Technol. Lett.*, vol. 2, no. 1, pp. 22–27, Feb 2015.

[72] V. Kuhn, F. Seguin, C. Lahuec, and C. Person, "A multi-tone RF energy harvester in body sensor area network context," in *2013 Loughbrgh. Antennas Propag. Conf.* IEEE, Nov 2013, pp. 238–241.

[73] D. J. Yeager, J. Holleman, R. Prasad, J. R. Smith, and B. P. Otis, "NeuralWISP: A Wirelessly Powered Neural Interface With 1-m Range," *IEEE Trans. Biomed. Circuits Syst.*, vol. 3, no. 6, pp. 379–387, Dec 2009.

[74] A. Sample, D. Yeager, P. Powledge, A. Mamishev, and J. Smith, "Design of an RFID-Based Battery-Free Programmable Sensing Platform," *IEEE Trans. Instrum. Meas.*, vol. 57, no. 11, pp. 2608–2615, Nov 2008.

[75] F. Pereira, R. Correia, and N. Carvalho, "Passive Sensors for Long Duration Internet of Things Networks," *Sensors*, vol. 17, no. 10, p. 2268, Oct 2017.

[76] P. Jankowski-Mihułowicz, M. Węglarski, G. Pitera, D. Kawalec, and W. Lichoń, "Development board of the autonomous semi-passive RFID transponder," *Bull. Pol. Ac. Tech. Bull. POLISH Acad. Sci. Tech. Sci.*, vol. 64, no. 3, 2016.

[77] W. Lerdsitsomboon and K. K. O, "Technique for Integration of a Wireless Switch in a 2.4 GHz Single Chip Radio," *IEEE J. Solid-State Circuits*, vol. 46, no. 2, pp. 368–377, Feb 2011.

[78] M. Winkler, T. Faseth, H. Arthaber, and G. Magerl, "An UHF RFID tag emulator for precise emulation of the physical layer," *Microw. Conf. (EuMC), 2010 Eur.*, no. September, pp. 273–276, 2010.

[79] D. M. Pozar, *Microwave engineering*. Wiley, 2012.

[80] J. Kimionis and M. M. Tentzeris, "Pulse shaping for backscatter radio," in *2016 IEEE MTT-S Int. Microw. Symp.* IEEE, May 2016, pp. 1–4.

[81] M. S. Trotter, C. R. Valenta, G. A. Koo, B. R. Marshall, and G. D. Durgin, "Multi-antenna techniques for enabling passive RFID tags and sensors at microwave frequencies," in *2012 IEEE Int. Conf. RFID*. IEEE, Apr 2012, pp. 1–7.

[82] A. Shirane, H. Tan, Y. Fang, T. Ibe, H. Ito, N. Ishihara, and K. Masu, "13.8 A 5.8GHz RF-powered transceiver with a 113μW 32-QAM transmitter employing the IF-based quadrature backscattering technique," in *2015 IEEE Int. Solid-State Circuits Conf. - Dig. Tech. Pap.* IEEE, Feb 2015, pp. 1–3.

[83] A. Tang, Y. Kim, and M.-C. F. Chang, "A 65 nm CMOS 330 Mb/s Microwave Backscatter Link at 2.4 to 2.9 GHz With Ambient Blocker Cancellation," *IEEE Microw. Wirel. Components Lett.*, vol. 26, no. 1, pp. 61–63, Jan 2016.

[84] R. Correia and N. B. Carvalho, "Ultrafast Backscatter Modulator With Low-Power Consumption and Wireless Power Transmission Capabilities," *IEEE Microw. Wirel. Components Lett.*, vol. 27, no. 12, pp. 1152–1154, Dec 2017.

[85] X. Fu, A. Sharma, E. Kampianakis, A. Pedross-Engel, D. Arnitz, and M. S. Reynolds, "A low cost 10.0-11.1 GHz X-band microwave backscatter communication testbed with integrated planar wideband antennas," in *2016 IEEE Int. Conf. RFID*. IEEE, May 2016, pp. 1–4.

[86] V. Liu, A. Parks, V. Talla, S. Gollakota, D. Wetherall, and J. R. Smith, "Ambient backscatter: wireless communication out of thin air," *ACM SIGCOMM Comput. Commun. Rev.*, vol. 43, no. 4, pp. 39–50, Oct. 2013.

[87] N. Van Huynh, D. T. Hoang, X. Lu, D. Niyato, P. Wang, and D. I. Kim, "Ambient backscatter communications: A contemporary survey," *arXiv preprint arXiv:1712.04804*, Dec. 2017.

[88] A. Wang, V. Iyer, V. Talla, J. R. Smith, and S. Gollakota, "FM backscatter: Enabling connected cities and smart fabrics," Boston, MA, Mar. 2017, pp. 243–258.

[89] S. N. Daskalakis, J. Kimionis, A. Collado, G. Goussetis, M. M. Tentzeris, and A. Georgiadis, "Ambient backscatterers using FM broadcasting for low cost and low power wireless applications," *IEEE Transactions on Microwave Theory and Techniques*, vol. PP, no. 99, pp. 1–12, Nov. 2017.

[90] A. N. Parks, A. Liu, S. Gollakota, J. R. Smith, A. N. Parks, A. Liu, S. Gollakota, and J. R. Smith, "Turbocharging ambient backscatter communication," *SIGCOMM Comput. Commun. Rev.*, vol. 44, no. 4, pp. 619–630, Aug 2014.

[91] A. Wang, V. Iyer, V. Talla, J. R. Smith, and S. Gollakota, "FM Backscatter: Enabling Connected Cities and Smart Fabrics," in *Proc. 14th USENIX Symp. Networked Syst. Des. Implement. (NSDI 17)*, 2017.

[92] D. Bharadia, K. R. Joshi, M. Kotaru, S. Katti, D. Bharadia, K. R. Joshi, M. Kotaru, and S. Katti, "BackFi: High Throughput WiFi Backscatter," in *ACM SIGCOMM Comput. Commun. Rev.*, vol. 45, no. 5. ACM, Aug 2015, pp. 283–296.

[93] J. Qian, F. Gao, G. Wang, S. Jin, and H. Zhu, "Noncoherent Detections for Ambient Backscatter System," *IEEE Trans. Wirel. Commun.*, vol. 16, no. 3, pp. 1412–1422, Mar 2017.

[94] Z. Shen, A. Athalye, and P. M. Djuric, "Phase Cancellation in Backscatter-Based Tag-to-Tag Communication Systems," *IEEE Internet Things J.*, vol. 3, no. 6, pp. 959–970, Dec 2016.

[95] G. Wang, F. Gao, R. Fan, and C. Tellambura, "Ambient Backscatter Communication Systems: Detection and Performance Analysis," *IEEE Trans. Commun.*, vol. 64, no. 11, pp. 4836–4846, Nov 2016.

[96] W. C. Barott, "Coherent Backscatter Communications Using Ambient Transmitters and Passive Radar Processing," in *2014 Natl. Wirel. Res. Collab. Symp.* IEEE, May 2014, pp. 15–20.

[97] P. ZHANG, M. Rostami, P. Hu, and D. Ganesan, "Enabling Practical Backscatter Communication for On-body Sensors," in *Proc. 2016 Conf. ACM SIGCOMM 2016 Conf. - SIGCOMM '16*. New York, New York, USA: ACM Press, 2016, pp. 370–383.

[98] C. Pérez-Penichet, A. Varshney, F. Hermans, C. Rohner, and T. Voigt, "Do Multiple Bits per Symbol Increase the Throughput of Ambient Backscatter Communications?" in *Proc. 2016 Int. Conf. Embed. Wirel. Syst. Networks*. Junction Publishing, 2016, pp. 355–360.

[99] V. Liu, V. Talla, and S. Gollakota, "Enabling instantaneous feedback with full-duplex backscatter," in *Proc. 20th Annu. Int. Conf. Mob. Comput. Netw. - MobiCom '14*. New York, New York, USA: ACM Press, 2014, pp. 67–78.

[100] Y. Liu, G. Wang, Z. Dou, and Z. Zhong, "Coding and Detection Schemes for Ambient Backscatter Communication Systems," *IEEE Access*, vol. 5, pp. 4947–4953, 2017.

[101] B. Kellogg, V. Talla, S. Gollakota, and J. R. Smith, "Passive Wi-Fi: Bringing Low Power to Wi-Fi Transmissions," in *Proc. 13th USENIX Symp. Networked Syst. Des. Implement. (NSDI '16)*, 2016.

[102] X. Zhou, G. Wang, Y. Wang, and J. Cheng, "An Approximate BER Analysis for Ambient Backscatter Communication Systems With Tag Selection," *IEEE Access*, vol. 5, pp. 22 552–22 558, 2017.

[103] D. Munir, S. T. Shah, W. J. Lee, and M. Y. Chung, "Low-power backscatter relay network," in *Proc. 11th Int. Conf. Ubiquitous Inf. Manag. Commun. - IMCOM '17*. New York, New York, USA: ACM Press, 2017, pp. 1–5.

[104] Y. Peng, L. Shangguan, Y. Hu, Y. Qian, X. Lin, X. Chen, D. Fang, and K. Jamieson, "PLoRa: A Passive Long-Range Data Network from Ambient LoRa Transmissions," in *Proc. 2018 Conf. ACM Spec. Interes. Gr. Data Commun. - SIGCOMM '18*. New York, New York, USA: ACM Press, 2018, pp. 147–160.

[105] S. N. Daskalakis, J. Kimionis, A. Collado, G. Goussetis, M. M. Tentzeris, and A. Georgiadis, "Ambient Backscatterers Using FM Broadcasting for Low Cost and Low Power Wireless Applications," *IEEE Trans. Microw. Theory Tech.*, vol. 65, no. 12, pp. 5251–5262, Dec 2017.

[106] S.-N. Daskalakis, R. Correia, G. Goussetis, M. Tentzeris, N. B. Carvalho, and A. Georgiadis, "Four-PAM Modulation of Ambient FM Backscattering for Spectrally Efficient

Low-Power Applications," *IEEE Trans. Microw. Theory Tech.*, vol. 66, no. 12, pp. 5909–5921, Dec 2018.

[107] B. Kellogg, V. Talla, J. R. Smith, and S. Gollakot, "PASSIVE WI-FI: Bringing Low Power to Wi-Fi Transmissions," *GetMobile Mob. Comput. Commun.*, vol. 20, no. 3, pp. 38–41, Jan 2017.

[108] J. F. Ensworth and M. S. Reynolds, "Every smart phone is a backscatter reader: Modulated backscatter compatibility with Bluetooth 4.0 Low Energy (BLE) devices," in *2015 IEEE Int. Conf. RFID*, Apr 2015, pp. 78–85.

[109] ——, "BLE-Backscatter: Ultralow-Power IoT Nodes Compatible With Bluetooth 4.0 Low Energy (BLE) Smartphones and Tablets," *IEEE Trans. Microw. Theory Tech.*, vol. 65, no. 9, pp. 3360–3368, Sep 2017.

[110] V. Iyer, V. Talla, B. Kellogg, S. Gollakota, and J. Smith, "Inter-Technology Backscatter: Towards Internet Connectivity for Implanted Devices," in *Proc. 2016 Conf. ACM SIGCOMM 2016 Conf. - SIGCOMM '16*, New York, New York, USA, pp. 356–369.

[111] C. Pérez-Penichet, F. Hermans, A. Varshney, and T. Voigt, "Augmenting IoT networks with backscatter-enabled passive sensor tags," in *Proc. 3rd Work. Hot Top. Wirel. - HotWireless '16*, 2016, pp. 23–27.

[112] V. Talla, M. Hessar, B. Kellogg, A. Najafi, J. R. Smith, and S. Gollakota, "LoRa Backscatter: Enabling The Vision of Ubiquitous Connectivity," *Proceedings of the ACM on Interactive, Mobile, Wearable and Ubiquitous Technologies*, vol. 1, no. 3, pp. 1–24, September 2017.

[113] J. Kimionis, A. Georgiadis, Sangkil Kim, A. Collado, K. Niotaki, and M. M. Tentzeris, "An enhanced-range RFID tag using an ambient energy powered reflection amplifier," in *2014 IEEE MTT-S Int. Microw. Symp.*, Jun 2014, pp. 1–4.

[114] P. Chan and V. Fusco, "Full duplex reflection amplifier tag," *IET Microwaves, Antennas Propag.*, vol. 7, no. 6, pp. 415–420, Apr 2013.

[115] A. Lazaro, A. Ramos, R. Villarino, and D. Girbau, "Time-Domain UWB RFID Tag Based on Reflection Amplifier," *IEEE Antennas Wirel. Propag. Lett.*, vol. 12, pp. 520–523, 2013.

[116] V. Vesterinen, J. Hassel, and H. Seppa, "Tunable Impedance Matching for Josephson Junction Reflection Amplifier," *IEEE Trans. Appl. Supercond.*, vol. 23, no. 3, pp. 1 500 104–1 500 104, Jun 2013.

[117] J.-F. Bousquet, S. Magierowski, and G. G. Messier, "A 4-GHz Active Scatterer in 130-nm CMOS for Phase Sweep Amplify-and-Forward," *IEEE Trans. Circuits Syst. I Regul. Pap.*, vol. 59, no. 3, pp. 529–540, Mar 2012.

[118] P. Chan and V. Fusco, "Bi-static 5.8GHz RFID range enhancement using retrodirective techniques," in *2011 41st Eur. Microw. Conf.*

[119] V. Fusco, H. Cantú, and S. Simms, "Microwave reflection amplifier for detection and tagging applications," *IET Microwaves, Antennas Propag.*, vol. 2, no. 2, pp. 115–119, Mar 2008.

[120] H. I. Cantu and V. F. Fusco, "A 21 GHZ Reflection Amplifier MMIC for Retro-Directive Antenna and RFID Applications," in *2006 IET Semin. MM-Wave Prod. Technol.*

[121] Shyh-Jong Chung, Shing-Ming Chen, and Yang-Chang Lee, "A novel bi-directional amplifier with applications in active van atta retrodirective arrays," *IEEE Trans. Microw. Theory Tech.*, vol. 51, no. 2, pp. 542–547, Feb 2003.

[122] F. Amato, C. W. Peterson, B. P. Degnan, and G. D. Durgin, "Tunneling RFID Tags for Long-Range and Low-Power Microwave Applications," *IEEE J. Radio Freq. Identif.*, vol. 2, no. 2, pp. 93–103, Jun 2018.

[123] S. Khaledian, F. Farzami, D. Erricolo, and B. Smida, "A Full-Duplex Bidirectional Amplifier With Low DC Power Consumption Using Tunnel Diodes," *IEEE Microw. Wirel. Components Lett.*, vol. 27, no. 12, pp. 1125–1127, Dec 2017.

[124] F. Farzami, S. Khaledian, B. Smida, and D. Erricolo, "Ultra-low power reflection amplifier using tunnel diode for RFID applications," in *2017 IEEE Int. Symp. Antennas Propag. Usn. Natl. Radio Sci. Meet.*, Jul 2017, pp. 2511–2512.

[125] F. Amato, C. W. Peterson, M. B. Akbar, and G. D. Durgin, "Long range and low powered RFID tags with tunnel diode," in *2015 IEEE Int. Conf. RFID Technol. Appl.*, Sep 2015, pp. 182–187.

[126] F. Amato, C. W. Peterson, B. P. Degnan, and G. D. Durgin, "A 45 uW bias power, 34 dB gain reflection amplifier exploiting the tunneling effect for RFID applications," in *2015 IEEE Int. Conf. RFID*, Apr 2015, pp. 137–144.

[127] I. D. Robertson and S. Lucyszyn, Eds., *RFIC and MMIC Design and Technology*. IET, 2001.

[128] M. Karkkainen, M. Kantanen, S. Caujolle-Bert, M. Varonen, R. Weber, A. Leuther, M. Seelmann-Eggebert, A. Alanne, P. Jukkala, T. Narhi, and K. A. I. Halonen, "MHEMT G -Band Low-Noise Amplifiers," *IEEE Trans. Terahertz Sci. Technol.*, vol. 4, no. 4, pp. 459–468, Jul 2014.

[129] R. Cleriti, W. Ciccognani, S. Colangeli, A. Serino, E. Limiti, P. Frijlink, M. Renvoise, R. Doerner, and M. Hossain, "D-band LNA using a 40-nm GaAs mHEMT technology," in *2017 12th Eur. Microw. Integr. Circuits Conf.* IEEE, Oct 2017, pp. 105–108.

[130] M. Micovic, A. Kurdoghlian, H. Moyer, P. Hashimoto, A. Schmitz, I. Milosavljevic, P. Willadsen, W.-S. Wong, J. Duvall, M. Hu, M. Wetzel, and D. Chow, "GaN MMIC technology for microwave and millimeter-wave applications," in *IEEE Compd. Semicond. Integr. Circuit Symp. 2005. CSIC '05.* IEEE, 2005, p. 3 pp.

[131] A. Brown, K. Brown, J. Chen, K. C. Hwang, N. Kolias, and R. Scott, "W-band GaN power amplifier MMICs," in *2011 IEEE MTT-S Int. Microw. Symp.* IEEE, Jun 2011, pp. 1–4.

[132] L. Zhou, C.-C. Wang, Z. Chen, and P. Heydari, "A W-band CMOS Receiver Chipset for Millimeter-Wave Radiometer Systems," *IEEE J. Solid-State Circuits*, vol. 46, no. 2, pp. 378–391, Feb 2011.

[133] L. Gilreath, V. Jain, and P. Heydari, "Design and Analysis of a W-Band SiGe Direct-Detection-Based Passive Imaging Receiver," *IEEE J. Solid-State Circuits*, vol. 46, no. 10, pp. 2240–2252, Oct 2011.

[134] P. Song, M. A. Oakley, A. C. Ulusoy, M. Kaynak, B. Tillack, G. A. Sadowy, and J. D. Cressler, "A Class-E Tuned W-Band SiGe Power Amplifier With 40.4% Power-Added Efficiency at 93 GHz," *IEEE Microw. Wirel. Components Lett.*, vol. 25, no. 10, pp. 663–665, Oct 2015.

[135] A. C. Ulusoy, M. Kaynak, V. Valenta, B. Tillack, and H. Schumacher, "A 110 GHz LNA with 20dB gain and 4dB noise figure in an 0.13μm SiGe BiCMOS technology," in *2013 IEEE MTT-S Int. Microw. Symp. Dig.* IEEE, Jun 2013, pp. 1–3.

[136] H. Rücker, B. Heinemann, and A. Fox, "SiGe BiCMOS Technologies for Applications above 100 GHz," in *2012 IEEE Compd. Semicond. Integr. Circuit Symp.* IEEE, Oct 2012, pp. 1–4.

[137] W. Zulehner, "Czochralski growth of silicon," *J. Cryst. Growth*, vol. 65, no. 1-3, pp. 189–213, Dec 1983.

[138] W. Shockley, "Circuit element utilizing semiconductive material," 1951.

[139] J. S. Kilby, "Miniaturized electronic circuits," 1964.

[140] R. F. Stewart, "Integrated semiconductor circuit device," 1964.

[141] J. S. Kilby, "Method of making miniaturized electronic circuits," 1966.

[142] R. N. Noyce, "Microelectronics," *Sci. Am.*, vol. 237, pp. 63–69, 1977.

[143] E. Mehal and R. Wacker, "GaAs Integrated Microwave Circuits," *IEEE Trans. Microw. Theory Tech.*, vol. 16, no. 7, pp. 451–454, Jul 1968.

[144] S. Mao, S. Jones, and G. Vendelin, "Millimeter-Wave Integrated Circuits," *IEEE J. Solid-State Circuits*, vol. 3, no. 2, pp. 117–123, Jun 1968.

[145] M. I. Skolnik, *Introduction to Radar Systems*, 3rd ed. New York: McGraw-Hill, 2001.

[146] V. Liepa and T. Senior, "Modification to the scattering behavior of a sphere by reactive loading," in *Proceedings of the IEEE*, vol. 53, no. 8, Aug 1965, pp. 1004–1011.

[147] A. E. Fuhs, "Radar cross section lectures." New York, USA: AIAA, 1982.

[148] P. Nikitin and K. Rao, "Theory and measurement of backscattering from RFID tags," *IEEE Antennas Propag. Mag.*, vol. 48, no. 6, pp. 212–218, Dec 2006.

[149] K. Penttila, M. Keskilammi, L. Sydanheimo, and M. Kivikoski, "Radar cross-section analysis for passive RFID systems," *IEE Proc. - Microwaves, Antennas Propag.*, vol. 153, no. 1, p. 103, 2006.

[150] J. Wang and R. Moore, "Precision experimental characterization of the scattering and radiation properties of antennas," *IEEE Trans. Antennas Propag.*, vol. 30, no. 1, pp. 108–112, Jan 1982.

[151] R. Schneider, "A re-look at antenna in-band RCSR via load mismatching," in *IEEE Antennas Propag. Soc. Int. Symp. 1996 Dig.*, vol. 2. IEEE, 1996, pp. 1398–1401.

[152] W. Wiesbeck and E. Heidrich, "Wide-band multiport antenna characterization by polarimetric RCS measurements," *IEEE Trans. Antennas Propag.*, vol. 46, no. 3, pp. 341–350, Mar 1998.

[153] R. Hansen, "Relationships between antennas as scatterers and as radiators," *Proc. IEEE*, vol. 77, no. 5, pp. 659–662, May 1989.

[154] R. B. Green, "The General Theory of Antenna Scattering," Ph.D. dissertation, Ohio State University, 1963.

[155] P. Pursula, "Analysis and Design of UHF and Millimetre Wave Radio Frequency Identification," Ph.D. dissertation, 2008.

[156] R. Correia, N. B. D. Carvalho, G. Fukuda, A. Miyaji, and S. Kawasaki, "Backscatter Wireless Sensor Network with WPT Capabilities," in *Int. Microw. Symp.*, 2015, pp. 1–4.

[157] Ming-Lin Chuang, "Dual-Band Impedance Transformer Using Two-Section Shunt Stubs," *IEEE Transactions on Microwave Theory and Techniques*, vol. 58, no. 5, pp. 1257–1263, May 2010.

[158] J. Heikkinen and M. Kivikoski, "A novel dual-frequency circularly polarized rectenna," *IEEE Antennas and Wireless Propagation Letters*, vol. 2, no. 1, pp. 330–333, 2003.

[159] K. Niotaki, S. Kim, S. Jeong, A. Collado, A. Georgiadis, and M. M. Tentzeris, "A Compact Dual-Band Rectenna Using Slot-Loaded Dual Band Folded Dipole Antenna," *IEEE Antennas and Wireless Propagation Letters*, vol. 12, pp. 1634–1637, 2013.

[160] Y. Chow and K. Wan, "A transformer of one-third wavelength in two sections - for a frequency and its first harmonic," *IEEE Microwave and Wireless Components Letters*, vol. 12, no. 1, pp. 22–23, Jan 2002.

[161] C. Monzon, "A small dual-frequency transformer in two sections," *IEEE Transactions on Microwave Theory and Techniques*, vol. 51, no. 4, pp. 1157–1161, Apr 2003.

[162] F. Giannini and L. Scucchia, "A Complete Class of Harmonic Matching Networks: Synthesis and Application," *IEEE Transactions on Microwave Theory and Techniques*, vol. 57, no. 3, pp. 612–619, Mar 2009.

[163] R. Harrington, "Small Resonant Scatterers and Their Use for Field Measurements," *IEEE Trans. Microw. Theory Tech.*, vol. 10, no. 3, pp. 165–174, May 1962.

[164] ——, "Electromagnetic scattering by antennas," *IEEE Trans. Antennas Propag.*, vol. 11, no. 5, pp. 595–596, Sep 1963.

[165] R. F. Harrington, "Theory of loaded scatterers," *Proc. Inst. Electr. Eng.*, vol. 111, no. 4, p. 617, 1964.

[166] *LM94021/LM94021Q Multi-Gain Analog Temperature Sensor*, Texas Instruments, 2013. [Online]. Available: http://www.ti.com/lit/ds/symlink/lm94021.pdf

[167] *Micropower, 3-Axis, 2 g/4 g/8 g Digital Output MEMS Accelerometer*, Analog Devices, 2016. [Online]. Available: https://www.analog.com/media/en/technical-documentation/data-sheets/adxl362.pdf

[168] *Mixed Signal Microcontroller MSP430F2132-EP*, Texas Instruments, 2013. [Online]. Available: http://www.ti.com/lit/ds/symlink/msp430f2132-ep.pdf

[169] R. Correia and N. B. Carvalho, "Design of high order modulation backscatter wireless sensor for passive IoT solutions," in *2016 IEEE Wirel. Power Transf. Conf.* IEEE, May 2016, pp. 1–3.

[170] Cong Tang, Xianqi Lin, Y. Fan, K. Song, and Daotong Li, "A new dual-band Wilkinson power divider," in *2015 IEEE Int. Wirel. Symp. (IWS 2015)*, Mar 2015, pp. 1–4.

[171] S. N. Daskalakis, R. Correia, G. Goussetis, M. M. Tentzeris, N. B. Carvalho, and A. Georgiadis, "Spectrally efficient 4-PAM ambient FM backscattering for wireless sensing and rfid applications," Philadelphia, Pennsylvania, USA, Jun. 2018.

[172] *PIC16LF1459, USB Microcontroller with Extreme Low-Power Technology, product manual*, Microchip Technology Inc., 2014. [Online]. Available: http://www.microchip.com/downloads/en/DeviceDoc/40001639B.pdf

[173] *SP3-37 Flexible Solar Panel 3V @ 22mA, product manual*, PowerFilm, 2009. [Online]. Available: https://goo.gl/q5ECXh

[174] *XC6504 Ultra Low Power Consumption Voltage Regulator, product manual*, Uorex Semiconductor, 2012. [Online]. Available: https://www.torexsemi.com/file/xc6504/XC6504.pdf

[175] K. Niotaki, A. Collado, A. Georgiadis, S. Kim, and M. M. Tentzeris, "Solar/Electromagnetic energy harvesting and wireless power transmission," vol. 102, no. 11, pp. 1712–1722, Nov. 2014.

[176] A. Bletsas, A. G. Dimitriou, and J. N. Sahalos, "Improving backscatter radio tag efficiency," *IEEE Transactions on Microwave Theory and Techniques*, vol. 58, no. 6, pp. 1502–1509, Jun. 2010.

[177] C. R. Johnson Jr, W. A. Sethares, and A. G. Klein, *Software receiver design: build your own digital communication system in five easy steps*. Cambridge Univ. Press, 2011.

[178] J. G. Proakis and M. Salehi, *Digital Communications fifth edition, 2007*. McGraw-Hill Companies, Inc., New York, NY, 2008.

[179] H. Heuermann, "Calibration of a Network Analyzer Without a Thru Connection for Nonlinear and Multiport Measurements," *IEEE Trans. Microw. Theory Tech.*, vol. 56, no. 11, pp. 2505–2510, Nov 2008.

Appendix A

Chirp Based Backscatter Modulation

Chirp Based Backscatter Modulation

Ricardo Correia*, Nuno Borges Carvalho*, Yuan Ding†, Spyridon Nektarios Daskalakis†
Panagiotis Petridis†, George Goussetis†, Apostolos Georgiadis†

*Instituto de Telecomunicações, Departamento de Electrónica, Telecomunicações e Informática
Universidade de Aveiro
†School of Engineering and Physical Sciences
Heriot-Watt University Edinburgh EH14 4AS, Scotland, UK

***Abstract* — The Internet of Things (IoT) envisions ubiquitous, cheap and low data rate connectivity between humans, machines and objects. The main technology that can satisfy this vision is wireless communication technology, but to embed this into objects at a large scale, some requirements like battery-free and long range communication should be considered.**

In this work we propose a modulator that can backscatter different chirps, based on Chirp Spread Spectrum (CSS) modulation which can achieve high sensitivities, meaning long range communication. Moreover, we prove with this design that we can reflect backscatter Long Range (LoRa) preamble symbols with a Spreading Factor (SF) of 7 and 125 kHz of bandwidth. Thus, it will be possible to reuse the LoRa receivers already developed.

***Keywords* — Backscatter modulation, chirp spread spectrum, internet of things, low power, .**

I. Introduction

In the Internet of Things (IoT) context, where billions of connected objects are expected to be ubiquitously deployed worldwide, the frequent battery maintenance of ubiquitous wireless nodes is undesirable or even impossible. The growth of the devices will be made possible only if the sensors battery needs are eliminated or reduced significantly. For low power sensors and devices, careful power management and power conservation are critical to device lifetime and effectiveness. One of the possible solutions is to change completely the paradigm of the radio transceivers in the wireless nodes of a IoT system. The backscatter communication, which consists in reflecting and modulating an incident radio signal, promises to be an excellent alternative to active radios, due to their low cost, low power and low complexity implementation.

In most Radio Frequency Identification (RFID) systems and passive sensors, the reader to tag communication is based on amplitude shift keying (ASK) or phase shift keying (PSK) that modulates either the amplitude, or both the amplitude and phase, of the reader's transmitted Radio Frequency (RF) carrier. However, the work [1] has shown that modulated backscatter can be extended to include higher order modulation schemes, such as Four-state Quadrature Amplitude Modulation (4-QAM). While ASK and PSK transmit 1 bit of data per symbol period, 4-QAM can transmit 2 bits per symbol period, thus increasing the data rate and leading to reduced on-chip power consumption and extended read range. In [2], [3] a 16-QAM modulator for backscatter communication was developed. Ambient radio waves can be used as a source to backscatter the data to a receiver, eliminating the need for dedicated RF transmitters. Several studies have shown the use of this technique to allow battery-free backscatter devices using broadcast FM stations [4], TV station [5] and Wi-Fi signals [6]. In [7] the authors present a tag that operates with ambient backscatter signals while featuring high-order modulation with ultra low power consumption.

As it is known, backscatter communication is a low power and low cost implementation, but it is limited to short ranges. Some recent studies implemented a backscatter modulator that can be compatible with Long Range (LoRa) hardware, and extend the range of communication [8]. The implementation can synthesize LoRa symbols, but has very low data rates which limits the scalability of the technology for other applications. In [9] the authors utilize ambient LoRa transmissions as the excitation signals, and shift the incoming active LoRa chirp by an amount of $BW/2$ and $-BW/2$ and then join them into a new chirp, respecting the LoRa standard. This implementation is totally dependent on LoRa communication, since it uses FSK modulation in an active LoRa chirp. Moreover, the data rate is very low, since the design can encodes only one bit per LoRa symbol.

In this work, we present a backscatter modulator that can synthesize Chirp Spread Spectrum (CSS) modulation or any kind of chirps and it is scalable for other type of applications due to its simple implementation. The modulator is composed by two transistors and a Wilkinson power divider and can achieve very low power consumption making it possible to adapt this technology into domains such as smart cities, precision agriculture and many others where backscatter is currently unfeasible.

The paper is organized as follows, Section II presents the operational principle of the system, Section III presents the results and Section IV the main conclusions.

II. Circuit Description

The circuit developed for this work is demonstrated in Fig. 1. The prototype implemented is composed by a Wilkinson power divider, two matching networks and two transistors (ATF-54143, Broadcom). This circuit was designed

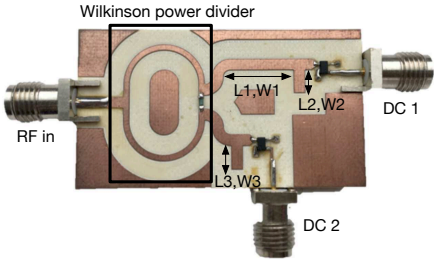

Fig. 1. Photograph of the backscatter circuit. Element values are L1 = 9.86 mm, W1 = 1.87 mm, L2 = 3.65 mm, W2 = 1.87 mm, L3 = 3.65 mm, W3 = 1.87 mm. Substrate for the transmission lines is Astra MT77, thickness = 0.762 mm, ε_r = 3.0, tan δ = 0.0017.

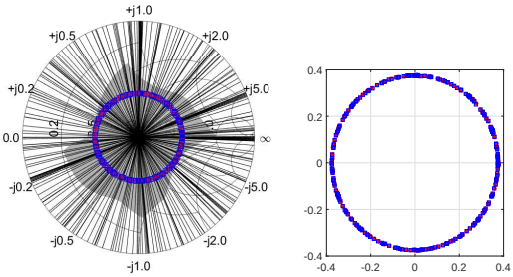

(a) (b)

Fig. 2. Simulations of the circuit developed. a) Reflection coefficients obtained from simulation and mapped with the intersection of 256 different phases with constant VSWR of 2.2. b) Detailed mapping of point obtained from simulations with the intersections.

for an operation frequency of 2.45 GHz and optimized with 0 dBm of input power. In Fig. 1 it is possible to observe the difference of line length which corresponds to 45°phase shift. The drain impedance of each transistor varies for different gate voltages, and it is possible to obtain different reflection coefficients. This means that is possible to determine different phases with a constant Voltage Standing Wave Ratio (VSWR).

As it was said previously, it is possible to alter the gate voltages at each transistor in order to achieve different reflection coefficients. Using ADS and through the Large-Signal S-Parameters (LSSP) simulation it was possible to characterize the circuit from 0 V to 0.6 V with a step of 1 mV, at each transistor. The result of this simulation can be seen in Fig. 2a represented by a gray shadow inside the Smithchart, with different reflection coefficients. Using this fine sweep of voltage it is possible to have a very accurate modulator, that can change, with a high precision, the phase of the reflected wave. In Fig. 2a it can be seen 256 different phases (represented with black lines in the Smithchart) and their intersection with a constant VSWR of 2.2 (represented in red in the Smithchart). Moreover, through our characterization, we match the reflection coefficients with the intersections (represented in blue in the Smithchart) and extract the voltages needed to the expected phases. These matching can be seen in more detail in Fig. 2b.

Considering an ideal chirp (signal whose frequency

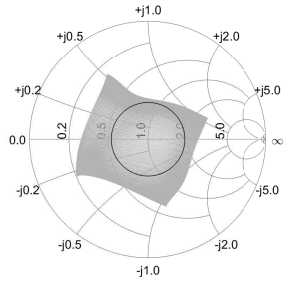

Fig. 3. Reflection coefficients obtained from measurements and a circle with a VSWR of 1.9. The voltages at each gate of transistor were swept from 0 V to 0.6 V with a step of 1 mV.

increases or decreases with time) it is possible to extract the phase of the time domain waveform at each time instant and based on the previous explanation of the circuit analysis we can obtain the regulated control voltage profiles in time domain to synthesize the chirp in the backscatered signal.

III. Results

Fig. 3 presents the results obtained from the measurements with voltages ranging from 0 V to 0.6 V with steps of 1 mV on each transistor at 2.45 GHz. Thus, it was necessary to determine a constant VSWR that fits into the mesh of the obtained reflection coefficients, as can be seen in Fig. 3, with a value of 1.9. The setup used for these measurements includes a Performance Network Analyzer (PNA) (E8361C, Agilent Technologies) and the Arbitrary Waveform Generator (AWG) (AWG5012C, Tektronix).

After acquiring the reflection coefficients it was possible to determine the control voltage profiles based on the chirp present in Fig. 4a.

Using the setup presented in Fig. 5 (composed by a Vector Signal Generator (VSG) (SMJ100A, Rohde & Schwarz), an AWG and an oscilloscope (DSO804A, Keysight)) and applying the voltages determined into the AWG a backscattered chirp signal was obtained, Fig. 4b, which is a linear chirp with 125 kHz of bandwidth and a duration of 2 ms.

This approach enables a large number of applications and the most important is the LoRa technology, which uses CSS modulation. LoRa can occupy three different bandwidth: 125 kHz, 250 kHz and 500 kHz. LoRa symbols are modulated over an up-chirp of 125 kHz bandwidth and different orthogonal Spreading Factors (SFs) (from 7 to 12) are used based on data rate requirements and channel conditions. The LoRa physical layer includes 8 preamble symbols, 2 synchronization symbols, physical payload and optional CRC.

Figure 6a presents a chirp which is based on one symbol from the LoRa preamble modulation with a SF of 7 and 125 kHz of bandwidth. Following the same procedure explained above the voltage profiles presented in Fig. 7 were obtained and synthesized using the AWG. The backscattered signal obtained can be seen in Fig. 6b.

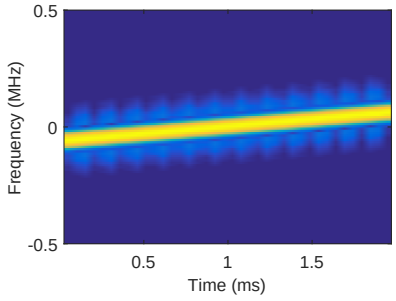

(a)

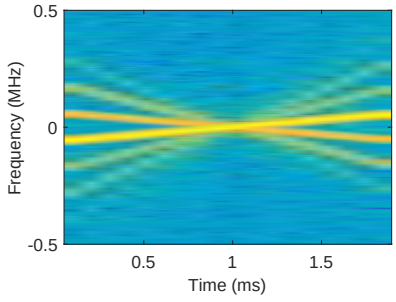

(b)

Fig. 4. Chirp with 125 kHz of bandwidth and time duration of 2 ms. a) Original chirp synthesized with our system. b) Obtained chirp from the measurement setup.

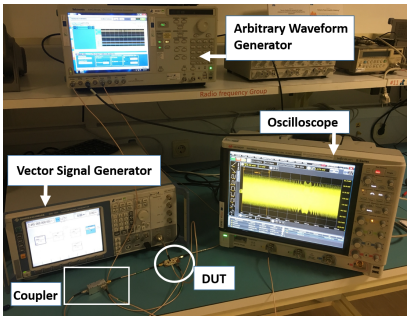

Fig. 5. Photograph of the measurement setup used to acquire the reflected chirps.

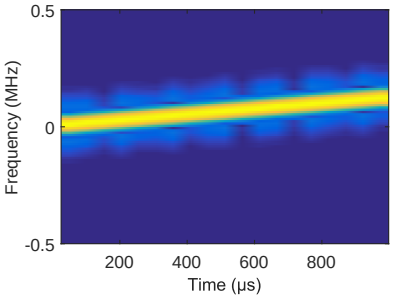

(a)

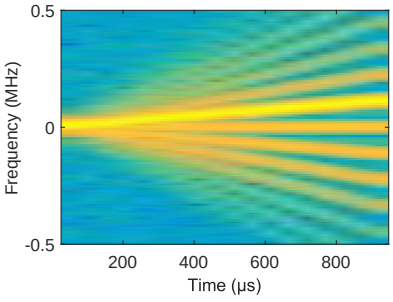

(b)

Fig. 6. Chirp based on one symbol from preamble of LoRa modulation with a SF of 7, with 125 kHz of bandwidth and time duration of 1 ms. a) Original chirp synthesized with our system. b) Obtained chirp from the measurement setup.

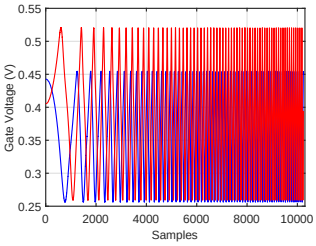

Fig. 7. Voltage profiles in time domain, obtained from mapping the phases synthesized from the chirp presented in Fig. 6 with reflections coefficients presented in Fig. 3.

Figures 4b and 6b present the obtained chirps from the measurements. As can be seen the chirps present some distortion that is caused by the transistors. There are some techniques to remove the harmonics, namely the backscatter harmonic cancellation presented in [8].

IV. Conclusions

In this paper, a novel approach for backscatter chirp signals was presented. The paper described a modulation technique that will enable long range reliable communication capabilities of radios at the low power and cost of backscatter hardware. Moreover, by synthesizing LoRa symbols it will be possible to use the already developed readers that offer sensitivities of -149 dBm and through this improve the range of communication of backscatter radios. As a future work we plan to build a LoRa frequency prototype including the digital logic that will be able to backscatter LoRa symbols.

References

[1] S. J. Thomas, E. Wheeler, J. Teizer, and M. S. Reynolds, "Quadrature amplitude modulated backscatter in passive and semipassive UHF RFID systems," *IEEE Trans. Microw. Theory Tech.*, vol. 60, no. 4, pp. 1175–1182, 2012.

[2] S. J. Thomas and M. S. Reynolds, "A 96 Mbit/sec, 15.5 pJ/bit 16-QAM modulator for UHF backscatter communication," in *2012 IEEE Int. Conf. RFID*, Apr 2012, pp. 185–190.

[3] R. Correia, A. Boaventura, and N. Borges Carvalho, "Quadrature Amplitude Backscatter Modulator for Passive Wireless Sensors in IoT Applications," *IEEE Trans. Microw. Theory Tech.*, vol. 65, no. 4, pp. 1103–1110, Apr 2017.

[4] S. N. Daskalakis, J. Kimionis, A. Collado, G. Goussetis, M. M. Tentzeris, and A. Georgiadis, "Ambient Backscatterers Using FM Broadcasting for Low Cost and Low Power Wireless Applications," *IEEE Trans. Microw. Theory Tech.*, pp. 1–12, 2017.

[5] V. Liu, A. Parks, V. Talla, S. Gollakota, D. Wetherall, J. R. Smith, V. Liu, A. Parks, V. Talla, S. Gollakota, D. Wetherall, and J. R. Smith, "Ambient backscatter: wireless communication out of thin air," *SIGCOMM Comput. Commun. Rev.*, vol. 43, no. 4, p. 39, 2013.

[6] B. Kellogg, A. Parks, S. Gollakota, J. R. Smith, and D. Wetherall, "Wi-fi backscatter: internet connectivity for rf-powered devices," *SIGCOMM Comput. Commun. Rev.*, vol. 44, no. 4, pp. 607–618, 2014.

[7] S. N. Daskalakis, R. Correia, G. Goussetis, M. M. Tentzeris, N. B. Carvalho, and A. Georgiadis, "Spectrally Efficient 4-PAM Ambient FM Backscattering for Wireless Sensing and RFID Applications," in *IEEE/MTT-S Int. Microw. Symp. - IMS*, Jun 2018, pp. 266–269.

[8] V. Talla, M. Hessar, B. Kellogg, A. Najafi, J. R. Smith, and S. Gollakota, "LoRa Backscatter: Enabling The Vision of Ubiquitous Connectivity," *Proc. ACM Interactive, Mobile, Wearable Ubiquitous Technol.*, vol. 1, no. 3, pp. 1–24, Sep 2017.

[9] Y. Peng, L. Shangguan, Y. Hu, Y. Qian, X. Lin, X. Chen, D. Fang, and K. Jamieson, "PLoRa: A Passive Long-Range Data Network from Ambient LoRa Transmissions," in *Proc. 2018 Conf. ACM Spec. Interes. Gr. Data Commun. - SIGCOMM '18*. New York, New York, USA: ACM Press, 2018, pp. 147–160.